

Title	Rapid separation of phenolic flavourings by liquid chromatography and nanomolar electrochemical detection at a boron-doped diamond electrode
Authors	Hayes, Phyllis E.
Publication date	2021-01
Original Citation	Hayes, P. E. 2021. Rapid separation of phenolic flavourings by liquid chromatography and nanomolar electrochemical detection at a boron-doped diamond electrode. PhD Thesis, University College Cork.
Type of publication	Doctoral thesis
Rights	© 2021, Phyllis E. Hayes. - <a href="https://creativecommons.org/licenses/by-nc-nd/4.0/">https://creativecommons.org/licenses/by-nc-nd/4.0/</a>
Download date	2023-05-05 19:05:28
Item downloaded from	<a href="http://hdl.handle.net/10468/11855">http://hdl.handle.net/10468/11855</a>

# **Rapid Separation of Phenolic Flavourings by Liquid Chromatography and Nanomolar Electrochemical Detection at a Boron-Doped Diamond Electrode**

by

**Phyllis Hayes BSc. MSc.**

A thesis submitted to the National University of Ireland  
for the degree of Doctor of Philosophy

January 2021

Under the supervision of Prof. Jeremy D. Glennon  
Head of School: Dr. Humphrey Moynihan



# UCC

Coláiste na hOllscoile Corcaigh, Éire  
University College Cork, Ireland

School of Chemistry  
National University of Ireland, Cork,  
Ireland

## **Declaration**

This is to certify that the work I am submitting is my own and has not been submitted for another degree, either at University College Cork or elsewhere. All external references and sources are clearly acknowledged and identified within the contents. I have read and understood the regulations of University College Cork concerning plagiarism.

Digital signature of the candidate: Phyllis Kager

## Abstract

In recent years, there has been considerable research focus on natural plant phenolics. They are present as key contributors to the flavour of food and beverages and are also proven to function as antioxidants, providing a wide range of physiological properties including anti-cancer, anti-inflammatory and anti-microbial. Their investigation and detection in plants, food and beverages require the development of rapid, selective and sensitive analytical methods.

In this thesis, an overview of plant secondary metabolites, their classification and physiological properties are given. The characteristics of the boron-doped diamond (BDD) electrode and the coupling of liquid chromatography (LC) with electrochemical detection (ECD) are also described. This work focuses on determining the phenolic analytes that are associated with the distinct flavour of whiskey. Initially, the whiskey is analysed using direct electroanalysis at a Nafion-modified BDD electrode. Inclusion complexation with cyclodextrins (CDs) and peak deconvolution reveals guaiacols, phenols and cresol isomers as the phenolic molecular fingerprint of whiskey. Pre-concentration with Nafion on the electrode surface results in a 5-fold decrease in the limit of detection (LOD) compared to the bare BDD electrode. The electro-oxidation mechanisms of the analytes are also investigated with cyclic voltammetry (CV).

To specifically determine the flavour contributing analytes and to differentiate whiskey based on geographical origin, detection at the BDD electrode is preceded by chromatographic separation with a C<sub>18</sub> core-shell column. Significantly higher concentrations of the phenolic compounds are determined in Islay whiskey, attributed to its unique production process. The detection limit ( $S/N = 3$ ) of guaiacol with LC-ECD is 5 nM, 80-fold lower than that obtained with LC-ultraviolet (UV) detection (2  $\mu$ M).

Attention was then turned to the separation and detection of gallic acid (GA) and ellagic acid (EA) in whiskey. GA and EA are present in the oak casks used for maturation and so their presence can be used as markers of authentic whiskey. Chromatographic separation using a reversed-phase (RP) C<sub>18</sub> column with gradient elution is followed by amperometric detection at a BDD electrode. LODs of 60 and

200 nM are obtained for GA and EA, respectively, with the highest concentrations of both acids found in a 14-year-old whiskey.

Rapid and sensitive analytical methods are required for the detection of spoilage metabolites in the food and beverage manufacturing industries. In beverages, guaiacol may be present as a result of microbial metabolism, resulting in the formation of a medicinal off-odour with subsequent financial implications. LC-ECD at a BDD electrode provides LODs of 10-30 nM for guaiacol and its phenolic precursors. Notably, separation is achieved within 60 s, providing a rapid alternative to traditional microbiological culturing methods.

The outcomes presented represent an advancement in the separation and selective sensing of phenolic analytes, and are of importance in the food and beverage sectors.

## **Acknowledgements**

First and foremost, I want to thank Professor Jeremy Glennon for providing me with the opportunity to undertake this PhD, and for his expertise, guidance and enthusiasm shown throughout this research. Thank you to the Irish Research Council, PepsiCo and Liam Reddy, without whom this PhD would not have been possible.

Thank you to Professor John Luong for the significant commitment, interest and time that he has devoted to this research. I am particularly grateful to Dr. Alyah Buzid for her continued support, practical suggestions and guidance since beginning this PhD.

I am also thankful to Dr. Anna Hogan for her advice, technical assistance and for never lacking the time to help. A special mention to Janine Boertjes for proofreading and for the endless entertainment, laughter and good memories that won't be forgotten.

Thank you to the academic, technical and administrative staff who assisted or contributed in any way to this research including Dr. Dara Fitzpatrick, Dr. Elizabeth Gilchrist, Johnny Ryan, Tony Hogan, Tina Kent, Denis Duggan, Kasia Pyrz, Claire Tobin, Niamh Daly and Mary O'Neill. A special mention of thanks to Dr. Tom O'Mahony for his technical support and assistance, and to Dr. Victor Langsi for his HPLC knowledge and advice.

Thank you to present and past lab members including Majidah, Huda and Dr. Xi Cao for making this experience an enjoyable one.

Finally, thanks to everyone at home for their continuous support and encouragement since beginning this research.

## Publications

1. **Phyllis E. Hayes**, Alyah Buzid, John H.T. Luong, Jeremy D. Glennon. “Rapid nanomolar detection of guaiacol from its precursors using a core-shell reversed-phase column coupled with a boron-doped diamond electrode”, **Electroanalysis**, 33 (2021) 766.
2. **Phyllis E. Hayes**, Jeremy D. Glennon, John H.T. Luong. “Electroanalysis of gallic and ellagic acids at a boron-doped diamond electrode coupled with high-performance liquid chromatography”, **Electroanalysis**, 32 (2020) 2027.
3. **Phyllis E. Hayes**, John H.T. Luong, Elizabeth S. Gilchrist, Alyah Buzid, Jeremy D. Glennon. “Profiling of phenolic flavourings using core-shell reversed-phase liquid chromatography with electrochemical detection at a boron-doped diamond electrode”, **Journal of Chromatography A**, 1612 (2020) 460649.
4. **Phyllis E. Hayes**, Jeremy D. Glennon, Alyah Buzid, John H.T. Luong. “Simultaneous electroanalysis of guaiacol and its analogues based on their differential complexation with  $\alpha$ -cyclodextrin on Nafion modified boron-doped diamond electrode”, **Electroanalysis**, 32 (2019) 119.
5. Alyah Buzid, **Phyllis E. Hayes**, Jeremy D. Glennon, John H.T. Luong. “Captavidin as a regenerable biorecognition element on boron-doped diamond for biotin sensing”, **Analytica Chimica Acta**, 1059 (2019) 42.
6. Alyah Buzid, Eoin Ó Muimhneacháin, F. Jerry Reen, **Phyllis E. Hayes**, Leticia M. Pardo, Fengjun Shang, Fergal O’Gara, Jonathan Sperry, John H. T. Luong, Jeremy D. Glennon, Gerard P. McGlacken. “Synthesis and electrochemical detection of a thiazolyl-indole natural product isolated from the nosocomial pathogen *Pseudomonas aeruginosa*”, **Analytical and Bioanalytical Chemistry**, 408 (2016) 6361.

## Poster Presentations

1. **Phyllis E. Hayes**, Alyah Buzid, John H.T. Luong, Elizabeth S. Gilchrist, Jeremy D. Glennon. “Profiling of phenolic flavourings in whiskey by reversed-phase liquid chromatography with electrochemical detection at a boron-doped diamond electrode”, **48<sup>th</sup> International Symposium on High-Performance Liquid Phase Separations and Related Techniques**, Milan, Italy. 16<sup>th</sup>-20<sup>th</sup>, June 2019.
2. **Phyllis E. Hayes**, Alyah Buzid, Jeremy D. Glennon. “Liquid chromatography-mass spectrometric determination of guaiacol and its phenolic precursors associated with *Alicyclobacillus* contamination in fruit juice and beverages”, **32<sup>nd</sup> International Symposium on Chromatography (ISC 2018)**, Cannes-Mandelieu, France. 23<sup>rd</sup>-27<sup>th</sup>, September 2018.
3. **Phyllis E. Hayes**, Emma Birney, Alyah Buzid, Eoin Ó Muimhneacháin, F. Jerry Reen, Fergal O’Gara, Gerard P. McGlacken, Jeremy D. Glennon. “Chromatographic determination of the *Pseudomonas aeruginosa* Molecular Signature using liquid chromatography-mass spectrometry”, **32<sup>nd</sup> International Symposium on Chromatography (ISC 2018)**, Cannes-Mandelieu, France. 23<sup>rd</sup>-27<sup>th</sup>, September 2018.
4. Alyah Buzid, **Phyllis E. Hayes**, Gerard P. McGlacken, John H.T. Luong, Jeremy D. Glennon. “Fast liquid chromatography coupled with electrochemical detection for the determination of *Pseudomonas aeruginosa* signalling molecules”, **32<sup>nd</sup> International Symposium on Chromatography (ISC 2018)**, Cannes-Mandelieu, France. 23<sup>rd</sup>-27<sup>th</sup>, September 2018.
5. **Phyllis E. Hayes**, Alyah Buzid, Valery Taustsiakou, Eoghan Ryan, Eoin Ó Muimhneacháin, F. Jerry Reen, Fergal O’Gara, Gerard P. McGlacken, Jeremy D. Glennon. “Mixed-mode chromatographic analysis of *Pseudomonas aeruginosa* quorum sensing signalling molecules”, **23<sup>rd</sup> International Symposium on Separation Sciences (ISSS)**, Vienna, Austria. 19<sup>th</sup>-22<sup>nd</sup>, September 2017.



- 6     **Phyllis E. Hayes**, Alyah Buzid, Elizabeth S. Gilchrist, Jeremy D. Glennon.  
“High performance liquid chromatographic analysis of guaiacol and its  
phenolic precursors associated with *Alicyclobacillus* spp. contamination in  
beverages”, **69<sup>th</sup> Irish Universities Research Colloquium**, Dublin City  
University, Ireland. 22<sup>nd</sup>-23<sup>rd</sup>, June 2017.

## List of Figures and Schemes

		Page
Scheme 1.1	Biosynthesis of phenolic compounds in the pentose phosphate, shikimate and phenylpropanoid pathways in plants.	3
Figure 1.1	Chemical structures of phenol (A), phenoxide ion (B) and resonance structures (C).	4
Figure 1.2	Chemical structure of the polyphenol, ellagic acid.	4
Scheme 1.2	Main classes of polyphenolic compounds.	5
Figure 1.3	Examples of hydroxybenzoic (A) and hydroxycinnamic (B) acids.	7
Figure 1.4	The basic structure of a flavonoid molecule.	8
Figure 1.5	Chemical structure of quercetin (A) and kaempferol (B).	10
Figure 1.6	Chemical structure of (-)-epicatechin.	11
Figure 1.7	Chemical structure of (A) cis- and (B) trans-resveratrol.	12
Figure 1.8	SEM images of different diamond films. Upper: nanocrystalline diamond – (i) grain structure and (ii) surface morphology where the typical roughness is in the range of 30-50 nm. Lower: polycrystalline diamond – (iii) grain structure and (iv) surface morphology with a surface roughness of several tens of microns.	15
Figure 1.9	CVs of BDD electrodes with different boron-doping concentrations in an aqueous solution of 10 mM $[\text{Fe}(\text{CN})_6]^{4-}$ and 0.1 M KCl. Scanning rate: 100 mV s <sup>-1</sup> .	17
Figure 1.10	Contact angle measurements of (A) H-terminated and (B) O-terminated boron-doped diamond surfaces.	19
Figure 1.11	A schematic diagram of a CV highlighting the anodic peak potential ( $E_{pa}$ ), cathodic peak potential ( $E_{pc}$ ), anodic current ( $i_{pa}$ ) and cathodic current ( $i_{pc}$ ).	19
Figure 1.12	The contributing parameters to the Fundamental Resolution Equation.	23
Figure 1.13	SEM images of (A) spherically shaped and (B) irregular shaped porous silica particles.	24
Figure 1.14	Data from Scopus showing the increasing number of core-shell related studies from 2001-2018.	26
Figure 1.15	A representation of a superficially porous particle with a diameter of 2.7 $\mu\text{m}$ and a solid core of 1.7 $\mu\text{m}$ .	27
Figure 1.16	The van Deemter plot. Where A, B and C represent the diffusion coefficients; $v$ is the linear velocity of the mobile phase and HETP is the height equivalent to a theoretical plate.	27
Figure 1.17	The effect on peak performance by the means of the difference between wide particle distribution (conventional silica) and narrow particle distribution (core-shell silica).	28

Figure 1.18	Comparative separations with 5 $\mu\text{m}$ particles: core-shell vs. fully porous. Columns: 4.6 x 150 mm. A noticeable reduction in retention time and an increase in column efficiency is evident with the core-shell particles.	30
Figure 1.19	Thin-layer cell amperometric detector: (A) inlet, (B) outlet, (C) working electrode and (D) spacer gasket.	33
Figure 1.20	Wall-jet amperometric detector: (A) inlet, (B) outlet, (C) working electrode and (D) spacer gasket.	34
Figure 1.21	Parallel and series configurations for dual electrode detection systems. $W_1$ = working electrode 1; $W_2$ = working electrode 2. (A) parallel; (B) series and (C) parallel adjacent. Arrow indicates the direction of flow.	35
Figure 1.22	The simplest PAD waveform. The analyte is detected by the application of the detection potential ( $E_{\text{det}}$ ) at the electrode surface for a period of time. Then the anodic oxidative potential ( $E_{\text{oxd}}$ ) is applied for a time to produce a surface oxide on the electrode surface. Finally, a cathodic reductive potential ( $E_{\text{red}}$ ) is applied to reactivate the electrode.	36
Figure 1.23	A comparison of electrode efficiency as a function of flow rate for coulometric and amperometric detection. Conversion efficiency decreases for the thin-layer amperometric electrode but remains at 100 % for the coulometric electrode.	37
Figure 1.24	A cross-section through a dual coulometric electrode showing the placement of working, counter and reference electrodes.	38
Figure 1.25	A homemade electrochemical flow cell. The working electrode (A), the counter electrode (B) and the reference electrode (C).	39
Figure 1.26	An example of a whiskey flavour wheel.	46
Figure 1.27	The whiskey lactones. (A) cis-3-methyl-4-octanolide and (B) trans-3-methyl-4-octanolide.	47
Figure 1.28	Chemical structures of (A) syringaldehyde and (B) furfural.	48
Figure 1.29	HPLC-FL detection of a 100 ppb phenolic standard mixture.	49
Scheme 2.1	The electrochemical oxidation pathway and the main oxidation product of guaiacol. The formation of three possible radicals with $R_1$ as the predominant radical. $C_1$ is then subject to further oxidation to form o-quinone together with the release of methanol, which is also electroactive on the BDD electrode.	78
Figure 2.1	CVs of the bare BDD electrode for (A) guaiacol and (B) 4-EG. The concentration of each analyte is 100 $\mu\text{M}$ in 100 mM phosphate buffer, pH 2 with 5 % EtOH at the scan rate of 100 $\text{mV s}^{-1}$ .	80
Scheme 2.2	Two plausible minor oxidation products of guaiacol as postulated in the literature.	80
Figure 2.2	CVs of the bare BDD electrode for (A) phenol, (B) 4-EP, (C) o-cresol, (D) m-cresol and (E) p-cresol. The concentration of each analyte is 100 $\mu\text{M}$ in 100 mM phosphate buffer, pH 2 with 5 % EtOH at the scan rate of 100 $\text{mV s}^{-1}$ .	81

Figure 2.3	CVs of the Nafion modified BDD electrode for (A) guaiacol and (B) 4-EG. The concentration of each analyte is 100 $\mu\text{M}$ in 100 mM phosphate buffer, pH 2 with 5 % EtOH at the scan rate of 100 $\text{mV s}^{-1}$ .	82
Figure 2.4	CVs of the Nafion modified BDD electrode for (A) phenol, (B) 4-EP, (C) o-cresol, (D) m-cresol and (E) p-cresol. The concentration of each analyte is 100 $\mu\text{M}$ in 100 mM phosphate buffer, pH 2 with 5 % EtOH at the scan rate of 100 $\text{mV s}^{-1}$ .	83
Figure 2.5	CVs of the (A) bare and (B) Nafion modified BDD electrodes in 5 mM $\text{Fe}(\text{CN})_6^{4-/3-}$ prepared in 1 M KCl, at the scan rate of 50 $\text{mV s}^{-1}$ .	84
Figure 2.6	(A) EIS of the bare (red dotted line) and Nafion (black dotted line) modified BDD electrodes in 10 mM $\text{Fe}(\text{CN})_6^{4-/3-}$ prepared in 0.1 M KCl. Insert: (B) the modified Randles circuit.	85
Figure 2.7	Chronocoulometry curves of 10 $\mu\text{M}$ guaiacol on (A) bare and (B) Nafion modified BDD electrodes, using 100 mM phosphate buffer, pH 7.	86
Figure 2.8	SWV of a standard mixture of 4-EG and p-cresol (4 $\mu\text{M}$ each) at different pH values (2, 5, and 7), with 5 % EtOH and 10 mM $\alpha\text{-CD}$ . Detection was achieved on the Nafion modified BDD electrode vs. Ag/AgCl.	87
Figure 2.9	SWV of 4 $\mu\text{M}$ (A) phenol, (B) guaiacol, (C) m-cresol, (D) 4-EP and (E) 4-EG, using 100 mM phosphate buffer, pH 2 with 5 % EtOH in the absence (black lines) and presence (red lines) of 10 mM $\alpha\text{-CD}$ . Detection was achieved on the bare BDD electrode vs. Ag/AgCl.	88
Figure 2.10	SWV of a standard mixture of phenol, guaiacol, o-cresol, m-cresol, p-cresol, 4-EP and 4-EG at 4 $\mu\text{M}$ each, using 100 mM phosphate buffer, pH 2 with 5 % EtOH in the (A) absence and (B) presence of 10 mM $\alpha\text{-CD}$ . Detection was achieved on the bare BDD electrode vs. Ag/AgCl.	88
Figure 2.11	SWV of 4 $\mu\text{M}$ each (A) phenol, (B) guaiacol, (C) m-cresol, (D) 4-EP and (E) 4-EG, using 100 mM phosphate buffer, pH 2 with 5 % EtOH in the absence (black lines) and presence (red lines) of 10 mM $\alpha\text{-CD}$ . Detection was achieved on the Nafion modified BDD electrode vs. Ag/AgCl.	89
Figure 2.12	SWV of a standard mixture of phenol, guaiacol, m-cresol, 4-EP and 4-EG at 4 $\mu\text{M}$ each using 100 mM phosphate buffer, pH 2 with 5 % EtOH in the absence (black line) and presence (red line) of 10 mM $\alpha\text{-CD}$ . Detection was achieved on the Nafion modified BDD electrode vs. Ag/AgCl.	90
Figure 2.13	Resolved SWV of standard mixtures at 4 $\mu\text{M}$ each of 4-EG, guaiacol, 4-EP, o-cresol, p-cresol, m-cresol, and phenol after the application of peak deconvolution using Origin Pro 8.5.1. The electrolyte was 100 mM phosphate buffer, pH 2 with 5 % EtOH containing 10 mM $\alpha\text{-CD}$ . Detection was achieved on the Nafion modified BDD electrode vs. Ag/AgCl.	90
Figure 2.14	(A) Calibration curve and (B) plot of phenol; (C) calibration curve and (D) plot of guaiacol; (E) calibration curve and (F) plot of o-cresol and (G) calibration curve and (H) plot of m-cresol. The electrolyte was 100 mM phosphate, pH 2 with 5 % EtOH containing 10 mM $\alpha\text{-CD}$ .	94

	Detection was achieved on the Nafion modified BDD electrode vs. Ag/AgCl. Error bars represent the standard deviation.	
Figure 2.15	(A) Calibration curve and (B) plot of p-cresol; (C) calibration curve and (D) plot of 4-EP; and (E) calibration curve and (F) plot of 4-EG. The electrolyte was 100 mM phosphate, pH 2 with 5 % EtOH containing 10 mM $\alpha$ -CD. Detection was achieved on the Nafion modified BDD electrode vs. Ag/AgCl. Error bars represent the standard deviation.	95
Figure 2.16	The stability of the Nafion modified BDD electrode towards 4 $\mu$ M each of 4-EG and p-cresol using SWV. The electrolyte was 100 mM phosphate buffer, pH 2 with 5 % EtOH containing 10 mM $\alpha$ -CD.	96
Figure 2.17	Resolved SWV of Islay whiskey after application of peak deconvolution using Origin Pro 8.5.1 on the Nafion modified BDD electrode vs. Ag/AgCl. The electrolyte was 100 mM phosphate buffer, pH 2 with 5 % EtOH containing 10 mM $\alpha$ -CD.	97
Figure 2.18	SWV of Islay whiskey in the (A) absence and the (B) presence of $\alpha$ -CD using 100 mM phosphate buffer, pH 2 with 5 % EtOH on the Nafion modified BDD electrode vs. Ag/AgCl.	97
Figure 2.19	SWV of blank Islay whiskey (black lines) and spiked (red lines) with 5 $\mu$ M each of (A) phenol, (B) guaiacol, (C) o-cresol, (D) m-cresol, (E) p-cresol, (F) 4-EP and (G) 4-EG, using 100 mM phosphate buffer, pH 2 with 5 % EtOH containing 10 mM $\alpha$ -CD. Detection was achieved on the Nafion modified BDD electrode vs. Ag/AgCl.	98
Figure 2.20	SWV of Islay whiskey using 100 mM phosphate buffer, pH 2, with 5 % EtOH containing (A) S- $\beta$ -CD, (B) $\beta$ -CD, (C) M- $\beta$ -CD, (D) a mixture of $\alpha$ -CD and M- $\beta$ -CD, and (E) a mixture of $\alpha$ -CD and $\beta$ -CD. Detection was achieved on the Nafion modified BDD electrode vs. Ag/AgCl.	99
Figure 2.21	SWV of a standard mixture 4-VG, 4-EG, eugenol, and guaiacol (1 $\mu$ M each) using 100 mM phosphate buffer, pH 2 with 5 % EtOH containing (A) 10 mM $\alpha$ -CD and (B) 20 mM $\alpha$ -CD. Detection was achieved on the Nafion modified BDD electrode vs. Ag/AgCl.	100
Figure 2.22	Key dimensions of $\alpha$ -CD and 4-EG.	101
Figure 2.23	DPV before and after the anodic treatment at + 2 V for 1 min on (A) bare and (B) Nafion modified BDD electrodes after they were exposed to 1 mM guaiacol in 100 mM phosphate buffer, pH 7.	102
Figure 2.24	DPV and SWV of Islay whiskey on the bare BDD electrode vs. Ag/AgCl, using 100 mM phosphate buffer, pH 2 with 5 % EtOH containing 10 mM $\alpha$ -CD.	102
Figure 2.25	HPLC chromatograms of the 10-year-old blank Islay whiskey (black line) and spiked whiskey (red line) with 20 $\mu$ M of each standard. Column: Agilent Eclipse XDB C <sub>18</sub> (4.6 x 150 mm, 5 $\mu$ m), mobile phase: 30: 70 ACN: H <sub>2</sub> O (v/v, %) flow rate: 1 mL/min, injection volume: 5 $\mu$ L, column temperature: 25 °C, UV detection: 210 nm.	103
Figure 2.26	HPLC chromatograms of 40 $\mu$ M of each standard at different wavelengths (210, 254, and 280 nm). Column: Agilent Eclipse XDB	103

C<sub>18</sub> (4.6 x 150 mm, 5 μm), mobile phase: 30: 70 ACN: H<sub>2</sub>O (v/v, %), flow rate: 1 mL/min, injection volume: 5 μL, column temperature: 25 °C.

Figure 3.1	CV response in the absence (dashed lines) and presence (solid lines) of 100 μM each for (A) guaiacol; (B) 4-EG; (C) phenol; and (D) o-cresol on the bare BDD electrode vs. Ag/AgCl in 100 mM phosphate buffer, 5 % EtOH, pH 2, with a scan rate of 50 mV s <sup>-1</sup> .	115
Scheme 3.1	Electrochemical oxidation of (A) guaiacol and its derivatives and (B) phenols and cresol isomers.	116
Figure 3.2	The effect of mobile phase % ACN on the retention time of 20 μM each of phenol, guaiacol, m-cresol, p-cresol, o-cresol, 4-VG, 4-EP, 4-EG, and eugenol. Mobile phase: ACN:10 mM formate pH 3 (A) 15:85, (B) 20:80 and (C) 25:75. Column: HALO C <sub>18</sub> core-shell (3 x 50 mm, 2.7 μm), flow rate: 1 mL/min, injection volume: 5 μL, column temperature: 25 °C, UV detection: 210 nm.	117
Figure 3.3	Plot of k versus % ACN. Mobile phase: ACN:10 mM formate pH 3 (15:85), (20:80) and (25:75). Column: HALO C <sub>18</sub> core-shell (3 x 50 mm, 2.7 μm), flow rate: 1 mL/min, injection volume: 5 μL, column temperature: 25 °C, UV detection: 210 nm.	118
Figure 3.4	The effect of the mobile phase pH on the retention time of 20 μM each of phenol, guaiacol, m-cresol, p-cresol, o-cresol, 4-VG, 4-EP, 4-EG and eugenol. Mobile phase: 15:85, (A) ACN:10 mM formate pH 3 and (B) ACN: 10 mM acetate pH 5. Column: HALO C <sub>18</sub> core-shell (3 x 50 mm, 2.7 μm), flow rate: 1 mL/min, injection volume: 5 μL, column temperature: 25 °C, UV detection: 210 nm.	118
Figure 3.5	The effect of the mobile phase flow rate on the retention time of 20 μM each of phenol, guaiacol, m-cresol, p-cresol, o-cresol, 4-VG, 4-EP, 4-EG and eugenol. Mobile phase: 15:85, ACN:10 mM formate pH 3. Column: HALO C <sub>18</sub> core-shell (3 x 50 mm, 2.7 μm), flow rate: (A) 1 mL/min, (B) 1.2 mL/min and (C) 1.5 mL/min, injection volume: 5 μL, column temperature: 25 °C, UV detection: 210 nm.	119
Figure 3.6	The effect of oxidation potential on the detection of 20 μM each of phenol, guaiacol, m-cresol, p-cresol, o-cresol, 4-VG, 4-EP, 4-EG and eugenol. Oxidation potential: (A) + 1.2 V, (B) + 1.5 V, and (C) + 1.8 V on the BDD electrode vs. Pd/H <sub>2</sub> . Mobile phase: 15:85, ACN:10 mM formate pH 3. Column: HALO C <sub>18</sub> core-shell (3 x 50 mm, 2.7 μm), flow rate: 1.5 mL/min, injection volume: 5 μL.	120
Figure 3.7	The effect of oxidation potential on the detection of 20 μM each of phenol, guaiacol, m-cresol, p-cresol, o-cresol, 4-VG, 4-EP, 4-EG and eugenol at the BDD electrode vs. Pd/H <sub>2</sub> . Mobile phase: 15:85, ACN:10 mM formate pH 3. Column: HALO C <sub>18</sub> core-shell (3 x 50 mm, 2.7 μm), flow rate: 1.5 mL/min, injection volume: 5 μL.	120
Figure 3.8	Representative chromatograms of a mixed standard solution containing the nine compounds (20 μM each) analysed by (A) HPLC-UV at 210 nm and (B) HPLC-ECD at + 1.5 V. Mobile phase: 15:85, ACN:10 mM formate pH 3. Column: HALO C <sub>18</sub> core-shell (3 x 50 mm, 2.7 μm), flow rate: 1.5 mL/min, injection volume: 5 μL.	121
Figure 3.9	(A) Calibration curve and (B) plot of phenol; (C) calibration curve and (D) plot of guaiacol; (E) calibration curve and (F) plot of p-cresol.	125

	Mobile phase: 15:85, ACN:10 mM formate pH 3. Column: HALO C <sub>18</sub> core-shell (3 x 50 mm, 2.7 $\mu$ m), flow rate: 1.5 mL/min, injection volume: 5 $\mu$ L, oxidation potential: + 1.5 V on the BDD electrode vs. Pd/H <sub>2</sub> .	
Figure 3.10	(A) Calibration curve and (B) plot of m-cresol; (C) calibration curve and (D) plot of o-cresol; (E) calibration curve and (F) plot of 4-VG. Mobile phase: 15:85, ACN:10 mM formate pH 3. Column: HALO C <sub>18</sub> core-shell (3 x 50 mm, 2.7 $\mu$ m), flow rate: 1.5 mL/min, injection volume: 5 $\mu$ L, oxidation potential: + 1.5 V on the BDD electrode vs. Pd/H <sub>2</sub> .	126
Figure 3.11	(A) Calibration curve and (B) plot of 4-EP; (C) calibration curve and (D) plot of 4-EG; (E) calibration curve and (F) plot of eugenol. Mobile phase: 15:85, ACN:10 mM formate pH 3. Column: HALO C <sub>18</sub> core-shell (3 x 50 mm, 2.7 $\mu$ m), flow rate: 1.5 mL/min, injection volume: 5 $\mu$ L, oxidation potential: + 1.5 V on the BDD electrode vs. Pd/H <sub>2</sub> .	127
Figure 3.12	A representative HPLC-ECD chromatogram of Islay whiskey. Whiskey (black line) and spiked with 20 $\mu$ M each of phenol, guaiacol, m-cresol, p-cresol, o-cresol, 4-VG, 4-EP, 4-EG and eugenol (red line). Mobile phase: 15:85, ACN:10 mM formate pH 3. Column: HALO C <sub>18</sub> core-shell (3 x 50 mm, 2.7 $\mu$ m), flow rate: 1.5 mL/min, injection volume: 5 $\mu$ L, oxidation potential: + 1.5 V on the BDD electrode vs. Pd/H <sub>2</sub> .	129
Figure 3.13	A representative HPLC-ECD chromatogram of Highland (A), Scotch (B) and Irish (C) whiskey. Whiskey (black line) and spiked with 20 $\mu$ M each of phenol, guaiacol, m-cresol, p-cresol, o-cresol, 4-VG, 4-EP, 4-EG and eugenol (red line). Mobile phase: 15:85, ACN:10 mM formate pH 3. Column: HALO C <sub>18</sub> core-shell (3 x 50 mm, 2.7 $\mu$ m), flow rate: 1.5 mL/min, injection volume: 5 $\mu$ L, oxidation potential: + 1.5 V on the BDD electrode vs. Pd/H <sub>2</sub> .	130
Scheme 4.1	Chemical structures of (A) GA and (B) EA.	138
Figure 4.1	A representative 5 cycle CV of 100 $\mu$ M GA at pH 2 on the BDD electrode vs. Ag/AgCl. Supporting electrolyte: 100 mM phosphate buffer with 5 % EtOH at the scan rate of 100 mV s <sup>-1</sup> .	143
Scheme 4.2	Electro-oxidation of GA. The process involves the release of two electrons and two protons, i.e., electrochemistry of GA is pH-dependent. The first step represents irreversible oxidation of GA (a) to the semiquinone radical cation (b). The radical cation (b) then loses a proton to form the semiquinone radical (c, d1-d3). The one-electron oxidation product (d1-d3) is followed by a second irreversible electron transfer to the quinone cation (e). This quinone cation (e) is deprotonated to give the quinone (f) as the final product.	143
Figure 4.2	A plot of peak current versus square root of the scan rate ( $v^{1/2}$ (mV s <sup>-1</sup> )) for 100 $\mu$ M GA at pH 2 on the BDD electrode vs. Ag/AgCl. The supporting electrolyte was 100 mM phosphate buffer with 5 % EtOH.	144
Figure 4.3	CV response in the absence (dashed lines) and presence (solid lines) of 100 $\mu$ M GA at (A) pH 5 and (B) pH 7 on the BDD electrode vs. Ag/AgCl. The supporting electrolyte was 100 mM phosphate buffer with 5 % EtOH at the scan rate of 100 mV s <sup>-1</sup> .	145

Figure 4.4	A representative 5 cycle CV of 100 $\mu\text{M}$ EA at pH 2 on the BDD electrode vs. Ag/AgCl. The supporting electrolyte was 100 mM phosphate buffer with 5 % EtOH at the scan rate of 100 $\text{mV s}^{-1}$ .	146
Scheme 4.3	Two possible electrochemical oxidation pathways of EA to form its corresponding radicals. This first step involves the release of one electron and one $\text{H}^+$ .	146
Scheme 4.4	The formation of different quinones from three different radicals resulted from the electrochemical oxidation of EA.	147
Figure 4.5	A plot of peak current versus square root of the scan rate ( $v^{1/2}(\text{mV s}^{-1})$ ) for 100 $\mu\text{M}$ EA at pH 2 on the BDD electrode vs. Ag/AgCl. The supporting electrolyte was 100 mM phosphate buffer with 5 % EtOH.	148
Figure 4.6	CV response in the absence (dashed line) and presence (solid line) of 100 $\mu\text{M}$ EA at pH 7 on the BDD electrode vs. Ag/AgCl. The supporting electrolyte was 100 mM phosphate buffer with 5 % EtOH at the scan rate of 100 $\text{mV s}^{-1}$ .	148
Figure 4.7	CV responses in the absence (dashed line) and presence (solid line) of EA and GA on the GCE vs. Ag/AgCl. (A) EA and (B) GA at pH 2; (C) EA and (D) GA at pH 5; (E) EA and (F) GA at pH 7. The supporting electrolyte was 100 mM phosphate buffer with 5 % EtOH at pH 2 and 7, and 100 mM acetate buffer with 5 % EtOH at pH 5, at the scan rate of 100 $\text{mV s}^{-1}$ .	149
Figure 4.8	SWV in the absence (dashed lines) and presence (solid lines) of a standard mixture of EA (10 $\mu\text{M}$ ) and GA (2 $\mu\text{M}$ ) at (A) pH 2, (B) pH 5, (C) and pH 7 using 100 mM phosphate buffer, pH 2 with 5 % EtOH. Detection was achieved on the bare BDD electrode vs. Ag/AgCl.	150
Figure 4.9	Resolved SWV of a standard mixture (10 $\mu\text{M}$ GA and 3 $\mu\text{M}$ EA) upon application of peak deconvolution using Origin Pro 8.5.1. The supporting electrolyte was 100 mM phosphate buffer, pH 2 with 5 % EtOH containing (a) 1 % $\alpha$ -CD, (b) 1 % S- $\beta$ -CD and (c) 1 % HP $\beta$ -CD. Detection was achieved on the BDD electrode vs. Ag/AgCl.	151
Figure 4.10	A 50 $\mu\text{M}$ standard mixture of GA and EA. Column: Agilent XDB C <sub>18</sub> (4.6 x 150 mm, 5 $\mu\text{m}$ ), mobile phase flow rate: 1.5 mL/min, injection volume: 5 $\mu\text{L}$ , oxidation potential: + 1.4 V on the BDD electrode vs. Pd/H <sub>2</sub> .	152
Figure 4.11	The effect of oxidation potential on the detection of 100 $\mu\text{M}$ each of GA and EA. Oxidation potential: (A) + 1.2 V, (B) + 1.4 V, (C) + 1.6 V and (D) + 1.8 V on the BDD electrode vs. Pd/H <sub>2</sub> . Column: Agilent XDB C <sub>18</sub> (4.6 x 150 mm, 5 $\mu\text{m}$ ), mobile phase flow rate: 1.5 mL/min, injection volume: 5 $\mu\text{L}$ .	153
Figure 4.12	The plot of detection potential (V) versus current ( $\mu\text{A}$ ) on the BDD electrode vs. Pd/H <sub>2</sub> . Column: Agilent XDB C <sub>18</sub> (4.6 x 150 mm, 5 $\mu\text{m}$ ), mobile phase flow rate: 1.5 mL/min, injection volume: 5 $\mu\text{L}$ .	153
Figure 4.13	(A) Calibration curve and (B) plot of GA and (C) calibration curve and (D) plot of EA. Column: Agilent XDB C <sub>18</sub> column (4.6 x 150 mm, 5 $\mu\text{m}$ ), mobile phase flow rate: 1.5 mL/min, injection volume: 5 $\mu\text{L}$ , oxidation potential: + 1.4 V on the BDD electrode vs. Pd/H <sub>2</sub> .	155



Figure 4.14	Representative HPLC-ECD chromatograms of (A) Islay whiskey, (B) Highland whiskey and (C) Scotch whiskey. Whiskey (black line) and spiked with 10 $\mu$ M each of GA and EA (red line). Column: Agilent XDB C <sub>18</sub> (4.6 x 150 mm, 5 $\mu$ m), mobile phase flow rate: 1.5 mL/min, injection volume: 5 $\mu$ L, oxidation potential: + 1.4 V on the BDD electrode vs. Pd/H <sub>2</sub> .	156
Scheme 5.1	Guaiacol formation scheme from lignin as the starting product.	164
Figure 5.1	CV response in the absence (dashed lines) and presence (solid lines) of 100 $\mu$ M each for (A) VA, (B) vanillin, (C) FA and (D) guaiacol on the bare BDD electrode vs. Ag/AgCl in 100 mM phosphate buffer, pH 2, with a scan rate of 100 mV s <sup>-1</sup> .	168
Scheme 5.2	Electrochemical oxidation pathway of VA.	168
Scheme 5.3	The electrochemical oxidation of vanillin to form a 1,2-benzoquinone derivative.	169
Scheme 5.4	The electrochemical oxidation pathway of FA.	170
Scheme 5.5	The reduction of 3,4-dioxocinnamic acid to CA.	170
Figure 5.2	The effect of mobile phase % ACN on the retention time of 50 $\mu$ M each of VA, vanillin, FA and guaiacol. Mobile phase: ACN:10 mM formate pH 3 (v/v), (A) 15:85, (B) 17:83, (C) 20:80. Column: HALO C <sub>18</sub> core-shell (3.0 x 50 mm, 2.7 $\mu$ m), flow rate: 1 mL/min, injection volume: 5 $\mu$ L, UV detection: 210 nm.	171
Figure 5.3	A plot of % ACN versus k. Mobile phase: ACN:10 mM formate pH 3 (v/v), at 15, 17 and 20 % ACN. Column: HALO C <sub>18</sub> core-shell (3.0 x 50 mm, 2.7 $\mu$ m), flow rate: 1 mL/min, injection volume: 5 $\mu$ L, UV detection: 210 nm.	172
Figure 5.4	The effect of the mobile phase pH on the retention time of 50 $\mu$ M each of VA, vanillin, FA and guaiacol. Mobile phase: 17:83, (A) ACN:10 mM formate pH 3, (B) ACN:10 mM acetate pH 4.5, and (C) ACN:10 mM acetate pH 6. Column: HALO C <sub>18</sub> core-shell (3 x 50 mm, 2.7 $\mu$ m), flow rate: 1 mL/min, injection volume: 5 $\mu$ L, UV detection: 210 nm.	173
Figure 5.5	The plot of pH versus k. Mobile phase: ACN:10 mM formate pH 3, 17:83 (v/v) at pH 3, 4.5, and 6. Column: HALO C <sub>18</sub> core-shell (3.0 x 50 mm, 2.7 $\mu$ m), flow rate: (A) 0.7 mL/min, (B) 1 mL/min, (C) 1.3 mL/min, injection volume: 5 $\mu$ L, UV detection: 210 nm.	173
Figure 5.6	The effect of the mobile phase flow rate on the retention time of 50 $\mu$ M each of VA, vanillin, FA and guaiacol. Mobile phase: ACN:10 mM formate pH 3, 17:83 (v/v). Column: HALO C <sub>18</sub> core-shell (3.0 x 50 mm, 2.7 $\mu$ m), flow rate: (A) 0.7 mL/min, (B) 1 mL/min, (C) 1.3 mL/min, injection volume: 5 $\mu$ L, UV detection: 210 nm.	174
Figure 5.7	The effect of oxidation potential on the detection of 50 $\mu$ M each of VA, vanillin, FA and guaiacol. Oxidation potential: (A) + 1.4 V, (B) + 1.6 V, (C) + 1.8 V and (D) + 2.0 V on the BDD electrode vs. Pd/H <sub>2</sub> . Mobile phase: ACN:10 mM formate pH 3, 17:83 (v/v). Column: HALO C <sub>18</sub> core-shell (3.0 x 50 mm, 2.7 $\mu$ m), flow rate: 1.3 mL/min, injection volume: 5 $\mu$ L.	175

Figure 5.8	The plot of detection potential (V) versus current ( $\mu$ A) on the BDD electrode vs. Pd/H <sub>2</sub> . Mobile phase: ACN:10 mM formate pH 3 17:83, (v/v). Column: HALO C <sub>18</sub> core-shell (3 x 50 mm, 2.7 $\mu$ m), flow rate: 1.3 mL/min, injection volume: 5 $\mu$ L.	175
Figure 5.9	A representative HPLC-ECD chromatogram of a mixed standard solution (50 $\mu$ M each of VA, vanillin, FA, and guaiacol). Mobile phase: ACN:10 mM formate pH 3, 17:83 (v/v). Column: HALO C <sub>18</sub> core-shell (3.0 x 50 mm, 2.7 $\mu$ m), flow rate: 1.3 mL/min, injection volume: 5 $\mu$ L, oxidation potential: + 1.6 V on the BDD electrode vs. Pd/H <sub>2</sub> .	176
Figure 5.10	(A) The calibration curve and (B) plot of VA; (C) calibration curve and (D) plot of vanillin. Mobile phase: ACN:10 mM formate pH 3, 17:83 (v/v). Column: HALO C <sub>18</sub> core-shell (3 x 50 mm, 2.7 $\mu$ m), flow rate: 1.3 mL/min, injection volume: 5 $\mu$ L, oxidation potential: + 1.6 V on the BDD electrode vs. Pd/H <sub>2</sub> .	179
Figure 5.11	(A) Calibration curve and (B) plot of FA; (C) calibration curve and (D) plot of guaiacol. Mobile phase: ACN:10 mM formate pH 3, 17:83 (v/v). Column: HALO C <sub>18</sub> core-shell (3 x 50 mm, 2.7 $\mu$ m), flow rate: 1.3 mL/min, injection volume: 5 $\mu$ L, oxidation potential: + 1.6 V on the BDD electrode vs. Pd/H <sub>2</sub> .	180
Figure 5.12	A representative HPLC-ECD chromatogram of an energy drink (black line) and spiked energy drink (red line) with 10 $\mu$ M of each standard. Mobile phase: ACN:10 mM formate pH 3, 17:83 (v/v). Column: HALO C <sub>18</sub> core-shell (3.0 x 50 mm, 2.7 $\mu$ m), flow rate: 1.3 mL/min, injection volume: 5 $\mu$ L, oxidation potential: + 1.6 V on the BDD electrode vs. Pd/H <sub>2</sub> .	181

## List of Tables

		Page
Table 1.1	The occurrence of phenolic compounds in predominantly edible plants and plant-derived products.	6
Table 1.2	Chemical structures of the main classes of flavonoids.	9
Table 1.3	HPLC-ECD (amperometric) methods for the determination of plant phenolics in foods, beverages and plants.	41
Table 2.1	Parameters obtained for the bare and Nafion modified BDD electrodes using an equivalent circuit $R_s (Q (R_{ct}W))$ . The parameters were obtained by the ZnSimWin software.	85
Table 2.2	A comparison of LODs obtained using SWV at the bare and modified BDD electrodes using 100 mM phosphate buffer, pH 2 with 5 % EtOH containing 10 mM $\alpha$ -CD.	91
Table 2.3	A comparison of determined LODs with literature values.	92
Table 2.4	Linear regression parameters for the analytes using SWV on the Nafion modified BDD electrode.	93
Table 3.1	Chemical structures of the phenols, guaiacols and cresol isomers.	114
Table 3.2	A comparison of LODs obtained with ECD and UV detection.	122
Table 3.3	Linear regression parameters of calibration curves and precision data for the phenolic compounds detected with HPLC-ECD at + 1.5 V.	123
Table 3.4	Linear regression parameters of calibration curves and precision data for the phenolic compounds detected with HPLC-UV at 210 nm.	124
Table 3.5	The concentrations of the phenolic compounds in four whiskey samples (n=2).	129
Table 4.1	Linear regression parameters of calibration curves and precision data for EA and GA detected with HPLC-ECD at + 1.4 V.	154
Table 4.2	LODs obtained with ECD and UV detection.	154
Table 4.3	The concentrations of gallic and ellagic acids in three whiskey samples (n=3).	156
Table 5.1	The LODs obtained with ECD and UV detection.	177
Table 5.2	A comparison of literature LODs.	177
Table 5.3	Linear regression parameters of calibration curves and precision data for the phenolic compounds detected with HPLC-ECD at + 1.6 V.	178

## List of Abbreviations

ACN	acetonitrile
APT	anodic pre-treatment
BDD	boron-doped diamond
CA	caffeic acid
CD	cyclodextrin
CE	capillary electrophoresis
CFU	colony-forming units
CGA	chlorogenic acid
CNT	carbon nanotube
CPE	carbon paste electrode
CPT	cathodic pre-treatment
CQA	caffeoylquinic acid
CV	cyclic voltammetry
CVD	chemical vapour deposition
DAD	diode array detection
DMF	dimethylformamide
DMTS	dimethyl trisulfide
DNA	deoxyribonucleic acid
DPV	differential pulse voltammetry
EA	ellagic acid
EC	epicatechin
ECD	electrochemical detection
ECG	epicatechin-3-gallate
EG	ethylguaiaicol
EGC	epigallocatechin
EGCG	epigallocatechin-3-gallate
EIS	electrochemical impedance spectroscopy
ELISA	enzyme-linked immunosorbent assays
EP	ethylphenol
EtOH	ethanol
FA	ferulic acid
FASS	field-amplified sample stacking
FID	flame ionisation detector
FL	fluorescence detector
FTIR	Fourier-transform-infrared spectroscopy
GA	gallic acid
GC	gas chromatography
GCE	glassy carbon electrode
HETP	height equivalent to a theoretical plate
HILIC	hydrophilic interaction liquid chromatography
HPLC	high-performance liquid chromatography
K	partition coefficient
LC	liquid chromatography
LDA	linear discriminant analysis
LOD	limit of detection

LVI	large volume injection
<i>m</i>	meta
MRI	magnetic resonance imaging
MS	mass spectrometry
MWCNT	multi-walled carbon nanotubes
ND	not detected
<i>o</i>	ortho
O	olfactometry
<i>p</i>	para
PAD	pulsed amperometric detection
PCA	protocatechuic acid
PCR	polymerase chain reaction
PPM	parts per million
PTFE	polytetrafluoroethylene
RGO	reduced graphene oxide
RNA	ribonucleic acid
ROS	reactive oxygen species
RP	reversed-phase
RPLC	reversed-phase liquid chromatography
RSD	relative standard deviation
SAR	structure-activity relationship
SBSE	stir-bar sorbent extraction
SD	standard deviation
SDG	secoisolariciresinol diglucoside
SEM	scanning electron microscopy
SPE	screen-printed electrode
SPME	solid-phase microextraction
spp	species
SWV	square wave voltammetry
TBAHFP	tetrabutylammonium hexafluorophosphate
TD	thermal desorption
TLC	thin-layer chromatographic
UA	uric acid
UV	ultraviolet
VA	vanillic acid
VG	vinylguaiaicol
XDB	extra dense bonding

# Table of Contents

<i>Declaration</i> .....	<i>i</i>
<i>Abstract</i> .....	<i>ii</i>
<i>Acknowledgements</i> .....	<i>iv</i>
<i>Publications</i> .....	<i>v</i>
<i>Poster Presentations</i> .....	<i>vi</i>
<i>List of Figures and Schemes</i> .....	<i>viii</i>
<i>List of Tables</i> .....	<i>xvii</i>
<i>List of Abbreviations</i> .....	<i>xviii</i>

## Chapter 1: Introduction

<b>1.1 Secondary metabolism of plants</b> .....	<b>2</b>
1.1.1 Phenol and polyphenols .....	3
1.1.2 Antioxidant properties of plant phenolics .....	4
1.1.3 Structure and classification of plant phenolics .....	5
1.1.3.1 Phenolic acids .....	7
1.1.3.2 Flavonoids .....	8
1.1.3.3 Tannins .....	11
1.1.3.4 Stilbenes .....	12
1.1.3.5 Lignans .....	12
1.1.4 Chromatographic analysis of secondary metabolites .....	12
<b>1.2 Carbon electrode materials</b> .....	<b>13</b>
1.2.1 Boron-doped diamond electrode .....	14
1.2.1.1 Effect of boron doping levels, non-diamond impurities and surface termination .....	16
<b>1.3 Electrochemical methods of analysis</b> .....	<b>19</b>
1.3.1 Cyclic voltammetry .....	19
1.3.2 Square wave voltammetry .....	20
1.3.3 Electrochemical impedance spectroscopy .....	20
<b>1.4 High-performance liquid chromatography</b> .....	<b>20</b>
1.4.1 Fundamental parameters of separation .....	22
1.4.2 Stationary phases for RPLC .....	24
1.4.2.1 Core-shell particles .....	26
<b>1.5 HPLC – electrochemical detection</b> .....	<b>30</b>

1.5.1 Flow-cell design .....	32
1.5.1.1 Thin-layer amperometric detector .....	32
1.5.1.2 Wall-jet amperometric detector .....	33
1.5.1.3 Dual-electrodes detection systems .....	34
1.5.1.4 Pulsed amperometric detection .....	35
1.5.1.5 Coulometric detectors .....	37
1.5.2 HPLC-ECD of secondary metabolites in foods, beverages and plants .....	39
<b>1.6 Whiskey – an overview .....</b>	<b>42</b>
1.6.1 Malt whiskey production .....	42
1.6.2 Chemical composition of whiskey .....	44
1.6.3 Analytical methods for whiskey flavour analysis .....	48
<b>1.7 Objectives of the thesis .....</b>	<b>49</b>
<b>1.8 References .....</b>	<b>52</b>
<b>Chapter 2: Simultaneous electroanalysis of guaiacol and its analogues based on their differential complexation with <math>\alpha</math>-cyclodextrin on a Nafion modified boron-doped diamond electrode</b>	
<b>2.1 Introduction .....</b>	<b>75</b>
<b>2.2 Experimental .....</b>	<b>76</b>
2.2.1 Reagents, standard solutions and samples .....	76
2.2.2 Apparatus .....	76
2.2.3 Preparation of the modified electrodes .....	77
2.2.4 Electrochemical characterisation of the bare and modified BDD electrodes .....	77
2.2.5 High-performance liquid chromatography (HPLC) .....	77
<b>2.3 Results and discussion .....</b>	<b>78</b>
2.3.1 Electrochemical oxidation of the guaiacol analogues by the bare BDD electrode ...	78
2.3.2 Electrochemical oxidation of the guaiacol analogues by Nafion modified BDD electrode .....	81
2.3.3 Voltammetry, impedance spectroscopy, and chronocoulometry characterisation ....	83
2.3.4 SWV of the guaiacols .....	86
2.3.5 Profiling the guaiacols in whiskey samples .....	96
<b>2.4 Conclusions .....</b>	<b>104</b>
<b>2.5 References .....</b>	<b>105</b>
<b>Chapter 3: Profiling of phenolic flavourings using core-shell reversed-phase liquid chromatography with electrochemical detection at a boron-doped diamond electrode</b>	
<b>3.1 Introduction .....</b>	<b>110</b>

<b>3.2 Experimental .....</b>	<b>112</b>
3.2.1 Reagents, standard solutions and samples .....	112
3.2.2 Cyclic voltammetry .....	112
3.2.3 Apparatus .....	112
3.2.4 Chromatographic conditions .....	113
3.2.5 Method validation .....	113
<b>3.3 Results and discussion.....</b>	<b>114</b>
3.3.1 Electrochemical behaviour of guaiacol, 4-EG, phenol and <i>o</i> -cresol .....	114
3.3.2 Optimisation of HPLC separation conditions .....	117
3.3.3 Selection of detection potential .....	119
3.3.4 Analytical performance .....	121
3.3.5 Whiskey sample analysis.....	128
<b>3.4 Conclusions.....</b>	<b>131</b>
<b>3.5 References.....</b>	<b>132</b>
<b>Chapter 4: Electroanalysis of gallic and ellagic acids at a boron-doped diamond electrode and their determination by high-performance liquid chromatography with amperometric detection</b>	
<b>4.1 Introduction.....</b>	<b>138</b>
<b>4.2 Experimental .....</b>	<b>140</b>
4.2.1 Reagents, standard solutions and samples .....	140
4.2.2 Voltammetric analysis .....	140
4.2.3 Apparatus .....	141
4.2.4 Chromatographic conditions .....	141
4.2.5 Method validation .....	141
<b>4.3 Results and discussion.....</b>	<b>142</b>
4.3.1 CVs of GA on the BDD electrode .....	142
4.3.2 CVs of EA on the BDD electrode .....	145
4.3.3 CVs of EA and GA on the GCE .....	148
4.3.4 SWV of gallic and ellagic acids .....	150
4.3.5 HPLC coupled with the BDD electrode for separation and analysis of GA and EA .....	151
4.3.6 Analytical performance for the analysis of GA and EA in whiskey .....	154
4.3.7 Detection of gallic and ellagic acids in whiskey samples .....	155
<b>4.4 Conclusions.....</b>	<b>156</b>



<b>4.5 References.....</b>	<b>158</b>
<b>Chapter 5: Rapid nanomolar detection of guaiacol from its precursors using a core-shell reversed-phase column coupled with a boron-doped diamond electrode</b>	
<b>5.1 Introduction.....</b>	<b>163</b>
<b>5.2 Experimental .....</b>	<b>165</b>
5.2.1 Reagents, standard solutions, and samples .....	165
5.2.2 Cyclic voltammetry .....	166
5.2.3 Apparatus .....	166
5.2.4 Chromatographic conditions .....	167
5.2.5 Method validation .....	167
<b>5.3 Results and discussion.....</b>	<b>167</b>
5.3.1 Electrochemical behaviour of VA, vanillin, FA, and guaiacol .....	167
5.3.2 Optimisation of HPLC separation conditions .....	171
5.3.3 Selection of detection potential .....	174
5.3.4 Analytical performance .....	176
5.3.5 Beverage sample analysis.....	180
<b>5.4 Conclusions.....</b>	<b>181</b>
<b>5.5 References.....</b>	<b>182</b>
<b>Chapter 6: Summary and Future work</b>	
<b>6.1 Summary.....</b>	<b>188</b>
<b>6.2 Future work.....</b>	<b>190</b>
<b>6.3 References.....</b>	<b>192</b>

# **Chapter 1**

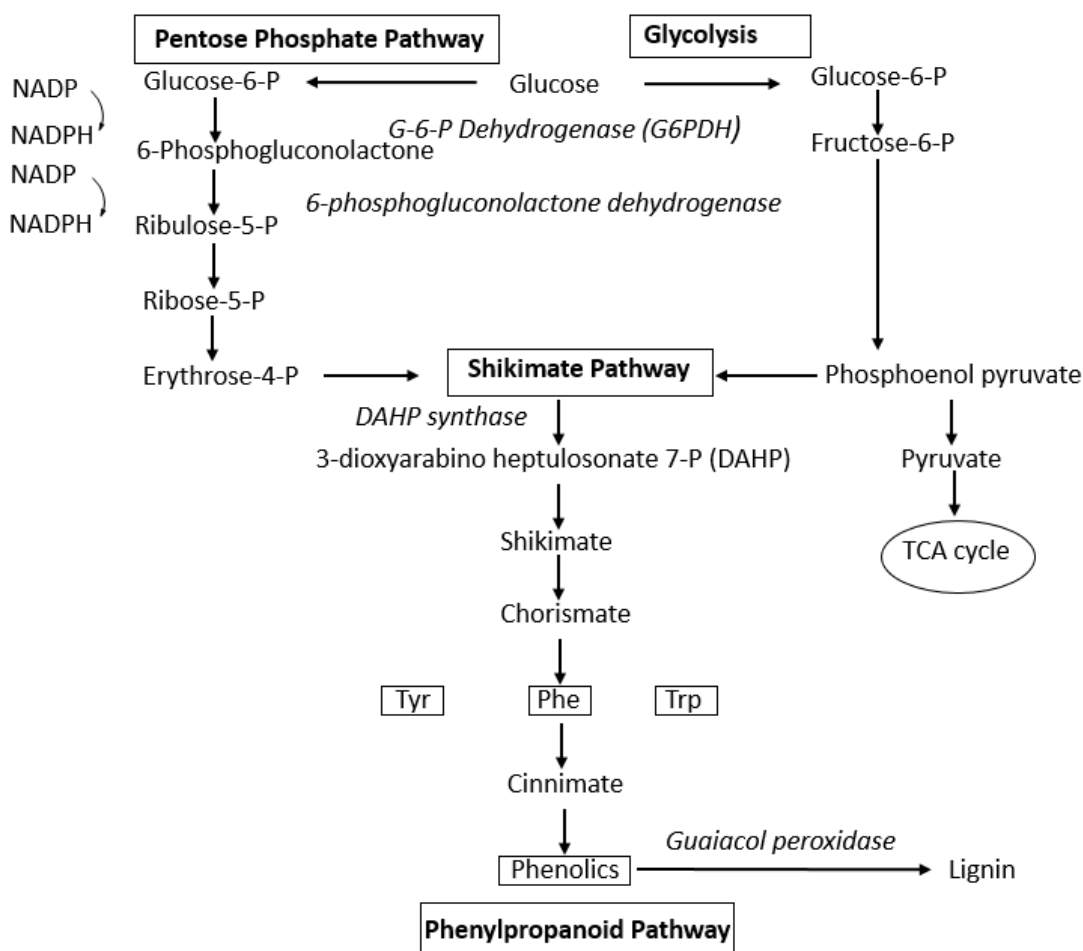
## **Introduction**

## 1.1 Secondary metabolism of plants

Plants contain a diverse array of both primary and secondary metabolites. Primary metabolites such as carbohydrates, proteins and lipids, are necessary for cell growth, development and reproduction<sup>1</sup>. Secondary metabolites are low-molecular-weight structures that are formed from biosynthetic pathways. They are non-essential to plant life, but play a key role in plants' survival in the environment, by protecting against stresses, both biotic (fungi, nematodes, insects, bacteria, or grazing by animals) and abiotic (moisture, shading, injury, higher temperatures, or presence of heavy metals)<sup>2</sup>. Over 100,000 secondary metabolites have been elucidated and classified according to their chemical structure<sup>3</sup>. The main groups in this classification include alkaloids, amines, glucosinolates, cyanogenic glucosides, non-protein amino acids, phenolics, quinones, organic acids, terpenoids, polyacetylenes, and peptides, with phenolic compounds accounting for one of the largest groups of secondary metabolites in plants<sup>3</sup>.

Biogenetically, secondary metabolites are primarily produced through the pentose phosphate/shikimate/phenylpropanoid metabolic pathways. The pentose phosphate pathway provides erythrose-4-phosphate as a precursor for the shikimate pathway. The shikimate pathway then converts these phosphates to aromatic amines, such as phenylalanine, which are used by the phenylpropanoid pathway to synthesise a wide variety of secondary metabolites<sup>4,5</sup> (**Scheme 1.1**). Additionally, secondary metabolites may also arise from the acetate/malonate metabolic pathway providing simple phenols, or a combination of the phosphate/shikimate/phenylpropanoid and acetate/malonate pathways producing both monomeric and polymeric phenols<sup>6</sup>.

There is growing research interest in natural plant phenolics as they are known to display a wide range of physiological properties including anti-allergenic<sup>7</sup>, anti-atherogenic<sup>8</sup>, anti-inflammatory<sup>9</sup> and anti-microbial<sup>10</sup> activity. Plant phenolics are best known for their natural antioxidant properties which are associated with a decreased risk of diseases related to oxidative stress, such as cancer and cardiovascular disease<sup>11-13</sup>.



**Scheme 1.1.** Biosynthesis of phenolic compounds in the pentose phosphate, shikimate and phenylpropanoid pathways in plants<sup>5</sup>.

### 1.1.1 Phenol and polyphenols

Phenol (carbolic acid) (**Figure 1.1A**) is a cyclic benzene compound that contains one or more hydroxyl groups attached to the ring. It is a weak acid with a pK<sub>a</sub> of ~10. It is slightly more acidic than the aliphatic alcohols and cyclohexanol, as it can lose a proton as the phenoxide ion is stabilised through delocalisation of the negative charge around the ring<sup>14</sup> (**Figure 1.1B-C**). The acidity of substituted phenols is dependent on the class of substituent, with electron-withdrawing groups increasing its acidity and electron-donating groups making it less acidic. Polyphenols are compounds that contain greater than one phenolic hydroxyl group attached to one or more benzene rings (**Figure 1.2**).

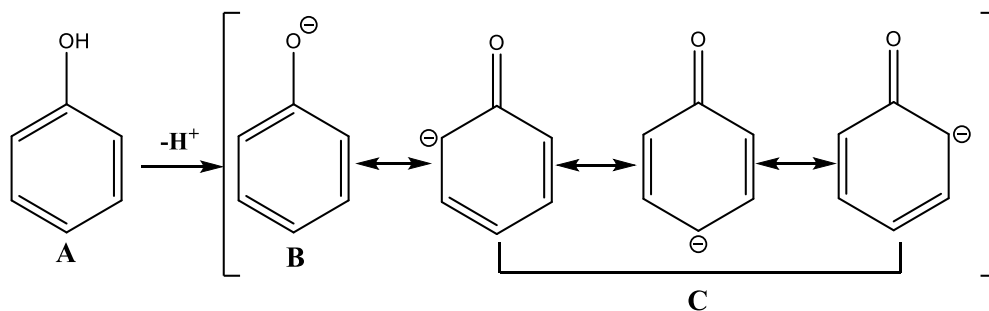


**Figure 1.1.** Chemical structures of phenol (A), phenoxide ion (B) and resonance structures (C).

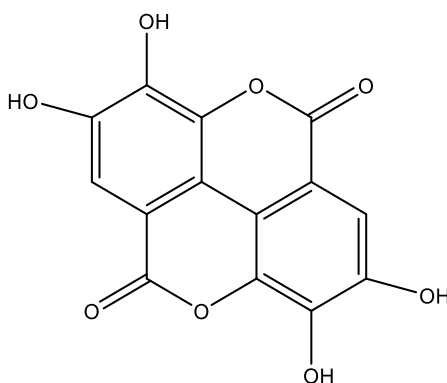


**Figure 1.2.** Chemical structure of the polyphenol, ellagic acid.

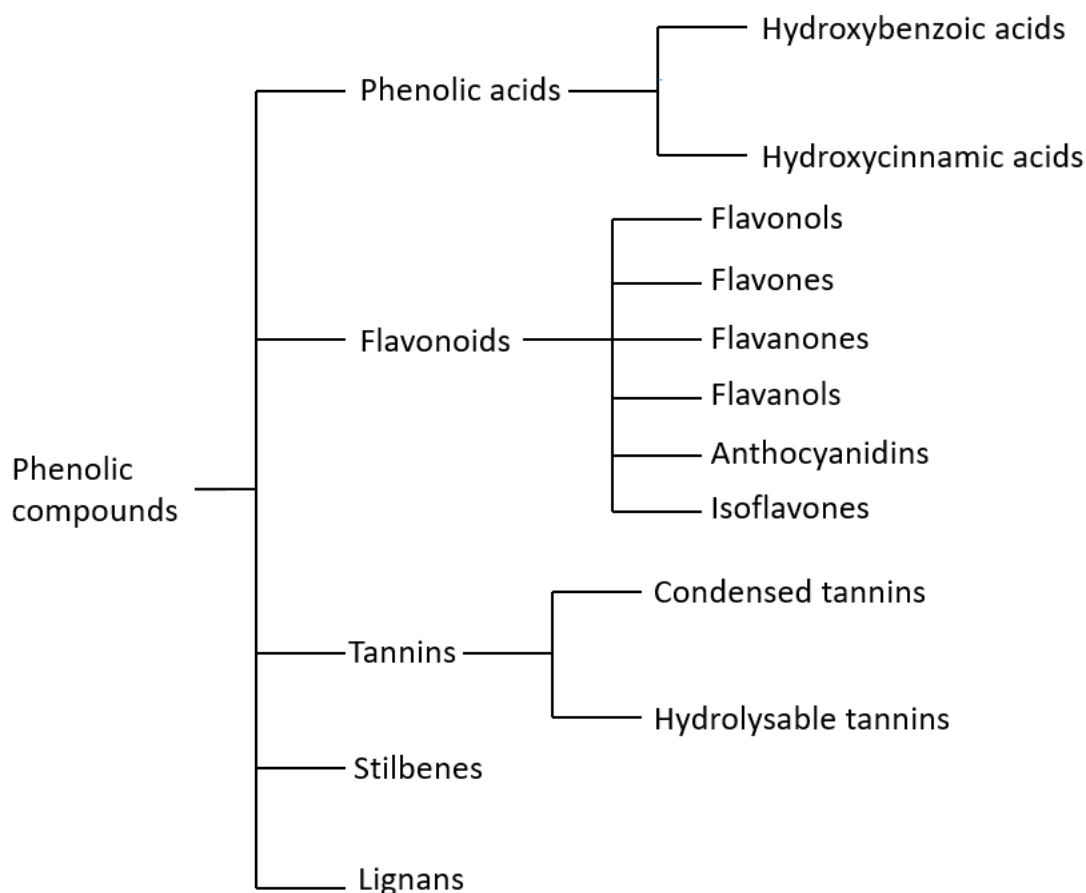
### 1.1.2 Antioxidant properties of plant phenolics

Reactive oxygen species (ROS) are reactive molecules and free radicals present as natural by-products of our body's metabolism, i.e., hydrogen peroxide, the superoxide anion and the hydroxyl radical<sup>15</sup>. In excess, they can pose a health risk by attacking biological molecules such as deoxyribonucleic acid (DNA), ribonucleic acid (RNA), enzymes, proteins and lipids, resulting in cell or tissue injury associated with degenerative diseases<sup>15,16</sup>. An antioxidant is a substance that when present at concentrations lower than the oxidisable compounds to be protected, can significantly delay or inhibit its oxidation<sup>17</sup>. The antioxidant ability of phenolics is mainly due to their redox properties, allowing them to function as reducing agents or as hydrogen atom donors. They react with reactive oxygen and nitrogen species, breaking the cycle of the generation of new radicals<sup>18</sup>. They can also function as antioxidants by chelating with metals such as Fe and Zn<sup>19</sup>. By strongly interfering with proteins, they can inhibit enzymes involved in radical generation including cytochrome P450 isoforms, lipoxygenases, cyclooxygenase and xanthine oxidase<sup>18</sup>. The radical scavenging and metal chelating properties of phenolics are determined by their chemical structure,

known as the structure-activity relationship (SAR). The antioxidant activity of the compound increases with an increase in hydroxyl groups. The position of the hydroxyl group is also important with the *ortho* (*o*)-position most active due to intramolecular hydrogen bonding, followed by the *para* (*p*)-position, with the *meta* (*m*)-position of compounds having the lowest activity<sup>20</sup>.

### 1.1.3 Structure and classification of plant phenolics

Plant phenolics refer strictly to those polyphenols that are produced through biosynthetic pathways and which fulfil a wide range of physiological roles in plants<sup>6</sup>. To date, over 8000 plant phenolic compounds have been identified<sup>21</sup>. Low-molecular-weight phenolics are found universally in higher plants, with others occurring in an array of plant species while some are species specific<sup>6</sup>. They are classified based on their number of phenol rings and the structural elements that bind these rings together<sup>22</sup> (Scheme 1.2).



**Scheme 1.2.** Main classes of polyphenolic compounds.

Polyphenols are widely present in foods and beverages such as fruits, vegetables, whole grains, chocolate, tea, coffee and alcoholic beverages (**Table 1.1**).

**Table 1.1.** The occurrence of phenolic compounds in predominantly edible plants and plant-derived products. Modified from Reference <sup>23</sup>.

Phenolic compounds		Occurrence in plants	References
Phenolic acids	Hydroxybenzoic acids	grapes, black currant, blackberries, lignin berries, strawberries, raspberries, onion, tea	24–26
	Hydroxycinnamic acids	apples, pears, cherries, apricots, peaches, black currant, blueberries, Ginkgo biloba and Morus alba leaves, tobacco leaves, potatoes, spinach, lettuce, potatoes, broccoli, olive oil, wine, coffee, citrus juice, grains	27–35
Flavonoids	Flavonols	apples, oranges, grapefruits, black grapes, black elderberries, blueberries, cabbage, radish, onion paprika, chicory, green tea, red wine, Ginkgo biloba leaves, Morus alba leaves	36–42
	Flavones	celery, cayenne pepper, red paprika, parsley, thyme, lemon, rose hip, peppermint	36,37,41–43
	Flavanones	tomatoes, mint, nigella seeds, citrus fruits (mainly oranges and grapefruits)	36,37,41–43
	Flavanols	fruits (berries, apples, pears), cocoa beans, nuts, green tea, legumes	44,45
	Anthocyanidins	cherries, strawberries, grapes, red wine, black currant, black elderberries, chokeberries, blueberries, red cabbage, rhubarb, radish, red onion	36,37,41,42,46
	Isoflavones	soy, soy products, legume	36,37,41,42,47–50
Tannins		green and black tea, red wine	38,51–54
Stilbenes		grapes, mulberries, peanuts, berries	48,55–58
Lignans		flaxseed, sunflower seeds, sesame seeds, grains, carrot, onion, chives, apples, cherries, blueberries, strawberries, nuts, tea, coffee	56,59–62

### 1.1.3.1 Phenolic acids

Phenolic acids refer to phenols that possess one carboxylic acid functionality. They serve as bioprecursors of polyphenols and are also metabolites of polyphenols<sup>63</sup>. Phenolic acids, or simple phenols, consist of two subgroups, i.e., the hydroxybenzoic and hydroxycinnamic acids (**Figure 1.3**).

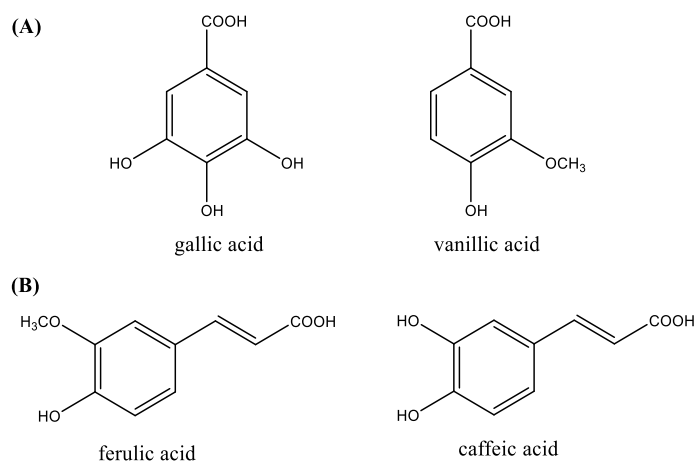


**Figure 1.3.** Examples of hydroxybenzoic (A) and hydroxycinnamic (B) acids.

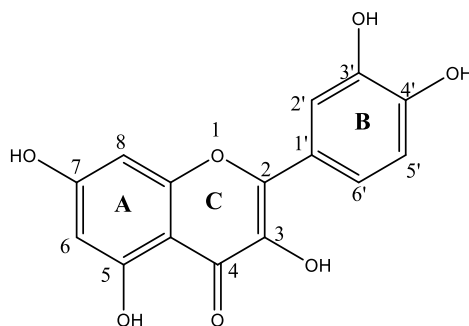
Hydroxybenzoic acids have the common C<sub>6</sub>-C<sub>1</sub> structure and are the simplest phenolic compounds found in nature. Examples of hydroxybenzoic acids include gallic, protocatechuic, vanillic, *p*-hydroxybenzoic, and syringic acids<sup>64</sup>. Gallic acid (GA) has many physiological properties including anti-cancer, anti-diabetic and cardiovascular activity. As an anti-cancer agent, it can exhibit both pro-oxidant and antioxidant properties<sup>65</sup>. It can autoxidate, producing significant levels of ROS which can kill cancer cells through apoptosis<sup>66</sup>. Several studies have recently been carried out on its ability to induce apoptosis<sup>67–69</sup>. In cardiovascular diseases, GA can inhibit the effects of free radicals by increasing the activity of antioxidant enzymes, and/or by increasing the activity of non-enzymatic antioxidant agents such as vitamin C and vitamin E<sup>70,71</sup>. GA can also protect the lining of the gastrointestinal tract from ulcer formation<sup>72</sup> and can inhibit diet-induced hyperglycaemia and hypertriglyceridemia<sup>73</sup>. Vanillic acid (VA), an oxidised form of vanillin, is a flavouring agent found in plants and fruits. It is best known as a food and beverage flavouring but also possesses antioxidant<sup>74</sup> and anti-hypertensive<sup>75</sup> activity.



The hydroxycinnamic acids contain a three-carbon side chain (C<sub>6</sub>-C<sub>3</sub>) and are more common than hydroxybenzoic acids. They consist mainly of caffeic, ferulic, *p*-coumaric and sinapic acids<sup>64,76</sup>. Ferulic acid (FA) is the main phenolic acid constituent of cereals, constituting up to 90 % of the total polyphenol content<sup>36</sup>. It stays in the blood longer than any other phenolic acid and possesses a number of physiological functions including anti-inflammatory, anti-microbial, and anti-thrombotic activity<sup>77</sup>, whilst also promoting angiogenesis<sup>78</sup>. It is widely used as an active ingredient in cosmetic products due to its photoprotective effect<sup>79</sup>. FA is also used as a sports supplement as it alleviates muscle fatigue and promotes muscle growth<sup>77,80</sup>. Caffeic acid (CA) is the most abundant phenolic acid in fruit, with a representation of 75-100 % of the total hydroxycinnamic acid content<sup>36</sup>. Similar to other phenolic acids, it exhibits many physiological effects, including antioxidant, anti-diabetic and anti-cancer activity<sup>81</sup>. CA is present in coffee, and in combination with caffeine may function as an antidepressant<sup>82</sup>.

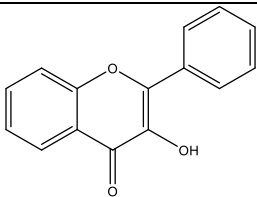
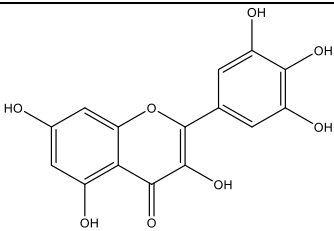
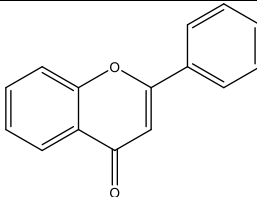
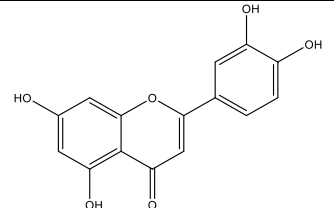
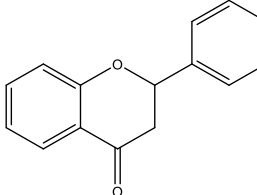
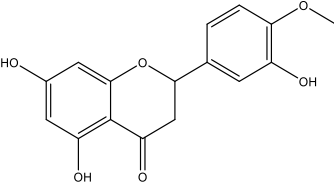
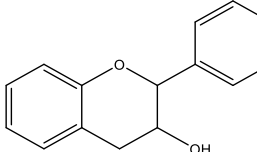
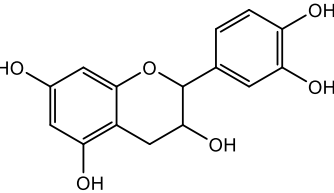
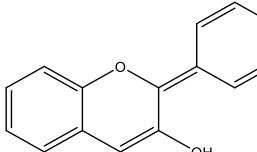
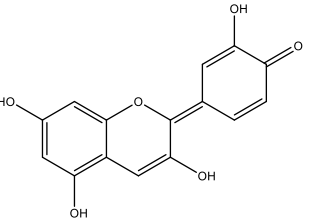
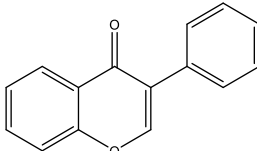
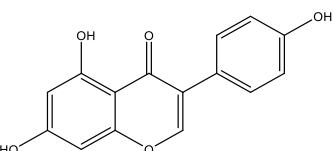
### 1.1.3.2 Flavonoids

Flavonoids are the largest group of plant phenolics, accounting for over half of the 8000 naturally occurring plant products identified<sup>64</sup>. They are characterised by a phenylbenzopyran chemical structure, consisting of a (C<sub>6</sub>-C<sub>3</sub>-C<sub>6</sub>) skeleton<sup>18</sup>. Their structure contains two aromatic rings, A and B, joined by a three carbon-bridge (C) (Figure 1.4). Ring A is derived from the acetate/malonate pathway, and ring B is derived from the shikimate pathway, *via* phenylalanine. The variation of the substituents of ring C leads to the formation of the different classes of the flavonoids<sup>64</sup>, whilst changes in substitutions of rings A and B differentiate the compounds within each class<sup>64</sup> (Table 1.2).



**Figure 1.4.** The basic structure of a flavonoid molecule.

**Table 1.2.** The chemical structures of the main classes of flavonoids.

Flavonoid	Basic structure	Example
Flavonols		 Myricetin
Flavones		 Luteolin
Flavanones		 Hesperitin
Flavanols		 Catechin
Anthocyanidins		 Cyanidin
Isoflavones		 Genisten

Flavonols are the most ubiquitous flavonoids and accumulate in the outer and aerial tissues (skin and leaves) of fruits as their synthesis is driven by sunlight<sup>36</sup>. They contain a hydroxyl group in position 3 of the C ring and may be present in their glycosylated form. They are found abundantly in blueberries, onions and leeks<sup>36</sup>. Quercetin is the most potent dietary flavonol. Its strong antioxidant ability is due to the presence of two pharmacophores within the molecule which have the optimum configuration for free radical scavenging<sup>83</sup> (**Figure 1.5A**). A recent study determined that quercetin inhibits biofilm formation in *Listeria monocytogenes*<sup>84</sup>. Kaempferol (**Figure 1.5B**), another strong antioxidant, shares the same backbone as quercetin but has one fewer hydroxyl group. This causes it to be more chemically stable and less reactive than quercetin<sup>85</sup>. Kaempferol is known to exhibit anti-arthritis activity by regulating the intestinal flora and microbiotic metabolism<sup>86</sup>. It also has significant potential as an anti-cancer agent, as it is a strong promoter of apoptosis and can regulate various signalling pathways<sup>87</sup>.

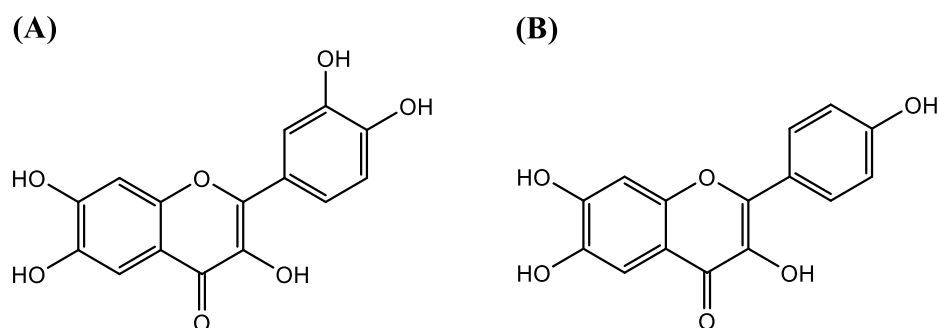


**Figure 1.5.** Chemical structure of quercetin (A) and kaempferol (B).

Flavones differ to flavonols in that they lack oxygenation at the C<sub>3</sub> position<sup>21</sup>. They are much less common than flavonols and are present as glucosides in leaves, flowers and fruits. Examples of flavones include luteolin and apigenin<sup>88</sup>. Recent research focuses on their anti-cancer activity<sup>89,90</sup>. Flavanones are only present in high concentrations in citrus fruit. The main flavanones are hesperetin, naringenin and eriodictyol, which are responsible for the bitter taste of citrus fruits<sup>36,88</sup>. Studies show that there is a direct link between citrus fruit intake and a significant reduction in cardiovascular risk factors<sup>91</sup>.

Flavanols (or catechins) are the 3-hydroxy derivatives of flavanones (**Figure 1.6**). They are the most complex forms of flavonoids, ranging from monomeric to

oligomeric to polymeric forms. They occur abundantly in green tea in the form of (-)-epicatechin-3-gallate (ECG), (-)-epigallocatechin (EGC), (-)-epicatechin (EC) and (-)-epigallocatechin-3-gallate (EGCG)<sup>92</sup>, and are primarily responsible for green tea's anti-carcinogenic, anti-inflammatory, anti-microbial, and antioxidant properties<sup>92</sup>.

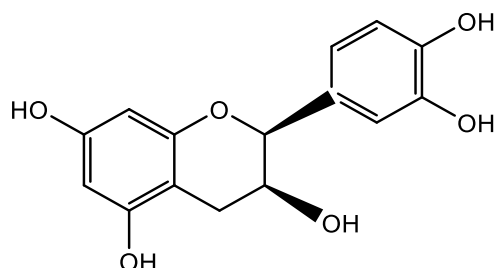


**Figure 1.6.** Chemical structure of (-)-epicatechin..

Anthocyanidins are found in flowers and fruits where they impart red, blue and purple colours<sup>21</sup>. Cyanidin, delphinidin and malvidin are the most studied, and they occur in fruits such as grapes and berries<sup>88</sup>. They have found use in the prevention and treatment of cancer<sup>93</sup>, diabetes<sup>94</sup> and obesity and inflammation<sup>95</sup>. Isoflavones are a unique class of flavonoids and their greatest dietary source are soybeans. They are classed as phytoestrogens and have the potential for treating a range of hormone-dependent conditions<sup>96</sup>. Common isoflavones include genisten and daidzein<sup>88</sup>.

### 1.1.3.3 Tannins

Tannins are high-molecular-weight compounds (500-3000 Daltons) naturally present in cereals, and mostly in fruits and vegetables<sup>97</sup>. They are subdivided into condensed and hydrolysable tannins and can contain up to 20 hydroxyl groups. Condensed tannins (or oligomeric proanthocyanidins) are oligomers of flavanols and are the most abundant plant-derived polyphenols<sup>97</sup>. Hydrolysable tannins are subdivided into gallotannins and ellagitannins. Gallotannins and ellagitannins can readily hydrolyse with dilute acid to form GA and EA monomers<sup>21</sup>. Tannins possess antioxidant, anti-inflammatory and anti-cancer activity<sup>98</sup>, whilst also promote blood clotting. However, certain tannins may inhibit iron bioavailability<sup>99</sup>.

### 1.1.3.4 Stilbenes

Stilbenes contain two phenyl groups that are connected by a two-carbon methylene bridge ( $C_6-C_2-C_6$ )<sup>21</sup>. In plants, most stilbenes act as antifungal compounds which are synthesised in response to injury or infection<sup>76</sup>. Their intake in the human diet is relatively low. One of the most studied stilbenes is resveratrol, found in grapes, wine, soya and peanuts<sup>21</sup>. Resveratrol exists in both *cis*- and *trans*-forms (**Figure 1.7**), and its beneficial activities include antioxidant, antitumour, anti-inflammatory and anti-ageing<sup>100</sup>.

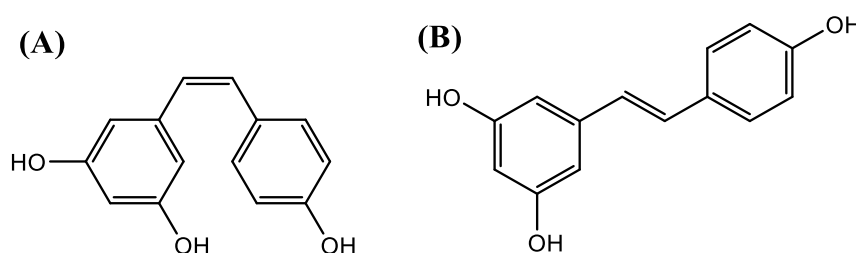


**Figure 1.7.** Chemical structure of (A) *cis*- and (B) *trans*-resveratrol.

### 1.1.3.5 Lignans

Lignans are dimeric compounds formed from dimerisation of two cinnamic acid residues<sup>76</sup>. They are commonly found in fibre rich foods including cereals, oilseed, nuts, vegetables and fruits. To date, more than 20 different lignans have been identified<sup>101</sup>. Secoisolariciresinol diglucoside (SDG) is found mainly in flaxseed and protects against cardiovascular diseases, cancer and diabetes<sup>102</sup>.

### 1.1.4 Chromatographic analysis of secondary metabolites

The analysis of phenolic compounds and flavonoids in foods and beverages is typically carried out using high-performance liquid chromatography (HPLC) with ultraviolet (UV) detection. Wang *et al.* optimised a reversed-phase (RP) HPLC-UV method for the analysis of phenolic compounds including GA, VA, FA, chlorogenic acid (CGA), and quercetin from 37 raspberry varieties. Studies of their antioxidant activities and intracellular ROS activity concluded that specific raspberry varieties possessed significantly higher antioxidant activities than others<sup>103</sup>. HPLC-UV was also applied to characterise the phenolic profile of wine<sup>104</sup>, cranberries<sup>105</sup> and plant

leaves<sup>106</sup>. Additionally, the structural information provided by liquid chromatography-mass spectrometry (LC-MS) is particularly attractive for the determination of the glycosidic derivatives and acylated conjugates of flavonoids<sup>107</sup>, and for the analysis of berry extracts<sup>108</sup> and medicinal herbs<sup>109</sup>.

It is also possible to apply gas chromatography-mass spectrometry (GC-MS) for the analysis of phenolic compounds, however, the analysis is limited to low-molecular-weight analytes (below 600 Daltons) and the high temperatures required may lead to sample decomposition<sup>110</sup>. GC-MS has been applied for the analysis of phenolic acids and flavonoids in medicinal plants<sup>111</sup> and plant leaves<sup>112</sup>.

In recent years, capillary electrophoresis (CE) has received growing interest for the analysis of phenolic compounds. Its advantages include short analysis time, high resolution and efficiency, and minimal sample and solvent consumption. The drawback is that the sensitivity of CE-UV is much less than that of HPLC-UV. This technique has been applied for the analysis of phenolic acids and flavonoids in plants<sup>113</sup>, tomato<sup>114</sup> and olive oil<sup>115</sup>.

## 1.2 Carbon electrode materials

Since the first application of graphite electrodes for the electrochemical production of alkali metals, carbon materials have been frequently studied in areas such as electroanalysis<sup>116,117</sup>, energy storage and conversion (supercapacitors<sup>118</sup>, fuel cells<sup>119</sup>, biofuel cells<sup>120</sup>, lithium batteries<sup>121</sup>), drinking water disinfection<sup>122</sup> and pollutant degradation<sup>123</sup>. Their advantages include low cost, high chemical stability, structural polymorphism, wide potential windows, and relatively inert electrochemistry<sup>124</sup>. Carbon electrode materials may be divided into three subgroups depending on their basic structures or hybridisation:  $sp^2$ ,  $sp^3$  or an  $sp^2$ - $sp^3$  combination. Carbon atoms with  $sp^2$  hybridisation consist of an intraplanar C-C bond length of 1.42 Å and interplanar spacing of 3.354 Å<sup>125</sup>. Examples of  $sp^2$  carbon electrodes include a pyrolytic graphite electrode, a glassy carbon electrode (GCE) and a carbon paste electrode (CPE)<sup>126</sup>. The disadvantage of  $sp^2$  bonded carbon electrode materials is their high susceptibility to electrode fouling, which significantly increases the background current and in turn reduces the signal-to-noise (S/N) ratio for detecting the analyte, and also the reproducibility of the analysis<sup>127</sup>.

### 1.2.1 Boron-doped diamond electrode

The boron-doped diamond (BDD) electrode is an example of a carbon electrode that is completely  $sp^3$  hybridised and tetrahedral, with a C-C bond length of  $1.54 \text{ \AA}$ <sup>125</sup>. They were first studied as potential electrode materials by Pleskov *et al.* in 1987<sup>128</sup>. Natural diamond is a very wide band gap semiconductor (a bandgap of 5.47 eV at  $T = 300 \text{ K}$ ) and with an extremely high inherent electrical resistivity ( $10^{16} \text{ } \Omega \text{ cm}$ ), and so cannot be used as an electrode material<sup>127</sup>. It, therefore, requires the introduction of impurities which increases the conductivity of diamond to make electrodes with marked electrochemical properties<sup>125</sup>. Boron, which is one electron deficient relative to carbon, is the most widely used dopant, resulting in p-type semiconductors, or electrodes with semi-metallic electronic properties depending on the level of doping. BDD thin films are prepared by substituting some of the  $sp^3$  hybridised carbon atoms on the diamond surface with boron atoms. This is most commonly achieved using chemical vapour deposition (CVD) methods on conductive and self-passivating substrates, such as graphite, titanium, tantalum, tungsten, and molybdenum<sup>129</sup>. CVD diamond thin film synthesis involves gas mixture activation and gas-phase reactions, followed by the transfer of diamond forming gas species onto the substrate surface with subsequent surface reactions resulting in the formation of a diamond thin film with a small fraction of non-diamond carbon ( $sp^2$ ) impurity<sup>129</sup>. Hydrocarbon/hydrogen gas mixtures are typically employed for this process. The most popular methods are microwave plasma-assisted CVD, where activation is achieved *via* energy transfer from gas-phase collisions with excited free electrons, and *via* the surface-mediated thermal process (hot-filament CVD) under a hydrogen atmosphere, resulting in hydrogen (H)-terminated surfaces.

Depending on the size of the crystal, BDD electrodes are divided into polycrystalline (grain size in  $\mu\text{m}$ ) and nanocrystalline (grain size  $< 100 \text{ nm}$ ) films<sup>130</sup>. The scanning electron microscopy (SEM) images of the polycrystalline and nanocrystalline diamond are shown in **Figure 1.8**. Polycrystalline BDD is made by vapour deposition from an  $\text{H}_2$  plasma comprising of methane ( $\text{CH}_4$ ) and a source of boron, usually diborane ( $\text{B}_2\text{H}_6$ ). It consists of randomly oriented crystallites with facets and grain boundaries. Nanocrystalline diamond is produced from a  $\text{CH}_4/\text{argon}$  (Ar) plasma

resulting in randomly oriented crystallites. These crystallites have a much greater surface/volume ratio than microcrystalline diamond<sup>125</sup>.

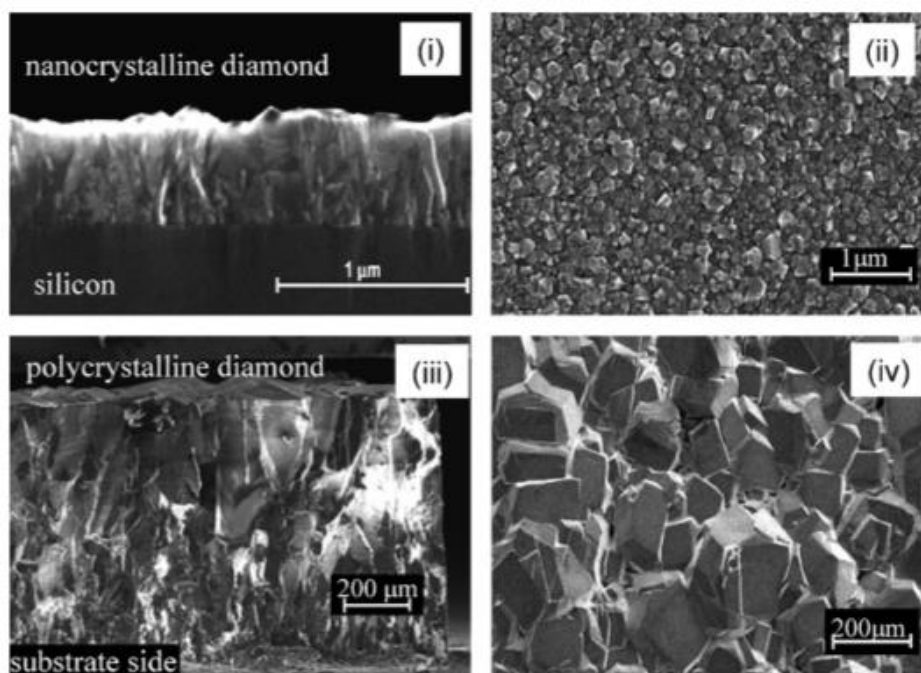


**Figure 1.8.** SEM images of different diamond films. Upper: nanocrystalline diamond – (i) grain structure and (ii) surface morphology where the typical roughness is in the range of 30-50 nm. Lower: polycrystalline diamond – (iii) grain structure and (iv) surface morphology with a surface roughness of several tens of microns<sup>131</sup>.

BDD electrodes have many attractive features over other carbon electrodes. These include<sup>127,130</sup>:

- (i) the largest electrochemical potential window for aqueous ( $\sim -3$  -  $+3.5$  V) and non-aqueous ( $\sim -5$  -  $+7.5$  V) electrolyte solutions. Oxygen and hydrogen decomposition reactions need catalytic sites on the electrode surface to undergo adsorption processes. BDD electrodes lack these sites and, therefore, electron transfer between the surface and a water molecule cannot take place. This allows the detection of molecules that oxidise or reduce at high potentials, which would otherwise be hidden by water decomposition reactions;
- (ii) low and stable capacitive background currents as a result of reduced background current stabilisation time. This is due to the low capacitance of the BDD electrode ( $10 \mu\text{F cm}^{-2}$ ) in comparison to traditional electrode materials including platinum (Pt) and gold (Au) ( $\sim 30 \mu\text{F cm}^{-2}$ );



(iii) long-term response stability. The electrodes high resistance to fouling by adsorption of species, and its insensitivity to oxygen dissolved in aqueous solutions, result in its high response reproducibility and long-term response stability;

(iv) low magnetic susceptibility in comparison to other electrode materials. This allows the hyphenation of electrochemistry with magnetic resonance imaging (MRI) without magnetic distortion for neurological studies;

(v) the  $sp^3$ -bonded carbon is resistant to fouling and biocompatible with organisms. This makes it possible for use in *in vivo* real-time detection.

#### **1.2.1.1 Effect of boron doping levels, non-diamond impurities and surface termination**

The electrochemical properties of BDD electrodes are dependent on boron doping levels, non-diamond impurities ( $sp^2$  carbon) and surface termination (hydrogen or oxygen). The boron content is given by the B/C ratio, where B and C indicate the boron and carbon contents in the gaseous phase for the CVD procedure, with values usually ranging from 100 to 15000 parts per million (ppm). The transition of the diamond from a semiconductor to metal occurs at the boron doping levels of approximately 1000-2000 ppm. In general, increasing the B/C ratio leads to an increase in sensitivity by increasing the conductivity of the electrode. However, as boron sites are directly involved in the adsorption steps required for gas evolution reactions, increasing the boron content causes a reduction in the width of the potential window<sup>127</sup>. Consequently, the oxidation potential of the analytes should be taken into consideration when choosing the specific type (B/C content) of BDD electrode for analysis. Yu *et al.* investigated the influence of the boron content (3500-7500 ppm) of BDD electrodes prepared by hot filament CVD for the detection of uric acid (UA). Differential pulse voltammetry (DPV) demonstrated that the BDD electrode containing the highest boron content exhibited greater sensitivity to UA, a lower limit of detection (LOD), a wider linear range and higher stability<sup>132</sup>. Cyclic voltammograms (CVs) of  $[Fe(CN)_6]^{4-}$  in 0.1 M KCl show increasing current densities with increasing boron-doped levels (**Figure 1.9**).

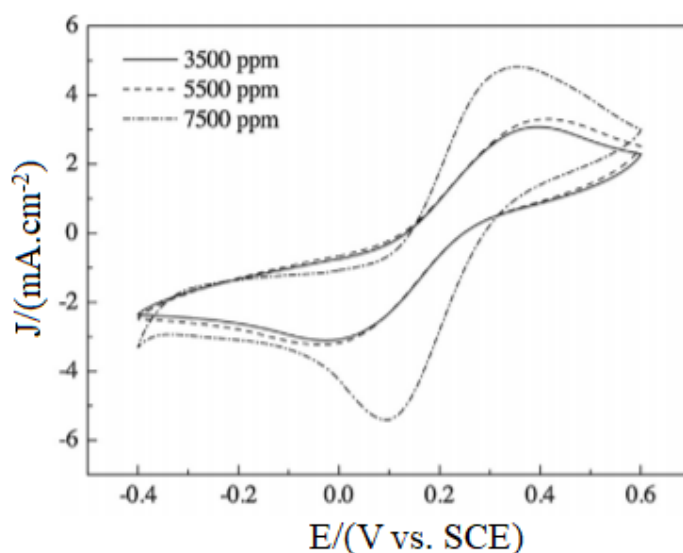


**Figure 1.9.** CVs of BDD electrodes with different boron-doping concentrations in an aqueous solution of 10 mM  $[\text{Fe}(\text{CN})_6]^{4-}$  and 0.1 M KCl. Scanning rate:  $100 \text{ mV s}^{-1}$  <sup>132</sup>.

The ratio of  $\text{sp}^3$  (diamond)/ $\text{sp}^2$  (graphite) also plays a key role in the performance of BDD electrodes. Materials with  $\text{sp}^2$  hybridisation react with oxygen and water to form oxygen-containing functional groups such as phenols, lactones and carbonyls, which can result in a reduced potential window, increased background currents, and susceptibility to corrosion<sup>127</sup>. CVD conditions are selected to reduce the development of  $\text{sp}^2$ -bonded non-diamond carbon impurities, however, they may be introduced by altering the gas mixture ratio used in the deposition. Bennett *et al.* determined that increasing the  $\text{sp}^2$ -bonded non-diamond carbon impurity had minimal effect on the CV peak separation and peak current for the  $[\text{Fe}(\text{CN})_6]^{4-}$  and  $\text{Ru}(\text{NH}_3)_6^{3+/2+}$  redox systems, however, the peak separation decreased proportionally with increased  $\text{sp}^2$ -bonded carbon content for the  $\text{Fe}^{3+/2+}$  and 4-*tert*-butylcatechol systems<sup>133</sup>.

BDD electrodes produced under  $\text{H}_2$  automatically result in an H-terminated surface. H-BDD electrodes have higher conductivity due to the extra surface conductivity. However, they are quickly changed to oxygen (O)-terminated surfaces during anodic oxidation in aqueous solutions, by oxygen plasma treatment, UV, boiling in strong acid and oxidation by a strong oxidant<sup>131,134</sup>. H-terminated surfaces exhibit hydrophobic character, whilst O-terminated surfaces display hydrophilic tendencies and can be changed back to H-terminated by a hydrogen flame or hydrogen plasma treatment. The surface termination of the BDD electrode can also be altered by the

type of pre-treatment applied; anodic (APT) or cathodic (CPT). APT results in the incorporation of oxygen atoms into the BDD surface. These oxygen atoms are a product of water decomposition through applied positive potentials ( $> +2.0$  V) or high anodic current densities for a few seconds to minutes. This process results in the formation of O-terminated BDD electrodes. CPT produces H-terminated BDD electrodes by applying high negative potentials ( $< -2.0$  V) or negative current densities<sup>126</sup>, with the transfer of several thousand electrons per second and per carbon atom resulting in the presence of H atoms on the surface. O-BDD electrodes are known to have a significantly wider working potential window than H-BDD electrodes<sup>134</sup>. They are also favourable for compounds that tend to foul the electrode surface, as the HO• formed during water decomposition reactivates the BDD surface through oxidation of the passivating film<sup>126</sup>. However, in recent years the application of H-BDD electrodes have become more favourable. This is due to a reported increase in voltammetric peak currents and potential shifts to less positive/negative values on H-BDD electrodes after cathodic conversion from O-terminated electrodes. This current increase is reflective of the faster charge transfer kinetics associated with the enhanced surface conductivity of H-BDD electrodes<sup>126</sup>.

Alpar *et al.* demonstrated the effect of electrochemical pre-treatment on signal intensities during the simultaneous determination of 5-*O*-caffeoylquinic acid (5-CQA), vanillin and caffeine. They found that the signal of 5-CQA was always lower on the APT electrode than on the CPT electrode. This was explained by its low  $pK_{a1}$  value (3.51). At a  $pH > 3.5$ , 5-CQA is in its anionic form and, therefore, is electrostatically repulsed from the negatively charged electrode surface<sup>135</sup>.

Contact angle measurements of H-terminated and O-terminated BDD surfaces are illustrated in **Figure 1.10**.

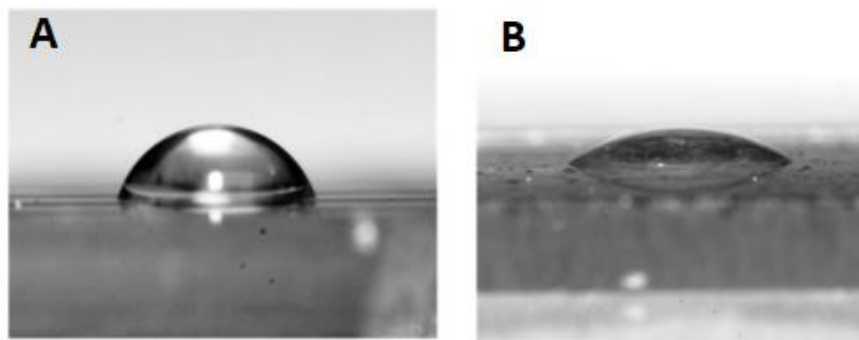


**Figure 1.10.** Contact angle measurements of (A) H-terminated and (B) O-terminated boron-doped diamond surfaces<sup>136</sup>.

## 1.3 Electrochemical methods of analysis

### 1.3.1 Cyclic voltammetry

Cyclic voltammetry (CV) is classified as a potential sweep technique and is the most widely used technique for studying electrochemical reactions. With this technique, the current generated from the oxidation or reduction of an analyte is measured as a function of the linear potential applied. The potential is swept from an initial potential,  $V_1$ , at a fixed scan rate to  $V_2$ , then the scan is reversed and swept back to  $V_1$ . The current generated is a result of redox reactions in the solution (Faradaic current) and the capacitive current. A typical voltammogram is illustrated in **Figure 1.11**.

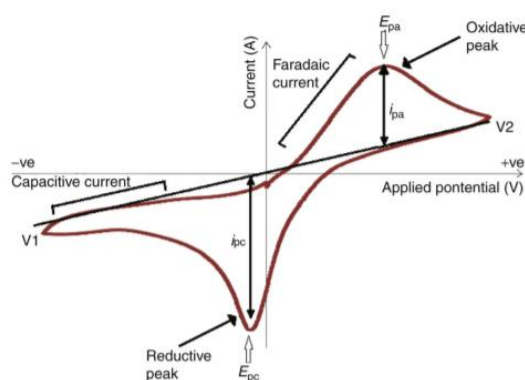


**Figure 1.11.** A schematic diagram of a CV highlighting the anodic peak potential ( $E_{pa}$ ), cathodic peak potential ( $E_{pc}$ ), anodic current ( $i_{pa}$ ) and cathodic current ( $i_{pc}$ )<sup>137</sup>.

CV is most useful for determining whether an analyte undergoes a reversible or an irreversible reaction. With reversible reactions, the rate of electron transfer is greater than the rate of mass transport and the voltammogram is characterised by a peak to

peak separation of 59 mV. Additionally, the peak potentials are independent of the scan rate and the ratio of the oxidation and reduction peak areas equals one. In irreversible reactions, the rate of electron transfer is smaller than the rate of mass transport. These voltammograms are depicted by a reduction in the peak magnitude and an increase in peak to peak separation<sup>138</sup>.

### **1.3.2 Square wave voltammetry**

Square wave voltammetry (SWV) has emerged as an advanced electroanalytical technique, combining the advantages of pulse techniques, CV and impedance techniques. In this technique, a potential waveform is applied to the working electrode. The current is measured in both a forward pulse and a reverse pulse. The resultant SWV is a graph of the difference between these two currents as a function of potential. The main advantage of SWV over CV is that the capacitive contributions to background current are reduced, therefore, it is more sensitive to analyte oxidation or reduction reactions. Other advantages include greater speed of analysis, lower consumption of the electroactive species and less problems with blocking of the electrode surface<sup>139</sup>.

### **1.3.3 Electrochemical impedance spectroscopy**

Electrochemical impedance spectroscopy (EIS) is a technique that has been widely used in areas such as biomedical devices, semiconductors, sensors, imaging and analytical chemistry. Impedance is described as the opposition force to current flow in a circuit. In EIS experiments, a fixed sinusoidal voltage is applied across a sample, and the time-dependent current is measured as a function of the frequency. EIS data can be represented as Nyquist or Bode plots, and is useful for determining the charge transfer resistance of electrode surfaces<sup>140</sup>.

## **1.4 High-performance liquid chromatography**

Liquid chromatography (LC) was defined in 1903 by the Russian botanist, Mikhail S. Tswett. His ground-breaking studies centred on separating leaf pigments extracted from plants using a solvent, in a column packed with particles of calcium carbonate. Before this, it was believed that plants had only two pigments, chlorophyll and

xanthophyll. However, from this experiment, Tswett established that there were two forms of chlorophyll as well as eight additional pigments<sup>141,142</sup>. In the 1960s, Horváth transformed classical LC into a modern instrumental technique, coining the expression “High-Pressure Liquid Chromatography”.

HPLC is an analytical technique used to separate, identify, and quantify individual components in a mixture, relying on a pump to pass a pressurised liquid solvent (mobile phase) containing the sample mixture through a column filled with a solid adsorbent material (stationary phase). Each sample component interacts differently with the stationary phase allowing the identification and quantification of individual sample components.

The reversed-phase mode of chromatography (RPLC) accounts for greater than 90 % of separations in the pharmaceutical, food industry, medical, biomedical, environmental and life science fields<sup>143,144</sup>. In RPLC, a non-polar stationary phase and a hydro-organic mobile phase (often containing buffer salts) are employed for separation. The retention of analytes increases with an increase of the (a) hydrophobicity of the analytes, (b) hydrophobicity of the stationary phase surface, and (c) the polarity of the mobile phase. Separation is reached through two processes, i.e., the partitioning process (where molecules immerse themselves entirely into the bonded phase) and/or the adsorption process (which occurs at the bonded-phase/solvent interface)<sup>143</sup>.

The partition coefficient ( $K$ ) is expressed as the ratio of the concentration of the analyte in the stationary and mobile phases:

$$K = \frac{C_s}{C_m} \quad (1.1)$$

where  $C_s$  and  $C_m$  are the concentrations of the analyte in the stationary and mobile phases, respectively.

Horváth *et al.* postulated that in the partitioning process, the retention is governed by the hydrophobic interactions of the analytes with the hydro-organic mobile phase. In contrast, Carr *et al.* believed that retention was due to the lipophilic interactions between the hydrophobic analytes and the nonpolar stationary phase<sup>143,145</sup>. The

contribution of partition or adsorption retention mechanisms was studied using molecular simulations. These results showed that nonpolar analytes are primarily retained through the adsorption mechanism on stationary phases with shorter ligands (e.g., C<sub>8</sub> phases), while with longer bonded phases (e.g., C<sub>18</sub> phases), both partition and adsorption significantly contribute to their retention<sup>143,146–148</sup>. For analytes with polar functional groups, adsorption represents the retention mechanism on alkyl-bonded phases, irrespective of the alkyl chain length<sup>146,149</sup>.

### 1.4.1 Fundamental parameters of separation

The four fundamental parameters of separation are:

- Resolution ( $R_s$ )
- Retention factor ( $k$ )
- Selectivity factor ( $\alpha$ )
- Number of theoretical plates ( $N$ )

The main goal of HPLC separation is to achieve the optimum  $R_s$  in the shortest time. The ideal  $R_s$  value between two peaks is 1.5 or more, as this ensures that the peaks are baseline separated.

$$R_s = \frac{2(tr_2 - tr_1)}{w_1 + w_2} \quad (1.2)$$

where  $tr_1$  and  $tr_2$  are the retention times, and  $W_1$  and  $W_2$  are the baseline peak widths of peak 1 and peak 2, respectively.

The Fundamental Resolution Equation states that resolution is a function of retention ( $k$ ), number of theoretical plates ( $N$ ), and selectivity ( $\alpha$ ) (**Figure 1.12**).

$$R_s = \frac{1}{4} \sqrt{N} \left( \frac{\alpha - 1}{\alpha} \right) \left( \frac{k}{1 + k} \right) \quad (1.3)$$

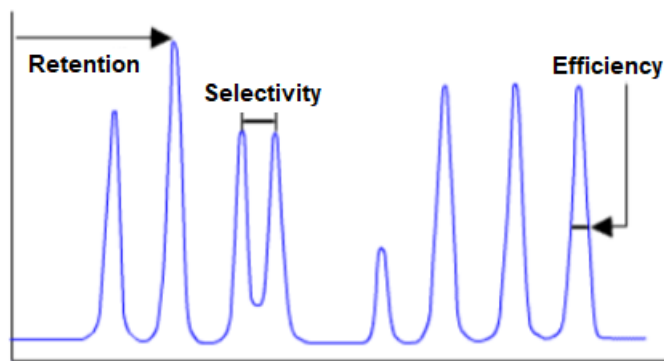


**Figure 1.12.** The contributing parameters to the Fundamental Resolution Equation.

The retention factor ( $k$ ) is a measurement of the time an analyte spends on the column. It is a ratio of the retention of a retained analyte to that of an unretained analyte. Unretained analytes are those analytes that have no affinity for the stationary phase and elute with the solvent front at a time ( $t_0$ ).  $k$  values are independent of column diameter and mobile phase flow rate. When the  $k$  value is between 1 and 5, the greatest gains in resolution are obtained.

$$k = \frac{(t_r - t_0)}{t_0} \quad (1.4)$$

where  $t_r$  is the retention time of the retained analyte and  $t_0$  is the retention time of the unretained analyte.

The selectivity factor ( $\alpha$ ) defines the ability of the chromatographic system to chemically distinguish between sample peaks. It is measured as a ratio of the  $k$  of two peaks and will have a value greater than 1 if peak separation has occurred.

$$\alpha = \frac{k_2}{k_1} \quad (1.5)$$

where  $k_2$  and  $k_1$  are the retention factors of peak 2 and peak 1, respectively.

Efficiency is a measure of the peak dispersion of an analyte as it travels through the chromatographic system. It is measured as the number of theoretical plates ( $N$ ) and can be increased by increasing the column length, by decreasing the flow rate or by decreasing the particle size.



$$N = 5.54 \left( \frac{t_r}{w_{1/2}} \right)^2 \quad (1.6)$$

where  $N$  is the number of theoretical plates,  $t_r$  is the retention time of the analyte and  $w_{1/2}$  is the peak width at half the height.

### 1.4.2 Stationary phases for RPLC

The column is viewed as the core of the chromatographic system. Its performance is dependent on many factors including the chemistry of the stationary phase, the type of medium (fully porous, monolithic or core-shell) and the geometry (surface area, diameter, pore-volume, size and shape) of the particle<sup>143</sup>. Silica is the most commonly used material for the preparation of stationary phases. It is physically and mechanically stable, with a well-known and controllable pore structure and morphology. These characteristics ensure its rapid mass transfer, high reproducibility and good loadability<sup>150</sup>. Silica can be classified into type A, type B and type C groups depending on the synthesis pathway. Type B, prepared by the sol-gel process, is favoured for stationary phase development. This is due to its stability at high pH (up to pH 7), its greater surface area and its overall better separation ability. Additionally, the high metal content of type A can lead to chelation with analytes resulting in strong retention or poor peak shape<sup>143</sup>. Silica particles can be prepared as either spherical or irregular in shape (**Figure 1.13**). Irregular particles are less expensive but they give poorer efficiency in comparison to spherical particles. This is due to how the particles pack in the column, with irregular particles giving less homogeneity<sup>151</sup>.

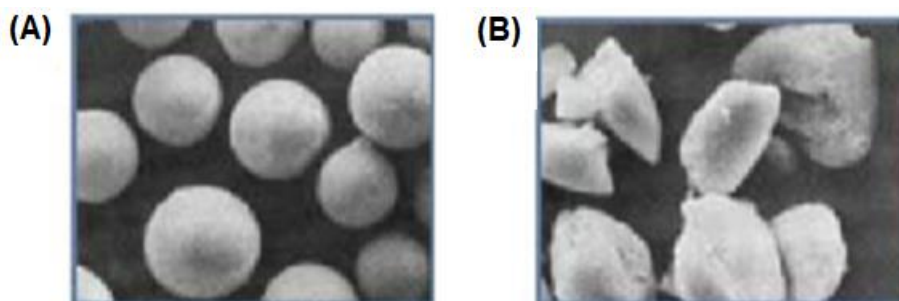


**Figure 1.13.** SEM images of (A) spherically shaped and (B) irregular shaped porous silica particles<sup>151</sup>.

Particle size plays a key role in column performance. Columns containing 3.0  $\mu\text{m}$  particles have now overtaken 5.0  $\mu\text{m}$  particles as the most popular in routine analysis,

providing higher efficiency. Sub-2.0  $\mu\text{m}$  particles provide even higher efficiency, however, their use requires specialised instrumentation that can tolerate pressures close to 15000 psi and a dead volume of fewer than 100  $\mu\text{L}$ <sup>143</sup>. The particle size distribution refers to the distribution of the size of particles used to pack the column. Narrow particle size distributions are desirable as this leads to columns with more homogenous bed packing, with a consequent increase in efficiency<sup>152</sup>.

To produce reversed-phase stationary phases, the desired ligand is covalently bonded to the silica material. These covalent bonds are formed by substitution reactions between organosilanes and the silanol moieties present on the silica surface<sup>143</sup>. The performance of the bonded phase is determined by the type and amount of stationary phase material. Hydrophobic alkyl-bonded phases ranging from  $\text{C}_2$  to  $\text{C}_{30}$  are available, with  $\text{C}_{18}$  and  $\text{C}_8$  the most widely used. Phenyl and aryl-bonded stationary phases are also important phases used in RPLC. These may be derivatised with fluorine to produce fluorinated stationary phases. The advantage of these is their ability to form  $\pi$ - $\pi$  interactions with analytes, giving a different selectivity to long-chain aliphatic columns.

In the chromatographic separation of basic compounds, peak tailing, and poor column efficiency and reproducibility are often observed. These problems are due to the analytes interacting with the acidic residual silanols of the support material rather than with the bonded phase. To overcome this problem, the residual silanols are reacted with hydrophobic or hydrophilic small molecules such as trimethylchlorosilane or amino- or hydroxyl-terminated silanes, in a process known as end-capping. This process significantly blocks and reduces the amount of residual silanols present, eliminating the strong adsorption of basic compounds<sup>143</sup>.

An alternative is the use of polar embedded stationary phases. These phases contain a polar constituent (e.g. urea, ether, amide, sulphonamide, or carbamate) between the silica material and the aliphatic chain. The advantages of these phases are that they produce more defined symmetrical peaks as a result of reduced silanol interactions, and they also provide a complementary selectivity pattern to regular alkyl phases. Additionally, they are more resistant to phase collapse in high or 100 % aqueous

mobile phases. This is due to hydrogen bonding between polar groups, leading to a more ordered alkyl chain structure<sup>153</sup>.

#### 1.4.2.1 Core-shell particles

Efficiency and rapid separation are the two key parameters associated with HPLC. The idea of core-shell particles in LC was initially devised by Horváth in 1967, when he developed 50  $\mu\text{m}$  particles covered by ion exchange resin, thereby creating the first superficially porous packing material<sup>154,155</sup>. This concept was later developed by Kirkland<sup>156</sup> but it was not until 2006 that HALO began large-scale manufacturing and commercialisation of 2.7  $\mu\text{m}$  core-shell particles<sup>157</sup>. Core-shell particles offer the benefits of highly efficient separations with fast flow rates and low back pressures, overcoming the problems associated with fully porous particles. **Figure 1.14** illustrates the increasing interest in core-shell particles over recent years<sup>158</sup>.

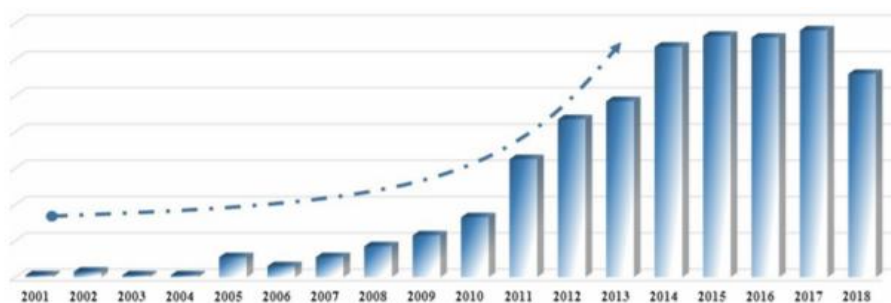


**Figure 1.14.** Data from Scopus showing the increasing number of core-shell related studies from 2001-2018<sup>158</sup>.

Core-shell particles are composed of a solid core and a porous shell (**Figure 1.15**), which can be made from the same or different materials. The inner core has a diameter of 0.9-3.7  $\mu\text{m}$  and can be a single structure, linkage of a group of spheres or a hollow shell filled in with small structures<sup>158</sup>. The outer shell can be an uninterrupted layer or can be formed by several layers of controlled porosity, chemically-modified silica<sup>157</sup>. Recent progress in core-shell particles include the development of Eiroshell<sup>159</sup> and thin-shell<sup>160</sup> particles.

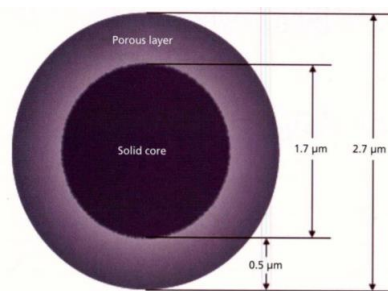


**Figure 1.15.** A representation of a superficially porous particle with a diameter of  $2.7\ \mu\text{m}$  and a solid core of  $1.7\ \mu\text{m}$ <sup>161</sup>.

The solid core together with the porous shell gives a larger particle size, and hence lower operating back pressures. Additionally, the solid core and porous shell offer a higher surface area for separation to occur. The size of the core particle, the shell thickness, and the porosity of the shell are influential to the chromatographic performance of core-shell particles<sup>158</sup>. As the thickness of the porous shell decreases, the faster mass transfer achieved can lead to greater column efficiency and faster analysis time<sup>162</sup>.

The advantages of core-shell particles are illustrated by the van Deemter equation. This equation (**Figure 1.16**) describes the relationship between the height equivalent to a theoretical plate (HETP) and the linear velocity of the mobile phase ( $v$ ), stating that a maximum efficiency will be obtained at a particular linear mobile phase velocity. The key contributors to HETP are diffusion coefficients including the eddy diffusion term ( $A$  term), the longitudinal diffusion term ( $B$  term) and the mass transfer term ( $C$  term).

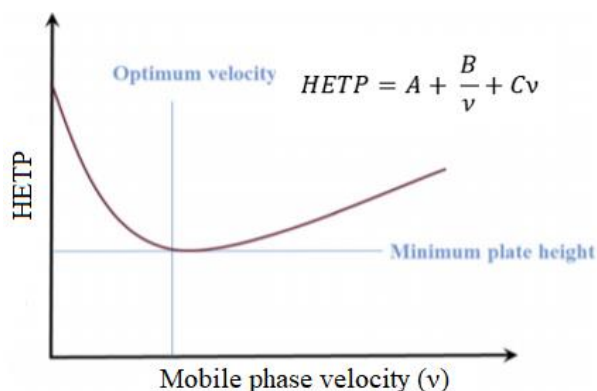


**Figure 1.16.** The van Deemter plot. Where  $A$ ,  $B$  and  $C$  represent the diffusion coefficients;  $v$  is the linear velocity of the mobile phase and HETP is the height equivalent to a theoretical plate<sup>158</sup>.

The *A*-term relates to the differences in the paths of analytes as they move between the stationary phase particles. As the routes analytes take vary in distance, the analyte distribution in the mobile phase tends to broaden as it moves through the column. The magnitude of this broadening is highly dependent on both the particle size and the quality of the packing. The high efficiency of core-shell particles is attributed to their monodisperse particle size which increases the overall column-packing homogeneity (**Figure 1.17**). As a result of this, a 40 % reduction in the *A*-term of the van Deemter equation occurs with core-shell particles<sup>163</sup>. Additionally, fully porous particles have a smooth outer surface and are easier to pack than core-shell particles. However, this smoothness allows the particles to slide over each other creating bed heterogeneity. On the other hand, core-shell particles are known to have a rough outer surface and, therefore, greater shear stress is applied to the particles as they are packed. Once packed, the amount of shear stress required to overcome the frictional forces associated with the roughened surfaces is so great that the movement of the particles and bed expansion is eliminated<sup>162</sup>. A previous report states that high efficiency is also associated with the density of core-shell particles which are approximately 30-70 % higher than fully porous particles. Denser particles can be packed more efficiently<sup>164</sup>.

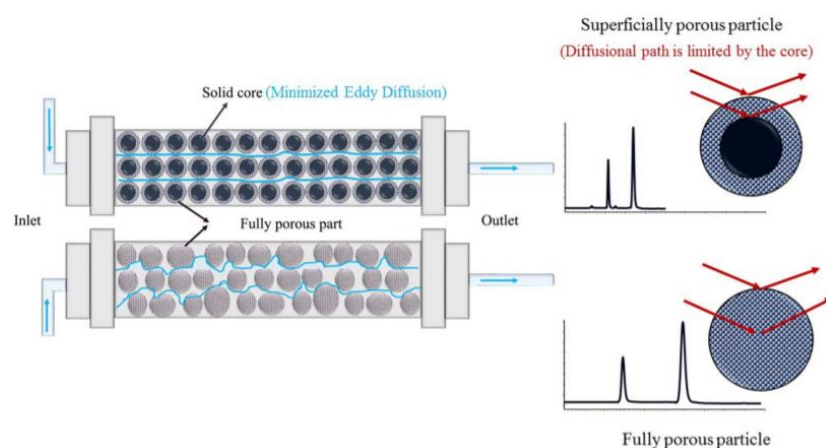


**Figure 1.17.** The effect on peak performance by the means of the difference between wide particle distribution (conventional silica) and narrow particle distribution (core-shell silica)<sup>158</sup>.

The *B*-term (longitudinal diffusion) relates to the axial diffusion of the analyte molecules as a band in the mobile phase, with molecules diffusing from areas of high concentration to areas of low concentration. This term is dependent on the mobile flow rate. With core-shell particles, the *B*-term is reduced by 25 % in comparison to fully

porous particles. This is because the higher permeability of core-shell columns allow faster flow rates, and also because 20 % of the column volume is occupied by non-porous silica which analytes cannot axially diffuse through<sup>163</sup>.

The *C*-term measures the mass-transfer resistances between the stationary and mobile phases. This term is divided into two separate mass transfer terms describing; (a) the contributions to peak broadening in the mobile phase and (b) the contributions to peak broadening in the stationary phase. As analyte molecules move through the column, they are continuously transferring from the mobile phase to the stationary phase, but they all do not transfer at the same rate. Molecules that are closest to the stationary phase enter it immediately, whilst those at a further distance enter it at a later stage. However, those molecules furthest away are carried along by the mobile phase and dispersed away from the molecules that were closest to the stationary phase. Concerning peak broadening attributed to the stationary phase, analyte molecules closest to the surface will enter the mobile phase faster than those that have diffused further into the stationary phase. Hence, those molecules that leave the stationary earlier are dispersed away from the molecules still diffusing from the stationary phase<sup>165</sup>. This resistance to mass-transfer is dependent on the flow rate of the mobile phase, with lower flow rates allowing greater equilibration of analyte molecules between the two phases. A reduction in the *C*-term with core-shell particles is only significant with high-molecular-weight compounds and fast flow rates<sup>166</sup>.

Chromatograms comparing 5  $\mu\text{m}$  fully porous particles and 5  $\mu\text{m}$  core-shell particles for the separation of non-steroidal anti-inflammatory drugs are shown in **Figure 1.18**. The separation was approximately twice as fast using the core-shell column, with a column efficiency of 60 % greater than that obtained with the fully porous column<sup>167</sup>. Furthermore, the shorter run times achievable with core-shell columns allow greater sample throughput and lower consumption of organic solvents.

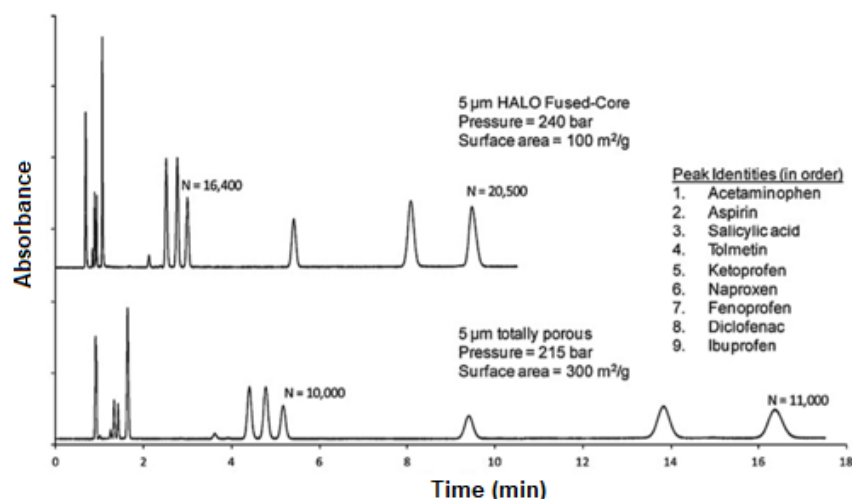


**Figure 1.18.** Comparative separations with 5  $\mu\text{m}$  particles: core-shell vs. fully porous. Columns: 4.6 x 150 mm. A noticeable reduction in retention time and an increase in column efficiency is evident with the core-shell particles<sup>167</sup>.

Core-shell particles have been applied for the simultaneous separation of 16 phenolic compounds including GA and VA in wine, using gradient elution with diode array detection (DAD). The separation was achieved within 20 min with resolution values of 1.64-3.87 between critical pairs<sup>168</sup>. Ferro *et al.* compared a biphenyl core-shell column with two conventional C<sub>18</sub> columns for the separation of phenolic compounds in olive oil. The biphenyl column exhibited a better performance in the fundamental concepts of chromatography ( $\alpha$ ,  $k$ ,  $R_s$  and peak capacity). An overall reduction in the retention time of 22.1 % was achieved with the biphenyl column<sup>169</sup>. A fast RPLC method using a core-shell column was developed for the separation of flavonoids in food supplements. Initially, three types of core-shell columns were investigated; RP-Amide, phenyl-hexyl and C<sub>18</sub>, all 100 x 3.0 mm and a particle size of 2.7  $\mu\text{m}$ . The phenyl-hexyl and C<sub>18</sub> columns were found not to be suitable for the flavonoid analysis as the resolution values were lower than 1.5 or the analysis time was longer than 5 min. Additionally, the phenyl-hexyl column showed an increase in backpressure after long-term use. The RP-Amide column proved optimal for rapid separation due to the embedded polar amide groups in the reversed-phase chains<sup>170</sup>.

## 1.5 HPLC – electrochemical detection

HPLC – electrochemical detection (ECD) couples the separation power of HPLC, with the selectivity and sensitivity provided by ECD for analytes that undergo oxidation or reduction at an electrode surface. In basic terms, the analytes are chromatographically

separated through their interactions with the mobile phase and stationary phase. After separation, they pass the electrochemical detector *via* a flow of mobile phase where they are detected based on their ability to oxidise or reduce. For detection to occur, the HPLC mobile phase must be electrically conductive (contain buffer salts). Electrochemical detectors consist of three separate electrodes; a working, a counter and a reference electrode. A fixed potential difference is applied between the working electrode and the reference electrode to produce an electrochemical reaction at the surface of the working electrode. The current produced by the oxidation or reduction of analytes at the working electrode is balanced by a relative current flowing in the opposite direction at the counter electrode<sup>171</sup>. According to Faraday's Law, when  $N$  moles of a substance reacts, a proportional electric charge  $Q$  passes across the electrode-electrolyte interface<sup>172</sup>:

$$Q = n F N \quad (1.7)$$

where  $Q$  = charge transferred (coulombs) in converting  $N$  moles of material;  $n$  = number of electrons transferred (equivalents/mole);  $F$  = Faraday's constant (96485 Coulombs per mole);  $N$  = moles of reactant (mole).

The derivative of equation 1.7 with respect to time leads to the following equation:

$$It = \frac{dQ}{dt} = nF \frac{dN}{dt} \quad (1.8)$$

where  $I$  is the current generated at the working electrode surface at time  $t$ .

Hence, Faraday's Law states that the rate of an electrode reaction is proportional to the size of the electrical current that crosses the electrode-electrolyte interface<sup>172</sup>.

The working electrode must: be electrically conducting; inert to the mobile phase, impurities in the mobile phase, and any reactive species formed by electrolysis of the analytes; withstand a constant flow of mobile phase, and be mechanically strong. Common working electrode materials include carbon, Au, silver (Ag) and Pt. HPLC



coupled with ECD at a GCE was first applied in 1976, for the determination of biogenic aromatic acids<sup>173</sup> and tricyclic psychotropic drugs<sup>174</sup>.

If, or how electrochemically active an analyte is, is dependent on its chemical structure. Analytes can be divided into three groups: those that are readily electrochemically active, those that are harder to measure electrochemically, and those that are completely unreactive at the electrode surface. Analytes that are readily electrochemically active have a hydroxyl or primary amine group capable of delocalising charge through conjugation with the  $\pi$  electrons of an aromatic nucleus. These mesomeric effects make electrochemical reactions more feasible as the charge is redistributed over several resonance structures, thus favouring the free energy of the reaction. Members of this group include catechols, phenols and phenylamines. The inability of aliphatic compounds with hydroxyl, amine or thiol groups to delocalise charge makes them less able to undergo electrochemical reactions at the electrode surface, often requiring a higher potential for the reaction to occur. For example, the oxidation of the aromatic analyte phenylamine requires an applied potential of + 600 mV (vs. Pd) on a flow-through graphite working electrode, while the oxidation of the aliphatic diethylamine requires an applied potential of > + 900 mV (vs. Pd). The group of analytes that are unreactive at the electrode surface include hydrocarbons, alcohols, aldehydes, ketones and primary aliphatic amines<sup>175</sup>. However, it is this selectivity that makes ECD extremely advantageous over other HPLC detection techniques.

### **1.5.1 Flow-cell design**

The two different modes most often applied are amperometry and coulometry. These differ in the geometry of the working electrode and the quantity of the analyte that interacts with the electrode. With amperometric detection, the analytes flow over the surface of the working electrode, while in coulometric detection, the analytes flow between the surfaces of the working electrode leading to greater conversion energies<sup>176</sup>.

#### **1.5.1.1 Thin-layer amperometric detector**

The thin-layer cell amperometric detector designed by Kissinger *et al.* is the most common and commercially successful amperometric detector cell. The mobile phase

enters the cell through a micro-port and flows through a narrow channel over the working electrode, continuing past the reference and counter electrodes<sup>177</sup> (**Figure 1.19**). The working electrode is set at a potential higher than the potential needed for electron transfer to occur. This produces an amperometric current which is proportional to the concentration of the analyte. As the concentration of the analyte flowing over the electrode changes with time, the classical peak shaped chromatogram is produced. The cell is constructed from two solid blocks which are separated by a thin polytetrafluoroethylene (PTFE) gasket acting as a spacer around the working electrode and the inlet and outlet openings. The block containing the working electrode is constructed from an inert material such as PTFE, and the second block acting as the counter electrode is produced from stainless steel<sup>177</sup>. This design allows for a smooth flow of eluent over the electrode surface, resulting in a reduction in the baseline noise with enhanced sensitivity<sup>176</sup>.

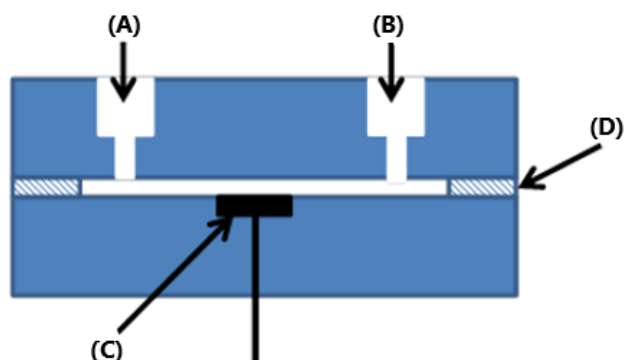


**Figure 1.19.** Thin-layer cell amperometric detector: (A) inlet, (B) outlet, (C) working electrode and (D) spacer gasket<sup>176</sup>.

### 1.5.1.2 Wall-jet amperometric detector

With the wall-jet amperometric detector, the mobile phase is directed perpendicularly onto the working electrode (**Figure 1.20**). The theory behind this design is that less fouling of the electrode occurs due to the cleansing effect of the solution jet. Also, it is believed that mass transfer of the analytes is improved, producing greater current amplitudes. However, with flow rates limited to 0.5-2.0 mL/min, the real wall-jet effect cannot occur and only minor improvements in sensitivity are achieved<sup>178</sup>. One disadvantage is the possible increase in baseline noise attributed to turbulence produced by the flow of jet of the mobile phase<sup>176</sup>. The signal intensity from the wall-jet amperometric detector depends on both the size of the electrode and the diameter

of the jet (the electrode diameter should be at least 10 times greater than the jet diameter).

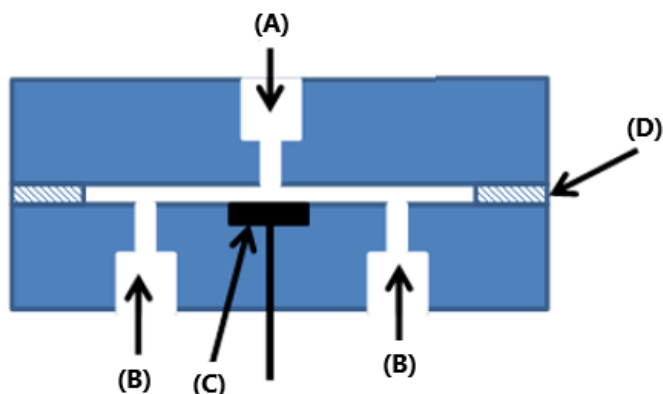


**Figure 1.20.** Wall-jet amperometric detector: (A) inlet, (B) outlet, (C) working electrode and (D) spacer gasket<sup>176</sup>.

### 1.5.1.3 Dual-electrodes detection systems

It is also common to use more than one working electrode to improve both the selectivity and sensitivity. These electrodes can be arranged in series, in parallel or parallel adjacent. In the parallel configuration, the mobile phase simultaneously contacts two identical working electrodes that are arranged side by side (**Figure 1.21A**). The advantage of this mode is that the electrodes can be held at two different potentials. The ratio of these currents is then measured confirming the identity and the peak purity of the analyte. Additionally, the simultaneous detection of both oxidisable and reducible analytes is possible by setting the electrode potentials in different modes<sup>178</sup>. This method is also useful for the determination of co-eluting compounds with different redox potentials. The potential of one electrode is set so that only the more easily oxidised or reduced analyte is detected. At the other electrode, both analytes are detected. The concentration of the second analyte is thus calculated by difference.

With the series configuration, the first working electrode is referred to as the generator and the second working electrode as a detector (**Figure 1.21B**). By either oxidation or reduction, the generator electrode creates an electrochemically active adduct which is then measured at the detector electrode. This electrochemical adduct has greater electrochemical properties, meaning it is more easily oxidised or reduced.

Furthermore, if possible interferents are present in the sample, they can be irreversibly oxidised or reduced at the generator electrode and, therefore, will not appear at the detector electrode. Both working electrodes can be independently potentiostatically controlled, and due to the low potentials applied, background currents are generally lower than those observed with direct electrochemical detection<sup>178</sup>.

The parallel adjacent detector is illustrated in **Figure 1.21C**. Here, the working electrodes are placed on opposite sides of a very thin channel. One electrode is set in oxidative mode and the other in reductive mode. When a thick spacer is used, the two electrodes can function as independent parallel dual electrodes, but when a thin spacer is used the products of one electrode can diffuse to the other and *vice versa*. If the electrodes are suitably large, each analyte particle undergoes several oxidation-reduction cycles, resulting in a significant amplification of the detector current<sup>176</sup>.

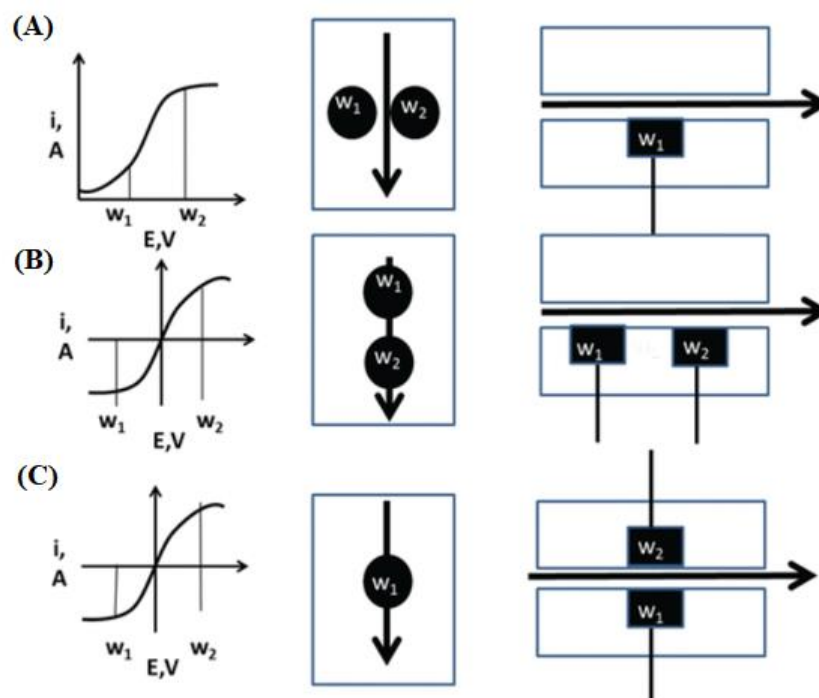


**Figure 1.21.** Parallel and series configurations for dual electrode detection systems.  $W_1$  = working electrode 1;  $W_2$  = working electrode 2. (A) parallel; (B) series and (C) parallel adjacent. Arrow indicates direction of flow<sup>176</sup>.

#### 1.5.1.4 Pulsed amperometric detection

A major disadvantage of amperometric detection is the adsorption or deposition of solution impurities or electrochemical reaction by-products leading to the deactivation

of the electrode surface. The rate at which this deactivation occurs depends on factors including the composition and pH of the mobile phase, the nature of the analyte, the type of electrode material, the mode of the electrode and the applied potential. At higher applied potentials, a higher quantity of the analytes will undergo electrochemical reactions. This leads to increased background currents which cause a reduction in sensitivity. A loss in selectivity is also possible due to a greater risk of interference. To overcome this problem, a pulsed amperometric potential is applied during amperometric measurements. With pulsed amperometric detection (PAD), alternate anodic and cathodic potentials are applied to reactivate the electrode surface and to increase the sensitivity and reproducibility of detection (**Figure 1.22**)<sup>171</sup>. To achieve a clean and reactive electrode surface, PAD must have three principal steps: (a) application of a potential to electrocatalytically oxidise the analyte, (b) oxidation by a large positive anodic potential resulting in the formation of a surface oxide, and (c) reduction by applying a large negative potential resulting in the removal of the oxide surface and a reactivated electrode surface<sup>179</sup>. PAD provides increased sensitivity for analytes generally considered as non-electroactive for detection under constant applied potential, for example, carbohydrates, amines and thiols<sup>176</sup>.

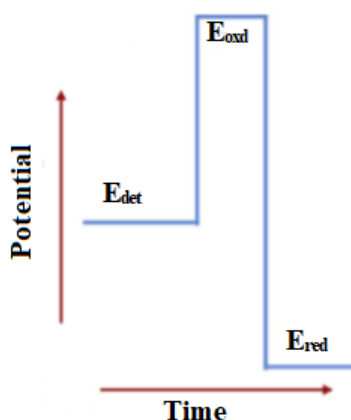


**Figure 1.22.** The simplest PAD waveform. The analyte is detected by the application of the detection potential ( $E_{det}$ ) at the electrode surface for a period of time. Then the anodic oxidative potential ( $E_{oxd}$ ) is applied for a time to produce a surface oxide on the electrode surface. Finally, a cathodic reductive potential ( $E_{red}$ ) is applied to reactivate the electrode<sup>179</sup>.

### 1.5.1.5 Coulometric detectors

A major disadvantage of amperometric detectors is that the efficiency for the conversion of the target analyte is only 1-10 %. This rate of efficiency is dependent on the electrode surface area, the channel thickness and the flow rate. As evident from **Figure 1.23**, the conversion efficiency of the thin-layer amperometric detector is highly dependent on the flow rate. At typical HPLC flow rates, the residence time of analytes over the electrode surface is only a couple of tens of milliseconds which is not enough time for analytes to diffuse laterally to the surface. Decreasing the flow rate results in higher conversion efficiencies, however, this is not always practical as slower flow rates result in prolonged retention times and poorer chromatographic efficiency.

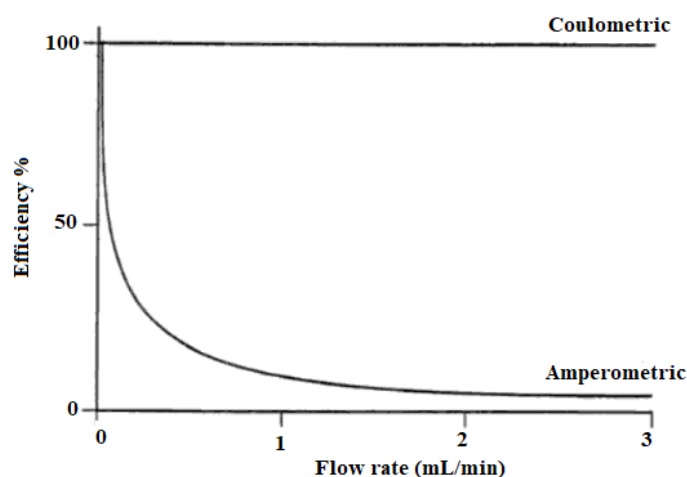


**Figure 1.23.** A comparison of electrode efficiency as a function of flow rate for coulometric and amperometric detection. Conversion efficiency decreases for the thin-layer amperometric electrode but remains at 100 % for the coulometric electrode<sup>175</sup>.

To overcome this problem, coulometric detectors are utilised. These detectors contain flow-through porous carbon electrodes consisting of high surface areas and reduced diffusion distances. This leads to a conversion efficiency of close to 100 % with a resultant increase in sensitivity<sup>176</sup>. Also, the conversion energy is unaffected by an increase in flow rate, allowing faster analysis in comparison to amperometric detection. Another advantage of coulometric detection is that due to the 100 % conversion efficiency, Faraday's Law can be used to predict the peak area if the amount of sample injected is known. Or if the peak area is known, the exact

concentration of the analyte can be determined. This is not possible with amperometric detection as the exact efficiency of the conversion is unknown and is continuously decreasing<sup>175</sup>. Additionally, due to the larger surface area, there is less electrode deactivation and fouling associated with coulometric electrodes than amperometric electrodes. A cross-section of a coulometric cell is illustrated in **Figure 1.24**.

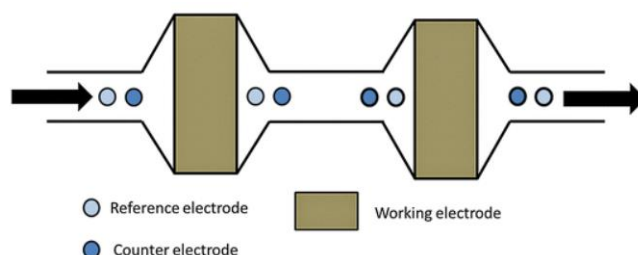


**Figure 1.24.** A cross-section through a dual coulometric electrode showing the placement of working, counter and reference electrodes<sup>176</sup>.

Two or more electrodes configured in series is known as the screening mode. When analytes elute from the HPLC column, they enter the first upstream electrode. This electrode is set to a potential high enough to oxidise or reduce possible interfering analytes. By correctly choosing this potential, the analytes of interest pass through unaffected and are then measured at the downstream detector in the absence of interferences. Another variation is the generator/detector mode. This is similar to that used with dual-electrode amperometric detection, however, the current response is much greater due to higher conversion energies<sup>176</sup>. A further advancement was the development of the coulometric array (CoulArray) detector, first applied to improve the selectivity and resolution of tissue neurotransmitters following chromatographic separation<sup>180</sup>. This model allows for the simultaneous evaluation of up to 16 different potentials, promoting the identification and quantitation of analytes with enhanced efficiency. Detection of analytes takes place in a four by four cell series configuration. This design allows the measurement of the number of electrons required to achieve complete oxidation from the analyte starting material to product, thus, providing a pathway to complete quantitation<sup>181</sup>.

### 1.5.2 HPLC-ECD of secondary metabolites in foods, beverages and plants

Freitas *et al.* developed an RPLC separation with PAD for the analysis of phenolic acids in sugarcane vinasse<sup>182</sup>. The detection of GA, VA, FA, CA and *p*-coumaric acid was conducted with a GCE following separation with a C<sub>8</sub> column. The use of PAD prevented adsorption of the analytes on the electrode surface. PAD was also applied for the determination of 12 phenolic acids and flavonoids in medicinal plants using an Au electrode following RPLC separation<sup>183</sup>. The addition of  $\beta$ -cyclodextrin ( $\beta$ -CD) to the mobile phase reduced the total analysis time, whilst also increasing detection sensitivity. Furthermore, Natale *et al.* utilised PAD at a GCE electrode for the determination of polyphenolic compounds in artichoke bract extracts and olive mill wastewaters, following chromatographic separation using a core-shell C<sub>18</sub> column<sup>184</sup>.

Lamarca *et al.* designed a homemade electrochemical flow cell for the simultaneous UV and amperometric detection of phenolic acids in palm oil samples (**Figure 1.25**)<sup>185</sup>. The separation was achieved on a reversed-phase C<sub>18</sub> column and a GCE was used as the working electrode for end-column detection.

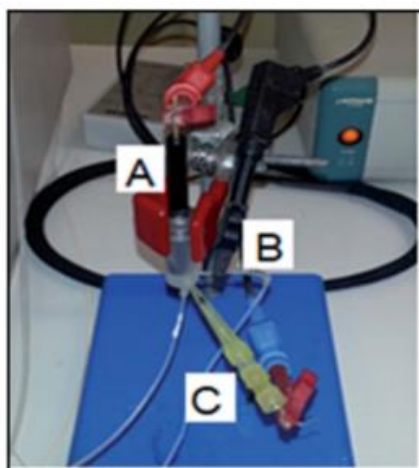


**Figure 1.25.** A homemade electrochemical flow cell. The working electrode (A), the counter electrode (B) and the reference electrode (C)<sup>185</sup>.

The detection of protocatechuic acid (PCA), CGA and CA in honey samples was also carried out by RPLC with simultaneous UV and ECD detection. ECD was achieved with a GCE and LODs were 123-200 fold times lower for ECD than UV detection<sup>186</sup>. In addition, Liang *et al.* optimised a sensitive method for the simultaneous separation



and detection of CA, FA, *p*-coumaric acid and hesperetin in Chinese citrus honey<sup>187</sup>. The separation was achieved with a core-shell C<sub>18</sub> column followed by detection at a GCE. The detection and quantification limits of the four analytes were 6-14 times greater with ECD than DAD detection. Novak *et al.* developed a RPLC-ECD method for the identification and quantification of flavonoids in red grape skin extracts using amperometric detection at a GCE<sup>188</sup>. The LODs achieved with ECD were 1000 times lower than those obtained with PDA detection. The RPLC-ECD of phenolic compounds in fruit extracts was determined using two detectors in series: a wall-jet flow cell detector with a GCE, followed by a thin-layer flow cell with a BDD electrode<sup>189</sup>. The BDD was set at a higher potential (+ 0.9 V) than the GCE (~ + 0.7 V), allowing the detection of phenolic compounds that were oxidised at higher potentials. This group also used the same system for the sensitive detection of flavonoids in the medicinal plant, *Calligonum polygonides*<sup>190</sup>. ECD enabled the identification of the analytes at lower concentrations than PDA detection and also eliminated interferences. Zhang *et al.* developed a sensitive method for the determination of CGA, rutin, hyperoside, quercitrin and quercetin in a Chinese medicinal herb<sup>191</sup>. The separation was obtained on a C<sub>18</sub> column followed by detection using a thin-layer cell and a GCE. LODs were 2.8-3.6 fold lower for ECD than UV detection at 360 nm.

The phenolic composition of 17 wines was determined using RPLC coupled in series to a PDA detector and an electrochemical wall-jet flow cell with a GCE<sup>192</sup>. The results showed that the total antioxidant capacity of red wine is much higher than that of white wine. A simple isocratic RPLC separation with amperometric detection was developed for the analysis and quantification of hydroxycinnamic acids and their corresponding aroma-active volatile in wort and beer<sup>193</sup>. The addition of *o*-phosphoric acid to the mobile phase improved the resolution by suppressing the dissociation of the weakly acidic phenolic compounds.

Gazdik *et al.* focused on the determination of neuroprotective phenolic acids and flavonoids in fruits. Separation of the analytes was carried out on a C<sub>18</sub> column followed by detection at a GCE<sup>194</sup>. The quantitative determination of phenolic acids in red wine, beer, and brandy, was achieved with RPLC separation followed by electrochemical detection at an Au polycrystalline electrode<sup>195</sup>. LODs of the analytes

ranged from 2-19 nM. Zheng *et al.* developed a sensitive method for the simultaneous separation and detection of phenolic acids in Chinese herbal medicine<sup>196</sup>. The separation was achieved on an RP C<sub>18</sub> column using combined PDA detection and ECD at a GCE. Detection and quantification limits achieved with ECD were 7-28 fold greater than those obtained with the PDA detector.

Bayram *et al.* analysed olive oil for phenolic compounds, including CA, FA, VA, and *p*-coumaric acid using HPLC coupled with coulometric ECD<sup>197</sup>. Detection was carried out on a 4-channell CoulArray detector with increasing applied potentials of + 250, + 400, + 500 and + 750 mV, following chromatographic separation using a core-shell C<sub>18</sub> column.

**Table 1.3.** HPLC-ECD (amperometric) methods for the determination of plant phenolics in foods, beverages and plants.

Technique	Electrode	Assayed analyte	Type of sample	Ref.
RPLC-PAD	GCE	GA, VA, FA, CA, <i>p</i> -coumaric acid	sugarcane vinasse	182
RPLC-PAD	Au	phenolic acids and flavonoids	medicinal plants	183
RPLC-PAD	GCE	vegetable origin samples	polyphenolic compounds	184
RPLC-UV-ECD	GCE	phenolic acids	palm oil	185
RPLC-UV-ECD	GCE	PCA, CGA, CA	honey	186
RPLC-ECD	GCE	CA, FA, <i>p</i> -coumaric acid and hesperetin	Chinese honey	187
RPLC-ECD	GCE	flavonoids	red grape skin extracts	188
RPLC-ECD	GCE/BDD electrode	flavonoids	fruit extracts	189
RPLC-ECD	GCE/BDD electrode	flavonoids	medicinal plant	190
RPLC-ECD	GCE	CGA, rutin, hyperoside, quercitrin and quercetin	Chinese medicinal herb	191
RPLC-UV-ECD	GCE	flavonoids	wine	192
RPLC-ECD	GCE	hydroxycinnamic acids	wort and beer	193
RPLC-ECD	GCE	phenolic acids and flavonoids	fruits	194
RPLC-ECD	Au	phenolic acids	beer, red wine, brandy	195
RPLC-UV-ECD	GCE	phenolic acids	Chinese herbal medicine	196

## 1.6 Whiskey – an overview

In the past, distilled alcoholic beverages, known in Latin as *aqua vitae* (water of life), were regarded as having great medicinal (almost spiritual) properties, and the tradition was to entrust their recipes to the religious clerics of that time. Whiskey, or in Gaelic, *uisge beatha* (also, water of life), is the generic name for a distilled product made from saccharified and fermented cereal extracts. The first recorded mention of whiskey in the world came from the Irish Annals of Clonmacnoise in 1405, referring to the death of a local chieftain after taking a “surfeit of *aqua vitae*”<sup>198</sup>. The first recorded commercial transaction involving the supply of whisky (Scottish spelling) took place between the Benedictine monastery at Lindores Abbey in Fife and the Court of King James IV at Holyrood, Edinburgh in 1494<sup>199</sup>. The monasteries retained exclusive whiskey production until the mid-1500s, when the English and Scottish monasteries were dissolved, allowing the widespread knowledge of whiskey production<sup>200</sup>.

Ireland, Scotland, the USA, Canada and Japan are the chief exporters of whiskey<sup>201</sup>. Scotch whiskey is divided into five categories; single malt, blended malt, single grain, blended grain and blended whiskey. Single malt whiskey is produced from single malted barley in a single distillery, whereas blended malt whiskey is a mixture of single malts produced from various distilleries. Single grain whiskey is not produced from barley, but from other cereal such as corn or wheat, with a small percentage of malted barley added as a catalyst. Blended grain whiskey is made from a blend of two or more single grain whiskeys from different distilleries, and is less common than blended malt whiskey. Blended whiskey is a mixture of malt and grain whiskeys. The ratio of malt to grain varies depending on the commercial brand<sup>201</sup>. Single pot still whiskey, a whiskey native and unique to Ireland, is made from a mixture of malted and unmalted barley and distilled in a pot still. Its spicier taste and thicker texture are attributed to the unmalted barley. For it to be classified as single pot whiskey, it must be distilled in one single distillery<sup>202</sup>.

### 1.6.1 Malt whiskey production

There are five stages to malt whiskey production: malting, mashing, fermentation, distillation and maturation.

### Step 1 – Malting

The malting step involves soaking the barley for 2-3 days in tanks of water known as steepers. Following this, the barley is spread out over a concrete floor and allowed to germinate. The time over which germination takes place can vary from 8-12 days, depending on factors such as the quality of the barley and the season of the year. During this process, the barley secretes diastase, an enzyme which converts the starch into soluble sugars to make the alcohol. The rate of germination and temperature is controlled by turning the barley at regular intervals. Once green shoots start to appear, the germination is stopped and the barley is dried in a malt kiln. Today, it is more common for malting to take place in Saladin boxes or in drum maltings, where the temperature and turning of the barley are controlled mechanically<sup>203</sup>.

### Step 2 – Mashing

After drying, the malt is ground down to a fine powder known as grist. This is then mixed with hot water in a large circular vessel called a mash tun, where the dissolved sugars are drawn to the bottom of the mash and extracted. The ensuing liquid is called wort<sup>204</sup>. This process is usually carried out three times, with an increase in temperature each time to extract as much sugar as possible. Only wort from the first two extractions is used with the third put back into the next batch of new grist<sup>205</sup>.

### Step 3 – Fermentation

After cooling, the wort is placed in large vessels called washbacks, where it is fermented by the addition of yeast (from the *Saccharomyces cerevisiae* species). Fermentation takes 48-96 hours and produces a liquid known as wash. This wash contains the alcohol (6-10 % in strength), some unfermentable matter and by-products of fermentation<sup>203,206</sup>.

### Step 4 – Distillation

Distillation takes place in copper stills which consist of a bowl shape at the bottom that raises to the neck at the top. Taller stills with longer necks give finer, lighter spirits, whereas shorter, fatter stills produce a fuller, richer spirit. The wash enters the first still where it is heated to the point where it starts to vaporise. The vapour rises through the still until it reaches the neck where it condenses. This distillate, known as

low wines, is then passed to another still where it is distilled for a second time. Alcohols produced at the beginning of the distillation (called foreshots) are very high in strength and very pungent, while the alcohol (called feints) produced at the end of the distillation is very low in strength and also pungent. Only the alcohol produced from the middle (or heart) is used for maturation. This alcohol has a strength of 65-70 % and determines the character of the spirit in terms of taste, smoothness and flavour<sup>207</sup>. In Scotland, whiskey is traditionally doubly distilled, whilst in Ireland, it is triply distilled, however, there are exceptions in both countries<sup>205</sup>.

#### Step 5 – Maturation

After distillation, the spirit is stored in wooden oak casks. In Scotland, it is a legal requirement that the spirit is matured for at least three years before it is allowed to be called whiskey. The most common oak casks are those that have been previously used in the American bourbon and Spanish sherry industries. Throughout the maturation process, natural flavourings from the casks are released, imparting flavour to the whiskey. Additionally, the surrounding environment also affects the characteristics of the whiskey<sup>205</sup>.

### 1.6.2 Chemical composition of whiskey

Whiskey comprises of a multitude of chemical compounds. These compounds originate in the raw materials but are further modified by the methods used in production. In the malting, mashing and fermentation processes, the sensory character is influenced by the type of cereal used, the constituents of the water used for the malting and mashing, and the type of heat used for the kilning. During the distillation process, some flavour compounds are eliminated while others are formed. The flavour formation is a result of Maillard reactions which occur between amino acids and sugars. The flavour of the final spirit also depends on the type of still used (batch or continuous). Batch distilled whiskeys have greater variation of flavour, ranging from light and floral to heavier, complex spirits<sup>208</sup>.

Maturation is one of the key factors affecting the quality of the whiskey. It is characterised by changes in the flavour and a reduction in both volume and alcoholic content. The colour also changes, with the whiskey developing a golden, amber colour

over time, attributed to the formation of melanoidins from the breakdown of cellulose<sup>209</sup>. The time required for acceptable maturation is dependent on the attributes of the distillate; the size, origin and treatment of the wood cask; and the environment where the maturation takes place<sup>210</sup>. In Scotland, whiskey is matured for 12-16 years in casks that must be less than 700-litre capacity. Changes in flavour during maturation are due to changes in the composition and concentration of the aroma producing chemical compounds through subtractive, additive and interactive reactions. These changes may be influenced by the direct extraction of wood compounds; the decomposition of wood macromolecules and extraction of their products into the distillate; possible reactions between constituents of the wood and the raw distillate; reactions involving only the wood components; reactions involving only the distillate components; and evaporation of volatile components<sup>210</sup>. Traditionally, whiskey is aged in white oak casks of various species. In the USA, wood oak is usually *Quercus alba*, and in Europe, it is typically *Quercus petraea* and *Quercus robur*, with most of the wood originating from France<sup>210</sup>. Each wood species has different characteristics and, therefore, contributes a specific aroma to the final whiskey. It is tradition to use casks that have previously been used to make bourbon. This serves as a pre-treatment for the casks as it removes most of the vanillin associated with white oak, eliminating a potential strong sweet vanilla flavour to the whiskey. Whiskey flavour wheels are often used to identify specific attributes and characteristics or identify common flavours between whiskeys (**Figure 1.26**).



amount of an oak wood polyphenol called ellagitannin. During construction of the oak casks in which the wood is charred or toasted, ellagitannin is hydrolysed to form GA and EA. Additionally, EA also finds its way into whiskey during the germination of barley.

Adding a few drops of water to whiskey before drinking is believed to further enhance the taste. Karlsson and Friedman carried out computer simulations of water-ethanol (EtOH) mixtures in the presence of guaiacol to study this theory<sup>216</sup>. They found that at concentrations greater than 59 % EtOH, guaiacol was driven away from the surface of the whiskey and into the bulk solution. However, at 45 % EtOH, guaiacol was more likely to stay present at the surface of the whiskey, enhancing both its odour and taste.

The whiskey lactones (*cis*- and *trans*-3-methyl-4-octanolide) originate from the oak casks in which the whiskey is stored (**Figure 1.27**). The *trans*-isomer contributes a woody, coconut flavour, whilst the *cis*-isomer gives a strong, spicy coconut flavor<sup>217</sup>.

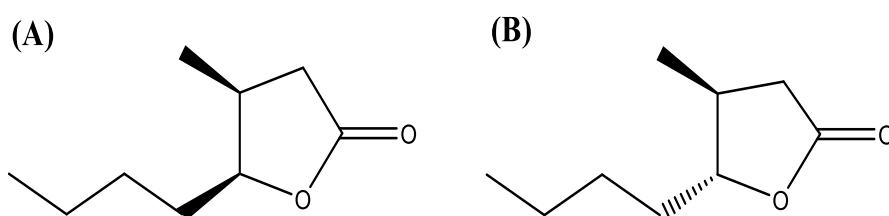


**Figure 1.27.** The whiskey lactones. (A) *cis*-3-methyl-4-octanolide and (B) *trans*-3-methyl-4-octanolide.

The largest group of flavour compounds in whiskey are the esters, with the majority consisting of ethyl esters of monocarboxylic acids<sup>218</sup>. They are produced during the fermentation process from the combination of alcohols and either fatty acids or the acetates produced during fermentation<sup>217</sup>. Ethyl hexanoate is the major ester present in the final spirit<sup>212</sup>. Other esters include ethyl lactate, ethyl octanoate, ethyl butyrate, ethyl decanoate, ethyl laurate, isoamyl acetate and ethyl acetate<sup>219</sup>. Isoamyl acetate is responsible for the banana-like aroma of whiskey, while ethyl hexanoate gives an apple-like aroma<sup>217</sup>.

Acetaldehyde represents more than 90 % of the total aldehyde content of whiskey<sup>218</sup>. Although some of it is lost in the distillation process, it contributes a pungent, sharp flavour to the whiskey. Other aldehydes present are attributed to the oak casks in which the whiskey is stored. Syringaldehyde contributes a spicy, smoky flavour, while



furfural provides an almond-like grainy flavour (**Figure 1.28**). Whiskey can also contain vanillin, coniferaldehyde, sinapaldehyde and hexanal<sup>217</sup>. Hexanal contributes a grassy, fruity flavour to the whiskey<sup>212</sup>.

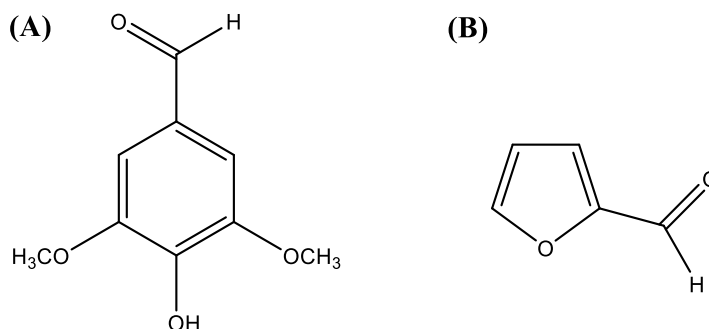


**Figure 1.28.** Chemical structures of (A) syringaldehyde and (B) furfural.

Sulphur containing compounds, in particular dimethyl trisulfide (DMTS), contribute unpleasant, gassy aromas to whiskey at high concentrations, but at lower levels make a positive contribution to whiskey aroma. DMTS is formed from methanethiol and hydrogen sulphide which are derived from the amino acids methionine and cysteine, respectively. Copper stills can both reduce and increase the levels of sulphur depending on the location of the still. Harrison *et al.* showed that copper is more effective at reducing sulphur levels in specific parts of the pot stills<sup>220</sup>.

### 1.6.3 Analytical methods for whiskey flavour analysis

Analytical methods employed for whiskey flavour analysis include HPLC, GC-MS and CE. Ng and Reuter applied HPLC with fluorescence (FL) detection for the analysis of 10 phenolic compounds in three Scotch whiskeys (**Figure 1.29**). The separation was achieved in just over nine minutes, with the co-elution of *m*- and *p*-cresol, and poor resolution between phenol and guaiacol observed<sup>221</sup>.

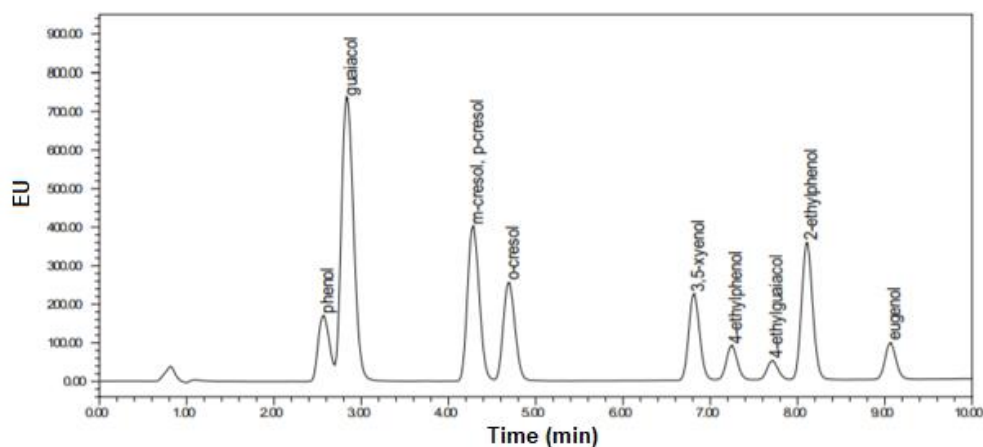


**Figure 1.29.** HPLC-FL detection of a 100 ppb phenolic standard mixture<sup>221</sup>.

Lehtonen analysed 12 whiskeys for the presence of volatile phenols using GC-MS. The results indicated that Scotch whiskeys have the highest concentrations of phenolics and that it is the presence of *o*-, *m*- and *p*-cresol that distinguishes between whiskeys produced from peated malt and those that are not<sup>222</sup>. White *et al.* used CE with field-amplified sample stacking (FASS) to establish the phenolic acid profile of three types of Irish whiskeys. This work evaluated the impact of the ageing process, ageing length, and whiskey mashbill on the phenolic acid profile. As expected, the length of ageing was shown to have a positive impact on the concentration of the phenolic acids present. Also, it was found that ageing in sherry casks produces a wider range of phenolic acids<sup>223</sup>.

Gas chromatography-olfactometry (GC-O) was used to identify key odourants of peated single malt whiskey<sup>224</sup>. The compounds found to have the highest flavour dilution values were guaiacol, 4-EG, 4-methylphenol, 4-VG and 4-ethyl-2-methylphenol. These key odourants were then used to successfully discriminate peated single malts from other whiskey types using principal component analysis (PCA) and linear discriminant analysis (LDA). Sample preparation techniques, including stir-bar sorbent extraction (SBSE) are commonly used before GC analysis for whiskey flavouring<sup>225–227</sup>.

## 1.7 Objectives of the thesis

This research aims to develop rapid and sensitive methods for the simultaneous detection of the key phenolic compounds that are the primary contributors to the aroma

and flavour of whiskey, and that in some circumstances may be present in beverages as an undesirable medicinal off odour due to microbial contamination.

**Chapter 2** - The attractive features of the BDD electrode including a wide potential window, low background currents and limited adsorption of analytes on the electrode surface, will be utilised for the direct electrochemical sensing of phenols, guaiacols and cresols as a molecular fingerprint for whiskey analysis. Modification of the bare electrode with Nafion is examined to enhance adsorption of the analytes on the electrode surface and, therefore, improve the sensitivity. CV and electrochemical impedance spectroscopy (EIS) will be used to characterise the bare and Nafion modified electrodes, and chronocoulometry will be applied to examine the kinetics and mechanism of electrode reactions for both electrodes. Addition of cyclodextrins (CDs) to the electrolyte will also be investigated. CDs can alter and improve the separation by forming inclusion complexes with analytes. Peak deconvolution will be applied to distinguish the guaiacols, phenols and cresols in the whiskey sample.

**Chapter 3** - This chapter will advance the work carried out in chapter 2 by chromatographically separating the analytes with a C<sub>18</sub> core-shell column before their detection with the BDD electrode using a thin-layer flow-through cell. The optimisation of HPLC separation conditions and ECD oxidation potentials will be carried out before applying the method to the identification and quantitation of the phenolic compounds in Islay, Irish, Highland and Scotch whiskeys, to identify the specific phenolic compounds attributed to smoky whiskey.

**Chapter 4** - This chapter will focus on the electrochemical behaviour and detection of EA and GA. Due to differing polarities, gradient elution will be applied for their chromatographic separation followed by detection at the BDD electrode. The optimised method will then be applied for their detection in Islay, Highland and Scotch whiskeys. Since EA and GA enter the whiskey from the oak casks during maturation, their analysis may be used as markers for the identification of authentic whiskey. Additionally, it is expected that higher concentrations of both acids will be present in whiskeys that undergo longer periods of maturation.

**Chapter 5** - This chapter will focus on the detection of guaiacol as an undesirable and taint producing metabolite associated with spoilage in beverages. Guaiacol is

metabolised by *Alicyclobacillus* spp. from its precursors VA, FA and vanillin, and its presence can have serious financial implications for manufacturers. Following optimisation, this work aims to provide a sensitive HPLC-BDD method that will provide manufacturers with a rapid alternative method to traditional microbiological methods.

**Chapter 6** - This chapter contains the overall conclusions of the thesis and also presents the proposed future work.

## 1.8 References

1. Zaynab, M. *et al.* Role of primary metabolites in plant defense against pathogens. *Microb. Pathog.* **137**, 103728 (2019).
2. Pagare, S., Bhatia, M., Tripathi, N., Pagare, S. & Bansal, Y. K. Secondary metabolites of plants and their role: Overview. *Curr. Trends Biotechnol. Pharm.* **9**, 293–304 (2015).
3. Wink, M. Plant secondary metabolites modulate insect behavior-steps toward addiction? *Front. Physiol.* **9**, 1–9 (2018).
4. Lin, D. *et al.* An overview of plant phenolic compounds and their importance in human nutrition and management of type 2 diabetes. *Molecules* **21**, (2016).
5. Randhir, R., Lin, Y. T. & Shetty, K. Stimulation of phenolics, antioxidant and antimicrobial activities in dark germinated mung bean sprouts in response to peptide and phytochemical elicitors. *Process Biochem.* **39**, 637–646 (2004).
6. Lattanzio, V. Phenolic Compounds: Introduction. in *Natural products* (ed. Ramawat, K.G., Mérillon, J. M.) (Springer-Verlag, 2013) pages 1543–1580.
7. Singh, A., Holvoet, S. & Mercenier, A. Dietary polyphenols in the prevention and treatment of allergic diseases. *Clin. Exp. Allergy* **41**, 1346–1359 (2011).
8. Borochoy-Neori, H. *et al.* Antioxidant and antiatherogenic properties of phenolic acid and flavonol fractions of fruits of ‘Amari’ and ‘Hallawi’ date (*Phoenix dactylifera* L.) varieties. *J. Agric. Food Chem.* **63**, 3189–3195 (2015).
9. Ruiz-Ruiz, J. C., Matus-Basto, A. J., Acereto-Escoffié, P. & Segura-Campos, M. R. Antioxidant and anti-inflammatory activities of phenolic compounds isolated from *Melipona beecheii* honey. *Food Agric. Immunol.* **28**, 1424–1437 (2017).
10. Bouarab-Chibane, L. *et al.* Antibacterial properties of polyphenols: Characterization and QSAR (Quantitative structure-activity relationship) models. *Front. Microbiol.* **10**, 1-23 (2019).
11. Lutz, M., Fuentes, E., Ávila, F., Alarcón, M. & Palomo, I. Roles of phenolic compounds in the reduction of risk factors of cardiovascular diseases.

*Molecules* **24**, 1–15 (2019).

12. Huyut, Z., Beydemir, Ş. & Gülçin, I. Antioxidant and antiradical properties of selected flavonoids and phenolic compounds. *Biochem. Res. Int.* **2017**, (2017).
13. Roleira, F. M. F. *et al.* Plant derived and dietary phenolic antioxidants: Anticancer properties. *Food Chem.* **183**, 235–258 (2015).
14. Ouellette, R. J., Rawn, J. D. Alcohols and Phenols. in *Principles of Organic Chemistry* 209–238 (Elsevier Inc., 2015), pages 226-227.
15. Held, B. P. & Instruments, B. An introduction to reactive oxygen species measurement of ROS in yeast cells. *TechNote* 1–21 (2015). doi:10.1017/CBO9781107415324.004
16. Amarowicz, R., Pegg, R. B., Rahimi-Moghaddam, P., Barl, B. & Weil, J. A. Free-radical scavenging capacity and antioxidant activity of selected plant species from the Canadian prairies. *Food Chem.* **84**, 551–562 (2004).
17. Pourreza, N. Phenolic compounds as potential antioxidant. *Jundishapur J. Nat. Pharm. Prod.* **8**, 149–150 (2013).
18. Pereira, D. M., Valentão, P., Pereira, J. A. & Andrade, P. B. Phenolics: From chemistry to biology. *Molecules* **14**, 2202–2211 (2009).
19. Cherrak, S. A. *et al.* In vitro antioxidant versus metal ion chelating properties of flavonoids: A structure-activity investigation. *PLoS One* **11**, 1–21 (2016).
20. Bendary, E., Francis, R. R., Ali, H. M. G., Sarwat, M. I. & El Hady, S. Antioxidant and structure–activity relationships (SARs) of some phenolic and anilines compounds. *Ann. Agric. Sci.* **58**, 173–181 (2013).
21. Ahmed, E. *et al.* Secondary metabolites and their multidimensional prospective in plant life. *J. Pharmacogn. Phytochem.* **6**, 205–214 (2017).
22. Tsao, R. Chemistry and biochemistry of dietary polyphenols. *Nutrients* **2**, 1231–1246 (2010).
23. Działo, M. *et al.* The potential of plant phenolics in prevention and therapy of skin disorders. *Int. J. Mol. Sci.* **17**, 1–41 (2016).

24. Puupponen-Pimiä, R., Nohynek, L., Alakomi, H. L. & Oksman-Caldentey, K. M. Bioactive berry compounds - Novel tools against human pathogens. *Appl. Microbiol. Biotechnol.* **67**, 8–18 (2005).
25. Robbins, R. J. Phenolic acids in foods: An overview of analytical methodology. *J. Agric. Food Chem.* **51**, 2866–2887 (2003).
26. Vinayagam, R., Jayachandran, M. & Xu, B. Antidiabetic effects of simple phenolic acids: A comprehensive review. *Phyther. Res.* **30**, 184–199 (2016).
27. Friedman, M. Chemistry, biochemistry, and dietary role of potato polyphenols. A review. *J. Agric. Food Chem.* **45**, 1523–1540 (1997).
28. King, A., Young, G. Characteristics and occurrence of phenolic phytochemicals. *J. Am. Diet. Assoc.* **99**, 213–218 (1999).
29. Slavin, J., Marquart, L., Jakobs, D. J. Consumption of whole-grain food and decreased risk of cancer: Proposed mechanisms. *Cereal Foods World* **45**, 54–58 (2000).
30. Baublis, A. J., Clydesal, F. M., Decker, E. A. Antioxidants in wheat-based breakfast cereals. *Cereal Foods World* **45**, 71–74 (2000).
31. Zielinski, H. Low molecular weight antioxidants in the cereal grains-A review. *Polish J. Food Nutr. Sci.* **11**, 3–9 (2002).
32. Antolovich, M. *et al.* LC-MS investigation of oxidation products of phenolic antioxidants. *J. Agric. Food Chem.* **52**, 962–971 (2004).
33. Kobus, J. *et al.* Phenolic compounds and antioxidant activity of extracts of Ginkgo leaves. *Eur. J. Lipid Sci. Technol.* **111**, 1150–1160 (2009).
34. Katsube, T. *et al.* Effect of flavonol glycoside in mulberry (*Morus alba* L.) leaf on glucose metabolism and oxidative stress in liver in diet-induced obese mice. *J. Sci. Food Agric.* **90**, 2386–2392 (2010).
35. King, A. & Young, G. Characteristics and occurrence of phenolic phytochemicals. *J. Am. Diet. Assoc.* **99**, 213–218 (1999).
36. Manach, C., Scalbert, A., Morand, C., Rémésy, C. & Jiménez, L. Polyphenols:

- Food sources and bioavailability. *Am. J. Clin. Nutr.* **79**, 727–747 (2004).
37. Aherne, S. A. & O'Brien, N. M. Dietary flavonols: chemistry, food content, and metabolism. *Nutrition* **18**, 75–81 (2002).
  38. Rice-Evans, C. A., Miller, N. J. & Paganga, G. Structure-antioxidant activity relationships of flavonoids and phenolic acids. *Free Radic. Biol. Med.* **20**, 933–956 (1996).
  39. Alvarez, S., Zaobornyj, T., Actis-Goretta, L., Fraga, C. G. & Boveris, A. polyphenols and red wine as peroxynitrite scavengers: A chemiluminescent assay. *Ann. N. Y. Acad. Sci.* **957**, 271–273 (2002).
  40. López-Vélez, M., Martínez-Martínez, F. & Del Valle-Ribes, C. The study of phenolic compounds as natural antioxidants in wine. *Crit. Rev. Food Sci. Nutr.* **43**, 233–244 (2003).
  41. Thilakarathna, S. H. & Vasantha Rupasinghe, H. P. Flavonoid bioavailability and attempts for bioavailability enhancement. *Nutrients* **5**, 3367–3387 (2013).
  42. Harnly, J. M., Doherty, R. F., Beecher, G. R., Holden, J. M., Haytowitz, D. B., Bhagwat, S., Gebhardt, S. Flavonoid content of U.S. fruits, vegetables, and nuts. *J. Agric. Food Chem.* **54**, 9966–9977 (2006).
  43. Yao, L. H. *et al.* Flavonoids in food and their health benefits. *Plant Foods Hum. Nutr.* **59**, 113–122 (2004).
  44. Vogiatzoglou, A. *et al.* Estimated dietary intakes and sources of flavanols in the German population (German National Nutrition Survey II). *Eur. J. Nutr.* **53**, 635–643 (2014).
  45. de Lima Oliveira, P. M. *et al.* Juá fruit (*Ziziphus joazeiro*) from Caatinga: A source of dietary fiber and bioaccessible flavanols. *Food Res. Int.* **129**, 108745 (2020).
  46. Sánchez-Moreno, C., Cao, G., Ou, B. & Prior, R. L. Anthocyanin and proanthocyanidin content in selected white and red wines. Oxygen radical absorbance capacity comparison with nontraditional wines obtained from highbush blueberry. *J. Agric. Food Chem.* **51**, 4889–4896 (2003).



47. Ibarreta, D., Daxenberger, A. & Meyer, H. H. D. Possible health impact of phytoestrogens and xenoestrogens in food. *Apmis* **109**, 161–184 (2001).
48. Cornwell, T., Cohick, W. & Raskin, I. Dietary phytoestrogens and health. *Phytochemistry* **65**, 995–1016 (2004).
49. Singh, P., Kumar, R., Sabapathy, S. N. & Bawa, A. S. Functional and edible uses of soy protein products. *Compr. Rev. Food Sci. Food Saf.* **7**, 14–28 (2008).
50. Cassidy, A., Hanley, B. & Lamuela-Raventos, R. M. Isoflavones, lignans and stilbenes - Origins, metabolism and potential importance to human health. *J. Sci. Food Agric.* **80**, 1044–1062. (2000).
51. Okuda, T. & Ito, H. Tannins of constant structure in medicinal and food plants- hydrolyzable tannins and polyphenols related to tannins. *Molecules* **16**, 2191–2217 (2011).
52. Clinton, C. Plant tannins: A novel approach to the treatment of ulcerative colitis. *Nat. Med. J.* **1**, 1–4 (2009).
53. Ostrowska, J., Łuczaj, W., Kasacka, I., Rózański, A. & Skrzydlewska, E. Green tea protects against ethanol-induced lipid peroxidation in rat organs. *Alcohol* **32**, 25–32 (2004).
54. Sang, S. *et al.* Chemical studies of the antioxidant mechanism of tea catechins: Radical reaction products of epicatechin with peroxy radicals. *Bioorganic Med. Chem.* **11**, 3371–3378 (2003).
55. Stervbo, U., Vang, O. & Bonnesen, C. A review of the content of the putative chemopreventive phytoalexin resveratrol in red wine. *Food Chem.* **101**, 449–457 (2007).
56. Ososki, A. L. & Kennelly, E. J. Phytoestrogens: A review of the present state of research. *Phyther. Res.* **17**, 845–869 (2003).
57. Medina-Bolivar, F. *et al.* Production and secretion of resveratrol in hairy root cultures of peanut. *Phytochemistry* **68**, 1992–2003 (2007).
58. Flamini, R., Mattivi, F., De Rosso, M., Arapitsas, P. & Bavaresco, L. Advanced knowledge of three important classes of grape phenolics: Anthocyanins,

- stilbenes and flavonols. *Int. J. Mol. Sci.* **14**, 19651–19669 (2013).
59. Lorenc-Kukuła, K. *et al.* Engineering flax with the GT family 1 *Solanum sogarandinum* glycosyltransferase SsGT1 confers increased resistance to fusarium infection. *J. Agric. Food Chem.* **57**, 6698–6705 (2009).
  60. Sainvitu, P. *et al.* Structure, properties and obtention routes of flaxseed lignan secoisolariciresinol: A review. *Biotechnol. Agron. Soc. Environ.* **16**, 115–124 (2012).
  61. Slavova-Kazakova, A., Karamać, M., Kancheva, V. & Amarowicz, R. Antioxidant activity of flaxseed extracts in lipid systems. *Molecules* **21**, (2016).
  62. Milder, I. E. J., Arts, I. C. W., Putte, B. van de, Venema, D. P. & Hollman, P. C. H. Lignan contents of Dutch plant foods: a database including lariciresinol, pinoresinol, secoisolariciresinol and matairesinol. *Br. J. Nutr.* **93**, 393–402 (2005).
  63. Zambonin, L. *et al.* Dietary phenolic acids act as effective antioxidants in membrane models and in cultured cells, exhibiting proapoptotic effects in leukaemia cells. *Oxid. Med. Cell. Longev.* **2012**, 839298 (2012).
  64. Balasundram, N., Sundram, K. & Samman, S. Phenolic compounds in plants and agri-industrial by-products: Antioxidant activity, occurrence, and potential uses. *Food Chem.* **99**, 191–203 (2006).
  65. Gao, J., Hu, J., Hu, D. & Yang, X. A role of gallic acid in oxidative damage diseases: A comprehensive review. *Nat. Prod. Commun.* **14**, 1934578X1987417 (2019).
  66. Russell, L. H. Autoxidation of gallic acid induces ROS-dependent death in human prostate cancer LNCaP cells. *Anticancer Res.* **32**, 1595–1602 (2012).
  67. Mehraban, Z. *et al.* Protective effect of gallic acid on apoptosis of sperm and in vitro fertilization in adult male mice treated with cyclophosphamide. *J. Cell. Biochem.* **120**, 17250–17257 (2019).
  68. Li, W., Yue, X. & Li, F. Gallic acid caused cultured mice TM4 Sertoli cells apoptosis and necrosis. *Asian-Australasian J. Anim. Sci.* **32**, 629–636 (2019).

69. Jin, L. *et al.* Gallic acid attenuates calcium calmodulin-dependent kinase II-induced apoptosis in spontaneously hypertensive rats. *J. Cell. Mol. Med.* **22**, 1517–1526 (2018).
70. Kahkeshani, N. *et al.* Pharmacological effects of gallic acid in health and disease: A mechanistic review. *Iran. J. Basic Med. Sci.* **22**, 225–237 (2019).
71. Priscilla, D. H. & Prince, P. S. M. Cardioprotective effect of gallic acid on cardiac troponin-T, cardiac marker enzymes, lipid peroxidation products and antioxidants in experimentally induced myocardial infarction in Wistar rats. *Chem. Biol. Interact.* **179**, 118–124 (2009).
72. Zakaria, Z. A. *et al.* Mechanism(s) of action underlying the gastroprotective effect of ethyl acetate fraction obtained from the crude methanolic leaves extract of *Muntingia calabura*. *BMC Complement. Altern. Med.* **16**, 1–18 (2016).
73. Bak, E. J. *et al.* Gallic acid improves glucose tolerance and triglyceride concentration in diet-induced obesity mice. *Scand. J. Clin. Lab. Invest.* **73**, 607–614 (2013).
74. Ul Amin, F., Shah, S. A. & Kim, M. O. Vanillic acid attenuates A $\beta$ 1-42-induced oxidative stress and cognitive impairment in mice. *Sci. Rep.* **7**, 1–15 (2017).
75. Kumar, S., Prahalathan, P. & Raja, B. Antihypertensive and antioxidant potential of vanillic acid, a phenolic compound in L-NAME-induced hypertensive rats: A dose-dependence study. *Redox Rep.* **16**, 208–215 (2011).
76. Pandey, K. B. & Rizvi, S. I. Plant polyphenols as dietary antioxidants in human health and disease. *Oxid. Med. Cell. Longev.* **2**, 270–278 (2009).
77. Zduńska, K., Dana, A., Kolodziejczak, A. & Rotsztein, H. Antioxidant properties of ferulic acid and its possible application. *Skin Pharmacol. Physiol.* **31**, 332–336 (2018).
78. Yang, G. W., Jiang, J. S. & Lu, W. Q. Ferulic acid exerts anti-angiogenic and anti-tumor activity by targeting fibroblast growth factor receptor 1-mediated angiogenesis. *Int. J. Mol. Sci.* **16**, 24011–24031 (2015).

79. Lo, H. Y. *et al.* Ferulic acid altered IL-17A/IL-17RA interaction and protected against imiquimod-induced psoriasis-like skin injury in mice. *Food Chem. Toxicol.* **129**, 365–375 (2019).
80. Wen, Y. & Ushio, H. Ferulic acid promotes hypertrophic growth of fast skeletal muscle in Zebrafish model. *Nutrients* **9**, (2017).
81. Monteiro Espíndola, K. M. *et al.* Chemical and pharmacological aspects of caffeic acid and its activity in hepatocarcinoma. *Front. Oncol.* **9**, 3–5 (2019).
82. Mudgal, J. *et al.* Effect of coffee constituents, caffeine and caffeic acid on anxiety and lipopolysaccharide-induced sickness behavior in mice. *J. Funct. Foods* **64**, 103638 (2020).
83. D’Andrea, G. Quercetin: A flavonol with multifaceted therapeutic applications? *Fitoterapia* **106**, 256–271 (2015).
84. Vazquez-Armenta, F. J. *et al.* Quercetin repressed the stress response factor (sigB) and virulence genes (prfA, actA, inlA, and inlC), lower the adhesion, and biofilm development of *L. monocytogenes*. *Food Microbiol.* **87**, 103377 (2020).
85. Dabeek, W. M. & Marra, M. V. Dietary quercetin and kaempferol: Bioavailability and potential cardiovascular-related bioactivity in humans. *Nutrients* **11**, 2288 (2019).
86. Aa, L. X., Fei, F., Qi, Q., Sun, R. B., Gu, S. H., Di, Z. Z., Aa, J. Y., Wang, G. J., Liu, C. X. Rebalancing of the gut flora and microbial metabolism is responsible for the anti-arthritis effect of kaempferol. *Acta Pharmacol. Sin.* **41**, 73–81 (2020).
87. Chen, A. Y., Chen, Y. C. A review of the dietary flavonoid, kaempferol on human health and cancer chemoprevention. *Food Chem.* **138**, 2099–2107 (2013).
88. Panche, A. N., Diwan, A. D. & Chandra, S. R. Flavonoids: An overview. *J. Nutr. Sci.* **5**, 1–15 (2016).
89. Kurata, M. *et al.* Food-derived compounds apigenin and luteolin modulate

- mRNA splicing of introns with weak splice sites. *iScience* **22**, 336–352 (2019).
90. Ganai, S. A., Farooq, Z., Banday, S., Altaf, M. In silico approaches for investigating the binding propensity of apigenin and luteolin against class I HDAC isoforms. *Future Med. Chem.* **10**, 1925–1945 (2018).
  91. Testai, L. & Calderone, V. Nutraceutical value of citrus flavanones and their implications in cardiovascular disease. *Nutrients* **9**, 1–13 (2017).
  92. Reygaert, W. C. Green tea catechins: Their use in treating and preventing infectious diseases. *Biomed Res. Int.* **2018**, 9105261 (2018).
  93. Lin, B. W., Gong, C. C., Song, H. F. & Cui, Y. Y. Effects of anthocyanins on the prevention and treatment of cancer. *Br. J. Pharmacol.* **174**, 1226–1243 (2017).
  94. Gowd, V., Jia, Z. & Chen, W. Anthocyanins as promising molecules and dietary bioactive components against diabetes – A review of recent advances. *Trends Food Sci. Technol.* **68**, 1–13 (2017).
  95. Lee, Y. M. *et al.* Dietary anthocyanins against obesity and inflammation. *Nutrients* **9**, 1–16 (2017).
  96. Vitale, D. C., Piazza, C., Melilli, B., Drago, F. & Salomone, S. Isoflavones: estrogenic activity, biological effect and bioavailability. *Eur. J. Drug Metab. Pharmacokinet.* **38**, 15–25 (2013).
  97. Smeriglio, A., Barreca, D., Bellocchio, E. & Trombetta, D. Proanthocyanidins and hydrolysable tannins: occurrence, dietary intake and pharmacological effects. *Br. J. Pharmacol.* **174**, 1244–1262 (2017).
  98. Sharma, K. *et al.* Health effects, sources, utilization and safety of tannins: a critical review. *Toxin Rev.* **0**, 1–13 (2019).
  99. Delimont, N. M., Haub, M. D. & Lindshield, B. L. The impact of tannin consumption on iron bioavailability and status: A narrative review. *Curr. Dev. Nutr.* **1**, e000042 (2017).
  100. Ahmadi, Z., Mohammadinejad, R. & Ashrafizadeh, M. Drug delivery systems for resveratrol, a non-flavonoid polyphenol: Emerging evidence in last decades.

*J. Drug Deliv. Sci. Technol.* **51**, 591–604 (2019).

101. Zhang, J., Chen, J., Liang, Z. & Zhao, C. New lignans and their biological activities. *Chem. Biodivers.* **11**, 1–54 (2014).
102. Kezimana, P., Dmitriev, A. A., Kudryavtseva, A. V., Romanova, E. V. & Melnikova, N. V. Secoisolariciresinol diglucoside of flaxseed and its metabolites: Biosynthesis and potential for nutraceuticals. *Front. Genet.* **9**, 1–9 (2018).
103. Wang, Y. *et al.* Quantitative analyses of nine phenolic compounds and their antioxidant activities from thirty-seven varieties of raspberry grown in the Qinghai-Tibetan Plateau region. *Molecules* **24**, 1–15 (2019).
104. Belajová, E. Determination of selected wine phenolic constituents as possible markers for differentiation of wines. *J. Food Nutr. Res.* **51**, 117–122 (2012).
105. Biswas, N. Identification of Phenolic Compounds in Processed Cranberries by HPLC Method. *J. Nutr. Food Sci.* **03**, 1–6 (2013).
106. Chem, B. *et al.* Validation of an optimized HPLC / UV method for the quantification of flavonoids in lotus. *Appl. Biol. Chem.* 4–9 (2020). doi:10.1186/s13765-020-00568-0
107. Kumar, B. R. Application of HPLC and ESI-MS techniques in the analysis of phenolic acids and flavonoids from green leafy vegetables (GLVs). *J. Pharm. Anal.* **7**, 349–364 (2017).
108. Pietrzak, W., Nowak, R., Gawlik-Dziki, U., Lemieszek, M. K. & Rzeski, W. LC-ESI-MS/MS identification of biologically active phenolic compounds in mistletoe berry extracts from different host trees. *Molecules* **22**, 1–15 (2017).
109. Matei, A. O., Gatea, F. & Radu, G. L. Analysis of phenolic compounds in some medicinal herbs by LC-MS. *J. Chromatogr. Sci.* **53**, 1147–1154 (2015).
110. Arceusz, A., Wesolowski, M. & Konieczynski, P. Methods for extraction and determination of phenolic acids in medicinal plants: A review. *Nat. Prod. Commun.* **8**, 1821–1829 (2013).
111. Fiamegos, Y. C., Nanos, C. G., Vervoort, J. & Stalikas, C. D. Analytical

- procedure for the in-vial derivatization - Extraction of phenolic acids and flavonoids in methanolic and aqueous plant extracts followed by gas chromatography with mass-selective detection. *J. Chromatogr. A* **1041**, 11–18 (2004).
112. Al-Owaisi, M., Al-Hadiwi, N. & Khan, S. A. GC-MS analysis, determination of total phenolics, flavonoid content and free radical scavenging activities of various crude extracts of *Moringa peregrina* (Forssk.) Fiori leaves. *Asian Pac. J. Trop. Biomed.* **4**, 964–970 (2014).
  113. Deng, Y., Lam, S. C., Zhao, J. & Li, S. P. Quantitative analysis of flavonoids and phenolic acid in *Coreopsis tinctoria* Nutt. by capillary zone electrophoresis. *Electrophoresis* **38**, 2654–2661 (2017).
  114. Martí, R., Valcárcel, M., Herrero-Martínez, J. M., Cebolla-Cornejo, J. & Roselló, S. Simultaneous determination of main phenolic acids and flavonoids in tomato by micellar electrokinetic capillary electrophoresis. *Food Chem.* **221**, 439–446 (2017).
  115. Ballus, C. A., Meinhart, A. D., Bruns, R. E. & Godoy, H. T. Use of multivariate statistical techniques to optimize the simultaneous separation of 13 phenolic compounds from extra-virgin olive oil by capillary electrophoresis. *Talanta* **83**, 1181–1187 (2011).
  116. Fan, J. *et al.* Simultaneous detection of hydroquinone and catechol with decreasing pH at a bare glassy carbon electrode surface. *Anal. Methods* **11**, 604–609 (2019).
  117. Areias, M. C. C., Shimizu, K. & Compton, R. G. Cysteine determination: Via adsorptive stripping voltammetry using a bare glassy carbon electrode. *Analyst* **141**, 5563–5570 (2016).
  118. Thomas, P., Lai, C. W. & Bin Johan, M. R. Recent developments in biomass-derived carbon as a potential sustainable material for super-capacitor-based energy storage and environmental applications. *J. Anal. Appl. Pyrolysis* **140**, 54–85 (2019).
  119. Bahru, R., Shaari, N. & Mohamed, M. A. Allotrope carbon materials in thermal

- interface materials and fuel cell applications: A review. *Int. J. Energy Res.* **44**, 2471–2498 (2020).
120. Beenish, Inamuddin & Asiri, A. M. Electrospun polyaniline/polyvinyl alcohol/multiwalled carbon nanotubes nanofibers as promising bioanode material for biofuel cells. *J. Electroanal. Chem.* **789**, 181–187 (2017).
  121. Möller, L. *et al.* CoFe<sub>2</sub>O<sub>4</sub>-filled carbon nanotubes as anode material for lithium-ion batteries. *J. Alloys Compd.* **834**, 155018 (2020).
  122. Wang, L. *et al.* Nanocarbon materials in water disinfection: State-of-the-art and future directions. *Nanoscale* **11**, 9819–9839 (2019).
  123. Perreault, F., Fonseca de Faria, A. & Elimelech, M. Environmental applications of graphene-based nanomaterials. *Chem. Soc. Rev.* **44**, 5861–5896 (2015).
  124. Zhang, W. *et al.* Recent development of carbon electrode materials and their bioanalytical and environmental applications. *Chem. Soc. Rev.* **45**, 715–752 (2016).
  125. McCreery, R. L. Advanced carbon electrode materials for molecular electrochemistry. *Chem. Rev.* **108**, 2646–2687 (2008).
  126. Baluchová, S. *et al.* Recent progress in the applications of boron doped diamond electrodes in electroanalysis of organic compounds and biomolecules – A review. *Anal. Chim. Acta* **1077**, 30–66 (2019).
  127. Muzyka, K. *et al.* Boron-doped diamond: Current progress and challenges in view of electroanalytical applications. *Anal. Methods* **11**, 397–414 (2019).
  128. Pelskov, Y. V., Sakharova, A. Y., Krotova, M. D., Bouilov, L. L., Spitsyn, B. V. Photoelectrochemical properties of semiconductor diamond. *J. Electroanal. Chem. Interfacial Electrochem.* **228**, 19–27 (1987).
  129. Srikanth, V. V. S. S., Sampath Kumar, P. & Kumar, V. B. A brief review on the in situ synthesis of boron-doped diamond thin films. *Int. J. Electrochem.* **2012**, 1–7 (2012).
  130. Zhou, Y. & Zhi, J. The application of boron-doped diamond electrodes in amperometric biosensors. *Talanta* **79**, 1189–1196 (2009).



131. Luong, J. H. T., Male, K. B. & Glennon, J. D. Boron-doped diamond electrode: synthesis, characterization, functionalization and analytical applications. *Analyst* **134**, 1965–79 (2009).
132. Yu, P., Zhang, J., Zheng, T. & Wang, T. Influence of boron doped level on the electrochemical behavior of boron doped diamond electrodes and uric acid detection. *Colloids Surfaces A Physicochem. Eng. Asp.* **494**, 241–247 (2016).
133. Bennett, J. A., Wang, J., Show, Y. & Swain, G. M. Effect of sp<sup>2</sup>-bonded nondiamond carbon impurity on the response of boron-doped polycrystalline diamond thin-film electrodes. *J. Electrochem. Soc.* **151**, E306 (2004).
134. Zhang, W. *et al.* Recent development of carbon electrode materials and their bioanalytical and environmental applications. *Chem. Soc. Rev.* **45**, 715–752 (2016).
135. Alpar, N., Yardım, Y. & Şentürk, Z. Selective and simultaneous determination of total chlorogenic acids, vanillin and caffeine in foods and beverages by adsorptive stripping voltammetry using a cathodically pretreated boron-doped diamond electrode. *Sensors Actuators, B Chem.* **257**, 398–408 (2018).
136. Macpherson, J. V. A practical guide to using boron doped diamond in electrochemical research. *Phys. Chem. Chem. Phys.* **17**, 2935–2949 (2015).
137. Guy, O. J. & Walker, K. D. Graphene Functionalization for Biosensor Applications. in *Silicon Carbide Biotechnology. A Biocompatible Semiconductor for Advanced Biomedical Devices and Applications* (ed. Sadow, S. E.) (Elsevier, 2016), page 104.
138. Elgrishi, N. *et al.* A practical beginner's guide to cyclic voltammetry. *J. Chem. Educ.* **95**, 197–206 (2018).
139. Mirceski, V. *et al.* Square-wave voltammetry: A review on the recent progress. *Electroanalysis* **25**, 2411–2422 (2013).
140. Randviir, E. P. & Banks, C. E. Electrochemical impedance spectroscopy: An overview of bioanalytical applications. *Anal. Methods* **5**, 1098–1115 (2013).
141. Who is Mikhail Tsvet? (2014). Available at:

<https://www.chromatographytoday.com/news/gc-mdgc/32/breaking-news/who-is-mikhail-tsvetnbs/32304>. (Accessed: 20th July 2020).

142. Narayana P. S., Varalakshmi, D., Pullaiah, T., Sambasiva Rao, K. R. S. *Research Methodology in Zoology*. (Scientific Publishers (India), 2018), page 99.
143. Žuvela, P. *et al.* Column characterization and selection systems in reversed-phase high-performance liquid chromatography. *Chem. Rev.* **119**, 3674–3729 (2019).
144. Major, E. R. Current trends in HPLC column usage. *LC GC Eur.* **25**, 1–7 (2012).
145. Carr, P. W., Li, J. J., Dallas, A. J. Revisionist look at solvophobic driving forces in reversed-phase liquid-chromatography. *J. Chromatogr. A* **656**, (1993).
146. Horváth, C., Melander, W., Molnar, I. Solvophobic interactions in liquid chromatography with nonpolar stationary phases. *J. Liq. Chromatogr. A* **125**, 129–156 (1976).
147. Rafferty, J. L., Siepmann, J. I. & Schure, M. R. Molecular-level comparison of alkylsilane and polar-embedded reversed-phase liquid chromatography systems. *Anal. Chem.* **80**, 6214–6221 (2008).
148. Rafferty, J. L., Siepmann, J. I. & Schure, M. R. The effects of chain length, embedded polar groups, pressure, and pore shape on structure and retention in reversed-phase liquid chromatography: Molecular-level insights from Monte Carlo simulations. *J. Chromatogr. A* **1216**, 2320–2331 (2009).
149. Lindsey, R. K., Rafferty, J. L., Eggimann, B. L., Siepmann, J. I. & Schure, M. R. Molecular simulation studies of reversed-phase liquid chromatography. *J. Chromatogr. A* **1287**, 60–82 (2013).
150. Bocian, S. & Buszewski, B. Residual silanols at reversed-phase silica in HPLC - A contribution for a better understanding. *J. Sep. Sci.* **35**, 1191–1200 (2012).
151. Reversed phase chromatography. *LC GC Chromacademy* Available at: [www.chromacademy.com](http://www.chromacademy.com). (Accessed: 22nd July 2020).
152. Horváth, K., Lukács, D., Sepsey, A. & Felinger, A. Effect of particle size

- distribution on the separation efficiency in liquid chromatography. *J. Chromatogr. A* **1361**, 203–208 (2014).
153. O’Sullivan, G. P., Scully, N. M. & Glennon, J. D. Polar-embedded and polar-endcapped stationary phases for LC. *Anal. Lett.* **43**, 1609–1629 (2010).
  154. Horváth, C. S., Preiss, B. A., Lipsky, S. R. Fast liquid chromatography. Investigation of operating parameters and the separation of nucleotides on pellicular ion exchangers. *Anal. Chem.* **39**, 1422–1428 (1967).
  155. Horváth, C., Lipsky, S. R. Column design in high pressure liquid chromatography. *J. Chromatogr. Sci.* **7**, 109–116 (1969).
  156. Kirkland, J. J. Controlled surface porosity supports for high-speed gas and liquid chromatography. *Anal. Chem.* **41**, 218–220 (1969).
  157. González-Ruiz, V., Olives, A. I. & Martín, M. A. Core-shell particles lead the way to renewing high-performance liquid chromatography. *TrAC - Trends Anal. Chem.* **64**, 17–28 (2015).
  158. Gumustas, M., Zalewski, P., Ozkan, S. A. & Uslu, B. The History of the Core–Shell Particles and Applications in Active Pharmaceutical Ingredients Via Liquid Chromatography. *Chromatographia* **82**, 17–48 (2019).
  159. Omamogho, J. O., Hanrahan, J. P., Tobin, J. & Glennon, J. D. Structural variation of solid core and thickness of porous shell of 1.7 $\mu$ m core-shell silica particles on chromatographic performance: Narrow bore columns. *J. Chromatogr. A* **1218**, 1942–1953 (2011).
  160. Langsi, V. K., Ashu-Arrah, B. A. & Glennon, J. D. Sub-2- $\mu$ m seeded growth mesoporous thin shell particles for high-performance liquid chromatography: Synthesis, functionalisation and characterisation. *J. Chromatogr. A* **1402**, 17–26 (2015).
  161. Bell, D. S. & Majors, R. E. Current state of superficially porous particle technology in liquid chromatography. *LC-GC North Am.* **33**, 386–395 (2015).
  162. Hayes, R., Ahmed, A., Edge, T. & Zhang, H. Core-shell particles: Preparation, fundamentals and applications in high performance liquid chromatography. *J.*

*Chromatogr. A* **1357**, 36–52 (2014).

163. Fekete, S., Oláh, E. & Fekete, J. Fast liquid chromatography: The domination of core-shell and very fine particles. *J. Chromatogr. A* **1228**, 57–71 (2012).
164. Snyder, L. R., Kirkland, J. J., Dolan, J. *Introduction to Modern Liquid Chromatography*. (John Wiley & Sons, 2010).
165. Scott, R. P. W. *Techniques and Practice of Chromatography*. (Marcel Dekker Inc., 1995), p 77-79.
166. Gritti, F. & Guiochon, G. Mass transfer mechanism in liquid chromatography columns packed with shell particles: Would there be an optimum shell structure? *J. Chromatogr. A* **1217**, 8167–8180 (2010).
167. DeStefano, J. J., Schuster, S. A., Lawhorn, J. M. & Kirkland, J. J. Performance characteristics of new superficially porous particles. *J. Chromatogr. A* **1258**, 76–83 (2012).
168. Krstonošić, M. A., Hogervorst, J. C., Mikulić, M. & Gojković-Bukarica, L. Development of HPLC method for determination of phenolic compounds on a core shell column by direct injection of wine samples. *Acta Chromatogr.* **32**, 134–138 (2019).
169. Ferro, M. D., Santos, S. A. O., Silvestre, A. J. D. & Duarte, M. F. Chromatographic separation of phenolic compounds from extra virgin olive oil: Development and validation of a new method based on a biphenyl HPLC column. *Int. J. Mol. Sci.* **20**, (2019).
170. Šatínský, D., Jägerová, K., Havlíková, L. & Solich, P. A new and fast HPLC method for determination of rutin, troxerutin, diosmin and hesperidin in food supplements using fused-core column technology. *Food Anal. Methods* **6**, 1353–1360 (2013).
171. Swartz, M. HPLC detectors: A brief review. *J. Liq. Chromatogr. Relat. Technol.* **33**, 1130–1150 (2010).
172. Landolt D. *Corrosion and surface chemistry of metals*. (EPFL Press, 2007), page 5.

173. Lankelma, J., Poppe, H. Design and characterization of a coulometric detector with a glassy carbon electrode for high-performance liquid chromatography. *J. Chromatogr. A* **125**, 375–388 (1976).
174. Tjaden, U. R., Lankelma, J., Poppe, H. Anodic coulometric detection with a glassy carbon electrode in combination with reversed-phase high-performance liquid chromatography : Determination of blood levels of perphenazine and fluphenazin. *J. Chromatogr. A* **124**, 275–286 (1976).
175. Acworth, I. N., Bowers, M. *Coulometric Electrode Array Detectors for HPLC Progress in HPLC-HPCE Vol. 6.* (VSP, 1997), pages 15-17.
176. Honeychurch, K. Review : The application of liquid chromatography electrochemical detection for the determination of drugs of abuse. *Separations* **3**, 28 (2016).
177. Smith, R.M., Flanagan, R.J., Perrett, D., Whelpton, R. The electrochemical detector. in *Electrochemical Detection in HPLC: Analysis of drugs and poisons* 21–55 (RSC Publishing - Royal Society of Chemistry, 2005), pages 30-31.
178. Honeychurch, K. C. Design and application of liquid chromatography dual electrode detection. in *Electrochemistry: Volume 13* (ed. Banks, C., Mortimer, R., McIntosh, S.) (RSC Publishing - Royal Society of Chemistry, 2016), page 5.
179. Islam, M. A., Mahbub, P., Nesterenko, P. N., Paull, B. & Macka, M. Prospects of pulsed amperometric detection in flow-based analytical systems - A review. *Anal. Chim. Acta* **1052**, 10–26 (2019).
180. Matson, W. R., Langlais, P., Volicer, L., Gamache, P. H., Bird, E., Mark, K. A. n-Electrode three-dimensional liquid chromatography with electrochemical detection for determination of neurotransmitters. *Clin. Chem.* **30**, 1477–1488 (1984).
181. Hicks, M. B. *et al.* Assessment of coulometric array electrochemical detection coupled with HPLC-UV for the absolute quantitation of pharmaceuticals. *Analyst* **142**, 525–536 (2017).

182. Freitas, P. V., da Silva, D. R., Beluomini, M. A., da Silva, J. L. & Stradiotto, N. R. Determination of phenolic acids in sugarcane vinasse by HPLC with pulse amperometry. *J. Anal. Methods Chem.* **2018**, 4869487 (2018).
183. da Silveira, G. D. *et al.* Determination of phenolic antioxidants in Amazonian medicinal plants by HPLC with pulsed amperometric detection. *J. Liq. Chromatogr. Relat. Technol.* **38**, 1259–1266 (2015).
184. Natale, A. *et al.* Development of an analytical method for the determination of polyphenolic compounds in vegetable origin samples by liquid chromatography and pulsed amperometric detection at a glassy carbon electrode. *J. Chromatogr. A* **1420**, 66–73 (2015).
185. Lamarca, R. S., Matos, R. C. & Costa Matos, M. A. Determination of phenolic acids in palm oil samples by HPLC-UV-AD using homemade flow cell. *Anal. Methods* **10**, 4535–4542 (2018).
186. Zhang, Z. *et al.* Simultaneous detection of protocatechuic acid, chlorogenic acid and caffeic acid in honey by HPLC with ultraviolet and electrochemical detectors. *Int. J. Electrochem. Sci.* **13**, 6655–6665 (2018).
187. Liang, Y., Cao, W., Chen, W. J., Xiao, X. H., Zheng, J. B. Simultaneous determination of four phenolic components in citrus honey by high performance liquid chromatography using electrochemical detection. *Food Chem.* **114**, 1537–1541 (2009).
188. Novak, I., Janeiro, P., Seruga, M. & Oliveira-Brett, A. M. Ultrasound extracted flavonoids from four varieties of Portuguese red grape skins determined by reverse-phase high-performance liquid chromatography with electrochemical detection. *Anal. Chim. Acta* **630**, 107–115 (2008).
189. Gomes, S. M. C., Ghica, M. E., Rodrigues, I. A., de Souza Gil, E. & Oliveira-Brett, A. M. Flavonoids electrochemical detection in fruit extracts and total antioxidant capacity evaluation. *Talanta* **154**, 284–291 (2016).
190. Gomes, S. M. C., Fernandes, I. P. G., Shekhawat, N. S., Kumbhat, S. & Oliveira-Brett, A. M. *Calligonum polygonoides* Linnaeus Extract: HPLC-EC and Total Antioxidant Capacity Evaluation. *Electroanalysis* **27**, 293–301

(2015).

191. Zhang, R., Wang, L., Liu, S. & Yang, G. J. Separation and detection of electrochemical active compounds in *Houttuynia cordata* Thunb. by reversed-phase high-performance liquid chromatography with electrochemical detection. *J. Liq. Chromatogr. Relat. Technol.* **38**, 733–739 (2015).
192. de Araújo Rodrigues, I., Gomes, S. M. C., Fernandes, I. P. G. & Oliveira-Brett, A. M. Phenolic composition and total antioxidant capacity by electrochemical, spectrophotometric and HPLC-EC evaluation in Portuguese red and white wines. *Electroanalysis* **31**, 936–945 (2019).
193. Vanbeneden, N., Delvaux, F. & Delvaux, F. R. Determination of hydroxycinnamic acids and volatile phenols in wort and beer by isocratic high-performance liquid chromatography using electrochemical detection. *J. Chromatogr. A* **1136**, 237–242 (2006).
194. Gazdik, Z. *et al.* Use of liquid chromatography with electrochemical detection for the determination of antioxidants in less common fruits. *Molecules* **13**, 2823–2836 (2008).
195. Casella, I. G., Colonna, C. & Contursi, M. Electroanalytical determination of some phenolic acids by high-performance liquid chromatography at gold electrodes. *Electroanalysis* **19**, 1503–1508 (2007).
196. Zheng, J. Bin, Suo, Z. R. & Liu, L. Simultaneous determination of four phenolic compounds and tanshinone IIA in Guanxintong tablets by LC using combined electrochemical detection and DAD. *Chromatographia* **63**, 39–44 (2006).
197. Bayram, B., Ozcelik, B., Schultheiss, G., Frank, J. & Rimbach, G. A validated method for the determination of selected phenolics in olive oil using high-performance liquid chromatography with coulometric electrochemical detection and a fused-core column. *Food Chem.* **138**, 1663–1669 (2013).
198. Seansbar.ie. Available at: <https://www.seansbar.ie/blog/233-Sean's-bar-launch-their-Single-Malt-Clonmacnoise>. (Accessed: 23rd July 2020)
199. Bathgate, G. N. History of the development of whisky distillation. in *Whisky*:

- Technology, Production and Marketing. Handbook of Alcoholic Beverages Series* (ed. Russell, I.) 1 (Academic Press, 2003), page 1.
200. Stewart, G., Russell, I., Anstruther, A. An introduction to whisk(e)y and the *Whisky Technology, Production and Marketing* development of Scotch whisky. in (ed. Russell, I., Stewart, G.) 1 (Academic Press, 2014), page 1.
  201. Offringa, H. *A Field Guide to Whisky: An Expert Compendium to Take Your Passion and Knowledge to the Next Level*. (Artisan, 2017). page 17-21.
  202. O'Connor, F. Single pot stills vs. other whiskey styles. A brief guide to Ireland's whiskey family. in *A Glass Apart: Irish Single Pot Still Whiskey* 8 (The Images Publishing Group Pty Ltd, 2015), page 8.
  203. Scotch whisky in the making. Available at: <http://www.dcs.ed.ac.uk/home/jhb/whisky/swa/chap3.html>. (Accessed: 24th July 2020)
  204. How is whisky distilled? Available at: <https://trulyexperiences.com/blog/how-is-whisky-distilled/>. (Accessed: 27th July 2020)
  205. How is whisky made? Available at: [http://www.whiskyforeveryone.com/whisky\\_basics/how\\_is\\_whisky\\_made.html](http://www.whiskyforeveryone.com/whisky_basics/how_is_whisky_made.html). (Accessed: 24th July 2020)
  206. Fermentation. Available at: <https://www.whisky.com/information/knowledge/production/details/fermentation.html>. (Accessed: 24th July 2020)
  207. Technical file setting out the specifications with which Irish whiskey/uisce beatha Eireannach/Irish whisky must comply. Food Industry Development Division Department of Agriculture, Food and the Marine. (2014), page 7.
  208. Jack, F. R. Whiskies: composition, sensory properties and sensory analysis. in *Alcoholic beverages Sensory Evaluation and Consumer Research* (ed. J, P.) 379–392 (2012), page 382.
  209. Bryson, L. The Barrel. in *Whiskey Master Class: The Ultimate Guide to Understanding Scotch, Bourbon, Rye, and More* 144 (The Harvard Common



Press, 2020), page 144.

210. Mosedale, J. R. & Puech, J. L. Wood maturation of distilled beverages. *Trends Food Sci. Technol.* **9**, 95–101 (1998).
211. Old line Scotch club. Available at: <https://thescotchclub.com/resources/>. (Accessed: 4th August 2020)
212. Lee, K. Y. M., Paterson, A., Piggott, J. R. & Richardson, G. D. Origins of flavour in whiskies and a revised flavour wheel: a review. *J. Inst. Brew.* **107**, 287–313 (2001).
213. Maga, J. A. Contribution of phenolic compounds to smoke flavor. in *Phenolic Compounds in Food and Their Effects on Health I* 170–179 (ACS Publications, 1992).
214. Harrison, B. *et al.* Differentiation of peats used in the preparation of malt for scotch whisky production using fourier transform infrared spectroscopy. *J. Inst. Brew.* **112**, 333–339 (2006).
215. Harrison, B. M. & Priest, F. G. Composition of peats used in the preparation of malt for Scotch whisky production - influence of geographical source and extraction depth. *J. Agric. Food Chem.* **57**, 2385–2391 (2009).
216. Karlsson, B. C. G. & Friedman, R. Dilution of whisky - The molecular perspective. *Sci. Rep.* **7**, 1–9 (2017).
217. The chemistry of whisky. Available at: <https://www.compoundchem.com/2015/03/31/whisky/>. (Accessed: 29th July 2020)
218. W. H. O. Alcohol Drinking. in *IARC Monographs on the Evaluation of Carcinogenic Risks to Humans, No. 44 IARC Working Group on the Evaluation of Carcinogenic Risks to Humans* (International Agency for Research on Cancer, 1988).
219. Nascimento, E. S. P., Cardoso, D. R. & Franco, D. W. Quantitative ester analysis in cachaça and distilled spirits by Gas Chromatography-Mass Spectrometry (GC-MS). *J. Agric. Food Chem.* **56**, 5488–5493 (2008).

220. Harrison, B., Fagnen, O., Jack, F. & Brosnan, J. The impact of copper in different parts of malt whisky pot stills on new make spirit composition and aroma. *J. Inst. Brew.* **117**, 106–112 (2011).
221. Ng, C. M. & Reuter, W. M. Analysis of phenols in whisky using HPLC with FL detection. *PerkinElmer.USA* 1–5 (2015).
222. Lehtonen, M. Phenols in whisky. *Chromatographia* **16**, 201–203 (1982).
223. White, B., Smyth, M. R. & Lunte, C. E. Determination of phenolic acids in a range of Irish whiskies, including single pot stills and aged single malts, using capillary electrophoresis with field amplified sample stacking. *Anal. Methods* **9**, 1248–1252 (2017).
224. Jeleń, H. H., Majcher, M. & Szwengiel, A. Key odorants in peated malt whisky and its differentiation from other whisky types using profiling of flavor and volatile compounds. *Lwt* **107**, 56–63 (2019).
225. Nie, Y., Kleine-Benne, E. Determining phenolic compounds in whisky using direct large volume injection and stir bar sorptive extraction. *Gerstel Glob. Anal. Solut Gerstel GmbH Co. KG, Appl. Note* 1–12 (2012).
226. Bicchi, C. *et al.* Dual-phase twistors: A new approach to headspace sorptive extraction and stir bar sorptive extraction. *J. Chromatogr. A* **1094**, 9–16 (2005).
227. Nie, Y., Kleine-Benne, E. Using three types of twister phases for stir bar sorptive extraction of whisky, wine and fruit juice. *Gerstel Glob. Anal. Solut Gerstel GmbH Co. KG, Appl. Note* 1–14 (2011).

## **Chapter 2**

### **Simultaneous electroanalysis of guaiacol and its analogues based on their differential complexation with $\alpha$ - cyclodextrin on a Nafion modified boron-doped diamond electrode**

## 2.1 Introduction

Several volatile phenols are identified in whiskeys including phenol, cresol isomers, guaiacol (2-methoxyphenol), and *p*-ethylguaiacol or 4-ethylguaiacol (4-EG). Their concentrations vary from one commercial brand to another and are highly dependent on the country of origin<sup>1</sup>. Whiskey distilleries do not provide any information relating to the composition and levels of the total phenols in the final product, thus, it is very difficult to know the exact level of such phenols, especially as the whiskey ages. During the process of drying the malted barley over a peat-fuelled fire, guaiacol is released from the lignin, thus, imparting a distinct smoky flavour to the whiskey. This practice is common in many Scottish distilleries, particularly the Isle of Islay, where peat is available as a cheap source of energy. Guaiacol and other phenols have been identified from various whiskey brands<sup>2,3</sup> together with guaiacol derivatives, phenol derivatives and cresols<sup>2,4,5</sup>.

Guaiacol, and its glycoconjugate, are also identified in smoke-affected grapes and wine prepared from such grapes yielding unpalatable smoky wine<sup>6</sup>. In the food and beverage manufacturing industries, guaiacol is also recognised as the principal spoilage metabolite responsible for an undesirable medicinal or antiseptic-like off-odour. It is produced from the microbial metabolism of *Alicyclobacillus* species (spp.) a thermoacidophilic spore-forming bacterium, with its odour becoming offensive when its concentration exceeds a sensorial threshold<sup>7</sup>. *Alicyclobacillus* spp. contamination is also damaging for manufacturers as it often results in the withdrawal of product batches from the market. Small amounts of guaiacol and its analogues can contribute to aromatic flavours in beers, wines and other beverages<sup>8</sup>. The presence of 4-EG in strawberries serves a useful indicator for the confirmation of leather or crown rot disease by a pathogenic fungus *Phytophthora cactorum*. About 50 % of the 1.3 million tons of strawberries produced in the USA are affected by this fungus<sup>9</sup>.

This study focuses on the electrochemical sensing of phenols, cresols, and guaiacols, as the fingerprint molecules in whiskey. The concept of detection is centered on the modification of the active surface of a boron-doped diamond (BDD) electrode with Nafion to impart different hydrophobic interactions with guaiacol and its analogues<sup>10</sup>. The inclusion complex of the guaiacols with  $\alpha$ -cyclodextrin ( $\alpha$ -CD) is also explored

considering the binding abilities of  $\alpha$ -CD for hydrophobic compounds are often different<sup>11</sup>. The BDD is well-known for its antifouling properties and a wide potential window, two key features required to circumvent the adsorption of phenol oxidation products. This simple electrochemical sensing technique is particularly appealing for spot analysis compared to lab-based instruments, which are costly, time-consuming and require a pre-sample treatment step.

## 2.2 Experimental

### 2.2.1 Reagents, standard solutions and samples

Sodium phosphate monobasic, sodium phosphate dibasic, phosphoric acid, ethanol (EtOH), potassium chloride (KCl), potassium hexacyanoferrate (III)  $[\text{Fe}(\text{CN})_6]^{3-}$ , potassium hexacyanoferrate (II) trihydrate  $[\text{Fe}(\text{CN})_6]^{4-}$ , acetonitrile (ACN), guaiacol, 4-EG, eugenol, phenol, 4-ethylphenol (4-EP), 4-vinylguaiacol (4-VG), *p*-cresol, *o*-cresol, *m*-cresol,  $\alpha$ -cyclodextrin ( $\alpha$ -CD),  $\beta$ -cyclodextrin ( $\beta$ -CD), methyl ( $\text{M-}\beta$ -CD), sulphated ( $\text{S-}\beta$ -CD), and Nafion perfluorinated resin (5 % in a mixture of lower aliphatic alcohols) were purchased from Sigma-Aldrich (Dublin, Ireland). Different buffer pHs were prepared; phosphate buffer at pH 2, acetate buffer at pH 5, phosphate buffer at pH 7, all at 100 mM with 5 % EtOH. 5 % EtOH was added to eliminate the effect of EtOH for the analysis of the phenols in whiskey samples. A stock solution of 1 mM of phenols, guaiacols, and cresol isomers was prepared in 100 mM phosphate buffer, pH 7 daily before use. All reagents used were of the analytical grade of the highest purity, and aqueous solutions were prepared in deionised water (Millipore, Ireland). Aqueous solutions were prepared in deionised water (Millipore, Ireland). Whiskey samples were obtained from a local store in Cork, Ireland.

### 2.2.2 Apparatus

Electrochemical impedance spectroscopy (EIS) measurement was performed at room temperature using a CHI660E electrochemical workstation (CH Instrument, Austin, TX). Differential pulse voltammetry (DPV), square wave voltammetry (SWV), cyclic voltammetry (CV) and chronocoulometry were used during electrochemical measurements using a CHI1040A electrochemical workstation (CH Instrument,

Austin, TX). The electrochemical cell consists of the three electrodes; a BDD electrode (B/C ratio in the gaseous phase of 1000 ppm, 3 mm diameter, Windsor Scientific, Slough Berkshire, UK), a silver/silver chloride (Ag/AgCl /3 M KCl) reference electrode (BASi Analytical Instruments, West Layette, IN), and a Pt wire counter electrode (Sigma-Aldrich, Dublin, Ireland). Peak deconvolution was carried out using the Peak Analyser function in Origin Pro 8.5.1 software. Gaussian peaks were fitted based on the oxidation potential of the analytes.

### **2.2.3 Preparation of the modified electrodes**

The Nafion-modified BDD electrode was obtained by drop-casting 5  $\mu$ L of the Nafion solution (2 %, prepared in EtOH) on a polished BDD electrode followed by vacuum drying.

### **2.2.4 Electrochemical characterisation of the bare and modified BDD electrodes**

The bare and modified electrodes were characterised by CV and EIS. The CV and EIS measurements were performed in 5 mM  $\text{K}_3\text{Fe}(\text{CN})_6^{4-/3-}$  prepared in 1 M KCl and 10 mM  $\text{K}_3\text{Fe}(\text{CN})_6^{4-/3-}$  supported by 0.1 M KCl, respectively. EIS was achieved with an AC frequency ranged between 1 Hz and 100 kHz.

### **2.2.5 High-performance liquid chromatography (HPLC)**

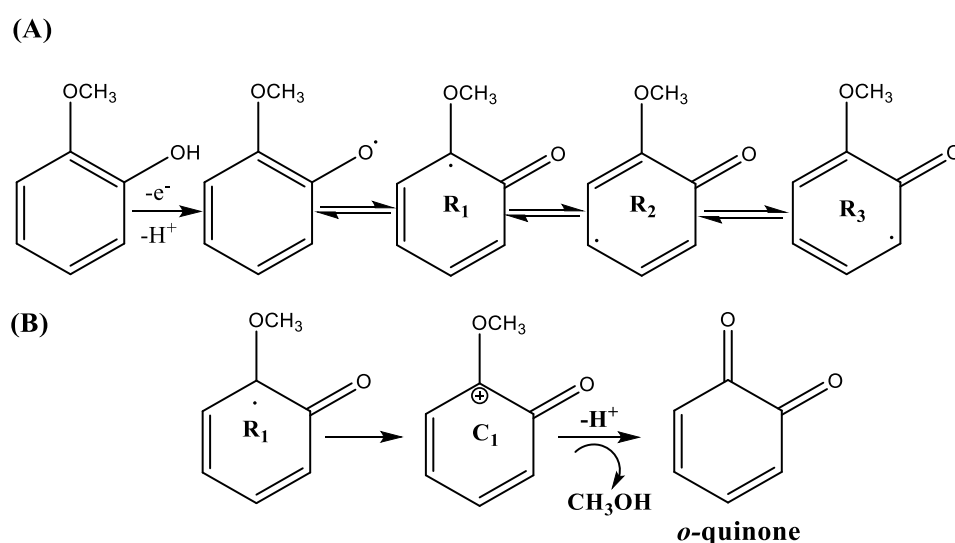
Chromatographic analysis was achieved on an Agilent 1200 HPLC system consisting of a binary pump (model G1312B), degasser (model G1379B), autosampler (model G1367D) and a UV diode array detector (model G1315C) system, employing an Agilent ChemStation software. The separation was performed on an Agilent Eclipse XDB  $\text{C}_{18}$  (4.6 x 150 mm, 5  $\mu$ m) column using an isocratic mobile phase of 30: 70 ACN:  $\text{H}_2\text{O}$  (v/v, %) and a flow rate of 1 mL/min. The injection volume was 5  $\mu$ L with a column temperature of 25  $^\circ\text{C}$ . The separation was monitored at 210 nm. The mobile phase was filtered through a 0.45  $\mu$ m Nylon Whatman filter (Sigma-Aldrich, Dublin, Ireland) and sonicated before use. The column was equilibrated with mobile phase for 20 min before injection. 1 mM stock solutions of guaiacol, 4-EG, 4-EP, 4-VG, eugenol, phenol, *o*-cresol, *m*-cresol, and *p*-cresol were prepared daily in ACN.

Standard solutions were prepared by diluting the stock solutions with the mobile phase.

## 2.3 Results and discussion

### 2.3.1 Electrochemical oxidation of the guaiacol analogues by the bare BDD electrode

It is widely known that the electrochemical oxidation of a phenol ring ( $pK_a = 10.00$ ) begins with an unstable phenoxy radical in a one-electron and one-proton step. This unstable radical exists in three isomeric forms, however, its highest spin is in the *o*- and *p*-positions. In the presence of water, *o*-quinone and *p*-quinone are the two major products. These quinones are reversibly reduced to catechol and hydroquinone in a two-electron and two-proton mechanism, respectively<sup>12</sup>. Similarly, guaiacol ( $pK_a = 9.83$ ) initially undergoes a first electron transfer to produce three plausible phenoxy radicals ( $R_1$ ,  $R_2$ , and  $R_3$ ) (**Scheme 2.1A**), which rapidly undergo a second electron transfer to form their corresponding carbocations<sup>13</sup> (**Scheme 2.1B**). The methoxy group of guaiacol with the electron-donating effect stabilises the cation  $C_1$ , the predominant form, which is subject to hydrolysis to form *o*-benzoquinone and methanol (**Scheme 2.1B**).



**Scheme 2.1.** The electrochemical oxidation pathway and the main oxidation product of guaiacol. The formation of three possible radicals with  $R_1$  as the predominant radical.  $C_1$  is then subject to further oxidation to form *o*-quinone together with the release of methanol, which is also electroactive on the BDD electrode.

The CV of guaiacol obtained by the bare BDD electrode displayed a broad and irreversible oxidation peak ( $I_a$ ) in the first scan (**Figure 2.1A**). The reverse scan exhibited one broad reduction peak ( $I_c$ ) and two well-defined reduction peaks, designated as  $II_c$  and  $III_c$ . The release of methanol was evinced by a small oxidation peak at + 1.4 V, whereas the  $I_c$  peak could be assigned as the formation of catechol in the reverse scan from *o*-benzoquinone. In the second cycle, two peaks at  $II_a$  and  $III_a$  emerged while the current of the  $I_a$  peak decreased due to the adsorption of guaiacol oxidation products<sup>13</sup>. Two minor products, 3-methoxy hydroquinone, and 3-methoxy catechol stem from the cation  $C_2$  and  $C_3$ , respectively (**Scheme 2.2**). The  $II_a$ - $III_c$  pair could be attributed to the reversible oxidation/reduction of methoxy hydroquinone and methoxy benzoquinone. The  $III_a$ - $II_c$  pair corresponds to the cyclic behaviour of methoxy catechol-methoxy quinone, in agreement with the literature<sup>13</sup>. The BDD electrode surface displays hydrophobicity, thus the carbocations only adhere slightly on this surface and easily diffuse into the reaction layer to react with nucleophilic species including water, catechol, and guaiacol in the bulk electrolyte.

The CV of 4-EG exhibited one irreversible oxidation peak ( $I_a$ ) and two reduction peaks ( $I_c$ ,  $II_c$ ). In the second scan, a new anodic peak ( $II_a$ ) emerged at + 0.35 V, whereas the main anodic peak decreased (**Figure 2.1B**). The reduction peak ( $II_c$ ) could be attributed to the formation of 4-ethyl-3-methoxy-phenol while the very small  $I_c$  peak is from the reduction of the 4-EG products to catechol. The  $II_a$  peak continued to increase with repeated scans, corresponding to the decrease of the  $I_a$  peak. This peak was assigned as the oxidation of 4-ethyl-3-methoxy-phenol to form a corresponding quinone. This mechanism is somewhat similar to the oxidation of eugenol to yield 4-allyl-3-methoxybenzoquinone and 4-allyl-*o*-quinone<sup>14</sup>. The CVs of phenol, 4-EP, *o*-cresol, *p*-cresol, and *m*-cresol on the bare BDD electrode are shown in **Figure 2.2**.



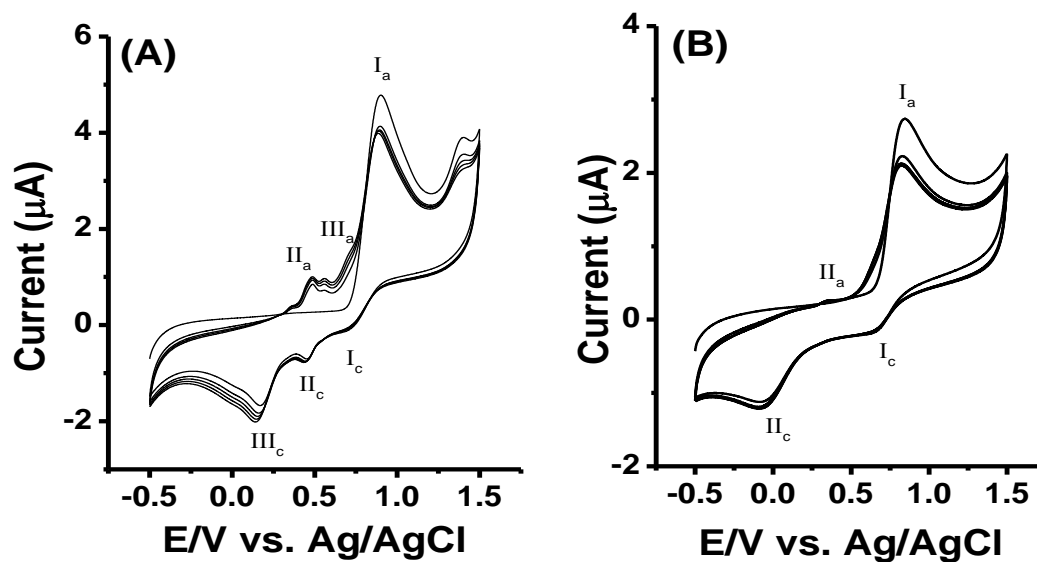
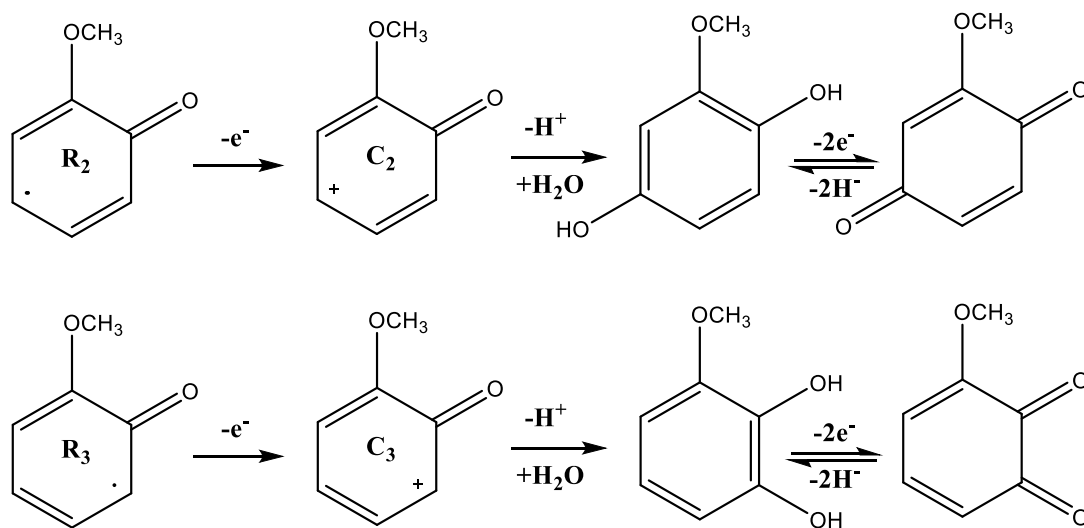


**Figure 2.1.** CVs of the bare BDD electrode for (A) guaiacol and (B) 4-EG. The concentration of each analyte is 100  $\mu\text{M}$  in 100 mM phosphate buffer, pH 2 with 5 % EtOH at the scan rate of 100  $\text{mV s}^{-1}$ .



**Scheme 2.2.** Two plausible minor oxidation products of guaiacol as postulated in the literature<sup>13</sup>.

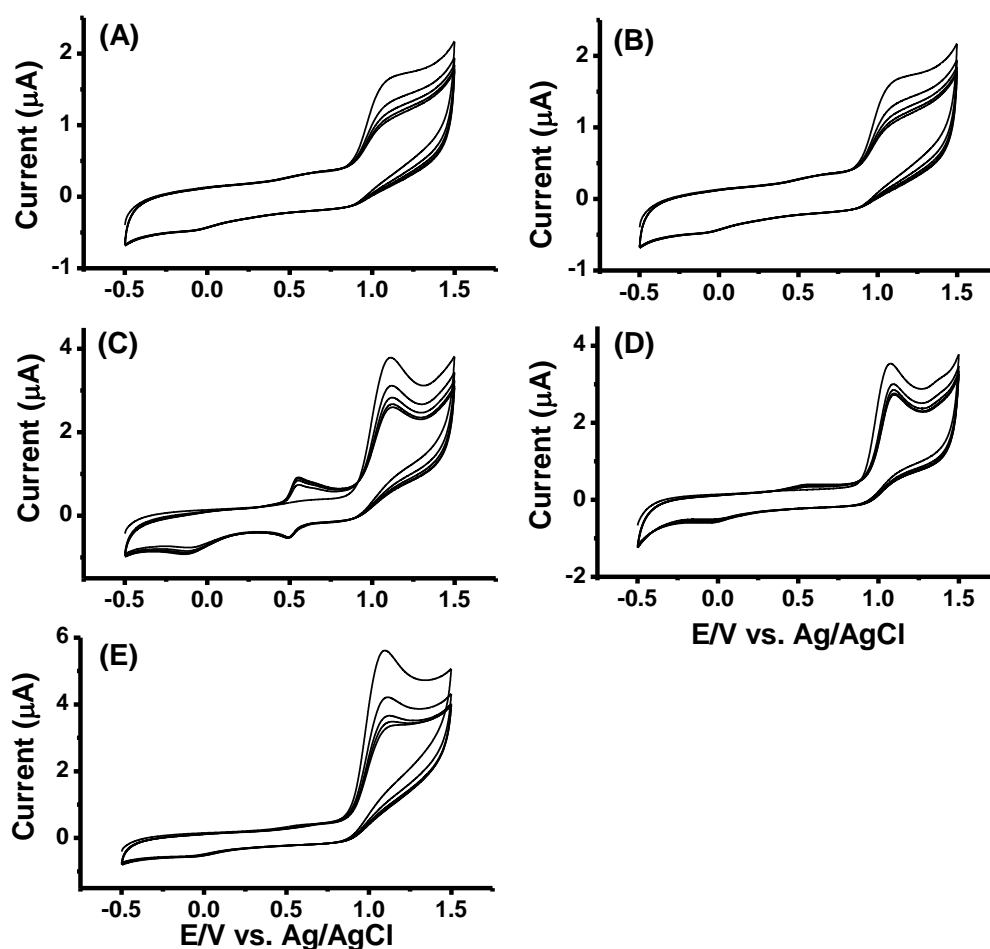


**Figure 2.2.** CVs of the bare BDD electrode for (A) phenol, (B) 4-EP, (C) o-cresol, (D) m-cresol and (E) p-cresol. The concentration of each analyte is 100  $\mu\text{M}$  in 100 mM phosphate buffer, pH 2 with 5 % EtOH at the scan rate of 100  $\text{mV s}^{-1}$ .

### 2.3.2 Electrochemical oxidation of the guaiacol analogues by Nafion modified BDD electrode

The BDD electrode was then modified by Nafion, a sulfonated tetrafluoroethylene-based fluoropolymer-copolymer. Nafion is negatively charged and its incorporation into the electrode has been widely used in several electroensing platforms to circumvent the interference of endogenous electroactive species in food and biological samples<sup>15</sup>. Nafion with superior conductive properties also plays an important role as a supercatalyst in diversified reactions. The CVs obtained for the Nafion modified electrode for the three guaiacols were very similar to those of the bare BDD electrode (**Figure 2.3**). However, the response signal was noticeably higher, illustrating the

interaction/adsorption of the guaiacols with Nafion on the electrode surface. The anodic peak ( $\text{II}_a$ ) was also shifted to a higher value on the Nafion modified BDD electrode compared to the bare electrode. Considering the high  $\text{pK}_a$  values for the guaiacols ( $\sim 10$ ), they are less deprotonated and display hydrophobic interactions with the tetrafluoroethylene moiety of Nafion. Consequently, they are concentrated on the electrode surface to impart high signal responses. At alkaline pH, the guaiacols are more deprotonated and thus, repulsed by the Nafion film. The modifier Nafion film also has other distinct features encompassing permselective, ion-exchange and antifouling properties. The ionic selectivity for hydrophobic organic compounds is achieved through hydrophobic interactions with the hydrophobic fluorocarbons of Nafion<sup>16</sup>. The CVs of phenol, 4-EP, *o*-cresol, *p*-cresol, and *m*-cresol on the Nafion modified BDD electrode are shown in **Figure 2.4**.

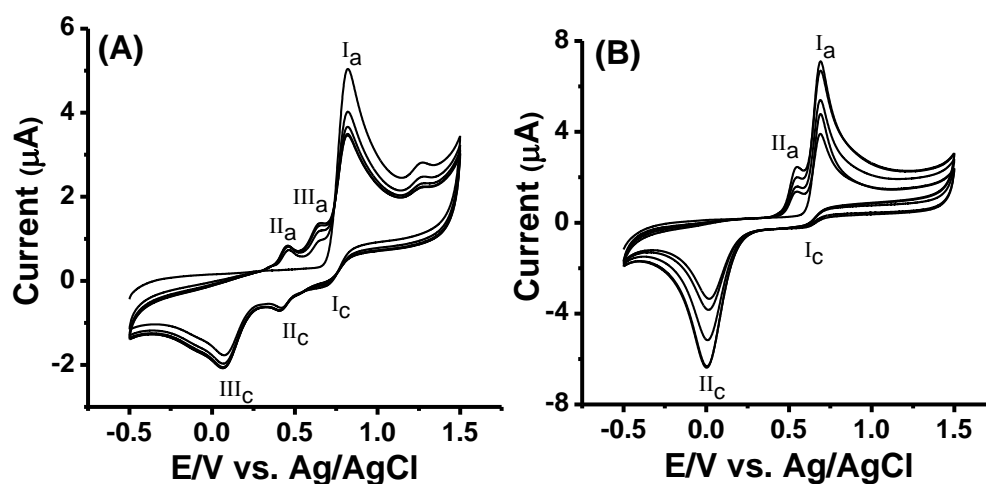


**Figure 2.3.** CVs of the Nafion modified BDD electrode for (A) guaiacol and (B) 4-EG. The concentration of each analyte is 100  $\mu\text{M}$  in 100 mM phosphate buffer, pH 2 with 5 % EtOH at the scan rate of 100  $\text{mV s}^{-1}$ .

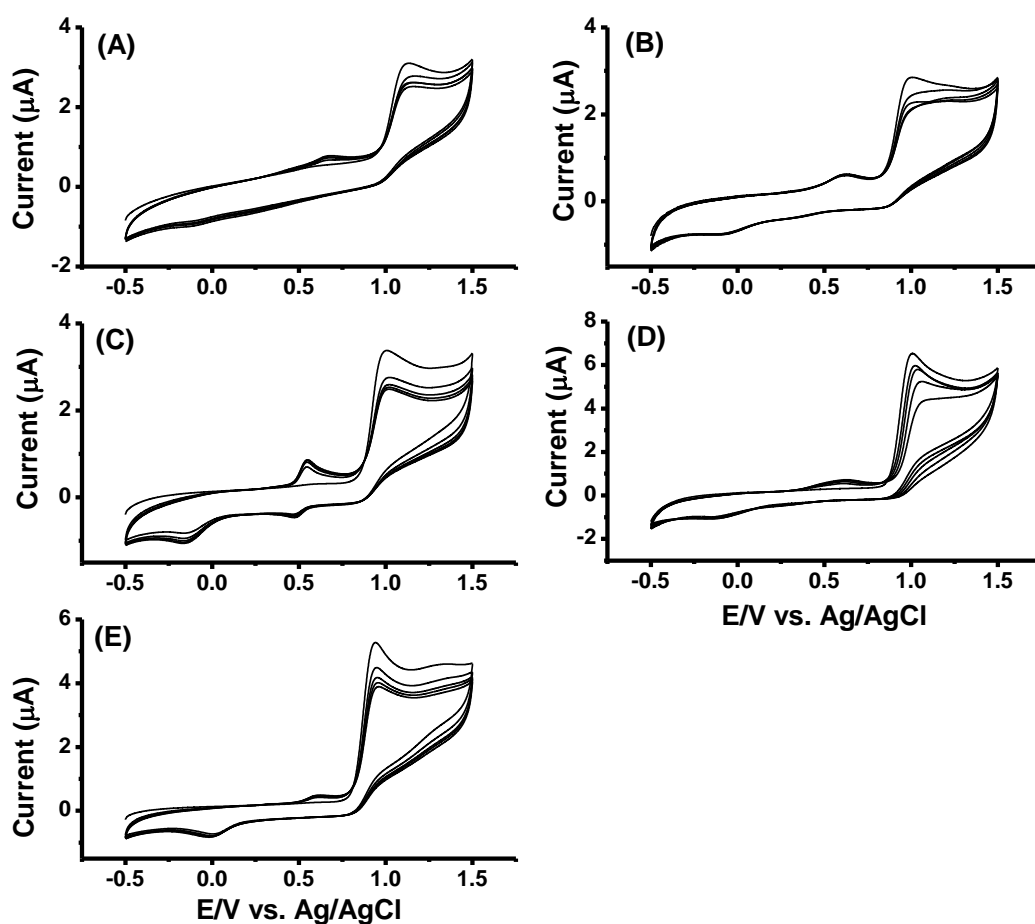


**Figure 2.4.** CVs of the Nafion modified BDD electrode for (A) phenol, (B) 4-EP, (C) o-cresol, (D) m-cresol and (E) p-cresol. The concentration of each analyte is 100  $\mu\text{M}$  in 100 mM phosphate buffer, pH 2 with 5 % EtOH at the scan rate of 100  $\text{mV s}^{-1}$ .

### 2.3.3 Voltammetry, impedance spectroscopy, and chronocoulometry characterisation

The bare and Nafion modified electrodes were also characterised by CV and EIS using  $\text{K}_3\text{Fe}(\text{CN})_6^{4-/3-}$  as the redox couple. In the CV mode (**Figure 2.5**), the peak current ( $I_p$ ) of the redox probe ( $\text{K}_3\text{Fe}(\text{CN})_6^{4-/3-}$ ) on the Nafion modified BDD electrode decreased  $\sim 70$ -fold in comparison to the value obtained by the bare electrode.

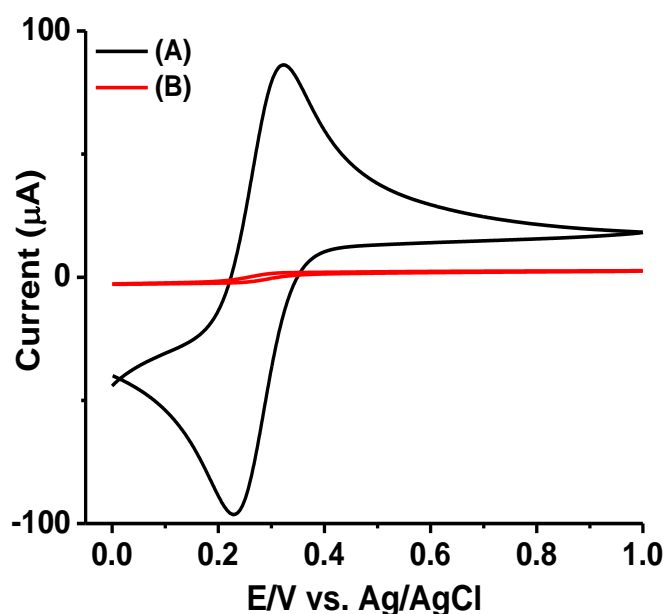


**Figure 2.5.** CVs of the (A) bare and (B) Nafion modified BDD electrodes in 5 mM  $\text{Fe}(\text{CN})_6^{4-/3-}$  prepared in 1 M KCl, at the scan rate of  $50 \text{ mV s}^{-1}$ .

The peak current is related to the electroactive surface area for the electroactive species. Randles-Sevcik equation<sup>17</sup> is used to calculate the electroactive area:

$$I_{pa} = 2.69 \times 10^5 n^{3/2} A C D_R^{1/2} \nu^{1/2} \quad (2.1)$$

where  $I_{pa}$  refers to the anodic peak current,  $n$  is the number of electron transfer ( $n=1$ ),  $A$  is the electrode surface area ( $\text{cm}^2$ ),  $D_R$  is the diffusion coefficient ( $7.6 \times 10^{-6} \text{ cm}^2 \text{ s}^{-1}$ ),  $C$  is the concentration of  $\text{K}_3\text{Fe}(\text{CN})_6^{4-/3-}$  (5 mM in 1 M KCl), and  $\nu$  is the scan rate ( $\text{mV s}^{-1}$ ). The surface areas of the bare and Nafion modified BDD electrodes are  $5.5 \times 10^{-12}$  and  $1.06 \times 10^{-13} \text{ cm}^2$ , respectively.

The bare and Nafion modified BDD electrodes were then characterised by EIS and modelled using the ZnSimWin software (**Figure 2.6**). The parameters obtained for the bare and Nafion modified BDD electrodes using an equivalent circuit  $R_s(Q(R_{ct}W))$  are shown in **Table 2.1**. The  $R_{ct}$  (charged transfer resistance) value of the Nafion modified BDD electrode was  $\sim 27$  times higher than the bare BDD electrode, an indication of the blocking of the active surface of the electrode in corroboration with CV results.

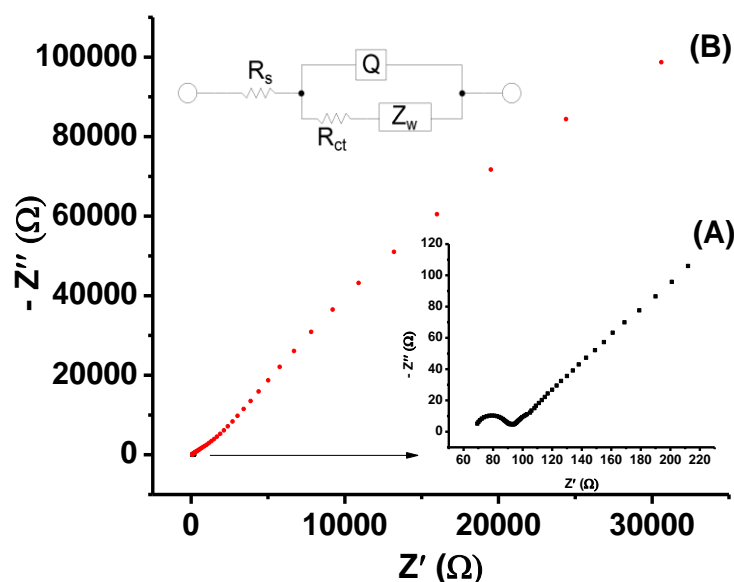


**Figure 2.6.** (A) EIS of the bare (red dotted line) and Nafion (black dotted line) modified BDD electrodes in 10 mM  $\text{Fe}(\text{CN})_6^{4-/3-}$  prepared in 0.1 M KCl. Insert: (B) the modified Randles circuit.

**Table 2.1.** Parameters obtained for the bare and Nafion modified BDD electrodes using an equivalent circuit  $R_s(Q(R_{ct}W))$ . The parameters were obtained by the ZnSimWin software.

	Bare BDD	Nafion BDD
<b><math>R_s</math> (Ω)-solution</b>	60.31	63.3
<b><math>Q</math> (Ω<sup>-1</sup> s<sup>n</sup>)</b>	$1.28 \times 10^{-6}$	$2.34 \times 10^{-6}$
<b><math>n</math></b>	0.86	0.80
<b><math>R_{ct}</math> (Ω)- charge transfer</b>	23.55	637.4
<b><math>Z_w</math> (Ω s<sup>-1/2</sup>)-Warburg model</b>	0.0027	$3.86 \times 10^{-20}$
<b>Chi Square</b>	0.0003	0.003

Chronocoulometry was then conducted to examine the kinetics and mechanism of electrode reactions for the bare and Nafion modified BDD electrode. This technique provides two important parameters: the diffusion coefficient  $D$  and the adsorption charge  $Q_{ads}$ , which are estimated by Anson's equation<sup>18</sup>.

$$Q = 2nFAC\sqrt{DT/\pi} + Q_{ads} + Q_{dl} \quad (2.2)$$

where  $A$  is the surface area of the working electrode ( $5.5 \times 10^{-12}$  and  $1.06 \times 10^{-13} \text{ cm}^2$  for the bare and modified electrodes, respectively),  $C$  ( $10 \text{ μM}$  or  $10^{-8} \text{ mol/cm}^3$ ) is the concentration of guaiacol,  $D$  is the diffusion coefficient of guaiacol,  $t$  is time,  $Q_{dl}$  is

the double-layer charge and  $Q_{\text{ads}}$  is the faradic charge due to the oxidation of adsorbed guaiacol. The number of electrons transferred,  $n$ , is taken as 2 for guaiacol<sup>13</sup>, and  $F$  is the Faraday constant. The double-layer charge  $Q_{\text{dl}}$  can be estimated from the experiment in the absence of guaiacol. A simple  $Q$  vs.  $t^{1/2}$  plot provides a slope and an intercept for the determination of  $D$  and  $Q_{\text{ads}}$  (**Figure 2.7**). The  $Q_{\text{ads}}$  value is then used to estimate the surface concentration ( $\Gamma$ ) corresponding to a monolayer as follows:

$$Q_{\text{ads}} = nFA\Gamma \quad (2.3)$$

From the experimental data,  $D = 7.8 \times 10^{16}$  and  $7.7 \times 10^{20} \text{ cm}^2 \text{ s}^{-1}$  are estimated for bare BDD and Nafion modified BDD electrodes, respectively, corresponding to a surface concentration of ( $\Gamma$ ) of 0.42 and 45  $\text{mol cm}^{-2}$ . Such results clearly illustrated a faster diffusion rate and a stronger accumulation capacity of the Nafion film compared to bare BDD for the adsorption of guaiacol.

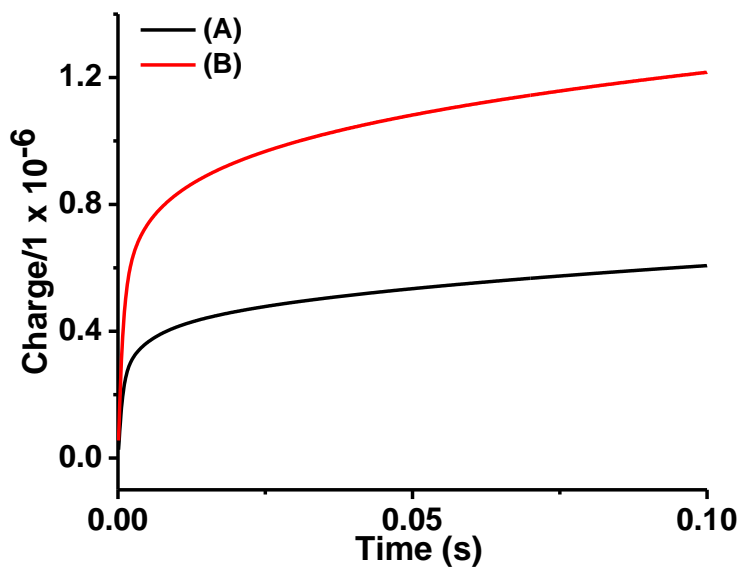


**Figure 2.7.** Chronocoulometry curves of 10  $\mu\text{M}$  guaiacol on (A) bare and (B) Nafion modified BDD electrodes, using 100 mM phosphate buffer, pH 7.

### 2.3.4 SWV of the guaiacols

Considering the overlapping oxidation peaks of the guaiacols, a simple amperometric detection ( $i$ - $t$  curve) cannot be used to distinguish such guaiacols. At best, it provides

an approximation of the total phenolic levels. Thus, SWV was conducted to obtain the lowest detection limit for the guaiacols and provide the plausible peak separation of the phenols. The detection limit is achieved by optimising the SWV amplitude, the potential increment, and the frequency, however, such parameters also cause peak merging and must be optimised accordingly. As a compromise between the detection sensitivity and the peak separation, the following parameters were considered optimal for SWV: amplitude ( $E_{sw}$ ) of 25 mV, a potential increment ( $\Delta E$ ) of 4 mV and a frequency ( $f$ ) of 5 Hz ( $t = 1/f$ , s). The effect of pH on the detection of the analytes was investigated (**Figure 2.8**). Upon increasing the pH, the peak currents substantially decrease, with only slight oxidation peaks visible at pH 7. Therefore, pH 2 was selected as the optimum pH for the separation.

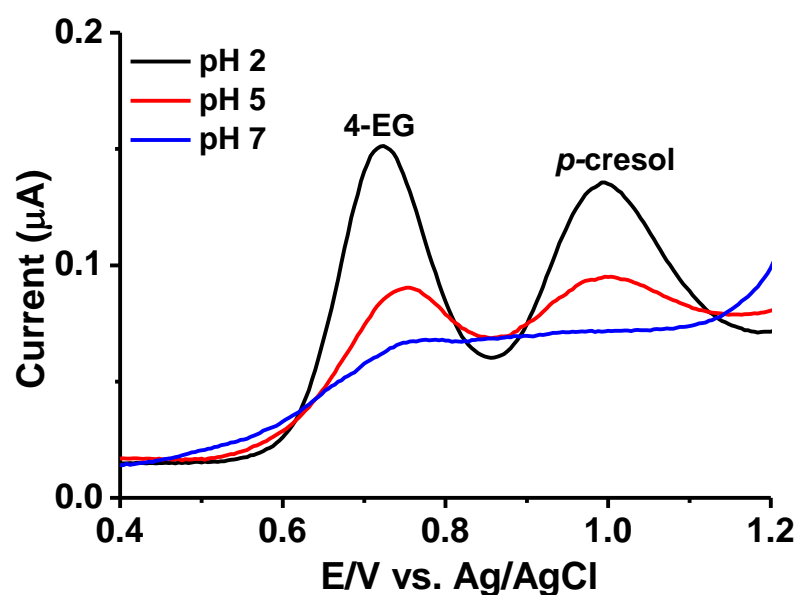


**Figure 2.8.** SWV of a standard mixture of 4-EG and p-cresol (4  $\mu M$  each) at different pH values (2, 5, and 7), with 5 % EtOH and 10 mM  $\alpha$ -CD. Detection was achieved on the Nafion modified BDD electrode vs.  $Ag/AgCl$ .

Our attention was then turned to the inclusion complexation between CDs and their “guest” hydrophobic compounds. Hydrophobic compounds including electroactive species form different inclusion complexes with the CD<sup>19</sup>. Initially, individual (**Figure 2.9**) and a standard mixture (**Figure 2.10**) of the analytes were investigated on the bare BDD electrode in the absence and presence of  $\alpha$ -CD. As evident from the graphs, the peak currents decrease in the presence of  $\alpha$ -CD. Also noticeable was a shift in oxidation potential of the analytes in the presence of  $\alpha$ -CD. Phenol, m-cresol and 4-



EG were shifted to a higher potential ( $\sim 60$  mV), the oxidation of guaiacol was shifted to a less positive potential ( $\sim 50$  mV), whereas the oxidation potential of 4-EP remained constant.

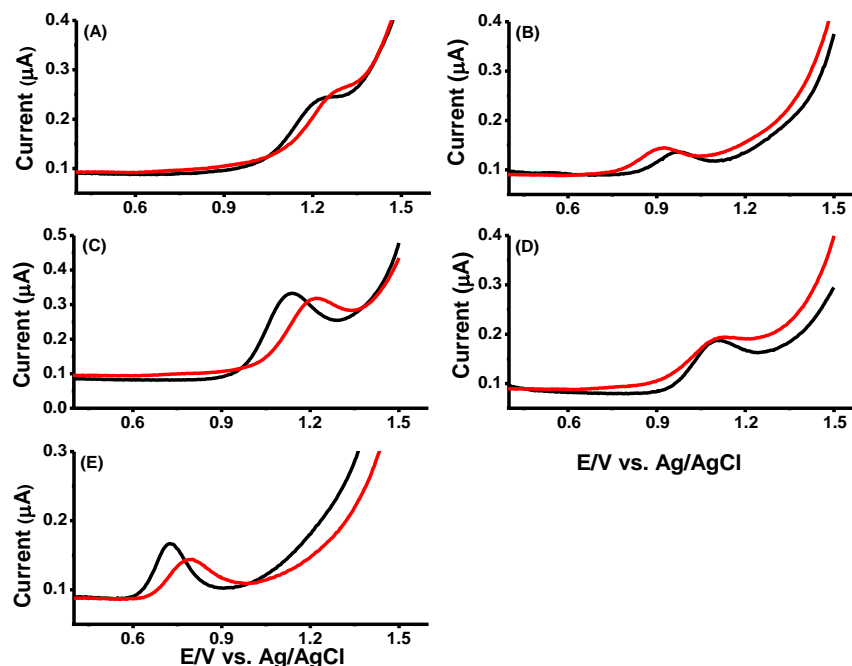


**Figure 2.9.** SWV of 4  $\mu\text{M}$  (A) phenol, (B) guaiacol, (C) m-cresol, (D) 4-EP and (E) 4-EG, using 100 mM phosphate buffer, pH 2 with 5 % EtOH in the absence (black lines) and presence (red lines) of 10 mM  $\alpha$ -CD. Detection was achieved on the bare BDD electrode vs. Ag/AgCl.

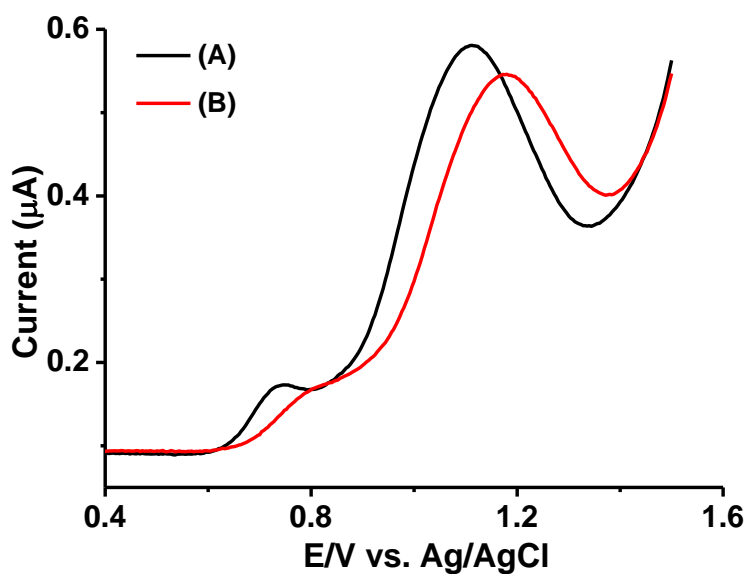


**Figure 2.10.** SWV of a standard mixture of phenol, guaiacol, o-cresol, m-cresol, p-cresol, 4-EP and 4-EG at 4  $\mu\text{M}$  each, using 100 mM phosphate buffer, pH 2 with 5 % EtOH in the (A) absence and (B) presence of 10 mM  $\alpha$ -CD. Detection was achieved on the bare BDD electrode vs. Ag/AgCl.

A representative SWV of phenol, guaiacol, *m*-cresol, 4-EP and 4-EG on the Nafion modified BDD electrode is shown in **Figure 2.11**. The oxidation of 4-EG occurred at a slightly lower potential (+ 0.65 V) than guaiacol (+ 0.76 V) with *m*-cresol oxidising at + 0.95 V. Such results were not unexpected due to the similar structures and  $pK_a$  values of guaiacols. The comparison of the standard mixture in the absence and presence of  $\alpha$ -CD on the Nafion modified BDD electrode is presented in **Figure 2.12**.

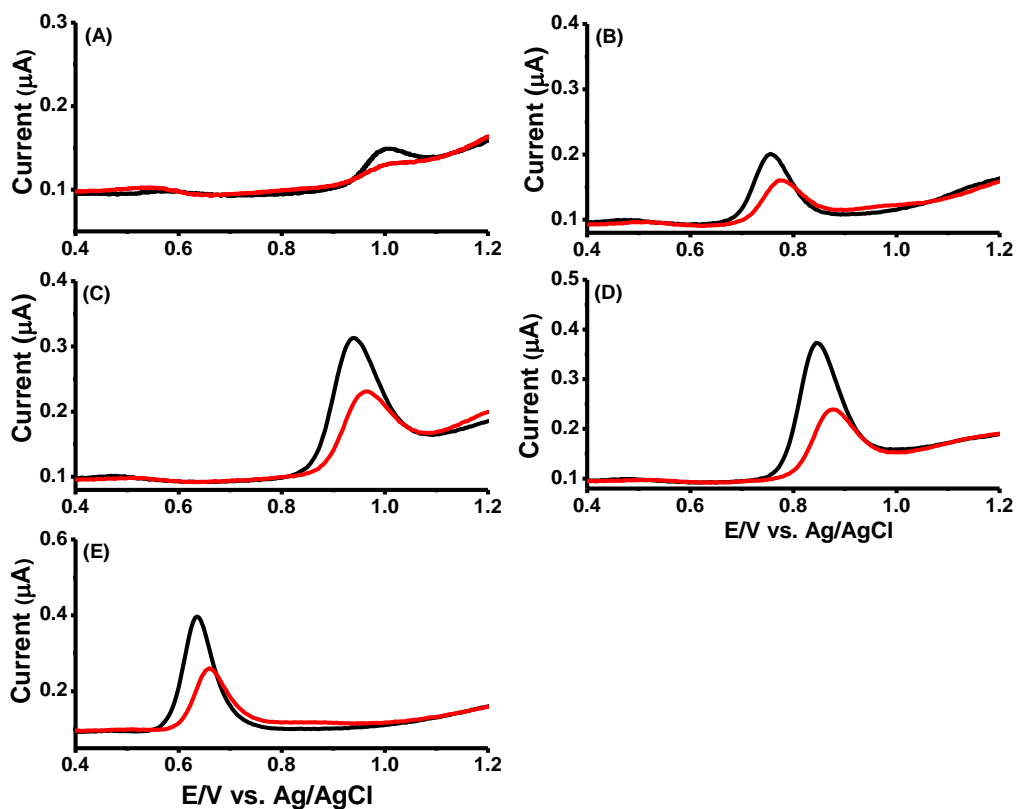


**Figure 2.11.** SWV of 4  $\mu$ M each (A) phenol, (B) guaiacol, (C) *m*-cresol, (D) 4-EP and (E) 4-EG, using 100 mM phosphate buffer, pH 2 with 5 % EtOH in the absence (black lines) and presence (red lines) of 10 mM  $\alpha$ -CD. Detection was achieved on the Nafion modified BDD electrode vs. Ag/AgCl.

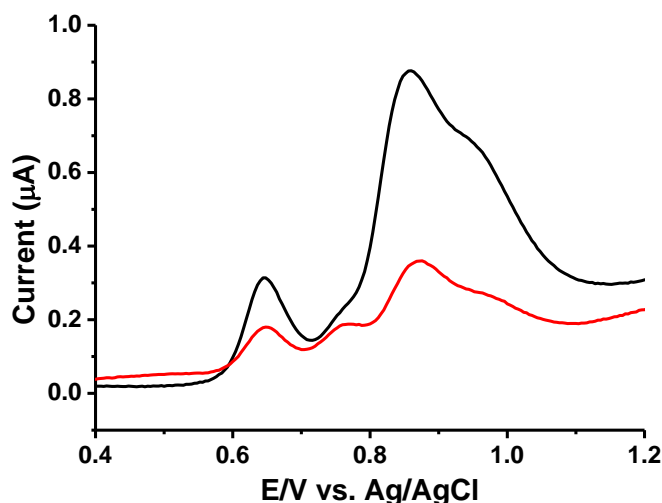


**Figure 2.12.** SWV of a standard mixture of phenol, guaiacol, *m*-cresol, 4-EP and 4-EG at 4  $\mu$ M each using 100 mM phosphate buffer, pH 2 with 5 % EtOH in the absence (black line) and presence (red line) of 10 mM  $\alpha$ -CD. Detection was achieved on the Nafion modified BDD electrode vs. Ag/AgCl.

The voltammogram of a mixture of *m*-cresol, *p*-cresol, *o*-cresol, guaiacol, 4-EG, phenol and 4-EP, following peak deconvolution, confirmed that 4-EG and guaiacol oxidised as two separate peaks. 4-EP, *p*-cresol, and *o*-cresol emerged as one single peak and *m*-cresol appeared as a right shoulder of this peak. The oxidation of phenol occurred at the highest potential (**Figure 2.13**).

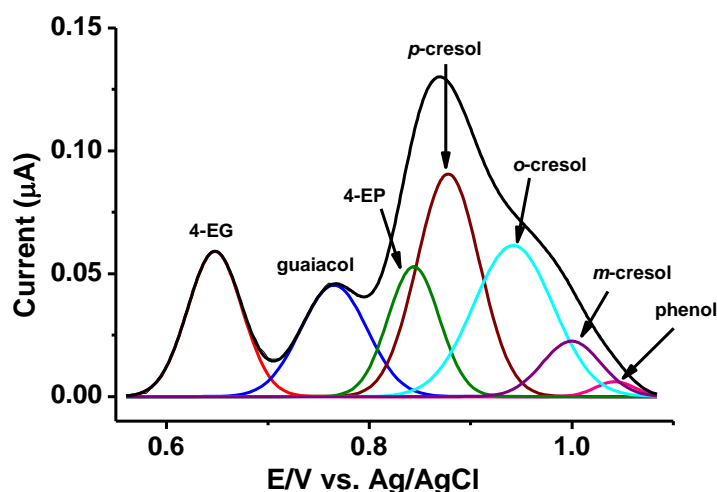


**Figure 2.13.** Resolved SWV of standard mixtures at 4  $\mu$ M each of 4-EG, guaiacol, 4-EP, *o*-cresol, *p*-cresol, *m*-cresol, and phenol after the application of peak deconvolution using Origin Pro 8.5.1. The electrolyte was 100 mM phosphate buffer, pH 2 with 5 % EtOH containing 10 mM  $\alpha$ -CD. Detection was achieved on the Nafion modified BDD electrode vs. Ag/AgCl.

A comparison of limits of detection (LODs) between the bare and Nafion modified BDD electrodes is illustrated in **Table 2.2**. Lower LODs were achieved for all analytes using the Nafion modified BDD electrode, highlighting its role in enhancing the signal response. The preferential concentration by Nafion was observed for *m*-cresol (12-fold), *o*-cresol (5-fold), guaiacol (5-fold), phenol (3-fold), and 4-EG (2-fold) but *p*-cresol and 4-EP were insignificantly affected.

**Table 2.2.** A comparison of LODs obtained using SWV at the bare and modified BDD electrodes using 100 mM phosphate buffer, pH 2 with 5 % EtOH containing 10 mM  $\alpha$ -CD.

Analyte	LOD Bare BDD	LOD Nafion BDD
phenol	1.5 $\mu$ M	0.5 $\mu$ M
guaiacol	1.0 $\mu$ M	0.2 $\mu$ M
<i>o</i> -cresol	2.0 $\mu$ M	0.4 $\mu$ M
<i>m</i> -cresol	1.2 $\mu$ M	0.1 $\mu$ M
<i>p</i> -cresol	0.4 $\mu$ M	0.3 $\mu$ M
4-EP	1.0 $\mu$ M	0.8 $\mu$ M
4-EG	0.2 $\mu$ M	0.1 $\mu$ M

The LODs obtained by alternative detection schemes is illustrated in **Table 2.3**.

**Table 2.3.** A comparison of determined LODs with literature values.

Analyte	Electrode material	LOD ( $\mu\text{M}$ )
<b>phenol</b>	Nafion modified BDD electrode	0.5*
	Bare glassy carbon electrode (GCE)	11.25 <sup>20</sup>
	Multi-walled carbon nanotubes (MWCNT)-Nafion-tyrosinase	0.13 <sup>21</sup>
	BDD film electrode	1.82 <sup>22</sup>
<b>guaiacol</b>	Nafion modified BDD electrode	0.2*
	Pt- $\gamma$ -Al <sub>2</sub> O <sub>3</sub> hollow spheres modified GCE	0.018 <sup>23</sup>
	Laccase/screen-printed carbon electrode	0.05 <sup>24</sup>
	Horseradish peroxidase–carbon nanotube–polypyrrole/Au electrode	0.3 <sup>25</sup>
	Reduced graphene oxide (RGO)/GCE	0.2 <sup>26</sup>
<b><i>o</i>-cresol</b>	Nafion modified BDD electrode	0.4*
	Bare GCE	42.01 <sup>20</sup>
<b><i>m</i>-cresol</b>	Nafion modified BDD electrode	0.1*
	MWCNT-Nafion-tyrosinase	0.28 <sup>21</sup>
	Enzyme tyrosinase/GCE	0.02 <sup>27</sup>
<b><i>p</i>-cresol</b>	Nafion modified BDD electrode	0.3*
	MWCNT-Nafion-tyrosinase	0.34 <sup>21</sup>
	Enzyme tyrosinase/GCE	0.02 <sup>27</sup>
<b>4-EP</b>	Nafion modified BDD electrode	0.8*
	Tyrosinase-modified carbon nanotube (CNT)/GCE	0.1 <sup>28</sup>
<b>4-EG</b>	Nafion modified BDD electrode	0.1*
	SnO <sub>2</sub> / SPE	0.06 <sup>29</sup>
	TiO <sub>2</sub> / SPE	0.04 <sup>29</sup>

\* LODs determined in this work

Analytical parameters, including linear regression equations, correlation coefficients (> 0.975) are shown in **Table 2.4**.

**Table 2.4.** Linear regression parameters for the analytes using SWV on the Nafion modified BDD electrode.

Analyte	Linear range ( $\mu\text{M}$ )	Linear regression equation	Correlation coefficient ( $R^2$ )
<b>phenol</b>	2-10	$I = 1.40 \times 10^{-8} C$ $- 6.86 \times 10^{-9}$	0.998
<b>guaiacol</b>	2-10	$I = 1.53 \times 10^{-8} C$ $- 5.23 \times 10^{-9}$	0.995
<b><i>o</i>-cresol</b>	2-10	$I = 1.35 \times 10^{-8} C$ $- 2.04 \times 10^{-8}$	0.996
<b><i>m</i>-cresol</b>	2-10	$I = 7.23 \times 10^{-8} C$ $- 5.64 \times 10^{-8}$	0.985
<b><i>p</i>-cresol</b>	2-10	$I = 1.65 \times 10^{-8} C$ $- 7.18 \times 10^{-10}$	0.976
<b>4-EP</b>	2-10	$I = 1.78 \times 10^{-8} C$ $- 2.80 \times 10^{-9}$	0.984
<b>4-EG</b>	2-10	$I = 2.70 \times 10^{-8} C$ $- 1.41 \times 10^{-8}$	0.991

Calibration curves and plots of the analytes are shown in **Figures 2.14** and **2.15**.

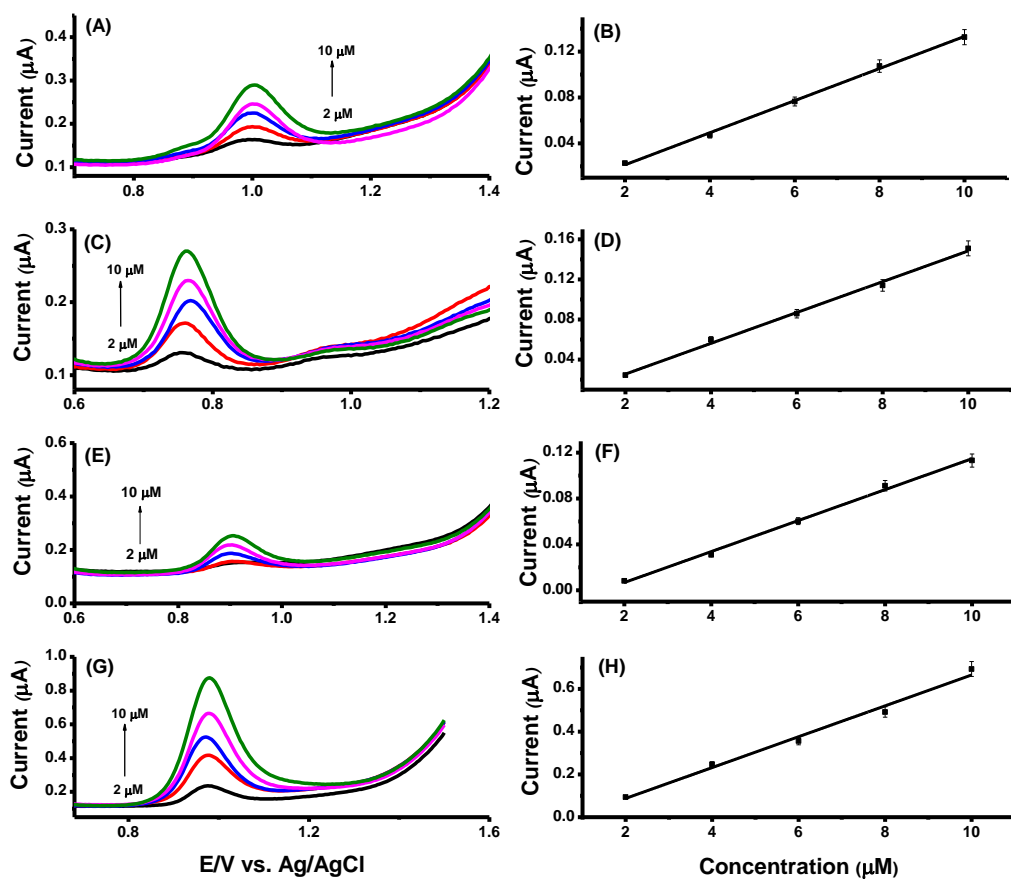


**Figure 2.14.** (A) Calibration curve and (B) plot of phenol; (C) calibration curve and (D) plot of guaiacol; (E) calibration curve and (F) plot of *o*-cresol and (G) calibration curve and (H) plot of *m*-cresol. The electrolyte was 100 mM phosphate, pH 2 with 5 % EtOH containing 10 mM  $\alpha$ -CD. Detection was achieved on the Nafion modified BDD electrode vs. Ag/AgCl. Error bars represent the standard deviation.

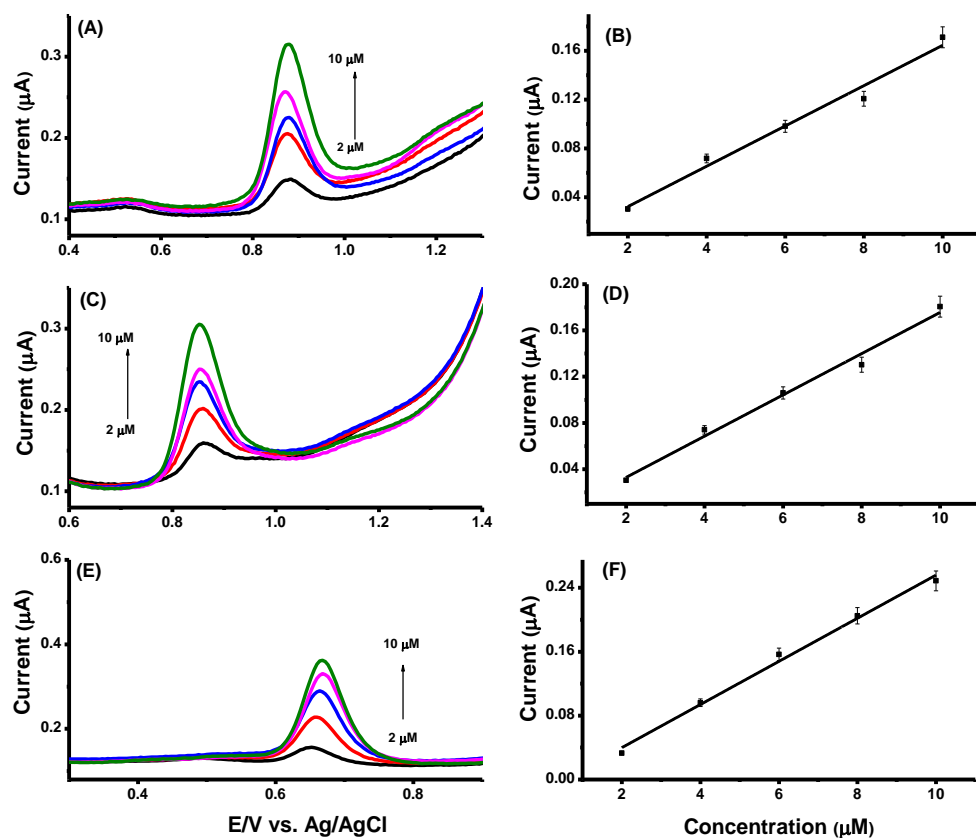


**Figure 2.15.** (A) Calibration curve and (B) plot of *p*-cresol; (C) calibration curve and (D) plot of 4-EP; and (E) calibration curve and (F) plot of 4-EG. The electrolyte was 100 mM phosphate, pH 2 with 5 % EtOH containing 10 mM  $\alpha$ -CD. Detection was achieved on the Nafion modified BDD electrode vs. Ag/AgCl. Error bars represent the standard deviation.



The stability of the Nafion modified BDD electrode toward 4-EG and *p*-cresol was investigated. **Figure 2.16** indicated that the oxidation potential was shifted to a higher value (5.3 and 2.7 %, respectively) after 30 runs.

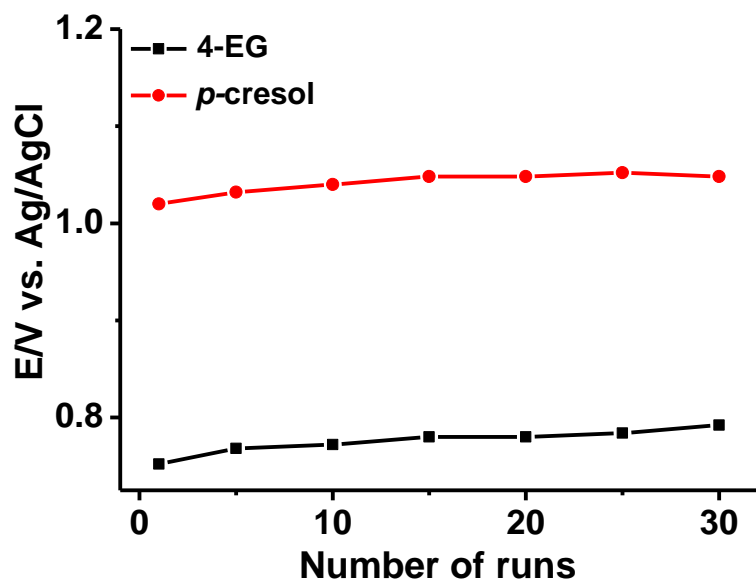


**Figure 2.16.** The stability of the Nafion modified BDD electrode towards 4  $\mu$ M each of 4-EG and *p*-cresol using SWV. The electrolyte was 100 mM phosphate buffer, pH 2 with 5 % EtOH containing 10 mM  $\alpha$ -CD.

### 2.3.5 Profiling the guaiacols in whiskey samples

Of importance is the use of  $\alpha$ -CD in the electrolyte to effectuate the peak separation of guaiacol from other analogues in the premium smoky whiskey (**Figure 2.17**). The SWV of the whiskey sample in the absence and presence of  $\alpha$ -CD is shown in **Figure 2.18**. The peak current of guaiacol and the other phenolics also became lower since the effective diffusion coefficient of such phenols decreased due to the formation of inclusion complexes with the large  $\alpha$ -CD molecule (Mw  $\sim$  973)<sup>19,30</sup>.

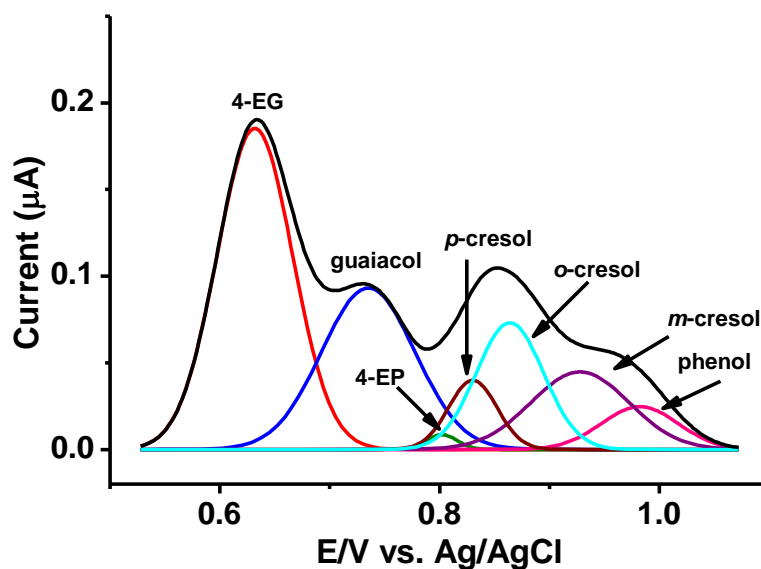


**Figure 2.17.** Resolved SWV of Islay whiskey after application of peak deconvolution using Origin Pro 8.5.1 on the Nafion modified BDD electrode vs. Ag/AgCl. The electrolyte was 100 mM phosphate buffer, pH 2 with 5 % EtOH containing 10 mM  $\alpha$ -CD.

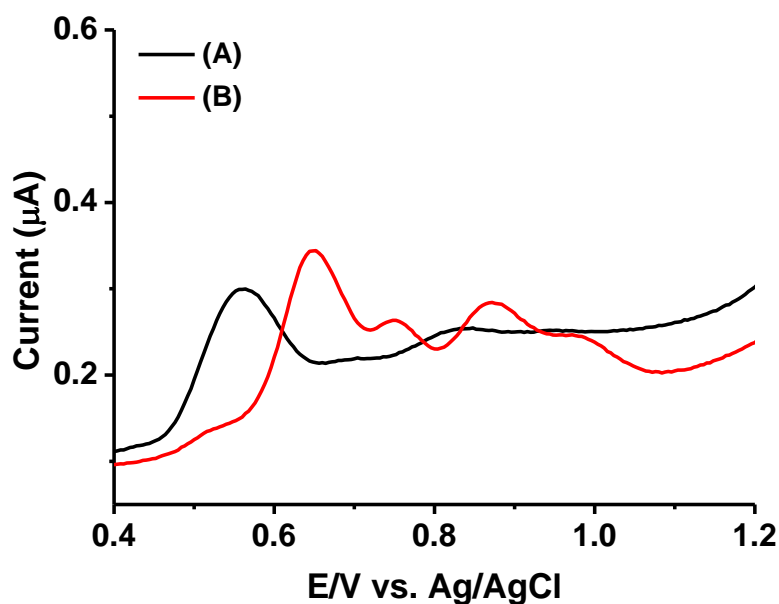


**Figure 2.18.** SWV of Islay whiskey in the (A) absence and the (B) presence of  $\alpha$ -CD using 100 mM phosphate buffer, pH 2 with 5 % EtOH on the Nafion modified BDD electrode vs. Ag/AgCl.

The peaks were identified by spiking the whiskey sample with individual standards (Figure 2.19).

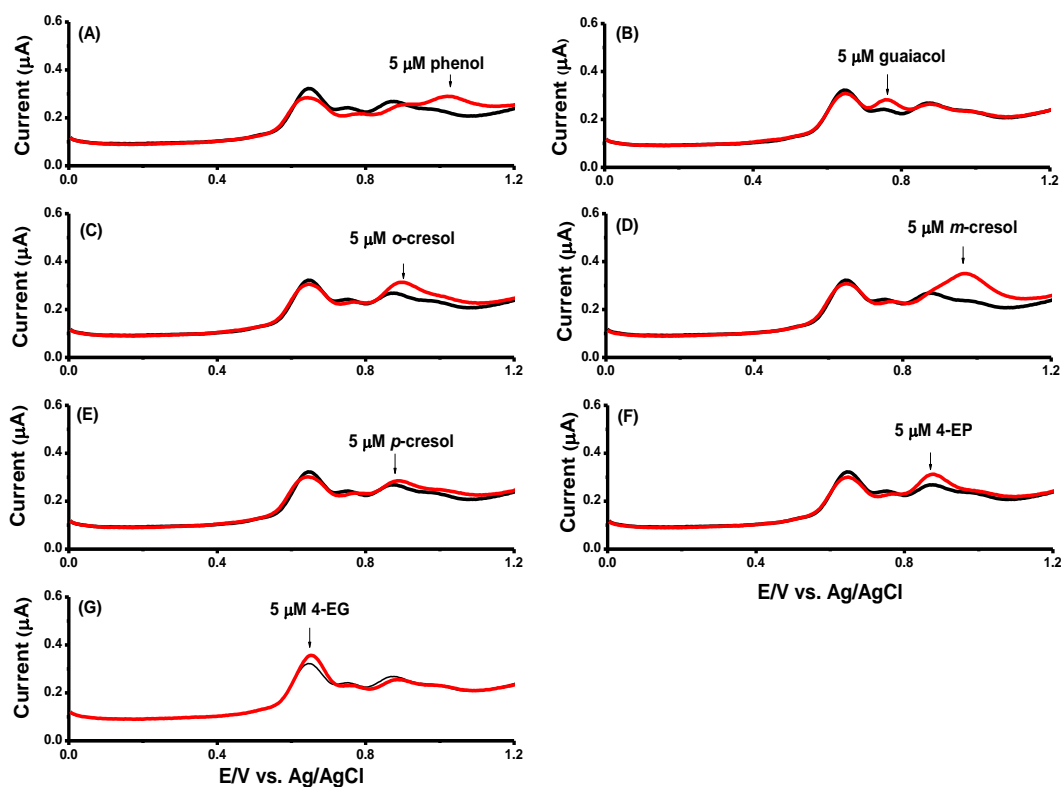


**Figure 2.19.** SWV of blank Islay whiskey (black lines) and spiked (red lines) with 5  $\mu\text{M}$  each of (A) phenol, (B) guaiacol, (C) *o*-cresol, (D) *m*-cresol, (E) *p*-cresol, (F) 4-EP and (G) 4-EG, using 100 mM phosphate buffer, pH 2 with 5 % EtOH containing 10 mM  $\alpha$ -CD. Detection was achieved on the Nafion modified BDD electrode vs. Ag/AgCl.

No improvement occurred when 10 mM of  $\alpha$ -CD was replaced by S- $\beta$ -CD,  $\beta$ -CD, or M- $\beta$ -CD at the same concentration. A mixture of  $\alpha$ -CD and M- $\beta$ -CD (10 mM each) or  $\alpha$ -CD and  $\beta$ -CD offered no improvement in peak separation (**Figure 2.20**). The same result was noted for doubling the amount of  $\alpha$ -CD in the electrolyte buffer (**Figure 2.21**).

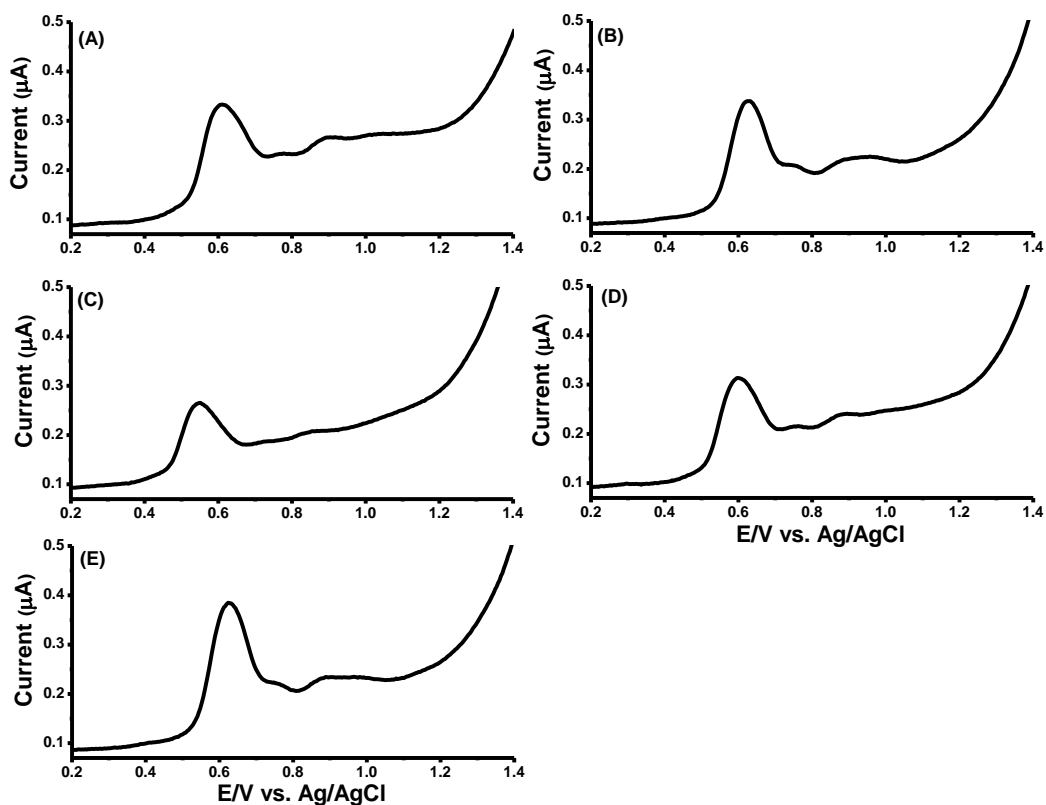


**Figure 2.20.** SWV of Islay whiskey using 100 mM phosphate buffer, pH 2, with 5 % EtOH containing (A) S- $\beta$ -CD, (B)  $\beta$ -CD, (C) M- $\beta$ -CD, (D) a mixture of  $\alpha$ -CD and M- $\beta$ -CD, and (E) a mixture of  $\alpha$ -CD and  $\beta$ -CD. Detection was achieved on the Nafion modified BDD electrode vs. Ag/AgCl.

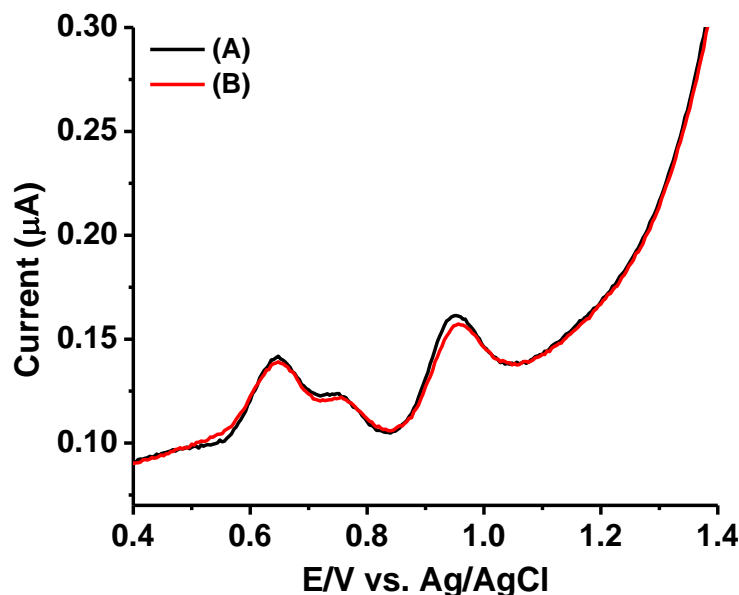


**Figure 2.21.** SWV of a standard mixture 4-VG, 4-EG, eugenol, and guaiacol ( $1\ \mu\text{M}$  each) using  $100\ \text{mM}$  phosphate buffer,  $\text{pH}\ 2$  with  $5\ \%$  EtOH containing (A)  $10\ \text{mM}$   $\alpha\text{-CD}$  and (B)  $20\ \text{mM}$   $\alpha\text{-CD}$ . Detection was achieved on the Nafion modified BDD electrode vs. Ag/AgCl.

Of relevance is the CV performance of *o*-nitrophenol and *p*-nitrophenol in the presence of  $\alpha\text{-CD}$ <sup>19</sup>. The *p*-nitrophenol reduction peak is significantly higher and overlaps with that of the *o*-isomer, thus, it is difficult to distinguish this pair by CV. The *p*-isomer forms an inclusion complex with  $\alpha\text{-CD}$ , enabling the peak shift towards a more negative potential ( $40\ \text{mV}$ ), whereas  $\alpha\text{-CD}$  exhibits no interaction with the *o*-isomer.

The hydrophobic cavity of  $\alpha\text{-CD}$  has an internal diameter of  $0.57\ \text{nm}$  and a corresponding height of  $0.78\ \text{nm}$ <sup>31</sup>. The phenol dimensions are  $0.43$  and  $0.57\ \text{nm}$ <sup>32</sup>, thus, this compound is completely enclosed in the hydrophobic cavity of  $\alpha\text{-CD}$ . 4-EG is most bulky and lengthy considering the bond lengths of C-C ( $0.154\ \text{nm}$ ) and C-O ( $0.143\ \text{nm}$ )<sup>33</sup>. The dimensions of 4-EG and its analogues are estimated by Chem3D (Perkin Elmer) and shown in **Figure 2.22**. One dimension of 4-EG is  $\sim 0.83\ \text{nm}$  (the length of  $-\text{CH}_2\text{-CH}_3$  is about  $0.26\ \text{nm}$ ) and the second one is  $0.68\ \text{nm}$  (with the  $-\text{O-CH}_3$  group). Accordingly, 4-EG cannot compete with other smaller counterparts to form an inclusion complex with  $\alpha\text{-CD}$ .

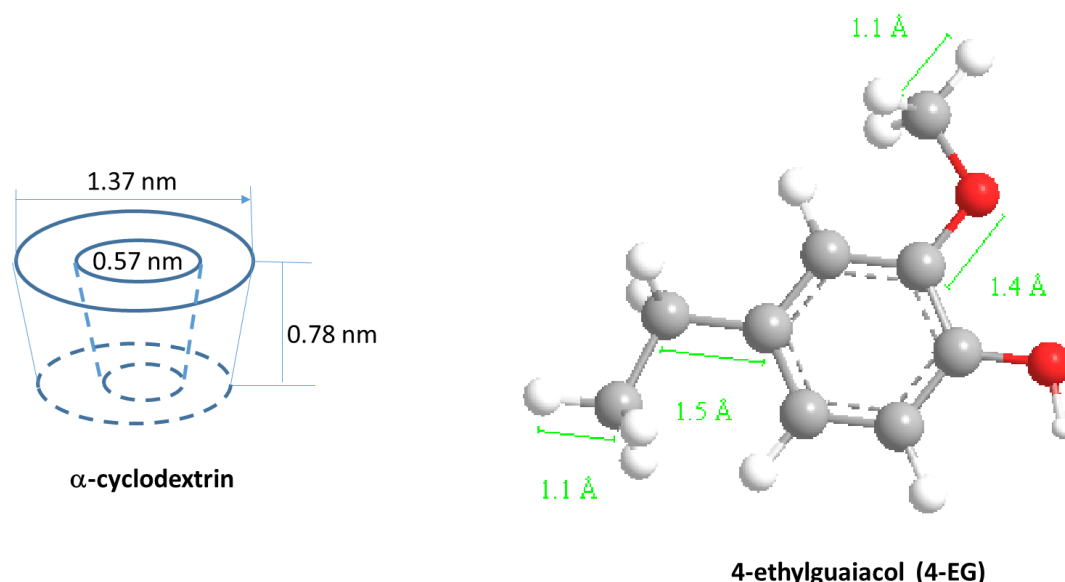


**Figure 2.22.** Key dimensions of  $\alpha$ -CD and 4-EG.

Similar arguments are applied to guaiacol and 4-EP for the likelihood to form inclusion complexes with  $\alpha$ -CD in the presence of the cresols and phenol. The cresols, with a methyl group, render them bigger (*o*- or *m*- position) or longer (*p*- position) than phenol. Considering the C-C bond length as mentioned earlier, both *p*- and *o*-cresol are still enclosed in the cavity of  $\alpha$ -CD, whereas partial inclusion complexation is expected for *m*-cresol. Phenol, *p*-cresol and *m*-cresol should be able to reside in the hydrophobic cavity of  $\alpha$ -CD, whereas partial complexation is anticipated for 4-EP and *m*-cresol, followed by guaiacol and 4-EG. Besides inclusion complexation, different hydrophobic interactions of the guaiacols with the hydrophobic regions of  $\alpha$ -CD are also anticipated and this behaviour could be exploited to profile guaiacol in the presence of other similar compounds.

Various strategies were attempted to renew the Nafion modified electrode after its subjection of repeated analysis of guaiacol since mechanical cleaning was no longer an option. CV cleaning in 100 mM phosphate buffer, pH 7 or 0.5 M H<sub>2</sub>SO<sub>4</sub> was less effective compared to the anodic treatment at + 2 V in the phosphate buffer for 1 min. The electrochemical reconditioning step was expected to produce a more hydrophilic surface, which promoted organic layer displacement by water<sup>34</sup>. After the anodic treatment, DPV confirmed that no peak was observed with the blanks (**Figure 2.23**).

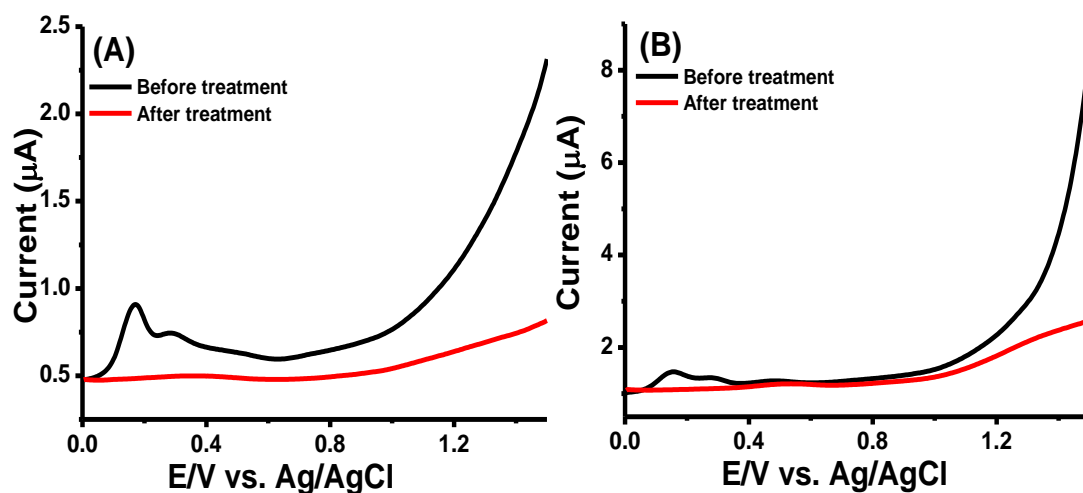


**Figure 2.23.** DPV before and after the anodic treatment at + 2 V for 1 min on (A) bare and (B) Nafion modified BDD electrodes after they were exposed to 1 mM guaiacol in 100 mM phosphate buffer, pH 7.

It is worth noting that slightly more resolved peaks were obtained with SWV over DPV (**Figure 2.24**).

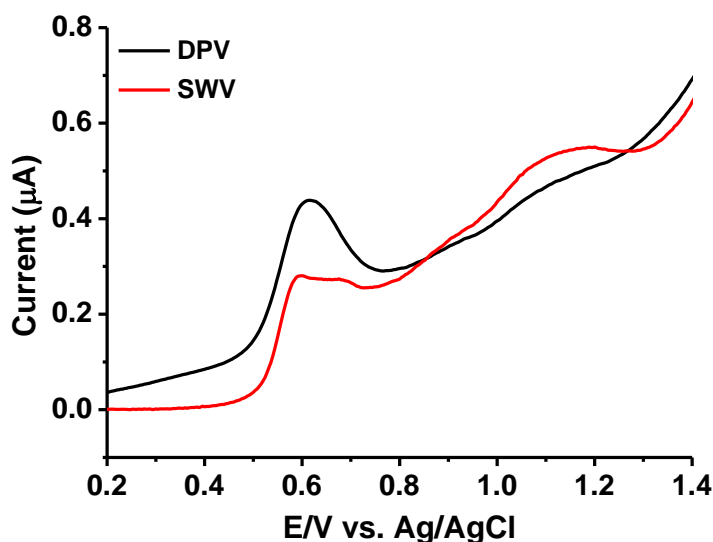


**Figure 2.24.** DPV and SWV of Islay whiskey on the bare BDD electrode vs. Ag/AgCl, using 100 mM phosphate buffer, pH 2 with 5 % EtOH containing 10 mM  $\alpha$ -CD.

HPLC was applied to confirm the presence of phenolic compounds in the Islay whiskey sample. **Figure 2.25** illustrates a blank whiskey sample and whiskey spiked with known concentrations of the phenols, guaiacols, and cresols. The chromatogram indicates the presence of phenol, guaiacol, *o*-cresol, *m*-cresol, *p*-cresol, 4-EP, and 4-EG, with *m*-cresol and *p*-cresol co-eluting. In agreement with Ng and Reuter<sup>2</sup>, 4-EP could not be quantitated as it appeared as part of a doublet.

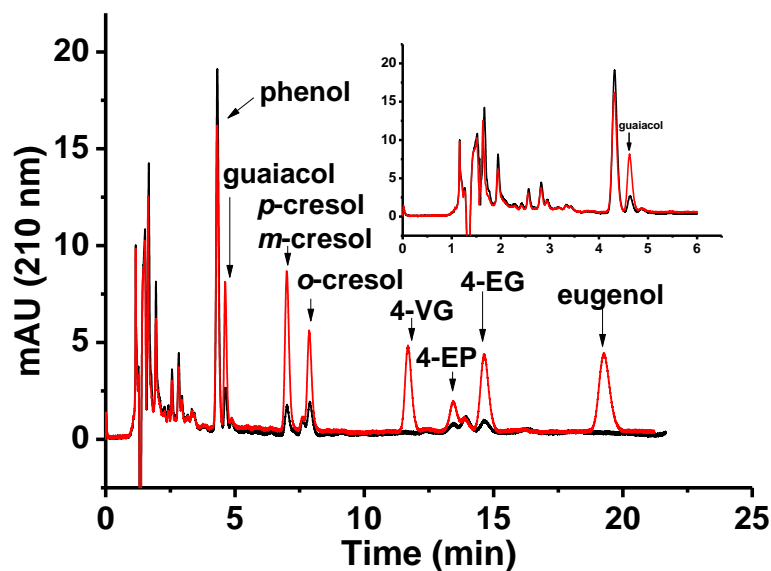


**Figure 2.25.** HPLC chromatograms of the 10-year-old blank Islay whiskey (black line) and spiked whiskey (red line) with 20  $\mu\text{M}$  of each standard. Column: Agilent Eclipse XDB  $\text{C}_{18}$  (4.6 x 150 mm, 5  $\mu\text{m}$ ), mobile phase: 30: 70 ACN:  $\text{H}_2\text{O}$  (v/v, %), flow rate: 1 mL/min, injection volume: 5  $\mu\text{L}$ , column temperature: 25  $^\circ\text{C}$ , UV detection: 210 nm.

Detection at 210 nm produced much greater signal responses than higher wavelengths (**Figure 2.26**).

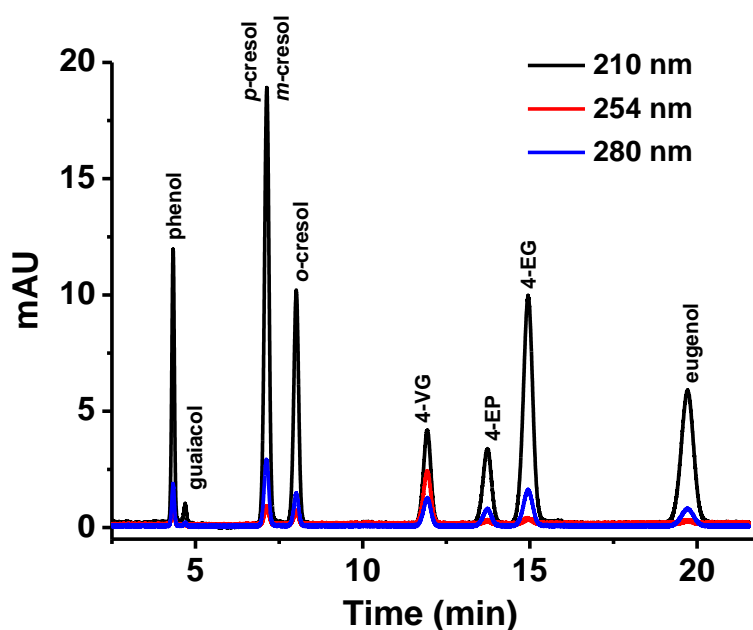


**Figure 2.26.** HPLC chromatograms of 40  $\mu\text{M}$  of each standard at different wavelengths (210, 254, and 280 nm). Column: Agilent Eclipse XDB  $\text{C}_{18}$  (4.6 x 150 mm, 5  $\mu\text{m}$ ), mobile phase: 30: 70 ACN:  $\text{H}_2\text{O}$  (v/v, %), flow rate: 1 mL/min, injection volume: 5  $\mu\text{L}$ , column temperature: 25  $^\circ\text{C}$ .



Biosensors have been reported for the detection of guaiacol in foods and beverages. They are based on the catalytic activity of redox enzymes, mainly tyrosinase<sup>27</sup>, peroxidase<sup>35</sup>, or laccase<sup>24</sup>. In general, the enzyme-based biosensors are not stable due to the leakage and stability of the immobilised enzymes during operation or storage. Other biosensors advocate the use of carbon nanotubes<sup>25</sup>, reduced graphene oxide<sup>26</sup>, and Pt- $\gamma$ -Al<sub>2</sub>O<sub>3</sub>/GCE<sup>23</sup>. Such sensors were only tested for various food samples, and in most cases, endogenous guaiacol was not found in these samples. The use of a complex system consisting of nanobiocomposites always raises a question about the reproducibility of fabrication, particularly for large-scale production.

## 2.4 Conclusions

Among a myriad of phenolics, guaiacol and its analogues are often present in smoky whiskey. The Nafion modified BDD electrode offers the profiling of guaiacol, 4-EG, and other phenols. This enzymeless approach circumvents several drawbacks associated with the use of enzymes and nanomaterials to fabricate biosensors. The inclusion complexes between  $\alpha$ -CD and the phenolics also play an important role to separate guaiacol from cresol isomers and other analogues. In particular, the simple electrochemical sensing together with peak deconvolution is appealing for spot analysis compared to lab-based gas chromatography-mass spectrometry (GC-MS), gas chromatography-flame ionisation detector (GC-FID), HPLC, and thin-layer chromatographic (TLC)-densitometric method. Besides their presence in beverages and foods, guaiacol, and its derivatives are abundant in nature as exemplified by their presence in the guaiac tree in significant amounts. The lignin from the tree is the largest renewable source for such aromatic compounds after oxidation. Consequently, the identification of such phenols and their oxidation products will be of importance for future applications.

## 2.5 References

1. Lehtonen, M. Phenols in whisky. *Chromatographia* **16**, 201–203 (1982).
2. Ng, C. M., Reuter, W. Analysis of phenols in whisky by HPLC with FL detection. *PerkinElmer.USA Appl. Note* (2015).
3. Nie, Y., Kleine-Benne, E. Determining phenolic compounds in whisky using direct large volume injection and stir bar sorptive extraction. *Gerstel Glob. Anal. Solut Gerstel GmbH Co. KG, Appl. Note* 1–12 (2012).
4. Arapitsas, P., Antonopoulos, A., Stefanou, E. & Dourtoglou, V. G. Artificial aging of wines using oak chips. *Food Chem.* **86**, 563–570 (2004).
5. Setzer, W. N. Volatile components of oak and cherry wood chips used in aging of beer, wine, and sprits. *Am. J. Essent. Oils Nat. Prod. AJEONP* **4**, 37–40 (2016).
6. Wiśniewska, P. *et al.* Authentication of whisky due to its botanical origin and way of production by instrumental analysis and multivariate classification methods. *Spectrochim. Acta - Part A Mol. Biomol. Spectrosc.* **173**, 849–853 (2017).
7. Chang, S. S. & Kang, D. H. *Alicyclobacillus* spp. in the fruit juice industry: history, characteristics, and current isolation/detection procedures. *Crit. Rev. Microbiol.* **30**, 55–74 (2004).
8. Valente, I. M., Santos, C. M., Moreira, M. M. & Rodrigues, J. A. New application of the QuEChERS methodology for the determination of volatile phenols in beverages by liquid chromatography. *J. Chromatogr. A* **1271**, 27–32 (2013).
9. Ellis, M. A., Grove, G. G. Leather rot in Ohio strawberries. *Plant Dis.* **67**, 549 (1998).
10. Szentirmay, M. N. & Martin, C. R. Ion-exchange selectivity of Nafion films on electrode surfaces. *Anal. Chem.* **56**, 1898–1902 (1984).
11. Saenger, W. *et al.* Structures of the common cyclodextrins and their larger analogues - beyond the doughnut. *Chem. Rev.* **98**, 1787–1802 (1998).

12. Enache, T. A. & Oliveira-Brett, A. M. Phenol and para-substituted phenols electrochemical oxidation pathways. *J. Electroanal. Chem.* **655**, 9–16 (2011).
13. Samet, Y., Abdelhedi, R., Savall, A. A study of the electrochemical oxidation of guaiacol. *Phys. Chem. News* **8**, 89–99 (2002).
14. Yildiz, G., Aydogmus, Z., Cinar, M. E., Senkal, F. & Ozturk, T. Electrochemical oxidation mechanism of eugenol on graphene modified carbon paste electrode and its analytical application to pharmaceutical analysis. *Talanta* **173**, 1–8 (2017).
15. Buzid, A., McGlacken, G. P., Glennon, J. D. & Luong, J. H. T. Electrochemical sensing of biotin using Nafion-modified boron-doped diamond electrode. *ACS Omega* **3**, 7776–7782 (2018).
16. Zhou, J. X., Wang, E. Ion exchange of cationic drugs at a Nafion-coated electrode in flow-through analysis. *Anal. Chim. Acta* **249**, 489–494 (1991).
17. Rezaei, B. & Mirahmadi Zare, S. Z. Modified glassy carbon electrode with multiwall carbon nanotubes as a voltammetric sensor for determination of nescapine in biological and pharmaceutical samples. *Sensors Actuators, B Chem.* **134**, 292–299 (2008).
18. Anson, F. C. Application of potentiostatic current integration to the study of the adsorption of cobalt(III)-(ethylenedinitrilo(tetraacetate) on mercury electrodes. *Anal. Chem.* **36**, 932–934 (1964).
19. Matsue, T., Fujihira, M. & Osa, T. Cyclic voltammetric determination of o-nitrophenol in the presence of p-nitrophenol by addition of  $\alpha$ -cyclodextrin. *Anal. Chem.* **53**, 722–723 (1981).
20. Fotouhi, L., Ganjavi, M. & Nematollahi, D. Electrochemical study of iodide in the presence of phenol and o-cresol: Application to the catalytic determination of phenol and o-cresol. *Sensors* **4**, 170–180 (2004).
21. Tsai, Y. C. & Chiu, C. C. Amperometric biosensors based on multiwalled carbon nanotube-Nafion-tyrosinase nanobiocomposites for the determination of phenolic compounds. *Sensors Actuators, B Chem.* **125**, 10–16 (2007).

22. Zhao, G. H., Tang, Y. T., Liu, M. C., Lei, Y. Z. & Xiao, X. E. Direct and simultaneous determination of phenol, hydroquinone and nitrophenol at boron-doped diamond film electrode. *Chinese J. Chem.* **25**, 1445–1450 (2007).
23. Sun, J. Y., Gan, T., Deng, Y. P., Shi, Z. X. & Lv, Z. Pt nanoparticles-functionalized hierarchically porous  $\gamma$ -Al<sub>2</sub>O<sub>3</sub> hollow spheres based electrochemical sensor for ultrasensitive guaiacol detection. *Sensors Actuators, B Chem.* **211**, 339–345 (2015).
24. Freire, R. S., Duran, N., Wang, J. & Kubota, L. T. Laccase-based screen printed electrode for amperometric detection of phenolic compounds. *Anal. Lett.* **35**, 29–38 (2002).
25. Korkut, S., Keskinler, B. & Erhan, E. An amperometric biosensor based on multiwalled carbon nanotube-poly(pyrrole)-horseradish peroxidase nanobiocomposite film for determination of phenol derivatives. *Talanta* **76**, 1147–1152 (2008).
26. Yan, W., Meng, H., NanNan, S. & WeiBing, H. Electrochemical detection of guaiacol in bamboo juice based on the enhancement effect of RGO nanosheets. *Anal. Methods* **6**, 2729–2735 (2014).
27. Adamski, J., Nowak, P. & Kochana, J. Simple sensor for the determination of phenol and its derivatives in water based on enzyme tyrosinase. *Electrochim. Acta* **55**, 2363–2367 (2010).
28. Fang, Y. & Ramasamy, R. P. Detection of p-ethylphenol, a major plant volatile organic compound, by tyrosinase-based electrochemical biosensor. *ECS J. Solid State Sci. Technol.* **5**, M3054–M3059 (2016).
29. Fang, Y., Umasankar, Y. & Ramasamy, R. P. Electrochemical detection of p-ethylguaiacol, a fungi infected fruit volatile using metal oxide nanoparticles. *Analyst* **139**, 3804–3810 (2014).
30. Osa, T, Matsue, T, Fujihira, M. Cyclodextrin-nitrophenol systems studied by polarography. *Heterocycles* **6**, 1833–1839 (1977).
31. Upadhyay, S. K. & Ali, S. M. Molecular recognition of flunarizine

- dihydrochloride and  $\beta$ -cyclodextrin inclusion complex by NMR and computational approaches. *Chem. Cent. J.* **12**, 1–9 (2018).
32. Lorenc-Grabowska, E. Effect of micropore size distribution on phenol adsorption on steam activated carbons. *Adsorption* **22**, 599–607 (2016).
33. Chemical bonding. Available at:  
[http://centros.edu.xunta.es/iesames/webantiga/webfq/EUSECTSUSO/chem\\_phys\\_bac/Chemistry\\_2/chemical\\_bonding.htm](http://centros.edu.xunta.es/iesames/webantiga/webfq/EUSECTSUSO/chem_phys_bac/Chemistry_2/chemical_bonding.htm).
34. Rice, M. E., Galus, Z., Adams, R. N. Graphite paste electrodes: Effects of paste composition and surface states on electron-transfer rates. *J. Electroanal. Chem. Interfacial Electrochem.* **143**, 89–102 (1983).
35. Doerge, D. R., Divi, R. L. & Churchwell, M. I. Identification of the colored guaiacol oxidation product produced by peroxidases. *Anal. Biochem.* **250**, 10–17 (1997).

## **Chapter 3**

### **Profiling of phenolic flavourings using core-shell reversed-phase liquid chromatography with electrochemical detection at a boron-doped diamond electrode**

### 3.1 Introduction

In the European Union, approximately 10000 tons of liquid smoke flavourings (mainly comprising of phenolic and carbonyl compounds) are consumed annually<sup>1</sup>. Differences in the chemical composition attained through the manufacturing process, are the result of variations in the process conditions including the wood type, wood moisture content, oxygen concentration, and temperature during the generation of smoke<sup>1-3</sup>. Several phenolic compounds, in particular guaiacol, are major contributors to the smoky flavour. Phenol and its derivatives are mostly related to lignin degradation. Initial degradation occurs by fission of heterocyclic pyran, furan ring and ether linkage of lignin, resulting in guaiacol production, which in turn degrades further to form cresols and phenol<sup>4</sup>. The essential flavouring phenolic compounds in whiskey are cresols, phenols, guaiacols, and xlenol<sup>5</sup>. The analysis of phenolic compounds is accomplished using gas chromatography (GC) and high-performance liquid chromatography (HPLC). Sample preparation techniques such as solid-phase microextraction (SPME)<sup>6</sup> and stir-bar sorbent extraction (SBSE)<sup>7-9</sup> are carried out for flavour profiling in whiskey. It is well known that Scottish distillers use peat fires to dry the barley during the malting process. Here, the barley adsorbs the phenolic compounds from the peat smoke contributing to the distinct phenolic flavour of whiskey<sup>10,11</sup>. Ten phenolics in three Scottish whiskeys were observed using HPLC coupled to a fluorescence detector (FL), and their level in the whiskey ranged from 0.17  $\mu\text{M}$  (phenol) to 1.97  $\mu\text{M}$  (eugenol)<sup>12</sup>.

HPLC coupled to electrochemical detection (ECD) offers superior selectivity and sensitivity over ultraviolet (UV) detection for phenolic compounds, with the additional advantages of reduced cost and portability compared to mass spectrometry (MS) detection. Of interest is the use of HPLC-ECD based on a glassy carbon electrode (GCE) for the separation/detection of phenolic compounds in honey samples<sup>13-15</sup>, refinery effluents<sup>16</sup>, sugarcane vinasse<sup>17</sup>, waste and river water<sup>18</sup>, beverages<sup>19</sup>, microbial metabolites<sup>20</sup>, wastewaters and effluent from pesticide-plant<sup>21</sup>, and seawater and marine sediments<sup>22</sup>. HPLC-ECD for phenolic compounds has also been reported using a boron-doped diamond (BDD) electrode<sup>23</sup> and a carbon-black/polyethylene tubular anode<sup>24</sup>.

A BDD electrode exhibits many advantages including a wide potential window, low background current over a wide potential range, and high resistance to fouling<sup>25,26</sup>. The initial application of a BDD electrode together with HPLC was introduced for the analysis of sulfa drugs<sup>27</sup>. The BDD electrode offered similar detection levels compared to a GCE; however, stable background currents were achieved faster with enhanced electrode stability. HPLC-BDD has been extended for the analysis of a wide range of analytes including bioamines, amino acids and their metabolites in rat plasma, cortex and hippocampus<sup>28,29</sup>, parabens in shampoo<sup>30</sup>, benzodiazepines in pharmaceutical preparations<sup>31</sup> and  $\alpha$ -lipoic acid in dietary supplements<sup>32</sup>. Muna *et al.* applied HPLC coupled to boron-doped microcrystalline and nanocrystalline diamond electrodes for the detection of phenol and chlorinated phenols in soil samples<sup>33</sup>. The determination of chlorophenols in water samples was investigated using HPLC combined with anodically pre-treated BDD thin-film electrodes with LODs of 0.18-1.8 nM<sup>23</sup>.

This study extended our previous work on the direct electrochemical sensing of flavourings in whiskey using a BDD electrode<sup>34</sup>. To our knowledge, this is the first reported method for the analysis of important phenolic compounds in whiskey samples that combines the superior separation power of core-shell particles coupled with the sensitivity of the ECD at the BDD electrode. The optimisation of HPLC separation conditions and ECD oxidation potentials was conducted before the quantitation of the nine phenolic compounds in whiskey samples of different geographical origins.



## 3.2 Experimental

### 3.2.1 Reagents, standard solutions and samples

Ammonium formate, ammonium acetate, formic acid, acetic acid, ethanol (EtOH), acetonitrile (ACN), guaiacol, 4-ethylguaiacol (4-EG), eugenol, phenol, 4-ethylphenol (4-EP), 4-vinylguaiacol (4-VG), *p*-cresol, *o*-cresol and *m*-cresol were purchased from Sigma-Aldrich (Dublin, Ireland). Chemical structures are available in **Table 3.1**. Stock solutions (1 mM) of phenols, guaiacols and cresol isomers were prepared in EtOH daily before use. Working solutions were prepared by dilution of stock solutions with the mobile phase. All reagents used were of the analytical grade of the highest purity. Aqueous solutions were prepared in deionised water (Millipore, Ireland). Islay, Irish, Scotch and Highland whiskeys were obtained from a local store in Co. Cork, Ireland. Whiskey samples were prepared by adding 500  $\mu$ L of whiskey to 1000  $\mu$ L of the mobile phase and were filtered through an Econofiltr Nylon membrane (13 mm, 0.2  $\mu$ m) before analysis.

### 3.2.2 Cyclic voltammetry

Cyclic voltammetry (CV) was used to evaluate the electrochemical behaviour of guaiacol, 4-EG, phenol and *o*-cresol using a CHI1040A electrochemical workstation (CH Instrument, Austin, TX). The electrochemical cell consists of the BDD electrode (B/C ratio in the gaseous phase of 1000 ppm, 3 mm diameter, Windsor Scientific, Slough Berkshire, UK), a silver/silver chloride (Ag/AgCl /3 M KCl) reference electrode (BASi Analytical Instruments, West Layette, IN) and a Pt wire counter electrode (Sigma-Aldrich, Dublin, Ireland). The supporting electrolyte was phosphate buffer (100 mM, pH 2) containing 5 % of EtOH. Stock solution (1 mM) of guaiacol, 4-EG, phenol, and *o*-cresol were prepared in 100 mM phosphate buffer, pH 7.

### 3.2.3 Apparatus

The HPLC-UV and HPLC-ECD analyses were performed on an Agilent HPLC system (Agilent 1200 LC series) equipped with a binary pump (model G1312B), degasser (model G1379B), autosampler (model G1367D) and a UV diode array detector (model G1315C). Agilent Chemstation was used for instrument control and UV data analysis.

Chromatographic separation was performed using a HALO C<sub>18</sub> core-shell column (3.0 x 50 mm, 2.7 µm particle size, Apex Scientific, Co. Kildare, Ireland). ECD was carried out using an Antec Flexcell thin layer flow cell with a cell volume of 0.7 µL (Apex Scientific, Co. Kildare, Ireland). The flow cell consists of a three-electrode configuration with a boron-doped diamond (BDD) working electrode (8 mm diameter), a HyREF (Pd/H<sub>2</sub>) reference electrode and carbon loaded polytetrafluoroethylene (PTFE) counter electrode. CHI660E electrochemical workstation was used for data analysis (CH Instrument, Austin, Texas).

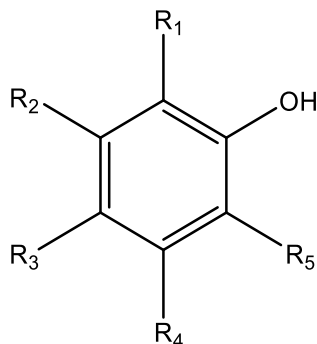
### **3.2.4 Chromatographic conditions**

The compounds were separated in isocratic mode with a mobile phase consisting of 10 mM formate, pH 3, and 15 % ACN (v/v). The mobile phase was filtered through a 0.45 µm Nylon Whatman filter (Sigma-Aldrich, Dublin, Ireland) and sonicated before use. The column was equilibrated with mobile phase for 20 min before injection. Total run time was 9 min. The flow rate was 1.5 mL/min with an injection volume of 5 µL. The column temperature was set at 25 °C. HPLC-UV detection was determined at 210 nm. HPLC-ECD was carried out independently at 1.5 V in oxidative mode.

### **3.2.5 Method validation**

The limits of detection (LODs) were determined based on a signal-to-noise ratio of 3 (S/N=3). Linearity was evaluated by linear regression with respect to the concentrations and chromatographic peak areas of each standard. The repeatability of the method was assessed by three repetitive measurements of a mixed standard solution (20 µM of each standard) within one day (intra-day) and over three days (inter-day). Precision was expressed as the relative standard deviation (RSD %).

**Table 3.1.** Chemical structures of the phenols, guaiacols and cresol isomers.



Analyte	R <sub>1</sub>	R <sub>2</sub>	R <sub>3</sub>	R <sub>4</sub>	R <sub>5</sub>
phenol	H	H	H	H	H
4-EP	H	H	CH <sub>2</sub> CH <sub>3</sub>	H	H
<i>o</i> -cresol	H	H	H	H	CH <sub>3</sub>
<i>m</i> -cresol	H	H	H	CH <sub>3</sub>	H
<i>p</i> -cresol	H	H	CH <sub>3</sub>	H	H
guaiacol	OCH <sub>3</sub>	H	H	H	H
4-EG	OCH <sub>3</sub>	H	CH <sub>2</sub> CH <sub>3</sub>	H	H
4-VG	OCH <sub>3</sub>	H	CH=CH <sub>2</sub>	H	H
eugenol	OCH <sub>3</sub>	H	CH <sub>2</sub> CH=CH <sub>2</sub>	H	H

### 3.3 Results and discussion

#### 3.3.1 Electrochemical behaviour of guaiacol, 4-EG, phenol and *o*-cresol

The electrochemical behaviour of guaiacol, 4-EG, phenol and *o*-cresol on a bare BDD electrode were investigated using CV (**Figure 3.1**). As previously discussed, guaiacol initially undergoes a one-electron transfer producing three phenoxy radicals which then undergo a second electron transfer to produce their corresponding carbocations. The electron-donating effect of the methoxy group stabilises carbocation C<sub>1</sub> making it the predominant form, which is then hydrolysed to form methanol and *o*-benzoquinone (**Scheme 3.1A**). The CV of guaiacol illustrates one broad irreversible oxidation peak at + 0.9 V (*o*-benzoquinone), with the formation of methanol indicated by a small oxidation peak at + 1.4 V. In the reverse scan, three reduction peaks are observed; catechol at + 0.7 V, methoxyquinone at + 0.5 V and methoxy benzoquinone at + 0.15

V<sup>34,35</sup> (**Figure 3.1A**). The CV of 4-EG displayed one broad irreversible oxidation peak (+0.8 V) and two reduction peaks (+0.6 V, -0.1 V) which may be due to the formation of catechol and 4-ethyl-3-methoxy-phenol, respectively<sup>34</sup> (**Figure 3.1B**). Phenol undergoes a one electron and one proton oxidation step to produce three unstable phenoxy radicals. The major products are *o*-quinone and *p*-quinone (+1.2 V) which are reversibly reduced to catechol and hydroquinone (-0.1 V), respectively in a two-electron and two proton mechanism<sup>36,37</sup> (**Figure 3.1C**). The CV of *o*-cresol (**Figure 3.1D**) indicates a sharp irreversible oxidation peak at +1.1 V with three small reduction peaks evident at +0.8 V, +0.5 V and -0.15 V (**Scheme 3.1B**).

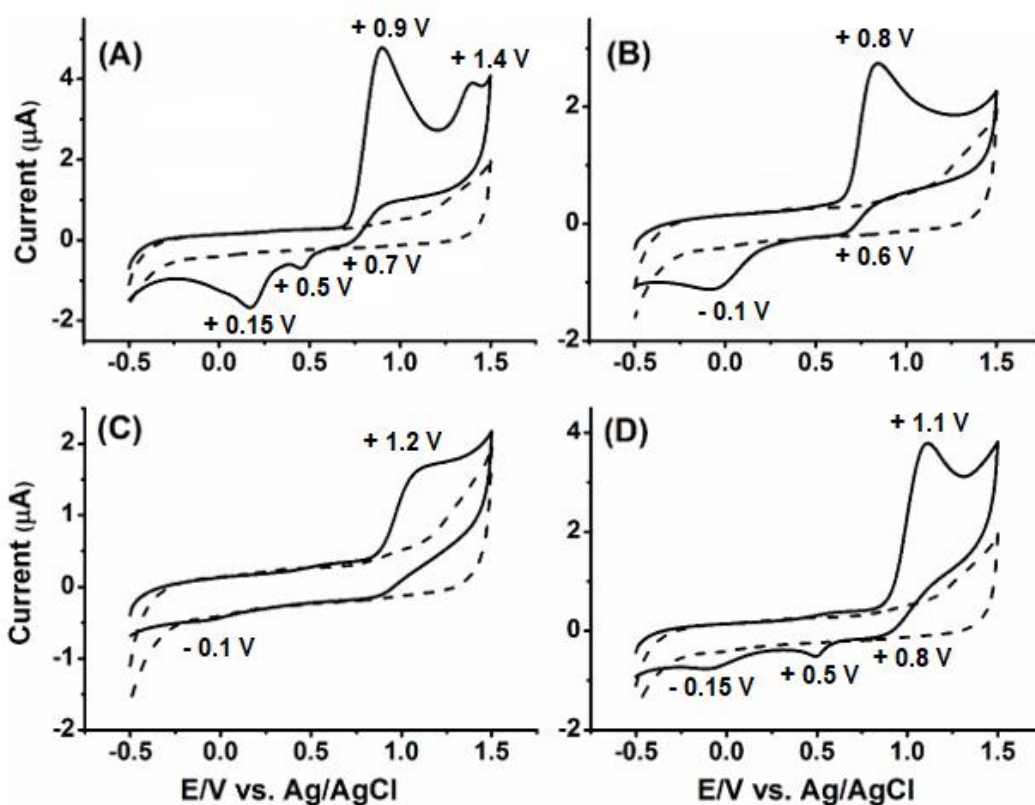
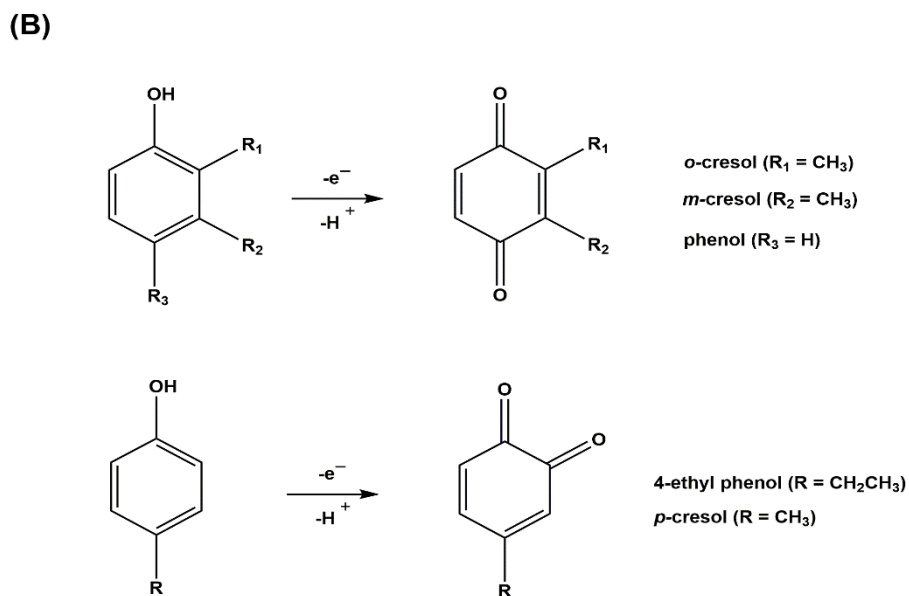
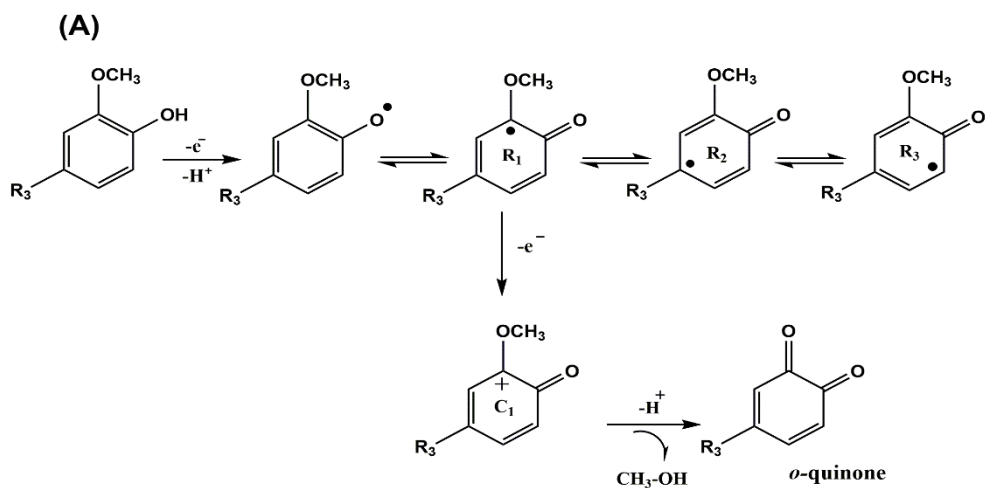


**Figure 3.1.** CV response in the absence (dashed lines) and presence (solid lines) of 100  $\mu\text{M}$  each for (A) guaiacol; (B) 4-EG; (C) phenol; and (D) *o*-cresol on the bare BDD electrode vs. Ag/AgCl in 100 mM phosphate buffer, 5 % EtOH, pH 2, with a scan rate of 50  $\text{mV s}^{-1}$ .



**Scheme 3.1.** Electrochemical oxidation of (A) guaiacol and its derivatives and (B) phenols and cresol isomers.

### 3.3.2 Optimisation of HPLC separation conditions

The phenols, guaiacols, and cresols were separated using a HALO C<sub>18</sub> core-shell column and initially optimised with UV detection at 210 nm under isocratic conditions. The mobile phase composition was investigated using different volumes of ACN: 10 mM formate (pH 3) at a flow rate of 1 mL/min (**Figure 3.2**). As the percentage of ACN in the mobile phase increased, shorter elution times (**Figure 3.3**) and sharper peaks were observed. However, with this increase, the resolution between the peaks reduced, and this was particularly evident when analysing the whiskey sample at 20: 80, ACN: 10 mM formate when guaiacol partially co-eluted with a constituent of the whiskey sample. To overcome this problem, 15: 85, ACN: 10 mM formate was selected as the optimum mobile phase composition. Of notice is the co-elution of *p*- and *m*-cresol.

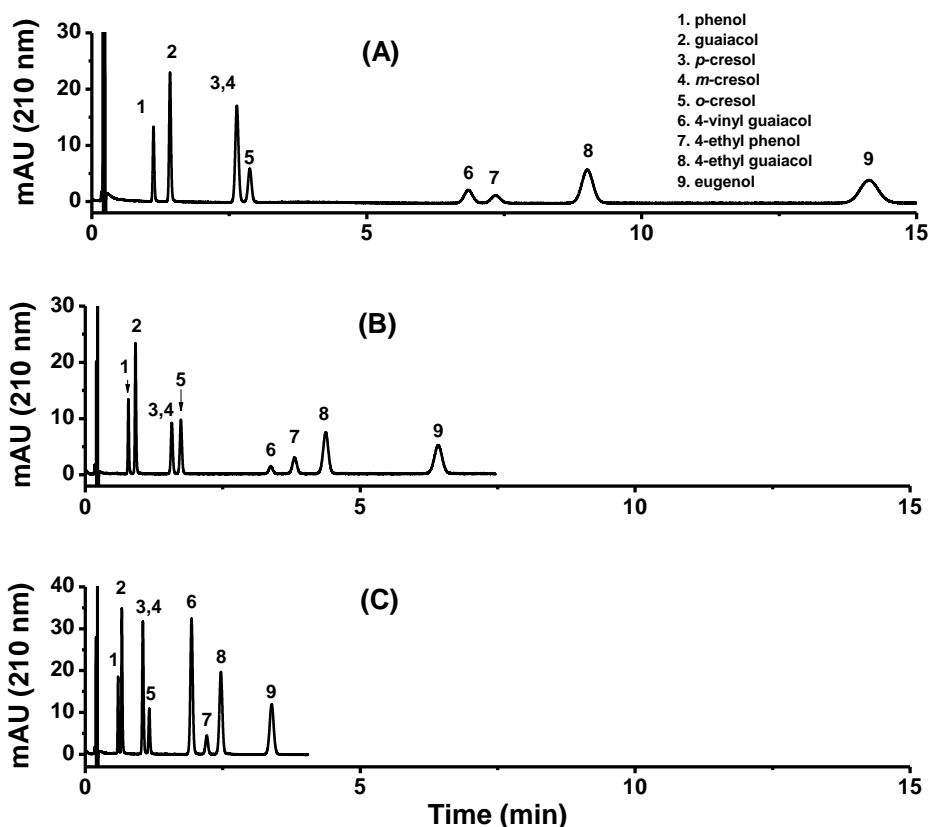


**Figure 3.2.** The effect of mobile phase %ACN on the retention time of 20  $\mu$ M each of phenol, guaiacol, *m*-cresol, *p*-cresol, *o*-cresol, 4-VG, 4-EP, 4-EG, and eugenol. Mobile phase: ACN:10 mM formate pH 3 (A) 15:85, (B) 20:80 and (C) 25:75. Column: HALO C<sub>18</sub> core-shell (3 x 50 mm, 2.7  $\mu$ m), flow rate: 1 mL/min, injection volume: 5  $\mu$ L, column temperature: 25  $^{\circ}$ C, UV detection: 210 nm.

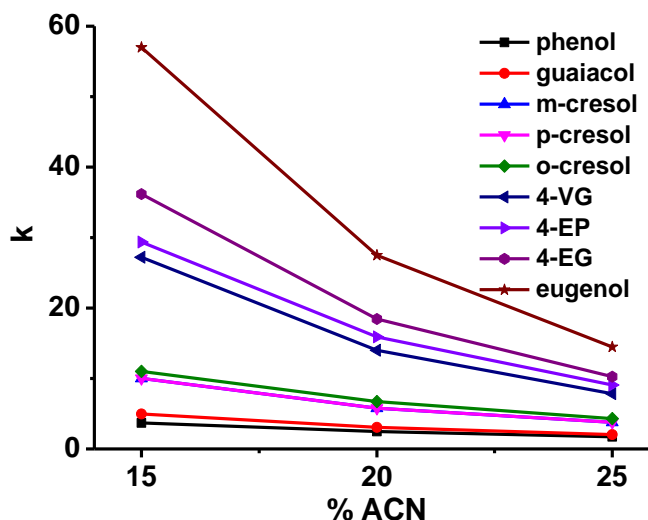


**Figure 3.3.** Plot of  $k$  versus % ACN. Mobile phase: ACN:10 mM formate pH 3 (15:85), (20:80) and (25:75). Column: HALO  $C_{18}$  core-shell (3 x 50 mm, 2.7  $\mu$ m), flow rate: 1 mL/min, injection volume: 5  $\mu$ L, column temperature: 25  $^{\circ}$ C, UV detection: 210 nm.

All of the phenolic flavourings have a high pKa value ( $\sim 10$ ) and their retention times were similar at pH 3 or pH 5. However, the peak intensities at pH 5 were reduced in comparison to pH 3 due to higher UV interference. Therefore, pH 3 was applied for subsequent experiments (**Figure 3.4**). The flow rate of the mobile phase was varied from 1.0 mL/min to 1.5 mL/min to enable the separation in under 9 min at a backpressure of 390 bar (**Figure 3.5**).

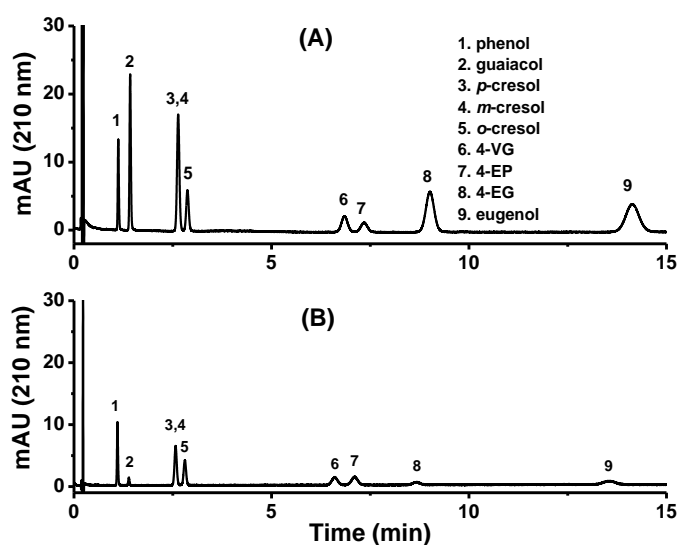


**Figure 3.4.** The effect of the mobile phase pH on the retention time of 20  $\mu$ M each of phenol, guaiacol, m-cresol, p-cresol, o-cresol, 4-VG, 4-EP, 4-EG and eugenol. Mobile phase: 15:85, (A) ACN:10 mM formate pH 3 and (B) ACN: 10 mM acetate pH 5. Column: HALO  $C_{18}$  core-shell (3 x 50 mm, 2.7  $\mu$ m), flow rate: 1 mL/min, injection volume: 5  $\mu$ L, column temperature: 25  $^{\circ}$ C, UV detection: 210 nm.

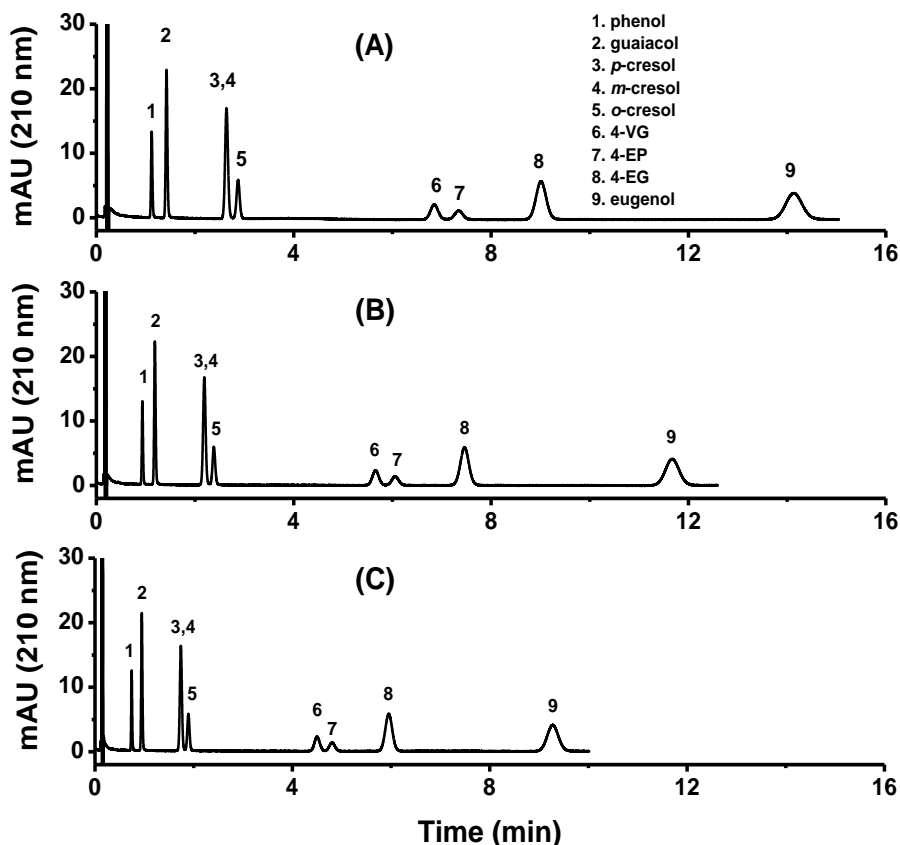


**Figure 3.5.** The effect of the mobile phase flow rate on the retention time of 20  $\mu$ M each of phenol, guaiacol, *m*-cresol, *p*-cresol, *o*-cresol, 4-VG, 4-EP, 4-EG and eugenol. Mobile phase: 15:85, ACN:10 mM formate pH 3. Column: HALO C<sub>18</sub> core-shell (3 x 50 mm, 2.7  $\mu$ m), flow rate: (A) 1 mL/min, (B) 1.2 mL/min and (C) 1.5 mL/min, injection volume: 5  $\mu$ L, column temperature: 25  $^{\circ}$ C, UV detection: 210 nm.

### 3.3.3 Selection of detection potential

The oxidation potential was investigated in the range of + 1.2 to + 1.8 V to provide the highest detection sensitivity of the analytes. The hydrodynamic voltammograms of analytes under the above separation conditions are shown in **Figure 3.6**. Guaiacols were slightly more oxidised at + 1.2 V, whereas 4-EP and the cresol isomers produced maximum currents at potentials of + 1.5 V. At + 1.8 V, phenol became slightly more oxidised, (**Figure 3.7**). However, due to the significant increase in background current at this potential, an oxidation potential of + 1.5 V was chosen for subsequent experiments.



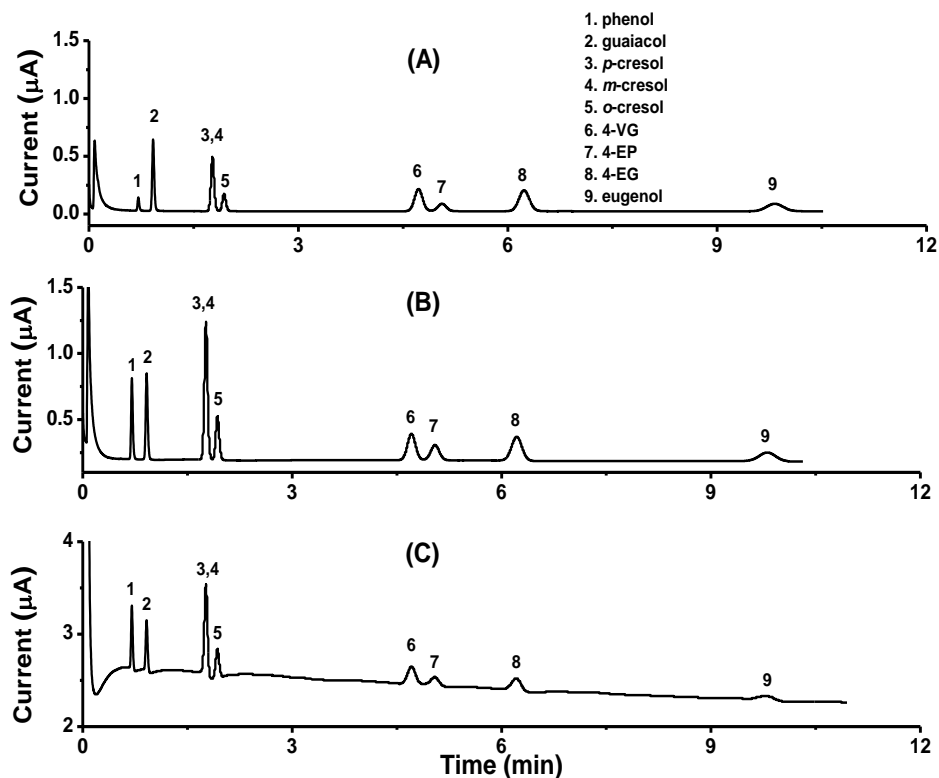


**Figure 3.6.** The effect of oxidation potential on the detection of 20  $\mu\text{M}$  each of phenol, guaiacol, *m*-cresol, *p*-cresol, *o*-cresol, 4-VG, 4-EP, 4-EG and eugenol. Oxidation potential: (A) + 1.2 V, (B) + 1.5 V, and (C) + 1.8 V on the BDD electrode vs. Pd/H<sub>2</sub>. Mobile phase: 15:85, ACN:10 mM formate pH 3. Column: HALO C<sub>18</sub> core-shell (3 x 50 mm, 2.7  $\mu\text{m}$ ), flow rate: 1.5 mL/min, injection volume: 5  $\mu\text{L}$ .

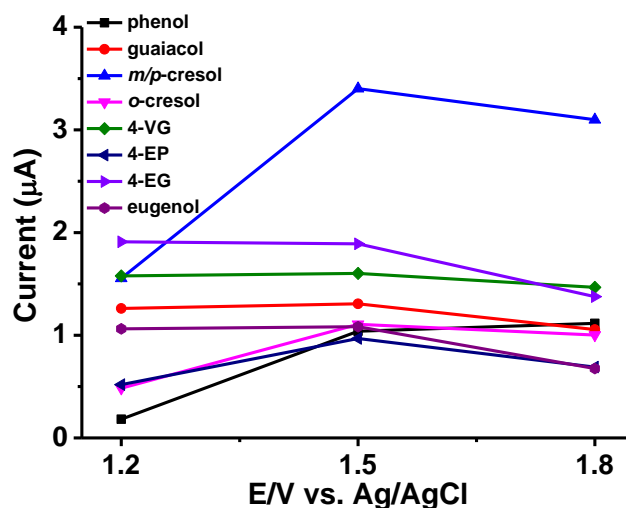


**Figure 3.7.** The effect of oxidation potential on the detection of 20  $\mu\text{M}$  each of phenol, guaiacol, *m*-cresol, *p*-cresol, *o*-cresol, 4-VG, 4-EP, 4-EG and eugenol at the BDD electrode vs. Pd/H<sub>2</sub>. Mobile phase: 15:85, ACN:10 mM formate pH 3. Column: HALO C<sub>18</sub> core-shell (3 x 50 mm, 2.7  $\mu\text{m}$ ), flow rate: 1.5 mL/min, injection volume: 5  $\mu\text{L}$ .

Typical chromatograms of a mixed standard solution containing the nine analytes analysed by both HPLC-ECD and HPLC-UV under optimum conditions are shown in **Figure 3.8**.

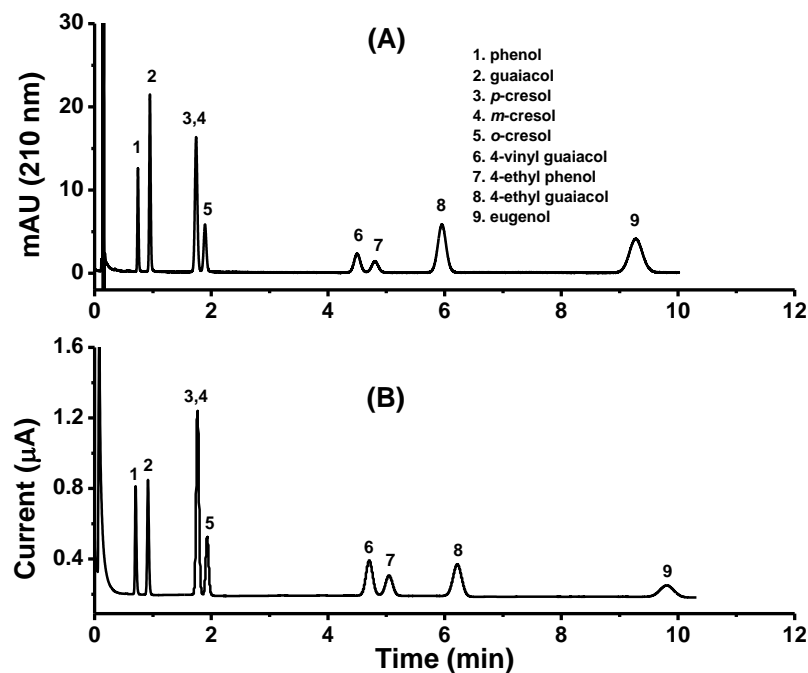


**Figure 3.8.** Representative chromatograms of a mixed standard solution containing the nine compounds (20  $\mu$ M each) analysed by (A) HPLC-UV at 210 nm and (B) HPLC-ECD at + 1.5 V. Mobile phase: 15:85, ACN:10 mM formate pH 3. Column: HALO  $C_{18}$  core-shell (3 x 50 mm, 2.7  $\mu$ m), flow rate: 1.5 mL/min, injection volume: 5  $\mu$ L.

### 3.3.4 Analytical performance

The detection methods were validated for guaiacols, cresol isomers, and phenolics in terms of linearity of the calibration curves, LODs and precision. The LODs for the nine analytes were in the range of 10 nM - 1  $\mu$ M for ECD. The LODs of analytes detected by ECD were significantly lower than those obtained by UV, indicating the high electrochemical and low UV response of the analytes (**Table 3.2**). The LODs for all analytes were considerably lower than those obtained with large volume injection (LVI)-GC-MS, whilst the LODs of phenol and *m*-cresol were lower than those achieved with SBSE-thermal desorption (TD)-GC-MS<sup>7</sup>. The response linearity of the nine analytes was evaluated by triplicated injection of the standard solution corresponding to each concentration. The calibration curves were established based on the corresponding relationship between the concentration and peak areas of the

analytes. The concentration range selected was based on the anticipated concentrations of the analytes in samples. The linearity of calibration curves correlation coefficient and precision data for ECD and UV detection are presented in **Table 3.3** and **Table 3.4**, respectively. The regression coefficient ( $R^2$ ) for all analytes was higher than 0.998 for ECD and 0.993 for UV detection. Intra-day and inter-day precision were in the range of 0.11-1.16 % and 1.53 - 2.89 %, respectively, for ECD. Intra-day precision in the range of 0.05-0.11 % and inter-day precision in the range of 0.54 - 1.09 % was obtained for UV detection, confirming the applicability of these methods for the analysis of phenols, cresol isomers, and guaiacols.

**Table 3.2.** A comparison of LODs obtained with ECD and UV detection.

<b>Analyte</b>	<b>LOD<sup>a</sup> HPLC-ECD</b>	<b>LOD<sup>b</sup> HPLC-UV</b>
<b>phenol</b>	25 nM	0.5 µM
<b>guaiacol</b>	25 nM	2 µM
<b><i>o</i>-cresol</b>	100 nM	5 µM
<b><i>m</i>-cresol</b>	10 nM	2 µM
<b><i>p</i>-cresol</b>	50 nM	5 µM
<b>4-VG</b>	250 nM	1.5 µM
<b>4-EP</b>	250 nM	10 µM
<b>4-EG</b>	500 nM	5 µM
<b>eugenol</b>	1 µM	5 µM

<sup>a</sup>LOD ( $S/N = 3$ ) at + 1.5 V.

<sup>b</sup>LOD ( $S/N = 3$ ) at 210 nm.

**Table 3.3.** Linear regression parameters of calibration curves and precision data for the phenolic compounds detected with HPLC-ECD at + 1.5 V.

Analyte	Linear range (μM)	Linear regression equation	Correlation coefficient ( $R^2$ )	Intra-day (%) <sup>a</sup>	Inter-day (%) <sup>b</sup>
<b>phenol</b>	1-20	$I = 1.09 \times 10^{-7} C - 8.33 \times 10^{-9}$	0.998	1.16	1.86
<b>guaiacol</b>	1-20	$I = 7.17 \times 10^{-8} C - 6.90 \times 10^{-9}$	0.999	1.06	1.53
<b><i>o</i>-cresol</b>	5-25	$I = 5.53 \times 10^{-8} C + 1.30 \times 10^{-8}$	0.998	0.56	1.78
<b><i>m</i>-cresol</b>	5-25	$I = 1.24 \times 10^{-7} C + 3.15 \times 10^{-8}$	0.999	0.61	1.87
<b><i>p</i>-cresol</b>	5-25	$I = 6.35 \times 10^{-8} C - 1.53 \times 10^{-8}$	0.999	0.61	1.87
<b>4-VG</b>	1-20	$I = 1.38 \times 10^{-7} C - 7.04 \times 10^{-8}$	0.999	0.23	1.64
<b>4-EP</b>	10-30	$I = 6.43 \times 10^{-8} C - 1.31 \times 10^{-8}$	0.998	0.21	2.89
<b>4-EG</b>	10-30	$I = 7.02 \times 10^{-8} C - 4.72 \times 10^{-8}$	0.999	0.17	2.82
<b>eugenol</b>	10-30	$I = 5.50 \times 10^{-8} C - 4.42 \times 10^{-8}$	0.998	0.11	2.30

<sup>a</sup> Intra-day (%) calculated from three measurements within one experiment for the retention time at 20 μM of each standard.

<sup>b</sup> Inter-day (%) calculated from three measurements within three different experiments for the retention time at 20 μM of each standard.

**Table 3.4.** Linear regression parameters of calibration curves and precision data for the phenolic compounds detected with HPLC-UV at 210 nm.

Analyte	Linear range (μM)	Linear regression equation	Correlation coefficient ( $R^2$ )	Intra-day (%) <sup>a</sup>	Inter-day (%) <sup>b</sup>
<b>phenol</b>	5-25	$y = 0.823 C + 0.076$	0.999	0.08	0.71
<b>guaiacol</b>	5-25	$y = 1.008 C - 0.001$	0.997	0.11	0.54
<b><i>o</i>-cresol</b>	20-100	$y = 0.813 C - 2.321$	0.999	0.05	0.72
<b><i>m</i>-cresol</b>	20-100	$y = 2.068 C - 2.712$	0.999	0.07	0.80
<b><i>p</i>-cresol</b>	5-25	$y = 2.391 C - 1.960$	0.999	0.07	0.80
<b>4-VG</b>	10-50	$y = 2.219 C + 0.426$	0.993	0.12	1.09
<b>4-EP</b>	20-100	$y = 0.547 C - 0.608$	0.999	0.06	1.01
<b>4-EG</b>	10-30	$y = 1.868 C - 1.862$	0.996	0.07	1.09
<b>eugenol</b>	20-100	$y = 4.021 C - 8.484$	0.999	0.09	0.87

<sup>a</sup> Intra-day (%) calculated from three measurements within one experiment for the retention time at 20 μM of each standard.

<sup>b</sup> Inter-day (%) calculated from three measurements within three different experiments for the retention time at 20 μM of each standard.

Calibration curves and plots for HPLC-ECD are illustrated in **Figure 3.9**, **Figure 3.10** and **Figure 3.11**.

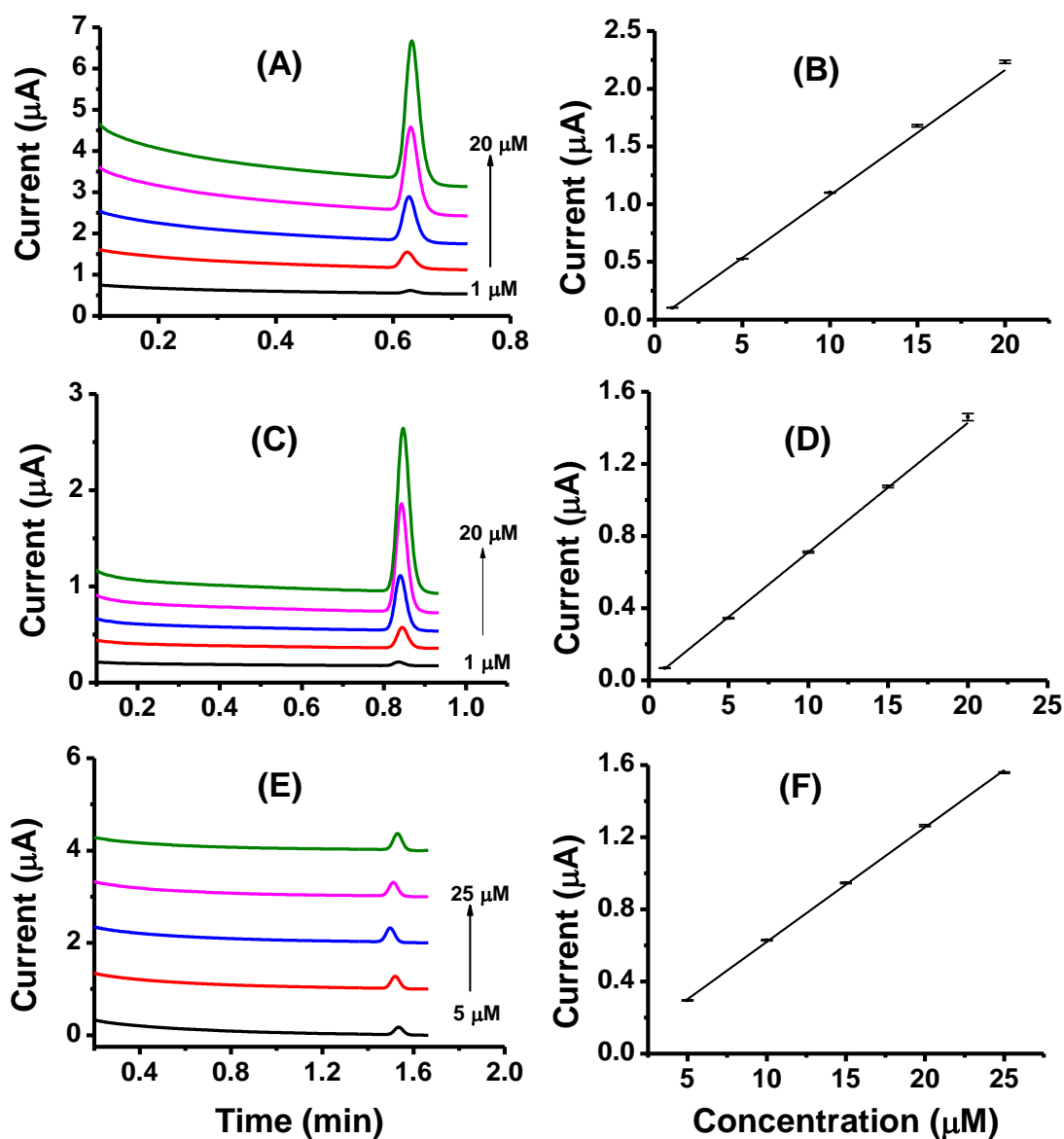


**Figure 3.9.** (A) Calibration curve and (B) plot of phenol; (C) calibration curve and (D) plot of guaiacol; (E) calibration curve and (F) plot of p-cresol. Mobile phase: 15:85, ACN:10 mM formate pH 3. Column: HALO  $C_{18}$  core-shell (3 x 50 mm, 2.7  $\mu$ m), flow rate: 1.5 mL/min, injection volume: 5  $\mu$ L, oxidation potential: + 1.5 V on the BDD electrode vs. Pd/H<sub>2</sub>.

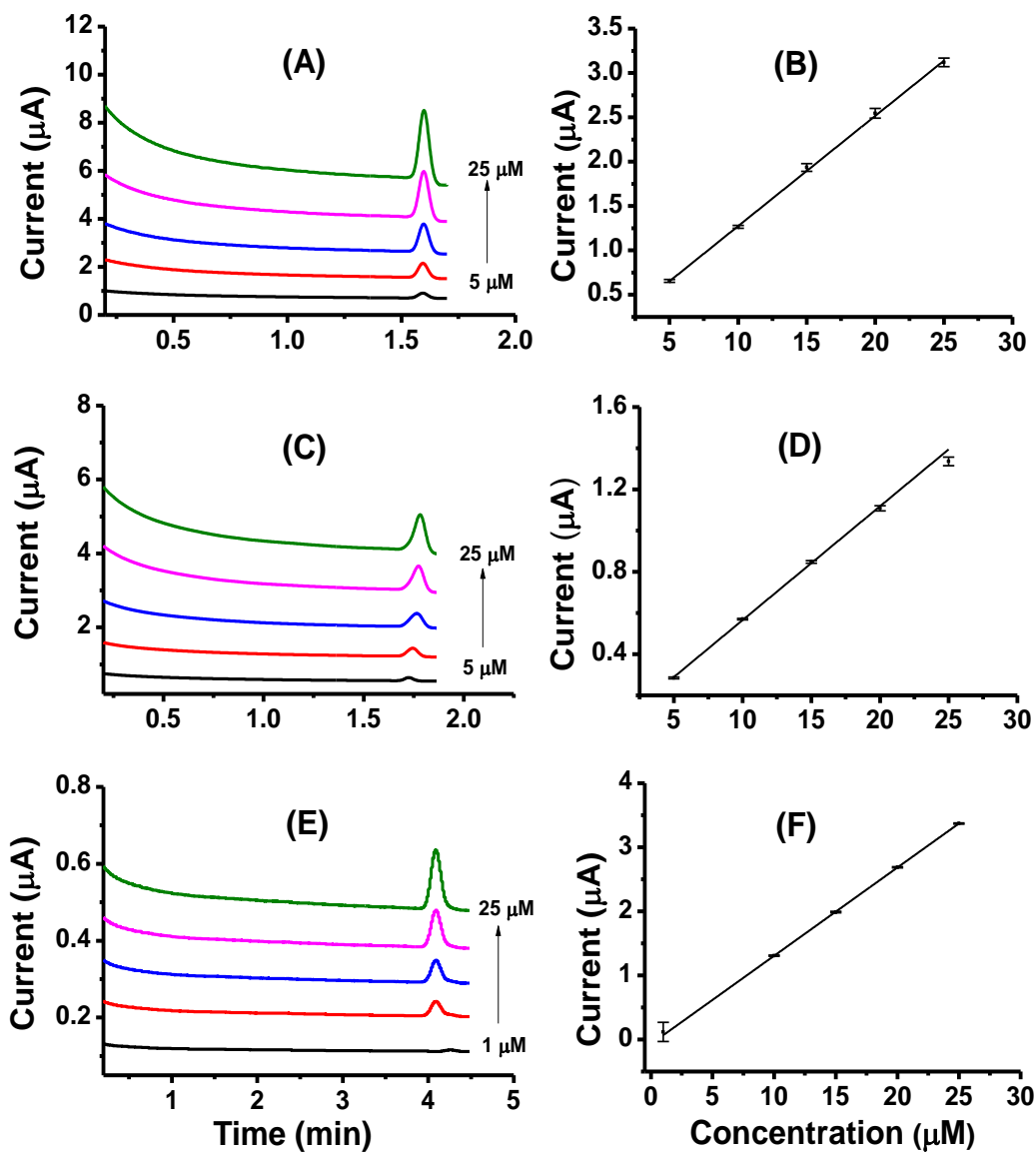


**Figure 3.10.** (A) Calibration curve and (B) plot of *m*-cresol; (C) calibration curve and (D) plot of *o*-cresol; (E) calibration curve and (F) plot of 4-VG. Mobile phase: 15:85, ACN:10 mM formate pH 3. Column: HALO  $C_{18}$  core-shell (3 x 50 mm, 2.7  $\mu$ m), flow rate: 1.5 mL/min, injection volume: 5  $\mu$ L, oxidation potential: + 1.5 V on the BDD electrode vs. Pd/H<sub>2</sub>.

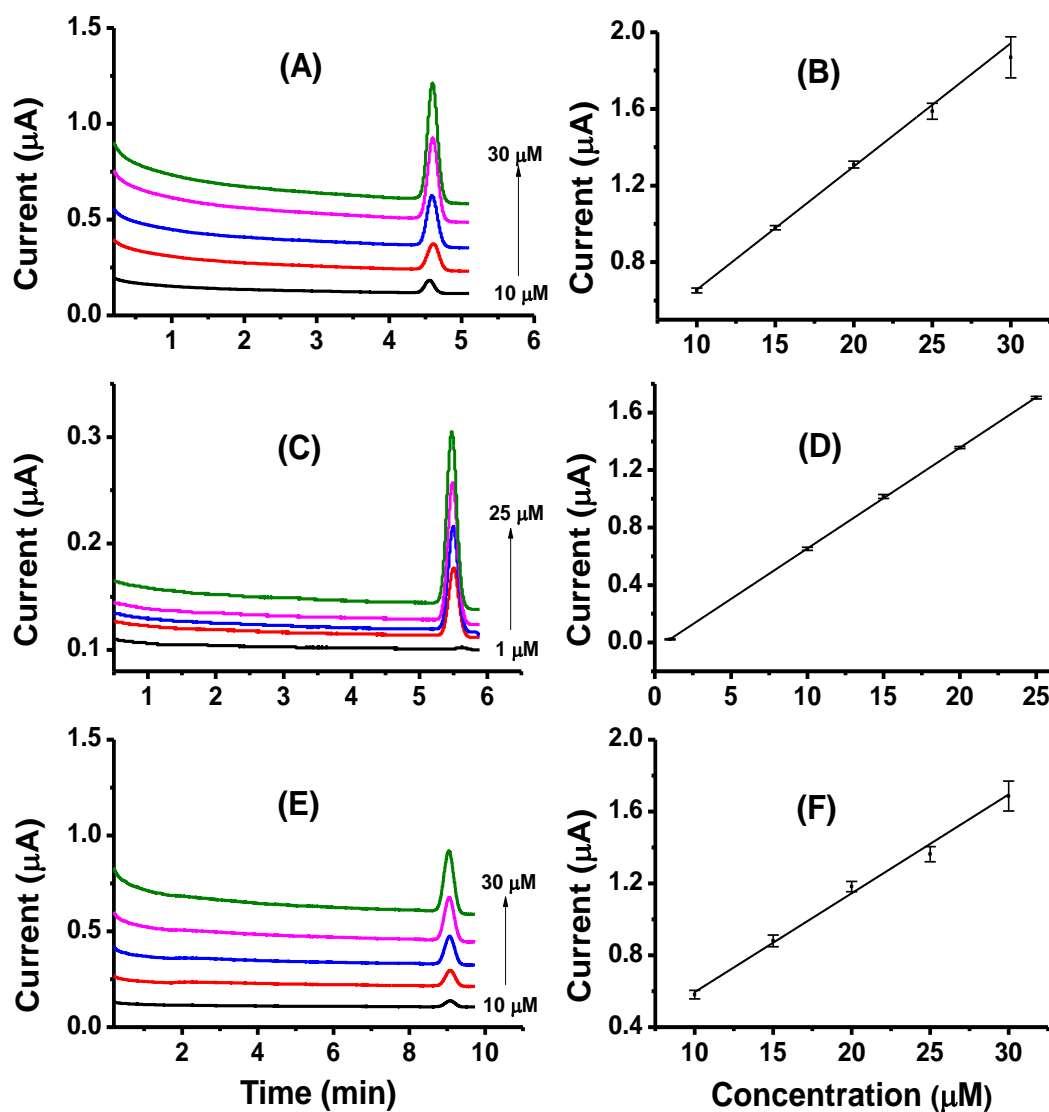


**Figure 3.11.** (A) Calibration curve and (B) plot of 4-EP; (C) calibration curve and (D) plot of 4-EG; (E) calibration curve and (F) plot of eugenol. Mobile phase: 15:85, ACN:10 mM formate pH 3. Column: HALO  $C_{18}$  core-shell (3 x 50 mm, 2.7  $\mu\text{m}$ ), flow rate: 1.5 mL/min, injection volume: 5  $\mu\text{L}$ , oxidation potential: + 1.5 V on the BDD electrode vs. Pd/H<sub>2</sub>.



### 3.3.5 Whiskey sample analysis

The optimised HPLC-ECD method was applied to the determination of the nine compounds in four whiskey samples of different geographical origin. The quantitative results for the flavourings in the four whiskey samples are shown in **Table 3.5**. **Figure 3.12** shows a chromatogram of the Islay whiskey sample. Chromatograms of Highland, Scotch, and Irish whiskeys are shown in **Figure 3.13**. Quantitation of *m*- and *p*-cresol was not possible due to coelution, whilst phenol could not be quantitated in Highland, Scotch, and Irish whiskeys due to coelution with another whiskey constituent. The concentrations of the phenolics determined by both ECD and UV detection were compared using the student's *t*-test, indicating no significant differences between the two methods for the quantitation of the analytes in whiskey samples. Of the four whiskeys analysed, Islay whiskey had significantly greater levels of guaiacols, phenols and cresols, with only trace levels determined in the other whiskeys. Islay whiskey is well known for its high level of smokiness attributed to the drying of the malted barley over a peat-fuelled fire (now largely confined to distilleries in the Scottish islands), releasing the phenolics to impart flavour to the whiskey. The parts per million (ppm) values stated by whiskey distilleries refer to the concentrations of the phenols after drying of the malted barley and not the concentrations of phenols in the final spirit. Phenols in the final whiskey are expected to be between 30-50 % of the original ppm concentration of the barley. This particular 10-year-old Islay whiskey is known to contain approximately 50 ppm of phenols before distillation and maturation, with a final concentration of between 17-24 ppm depending on the milling and mashing process<sup>38</sup>. Our results indicate a total concentration of approximately 20 ppm total phenolics in Islay whiskey, in agreement with a previous report<sup>38</sup>. The whiskey is bottled after the requisite ageing of several years. Although the glass is unreactive, the liquid inside is still volatile and may be subject to oxidation, reduction, and redox reactions if it is exposed to elevated temperature and/or sunlight.

**Table 3.5.** The concentrations of the phenolic compounds in four whiskey samples (n=2).

Analyte	$\mu\text{M}^{\text{a}}$			
	Islay	Highland	Irish	Scotch
<b>phenol</b>	$44.20 \pm 0.7$	N/A*	N/A*	N/A*
<b>guaiacol</b>	$19.35 \pm 0.4$	$0.93 \pm 0.3$	$0.79 \pm 0.1$	$0.94 \pm 0.1$
<b><i>m</i>-cresol</b>	N/A**	N/A**	N/A**	N/A**
<b><i>p</i>-cresol</b>	N/A**	N/A**	N/A**	N/A**
<b><i>o</i>-cresol</b>	$47.86 \pm 0.4$	$0.87 \pm 0.1$	ND***	ND***
<b>4-VG</b>	$5.11 \pm 0.8$	$2.6 \pm 0.1$	$1.78 \pm 0.1$	$1.75 \pm 0.1$
<b>4-EP</b>	$48.76 \pm 0.1$	$1.53 \pm 0.1$	$0.83 \pm 0.1$	$1.13 \pm 0.1$
<b>4-EG</b>	$10.97 \pm 0.2$	$5.48 \pm 0.1$	$3.26 \pm 0.1$	$2.81 \pm 0.1$
<b>eugenol</b>	ND***	ND***	ND***	ND***

<sup>a</sup> Represented as mean  $\pm$  SD (n = 2)

\* Not available: overlapping peak

\*\* Not available: *m*-cresol and *p*-cresol coeluted

\*\*\* Not detected

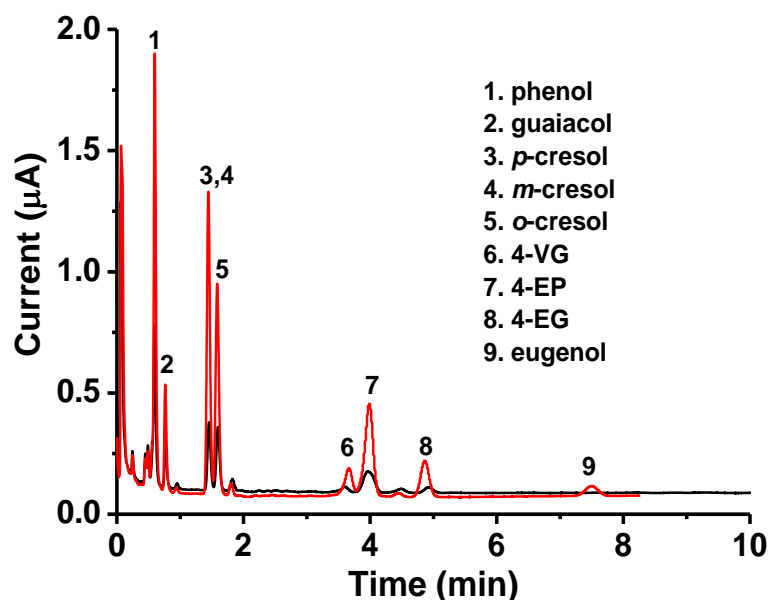


**Figure 3.12.** A representative HPLC-ECD chromatogram of Islay whiskey. Whiskey (black line) and spiked with 20  $\mu\text{M}$  each of phenol, guaiacol, *m*-cresol, *p*-cresol, *o*-cresol, 4-VG, 4-EP, 4-EG and eugenol (red line). Mobile phase: 15:85, ACN:10 mM formate pH 3. Column: HALO  $\text{C}_{18}$  core-shell (3 x 50 mm, 2.7  $\mu\text{m}$ ), flow rate: 1.5 mL/min, injection volume: 5  $\mu\text{L}$ , oxidation potential: + 1.5 V on the BDD electrode vs.  $\text{Pd}/\text{H}_2$ .

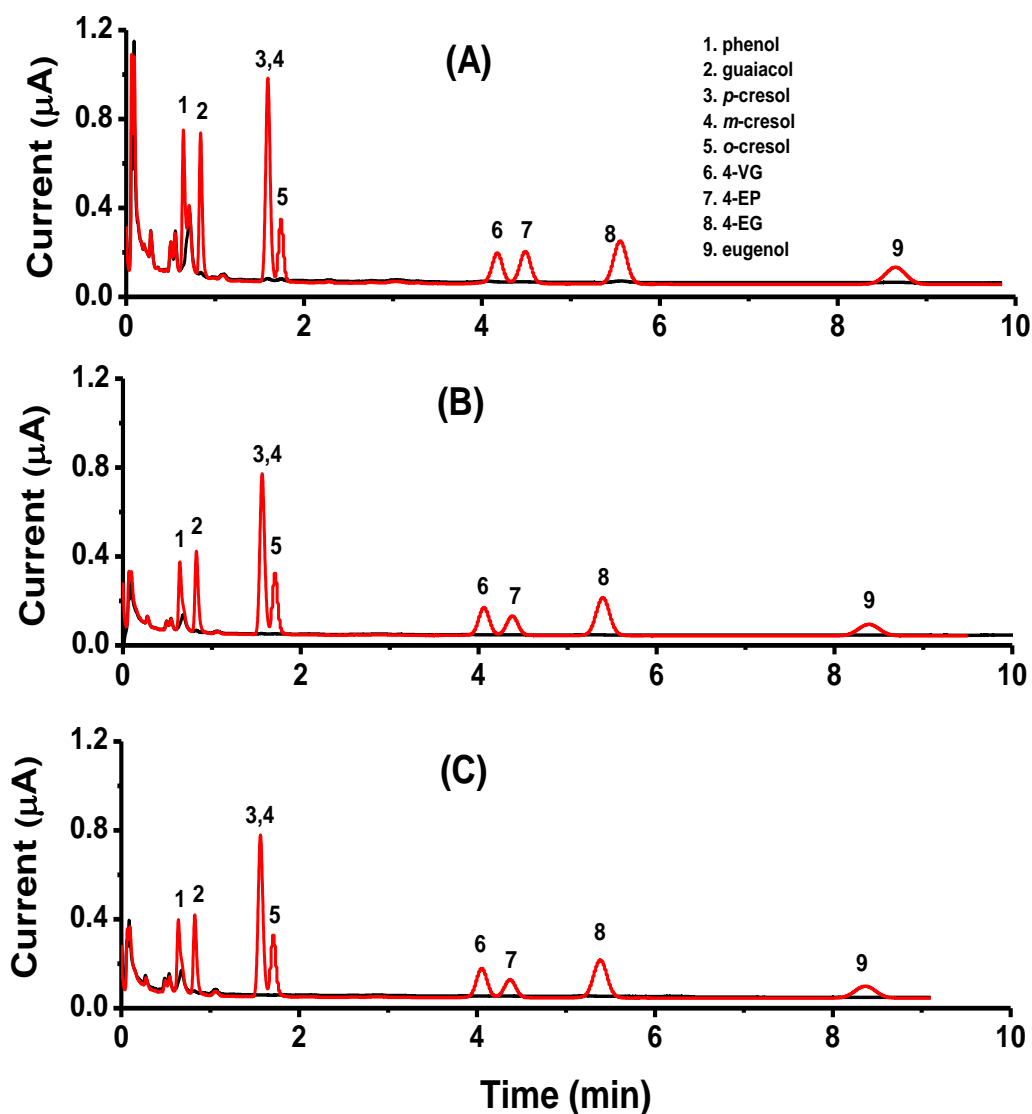


**Figure 3.13.** A representative HPLC-ECD chromatogram of Highland (A), Scotch (B) and Irish (C) whiskey. Whiskey (black line) and spiked with 20  $\mu\text{M}$  each of phenol, guaiacol, *m*-cresol, *p*-cresol, *o*-cresol, 4-VG, 4-EP, 4-EG and eugenol (red line). Mobile phase: 15:85, ACN:10 mM formate pH 3. Column: HALO  $\text{C}_{18}$  core-shell (3 x 50 mm, 2.7  $\mu\text{m}$ ), flow rate: 1.5 mL/min, injection volume: 5  $\mu\text{L}$ , oxidation potential: + 1.5 V on the BDD electrode vs.  $\text{Pd}/\text{H}_2$ .

### 3.4 Conclusions

ECD at the BDD electrode coupled to chromatographic separation using a C<sub>18</sub> HALO core-shell column, was successfully applied for the profiling of phenols, guaiacols and cresol isomers associated with the smoky flavour of whiskey. As expected, significantly higher levels of the flavourings were determined in Islay whiskey, attributed to drying of the barley over peat fuelled fires. The developed method presents adequate linearity and precision for the efficient separation of phenolics, which are detected by a downstream BDD electrode with remarkable detection sensitivity and selectivity. The entire system can be miniaturised and applied for routine assessments of smoky compounds in whiskey samples, originating from different countries and production processes.

These phenolic compounds can be easily added in counterfeit whiskeys and this practice is not new. Adulteration of spirit brands is a major concern and the regulatory has always looked for reliable markers to certify the authenticity of high-value products. During the germination of barley, its tannins are hydrolysed to form ellagic acid (EA), which is always present in authentic whiskey<sup>39</sup>. This electroactive polyphenol is the predominant phenolic constituent in distilled spirits, armagnac, cognac, bourbon, and single-malt Scotch, whereas its concentration is minimal in rum and brandy<sup>39</sup>. Another polyphenol is an isoprenoid derivate, which has been proven as a reliable indicator to differentiate authentic whiskeys from their counterfeit<sup>40</sup>.

Furthermore, this method is also applicable to the analysis of phenols as pollutants/contaminants, guaiacols as flavourings or as a food and beverage spoilage metabolite, eugenol for its antimicrobial/antioxidant properties, and cresols which are known to cause severe toxic effects.

### 3.5 References

1. Guillén, M. D. & Ibargoitia, M. L. Influence of the moisture content on the composition of the liquid smoke produced in the pyrolysis process of *Fagus sylvatica* L. wood. *J. Agric. Food Chem.* **47**, 4126–4136 (1999).
2. Cadwallader, K. R. Wood Smoke flavor. in *Handbook of meat, poultry and seafood quality* (Blackwell Publishing, 2007), pages 201-210.
3. Sikorski, Z. E. Smoking. in *Seafood: Resources, nutritional composition, and preservation* (CRC press, 1990), pages 163–180.
4. Maga, J. A. Contribution of phenolic compounds to smoke flavor. in *Phenolic compounds in food and their effects on health* (ACS Publications, 1992), pages 170–179.
5. Lee, K. Y. M., Paterson, A., Piggott, J. R. & Richardson, G. D. Origins of flavour in whiskies and a revised flavour wheel: a review. *J. Inst. Brew.* **107**, 287–313 (2001).
6. Giri, A., Zelinkova, Z. & Wenzl, T. Experimental design-based isotope-dilution SPME-GC/MS method development for the analysis of smoke flavouring products. *Food Addit. Contam. - Part A Chem. Anal. Control. Expo. Risk Assess.* **34**, 2069–2084 (2017).
7. Nie, Y., Kleine-Benne, E. Determining phenolic compounds in whisky using direct large volume injection and stir bar sorptive extraction. *Gerstel Glob. Anal. Solut Gerstel GmbH Co. KG, Appl. Note* 1–12 (2012).
8. Bicchi, C. *et al.* Dual-phase twistors: A new approach to headspace sorptive extraction and stir bar sorptive extraction. *J. Chromatogr. A* **1094**, 9–16 (2005).
9. Nie, Y., Kleine-Benne, E. Using three types of twister phases for stir bar sorptive extraction of whisky, wine and fruit juice. *Gerstel Glob. Anal. Solut Gerstel GmbH Co. KG, Appl. Note* 1–14 (2011).
10. Karlsson, B. C. G. & Friedman, R. Dilution of whisky - The molecular perspective. *Sci. Rep.* **7**, 1–9 (2017).
11. Lehtonen, M. Phenols in whisky. *Chromatographia* **16**, 201–203 (1982).

12. Ng, C. M., Reuter, W. Analysis of phenols in whisky by HPLC with FL detection. *PerkinElmer.USA Appl. Note* (2015).
13. Liang, Y., Cao, W., Chen, W. J., Xiao, X. H., Zheng, J. B. Simultaneous determination of four phenolic components in citrus honey by high performance liquid chromatography using electrochemical detection. *Food Chem.* **114**, 1537–1541 (2009).
14. Zhu, Z. *et al.* Sugaring-out assisted liquid-liquid extraction coupled with high performance liquid chromatography-electrochemical detection for the determination of 17 phenolic compounds in honey. *J. Chromatogr. A* **1601**, 104–114 (2019).
15. Gao, H. *et al.* Determination of thymol and phenol in honey by LC with electrochemical detection. *Chromatographia* **72**, 361–363 (2010).
16. Cardwell, T. J., Hamilton, I. C., McCormick, M. J., Symons, R. K. Determination of alkylphenols in refinery effluents by liquid-chromatography using electrochemical detection. *Int. J. Environ. Anal. Chem.* **24**, 23–35 (1986).
17. Freitas, P. V., da Silva, D. R., Beluomini, M. A., da Silva, J. L. & Stradiotto, N. R. Determination of phenolic acids in sugarcane vinasse by HPLC with pulse amperometry. *J. Anal. Methods Chem.* **2018**, 4869487 (2018).
18. Hagen, A., Mattusch, J. & Werner, G. Flow-rate varied HPLC-/EC-determination of phenols. *Fresenius. J. Anal. Chem.* **339**, 26–29 (1991).
19. Boston, D. A. & Kissinger, P. T. Identification of phenolic constituents in commercial beverages by liquid chromatography with electrochemical detection. *Anal. Chem.* **53**, 1695–1699 (1981).
20. Tesařová, E., Pacáková, V. & Štulík, K. High-performance liquid chromatography of biphenols and bis (hydroxyphenyl) propanes (dianes) with voltammetric and UV photometric detection. *Chromatographia* **23**, 102–108 (1987).
21. Whang, C. W. Analysis of phenolic priority pollutants by high-performance liquid-chromatography with electrochemical detection. *J. Chinese Chem. Soc.*

- 34**, 81–89 (1987).
22. Cardellicchio, N., Cavalli, S., Piangerelli, V., Giandomenico, S. & Ragone, P. Determination of phenols in environmental samples by liquid chromatography - Electrochemistry. *Fresenius. J. Anal. Chem.* **358**, 749–754 (1997).
  23. Terashima, C., Rao, T. N., Sarada, B. V, Tryk, D. A. & Fujishima, A. Electrochemical oxidation of chlorophenols at a boron-doped diamond electrode and their determination by high-performance liquid chromatography with amperometric detection. **74**, 895–902 (2002).
  24. Armentrout, D. N., McLean, J. D. & Long, M. W. Trace determination of phenolic compounds in water by reversed phase liquid chromatography with electrochemical detection using a carbon-polyethylene tubular anode. *Anal. Chem.* **51**, 1039–1045 (1979).
  25. Luong, J. H. T., Male, K. B. & Glennon, J. D. Boron-doped diamond electrode: synthesis, characterization, functionalization and analytical applications. *Analyst* **134**, 1965–79 (2009).
  26. Zhang, W. *et al.* Recent development of carbon electrode materials and their bioanalytical and environmental applications. *Chem. Soc. Rev.* **45**, 715–752 (2016).
  27. Rao, T. N., Sarada, B. V., Tryk, D. A. & Fujishima, A. Electroanalytical study of sulfa drugs at diamond electrodes and their determination by HPLC with amperometric detection. *J. Electroanal. Chem.* **491**, 175–181 (2000).
  28. Du, T. *et al.* Simultaneous determination of tryptophan , kynurenine , kynurenic acid and two monoamines in rat plasma by HPLC-ECD / DAD. *J. Pharm. Biomed. Anal.* **158**, 8–14 (2018).
  29. Zhang, L., Yang, J., Luo, Y., Shang, J. & Jiang, X. Simultaneous determination of eleven compounds related to metabolism of bioamines in rat cortex and hippocampus by HPLC-ECD with boron-doped diamond working electrode. *J. Pharm. Biomed. Anal.* **118**, 41–51 (2016).
  30. Martins, I. *et al.* Determination of parabens in shampoo using high performance

- liquid chromatography with amperometric detection on a boron-doped diamond electrode. *Talanta* **85**, 1–7 (2011).
31. Martins, I., de Souza Canaes, L., Doretto, K. M. & Rath, S. Boron-doped diamond electrode coupled to liquid chromatography: Application to simultaneous determination of benzodiazepines. *Electroanalysis* **22**, 455–462 (2010).
  32. Siangproh, W., Rattanarat, P. & Chailapakul, O. Reverse-phase liquid chromatographic determination of  $\alpha$ -lipoic acid in dietary supplements using a boron-doped diamond electrode. *J. Chromatogr. A* **1217**, 7699–7705 (2010).
  33. Muna, G. W., Tasheva, N. & Swain, G. M. Electro-oxidation and amperometric detection of chlorinated phenols at boron-doped diamond electrodes: A comparison of microcrystalline and nanocrystalline thin films. *Environ. Sci. Technol.* **38**, 3674–3682 (2004).
  34. Hayes, P. E., Glennon, J. D., Buzid, A. & Luong, J. H. T. Simultaneous electroanalysis of guaiacol and its analogs based on their differential complexation with  $\alpha$ -cyclodextrin on Nafion modified boron-doped diamond electrode. *Electroanalysis* **32**, 119–127 (2020).
  35. Samet, Y., Abdelhedi, R., Savall, A. A study of the electrochemical oxidation of guaiacol. *Phys. Chem. News* **8**, 89–99 (2002).
  36. Enache, T. A. & Oliveira-Brett, A. M. Phenol and para-substituted phenols electrochemical oxidation pathways. *J. Electroanal. Chem.* **655**, 9–16 (2011).
  37. Safavi, A., Maleki, N. & Tajabadi, F. Highly stable electrochemical oxidation of phenolic compounds at carbon ionic liquid electrode. *Analyst* **132**, 54–58 (2007).
  38. Brossard, P. Peat, phenol, and PPM. (2007). Available at: [https://www.whisky-news.com/En/reports/Peat\\_phenol\\_ppm.pdf](https://www.whisky-news.com/En/reports/Peat_phenol_ppm.pdf).
  39. Goldberg, D. M., Hoffman, B., Yang, J. & Soleas, G. J. Phenolic constituents, furans, and total antioxidant status of distilled spirits. *J. Agric. Food Chem.* **47**, 3978–3985 (1999).



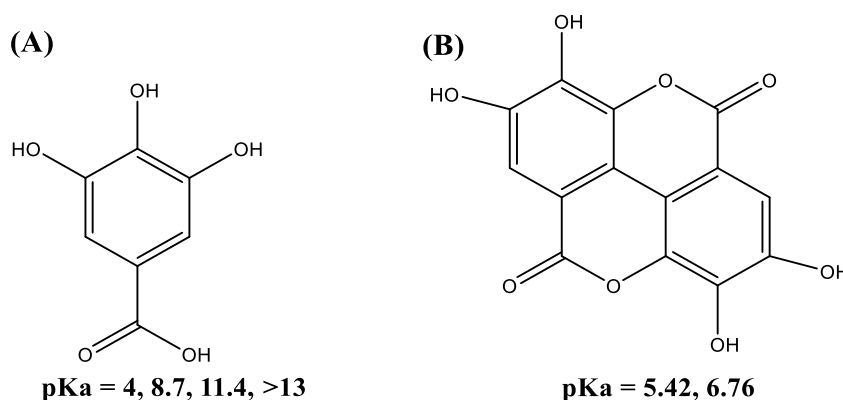
40. Garcia, J. S. *et al.* Whisky analysis by electrospray ionization-Fourier transform mass spectrometry. *Food Res. Int.* **51**, 98–106 (2013).

## **Chapter 4**

### **Electroanalysis of gallic and ellagic acids at a boron-doped diamond electrode and their determination by high-performance liquid chromatography with amperometric detection**

## 4.1 Introduction

Gallic acid (GA) and particularly its dimer, ellagic acid (EA), are a group of naturally occurring polyphenol antioxidants<sup>1</sup> which have a wide range of biological activities and applications. GA (3,4,5-trihydroxybenzoic acid) is found in most plants as both free and as part of hydrolysable tannins<sup>2</sup>. It is particularly abundant in red wine, green tea and other processed beverages<sup>3</sup>. GA is synthesised from 3-dehydroshikimate by shikimate dehydrogenase to form 3,5-didehydroshikimate, which undergoes tautomerisation to form gallate<sup>4</sup>. EA is a dimer of GA, which is also abundant in fruits and vegetables (**Scheme 4.1**). Ellagitannin is a more complex version of EA in some fruits but it is converted into EA in the body<sup>5</sup>. This acid, with antioxidative and antiviral properties, has been used in food preservation, herbal medicine, and dietary supplements prepared from fruit extracts.



**Scheme 4.1.** Chemical structures of (A) GA and (B) EA.

EA finds its way into whiskey during the germination of barley, one of the important stages of whiskey production in which ellagitannin is hydrolysed to form EA<sup>6</sup>. Also worth noting is the use of oak wood casks for the storage of whiskey, brandies, and other alcoholic beverages. During storage, a series of reactions and transfers occur between the wood and the beverage, resulting in GA levels ranging from 0-17.43 mg/L in brandies<sup>7</sup>. The difference in the GA concentrations is due to many factors such as the length of storage, wood type (French oak versus American oak), and the age and life of the cask (overused and exhausted).

Electroanalysis of GA in food matrices by different electrode materials has been attempted. A graphite electrode modified with thionine and nickel hexacyanoferrate

exhibits a limit of detection (LOD) for 1.66  $\mu\text{M}$  for GA<sup>8</sup>. A glassy carbon electrode (GCE) modified by polyepinephrine has a LOD of 0.66  $\mu\text{M}$  for GA, compared to 0.28  $\mu\text{M}$  for a GCE modified with silver nanoparticles and delphinidin, a plant pigment<sup>9</sup>. Delphinidin was selected in order to enhance the selective oxidation of GA.  $\text{TiO}_2$  nanoparticles have been used to modify a carbon paste electrode with a comparable LOD of 0.94  $\mu\text{M}$  for this acid<sup>10</sup>.

Pertaining to EA, bare platinum (Pt), gold (Au), and a GCE has been attempted for electroanalysis, and the best response signal is obtained by the GCE<sup>11</sup>. The GCE modified by a cobalt (II) ethylenediamine complex exhibits linearity of 0.1-929  $\mu\text{M}$  for this acid<sup>12</sup>. The application of this approach focuses on the determination of spiked EA (10-20  $\mu\text{M}$ ) in raspberry and strawberry<sup>12</sup>. The electroanalytical behaviours of GA and EA were studied using a screen-printed electrode (SPE) modified with graphene<sup>13</sup>. Both GA and EA are determined together with other phenols as a single peak to represent the total content of phenolic compounds in cork boiling water. Electroanalysis is a surface dependent method, thus, reproducibility of the active area of modified electrodes is still problematic.

Analysis of GA and EA is of importance for diversified fields, e.g., medical, biomedical, and pharmaceutical applications. Electrochemical sensors have offered several appealing features including enhanced detection sensitivity, cost-effectiveness and ease of fabrication. This study aims to develop a high-performance liquid chromatography (HPLC) technique coupled with a boron-doped diamond (BDD) electrode for the rapid co-analysis of GA and EA in whiskeys as a model. HPLC coupled to a BDD electrode provides enhanced selectivity and specificity for phenolic compounds over direct electrochemical detection and HPLC-ultraviolet (UV) detection. Electrochemistry of GA and EA on the BDD electrode is also investigated in-depth considering this topic has not been attempted. EA is the end product of the degradation of barley tannins and also present in oak wood. Thus, its analysis is useful for the identification of whiskey counterfeits by several analytical methods including gas chromatography equipped with mass spectroscopy (GC-MS)<sup>14</sup>.

## 4.2 Experimental

### 4.2.1 Reagents, standard solutions and samples

Phosphoric acid, acetic acid, formic acid, ammonium formate, sodium phosphate monobasic, sodium phosphate dibasic, sodium acetate, acetone, ethanol (EtOH), acetonitrile (ACN), dimethylformamide (DMF),  $\alpha$ -cyclodextrin ( $\alpha$ -CD), 2-hydroxypropyl  $\beta$ -cyclodextrin (HP- $\beta$ -CD), sulphated  $\beta$ -cyclodextrin (S- $\beta$ -CD), GA and EA were purchased from Sigma-Aldrich (Dublin, Ireland). All reagents used were of the analytical grade of the highest purity, and aqueous solutions were prepared in deionised water (Millipore, Ireland). Stock solutions (1 mM) of GA and EA were prepared in ACN and DMF, respectively. Highland, Scotch and Islay whiskeys were purchased from a local supermarket in Co. Cork, Ireland. Whiskey samples comprising of 500  $\mu$ L of whiskey and 1000  $\mu$ L of the mobile phase were filtered through an Econofltr Nylon membrane (13 mm, 0.2  $\mu$ m) before analysis.

### 4.2.2 Voltammetric analysis

Cyclic voltammetry (CV) and square wave voltammetry (SWV) were applied to investigate the electrochemical behaviour of GA and EA using a CHI1040A electrochemical workstation (CH Instrument, Austin, TX). The electrochemical cell consists of the BDD electrode (B/C ratio in the gaseous phase of 1000 ppm, 3 mm diameter, Windsor Scientific, Slough Berkshire, UK) and a GCE (BASi Analytical Instruments, West Lafayette, IN), a silver/silver chloride (Ag/AgCl /3 M KCl) reference electrode (BASi Analytical Instruments, West Layette, IN), and a Pt wire counter electrode (Sigma-Aldrich, Dublin, Ireland). Phosphate buffers at pH 2 and pH 7, and acetate buffer at pH 5, at a concentration of 100 mM and containing 5 % EtOH were used as supporting electrolytes. 5 % EtOH was used to eliminate the effect of EtOH in whiskey. Before analysis, the BDD electrode was polished with polishing papers (Buehler, UK) and subsequently with alumina (Buehler, UK) until a mirror finish was obtained. The electrode was then sonicated in ACN and deionised water for 5 min and 10 min, respectively. After sonication, the electrode was cleaned by CV between  $-1.0$  V and  $+1.5$  V versus Ag/AgCl (3 M KCl) at  $100 \text{ mV s}^{-1}$  in  $0.5 \text{ M H}_2\text{SO}_4$  and then in the respective buffers applied for analysis. Between measurements, the

electrode was also cleaned with 0.5 M H<sub>2</sub>SO<sub>4</sub> for 10 cycles at a scan rate of 100 mV s<sup>-1</sup> to remove adsorbed species from its surface.

### **4.2.3 Apparatus**

HPLC-ECD analyses were performed using an Agilent HPLC system (Agilent 1200 LC series) equipped with a binary pump (model G1312B), degasser (model G1379B), autosampler (model G1367D) and a UV diode array detector (model G1315C). Agilent Chemstation was used for instrument control and UV data analysis. ECD was carried out using an Antec Flexcell thin layer flow cell with a cell volume of 0.7  $\mu$ L (Apex Scientific, Co. Kildare, Ireland). The flow cell consists of a three-electrode configuration with a working BDD electrode (8 mm diameter), a HyREF (Pd/H<sub>2</sub>) reference electrode and a carbon loaded polytetrafluoroethylene (PTFE) counter electrode. CHI660E electrochemical workstation was used for data analysis (CH Instrument, Austin, Texas). Between measurements, the BDD electrode was cleaned by wiping its surface firstly with H<sub>2</sub>O then with acetone using MasterTex paper.

### **4.2.4 Chromatographic conditions**

Gradient chromatographic separation was performed using an Agilent XDB C<sub>18</sub> column (4.6 x 150 mm, 5  $\mu$ m particle size, Apex Scientific, Kildare, Ireland). Mobile phase A was 10 mM formate, pH 3 and mobile phase B was ACN. Gradient elution was performed starting with 2 % B followed by a linear increase to 30 % B until 3 min. The next linear increase was until 40 % B to 5 min followed by re-equilibration from 5 to 8 min with 2 % B. The injection volume was 5  $\mu$ L and the flow rate was set at 1.5 mL/min. The column temperature was set at 25 °C. HPLC-ECD was determined at + 1.4 V.

### **4.2.5 Method validation**

The method was validated for linearity, limits of detection (LODs) and precision (intra-day and inter-day). The linearity of the method was evaluated by linear regression analysis of six standard working solutions. All standards were run in triplicate. LODs were determined by the lowest concentration with a signal-to-noise ratio of 3 (S/N=3). Intra-day precision was carried out by five repetitive measurements

of a mixed standard solution (100  $\mu\text{M}$ ) within one day, and inter-day by five repetitive measurements of a mixed standard solution (100  $\mu\text{M}$ ) over four days. Precision was expressed as the relative standard deviation (RSD %).

### 4.3 Results and discussion

#### 4.3.1 CVs of GA on the BDD electrode

CVs of GA on the BDD electrode at pH 2 exhibited two irreversible anodic CV waves whereas the reverse scan only had three significantly smaller cathodic peaks (**Figure 4.1**). The significant difference in peak current areas and the large separation in peak potentials indicate that the electro-oxidation of GA is a quasi-reversible process followed by a chemical reaction. The first wave represents the irreversible oxidation of GA to the semiquinone radical cation ( $\text{GA}^{\bullet+}$ ) (**b**) by a single electron transfer process. This unstable radical cation then loses a proton to form four different semiquinone radicals ( $\text{GA}^{\bullet}$ ) (**c**, **d1-d3**). Further oxidation leads to the formation of the quinone cation ( $\text{GA}^+$ ) (**e**), followed by the deprotonation of the quinone cation ( $\text{GA}^+$ ) to complete the overall two-electron process and the final product is an *o*-quinone form (**f**) as shown in **Scheme 4.2**<sup>15</sup>. The two oxidation peaks diminished noticeably when the electrode was subject to repeated scanning, indicating the formation of electro inactive species on the electrode surface. In addition, the irreversible behaviour of GA on the BDD electrode implied the formation of inactive GA species on the electrode surface. The semiquinone radical cation ( $\text{GA}^{\bullet+}$ ) also reacted with free GA adsorbed on the electrode with the participation of the COOH or the -OH group. Indeed, the formation of ester and ether linkages between gallate monomers both in solution and in the adsorbed state has been reported<sup>16</sup>.

There was a decrease of the peak current and a shift of the peak potential towards more positive potentials for the five repeated CV waves (**Figure 4.1**). This behaviour could be attributed to the formation of electro inactive species to block the electrode surface including the possible formation of polygallic acid<sup>17</sup>.

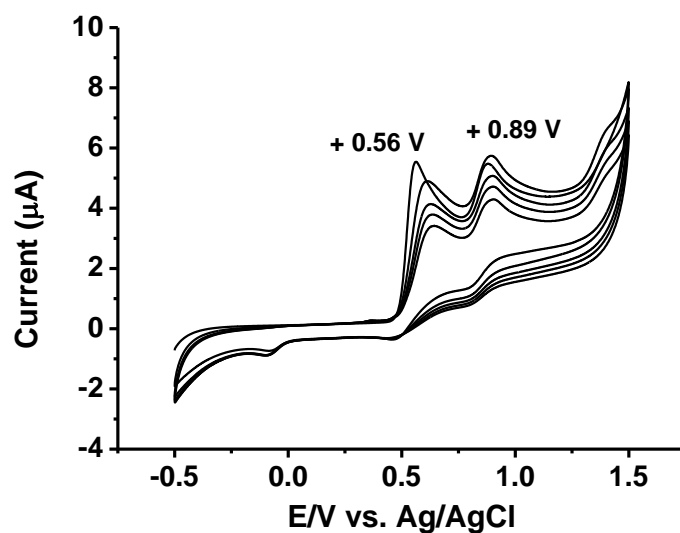
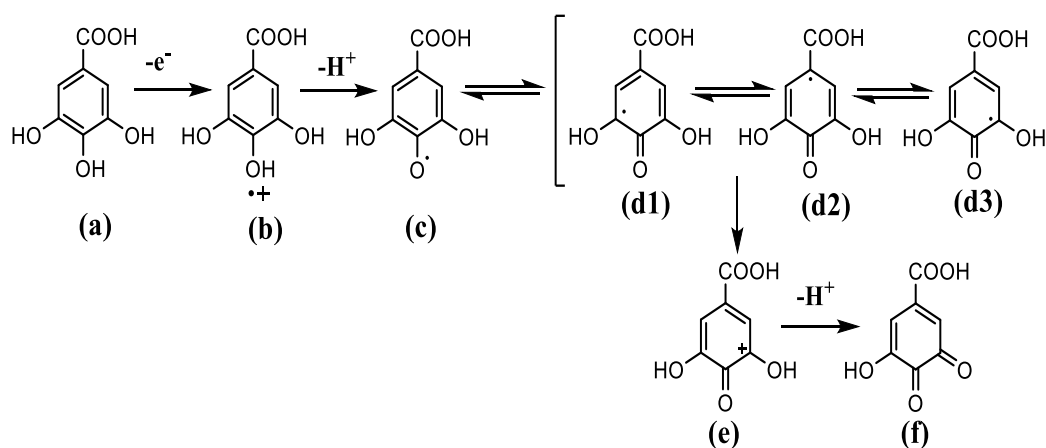


**Figure 4.1.** A representative 5 cycle CV of 100  $\mu\text{M}$  GA at pH 2 on the BDD electrode vs. Ag/AgCl. Supporting electrolyte: 100 mM phosphate buffer with 5 % EtOH at the scan rate of 100  $\text{mV s}^{-1}$ .



**Scheme 4.2.** Electro-oxidation of GA. The process involves the release of two electrons and two protons, i.e., electrochemistry of GA is pH-dependent. The first step represents irreversible oxidation of GA (a) to the semiquinone radical cation (b). The radical cation (b) then loses a proton to form the semiquinone radical (c, d1-d3). The one-electron oxidation product (d1-d3) is followed by a second irreversible electron transfer to the quinone cation (e). This quinone cation (e) is deprotonated to give the quinone (f) as the final product. Modified from Ref. <sup>15</sup>.



The anodic current corresponding to GA oxidation increased linearly with the square root of the scan rate indicating that the oxidation is a diffusion-controlled process at the electrode surface (**Figure 4.2**).

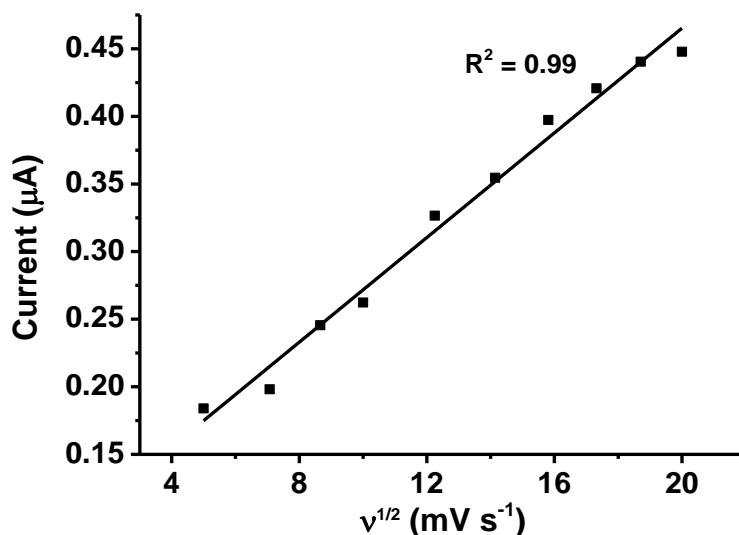


**Figure 4.2.** A plot of peak current versus square root of the scan rate ( $v^{1/2}$ (mV s<sup>-1</sup>)) for 100 μM GA at pH 2 on the BDD electrode vs. Ag/AgCl. The supporting electrolyte was 100 mM phosphate buffer with 5 % EtOH.

As expected from the participation of a proton (H<sup>+</sup>) in the redox step, the two peak potentials were shifted toward less positive values with increasing electrolyte pH (**Figure 4.3**). The two peak intensities at pH 5 and pH 7 became less pronounced than those obtained at pH 2 because GA was chemically deprotonated at high pH media. Such a result was similar to the electrochemical behaviour of GA in aqueous solutions at a GCE<sup>15</sup>. Free radicals produced by the oxidation of GA have been described from an electron paramagnetic resonance study<sup>18</sup>. However, GA produces two different radicals as a function of pH and the spectrum of the gallate free radical is a doublet of triplets in the pH range between 7-10<sup>18</sup>. Thus, this evidence supported the electrochemical oxidation pathway for GA as reported in the literature<sup>15</sup>.

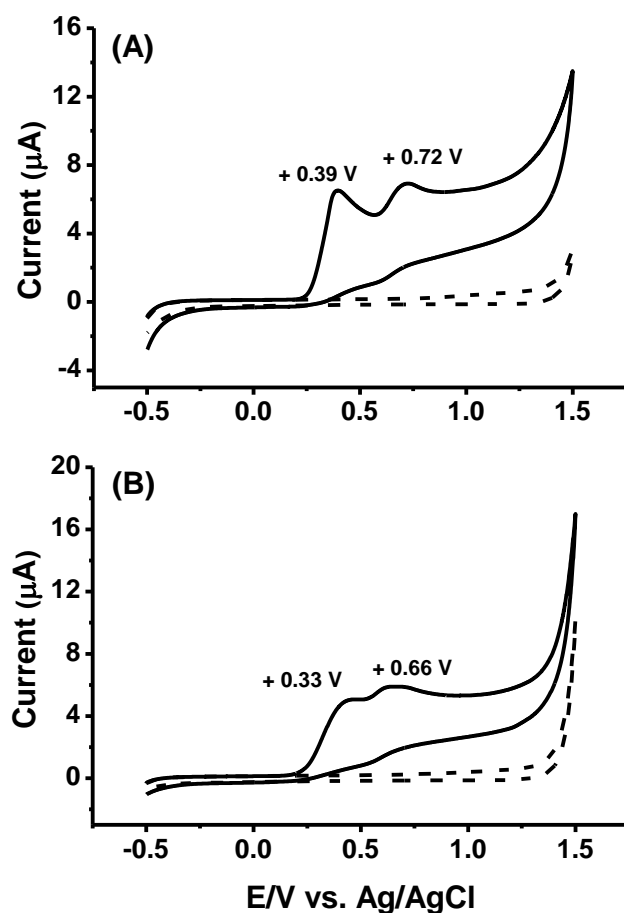


**Figure 4.3.** CV response in the absence (dashed lines) and presence (solid lines) of 100  $\mu\text{M}$  GA at (A) pH 5 and (B) pH 7 on the BDD electrode vs. Ag/AgCl. The supporting electrolyte was 100 mM phosphate buffer with 5 % EtOH at the scan rate of 100  $\text{mV s}^{-1}$ .

#### 4.3.2 CVs of EA on the BDD electrode

At pH 2, the CV of EA exhibited two anodic peaks with the first oxidation peak positioned as a shoulder of the second one (**Figure 4.4**). In the reverse scan, two significantly smaller peaks appear, indicating the electro-oxidation of EA was a quasi-reversible process. Peak 1 was attributed to the formation of the EA phenoxyl radical by the release of one-electron and one-proton (**Scheme 4.3**)<sup>19</sup>. At below pH 4.8, the phenoxyl radical formed in the first oxidation step was stable and underwent a further one-electron, one-proton charge-transfer reaction leading to peak 2 (**Scheme 4.4**)<sup>19</sup>.

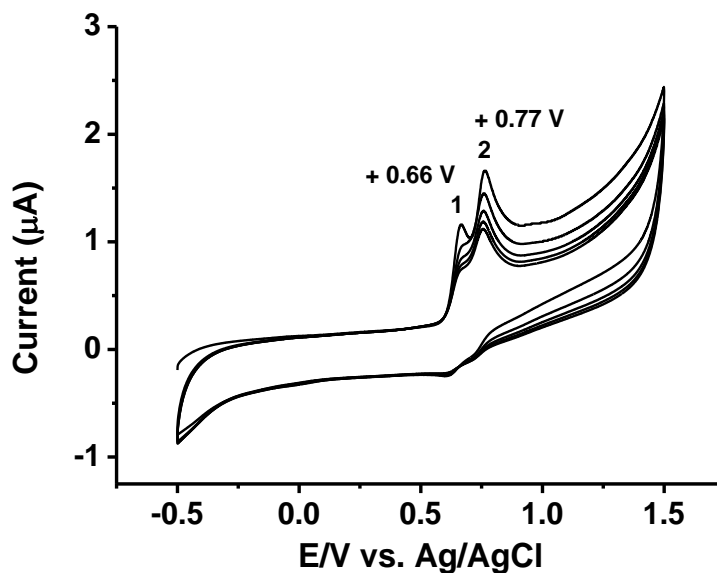
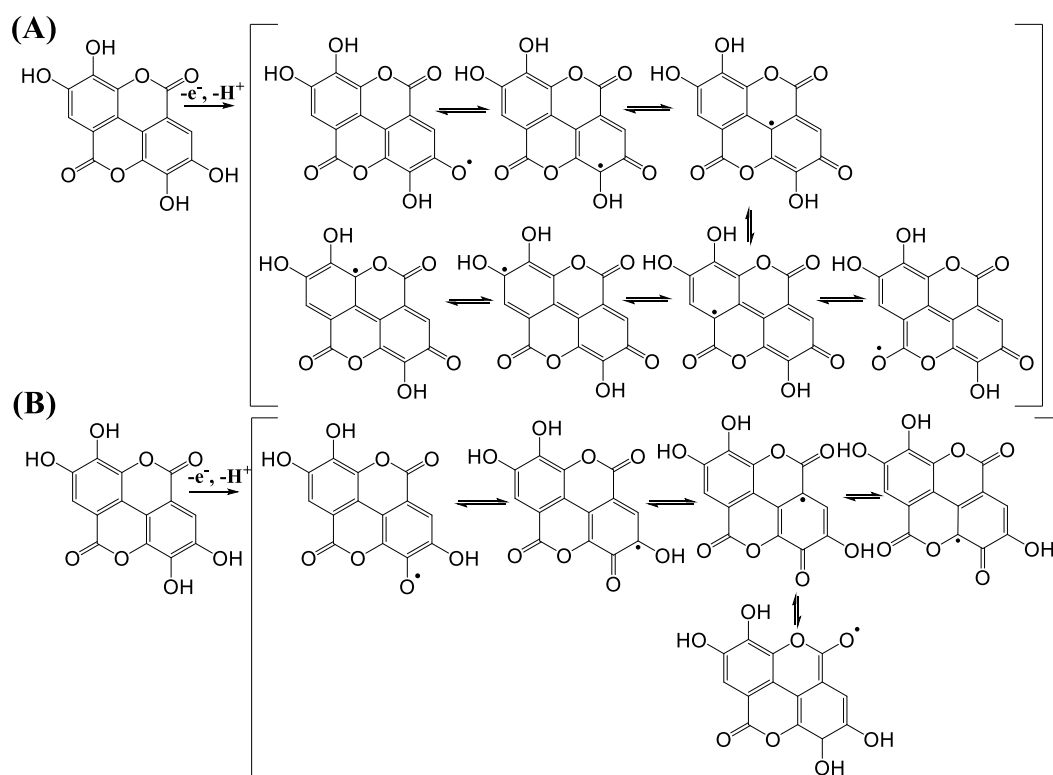
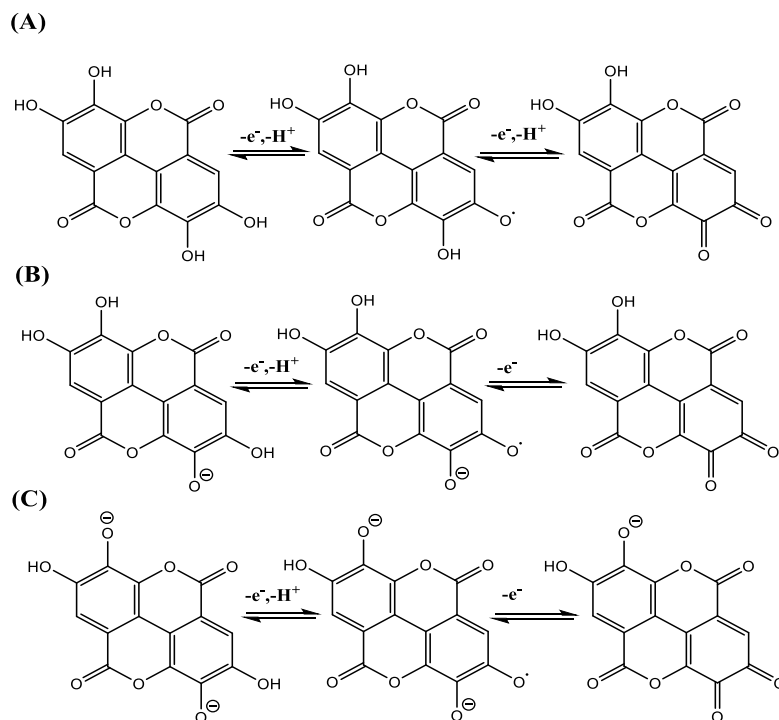


**Figure 4.4.** A representative 5 cycle CV of 100  $\mu\text{M}$  EA at pH 2 on the BDD electrode vs. Ag/AgCl. The supporting electrolyte was 100 mM phosphate buffer with 5 % EtOH at the scan rate of 100  $\text{mV s}^{-1}$ .



**Scheme 4.3.** Two possible electrochemical oxidation pathways of EA to form its corresponding radicals. This first step involves the release of one electron and one  $\text{H}^+$ . Modified from Ref.<sup>19</sup>.



**Scheme 4.4.** The formation of different quinones from three different radicals resulted from the electrochemical oxidation of EA. Modified from Ref.<sup>19</sup>.

A plot of peak current versus square root of the scan rate was linear, indicating that EA undergoes a diffusion-controlled process on the electrode surface (**Figure 4.5**). EA has four hydroxyl groups; thus, its electrochemical behaviour was significantly affected by pH. At neutral pH, the shoulder developed into a separate peak (**Figure 4.6**). In the reverse scan, two small peaks appeared, indicating the electro-oxidation of EA was similar to that of GA, i.e., a quasi-reversible process. It is also worth noting that EA with two carbonyl groups in the molecule can be reduced at the electrode surface, involving two electrons each<sup>20</sup>. However, the reduction potentials for both waves/peaks are close and co-emerged as one single peak.

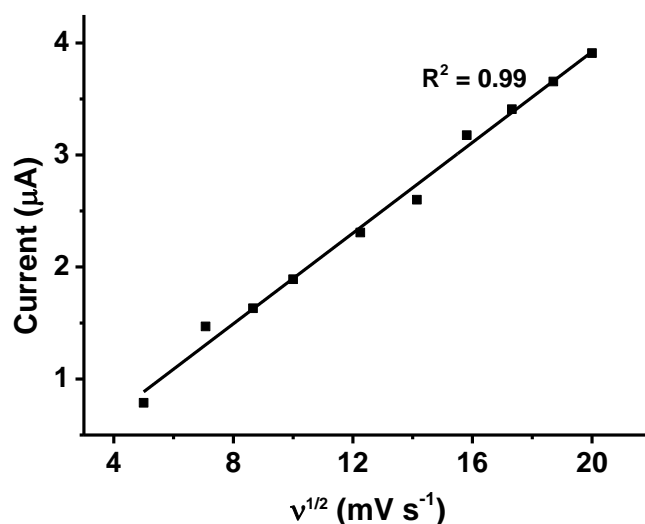


**Figure 4.5.** A plot of peak current versus square root of the scan rate ( $v^{1/2}(\text{mV s}^{-1})$ ) for 100  $\mu\text{M}$  EA at pH 2 on the BDD electrode vs. Ag/AgCl. The supporting electrolyte was 100 mM phosphate buffer with 5 % EtOH.

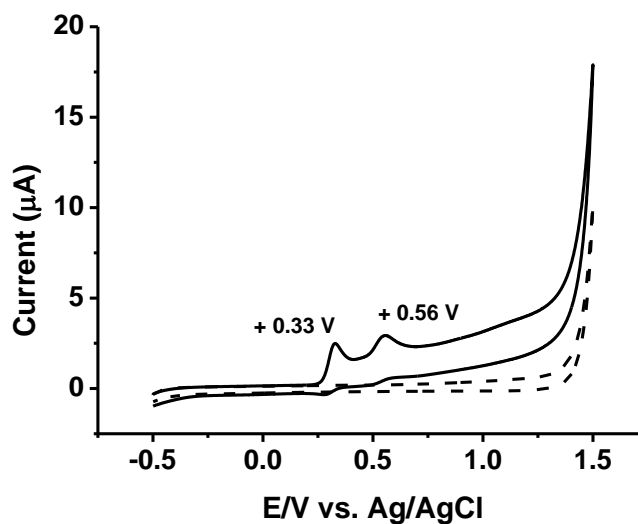


**Figure 4.6.** CV response in the absence (dashed line) and presence (solid line) of 100  $\mu\text{M}$  EA at pH 7 on the BDD electrode vs. Ag/AgCl. The supporting electrolyte was 100 mM phosphate buffer with 5 % EtOH at the scan rate of 100  $\text{mV s}^{-1}$ .

### 4.3.3 CVs of EA and GA on the GCE

For comparison, CVs of EA and GA were also studied using the GCE. As shown in **Figure 4.7**, both acids exhibited broader and poorly defined oxidation peaks, as well as lower peak currents at all three pHs in comparison to the responses generated at the BDD electrode. Furthermore, significantly higher background currents were generated with the GCE due to its  $\text{sp}^2$  hybridisation.

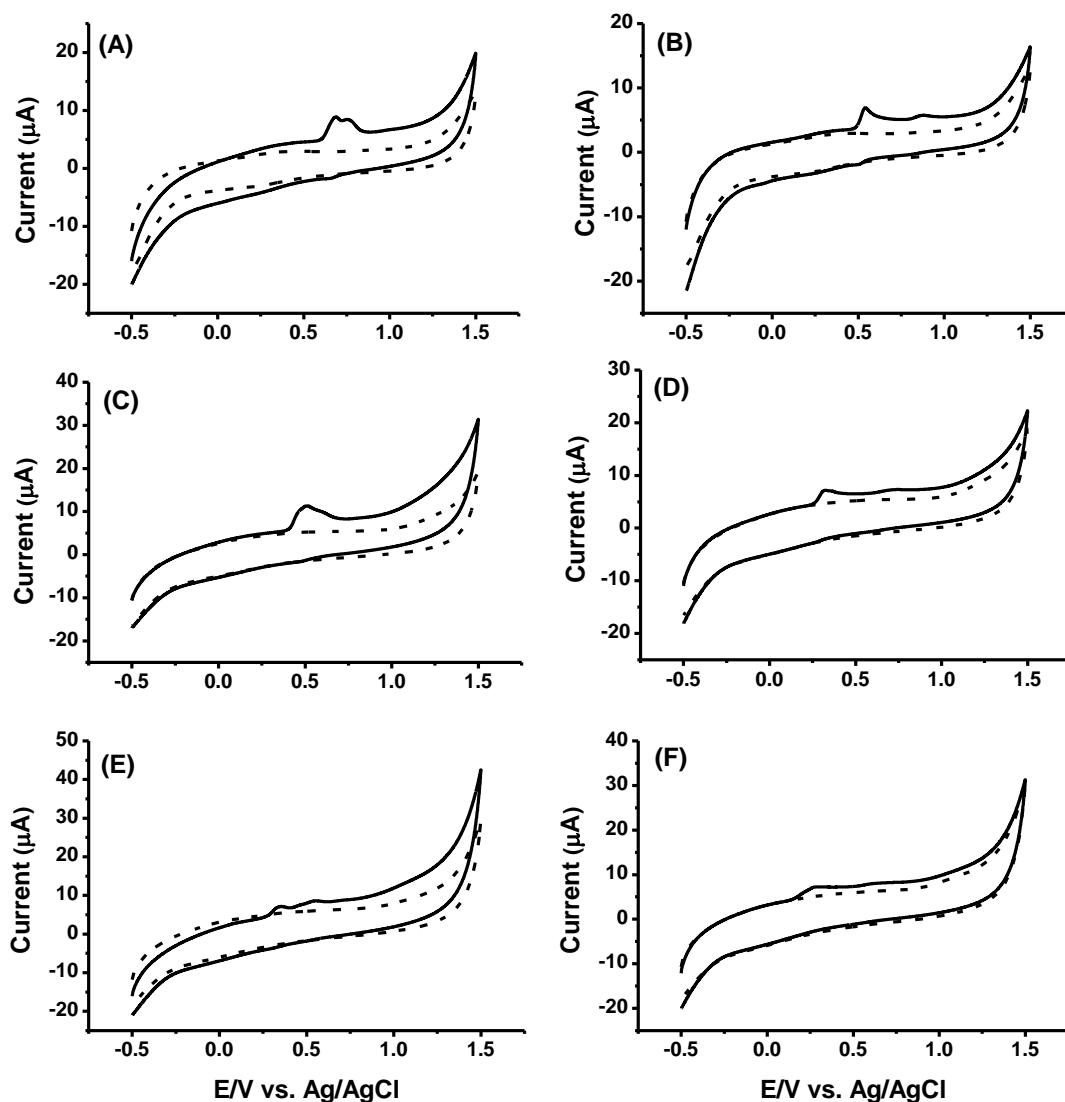


**Figure 4.7.** CV responses in the absence (dashed line) and presence (solid line) of EA and GA on the GCE vs. Ag/AgCl. (A) EA and (B) GA at pH 2; (C) EA and (D) GA at pH 5; (E) EA and (F) GA at pH 7. The supporting electrolyte was 100 mM phosphate buffer with 5 % EtOH at pH 2 and 7, and 100 mM acetate buffer with 5 % EtOH at pH 5, at the scan rate of  $100 \text{ mV s}^{-1}$ .

#### 4.3.4 SWV of gallic and ellagic acids

Due to their similar oxidation potentials, the GA-EA pair was not separated by SWV even at three different pH values: 2, 5, and 7 (**Figure 4.8**).

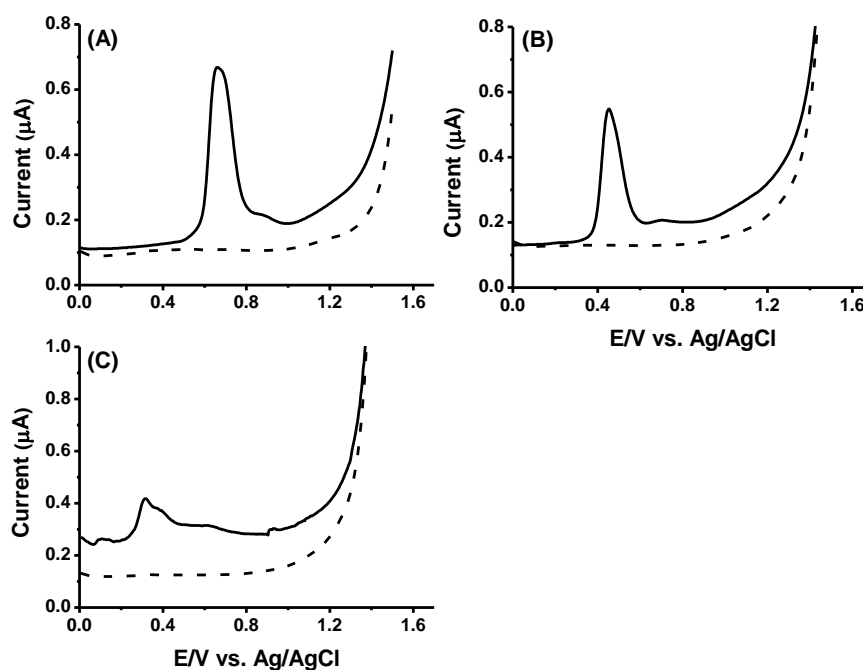


**Figure 4.8.** SWV in the absence (dashed lines) and presence (solid lines) of a standard mixture of EA ( $10\mu\text{M}$ ) and GA ( $2\mu\text{M}$ ) at (A) pH 2, (B) pH 5, (C) and pH 7 using 100 mM phosphate buffer, pH 2 with 5 % EtOH. Detection was achieved on the bare BDD electrode vs. Ag/AgCl.

A series of experiments were then conducted to investigate the presence of  $\alpha$ -CD, H- $\beta$ -CD and S- $\beta$ -CD in the electrolyte (**Figure 4.9**). Such cyclodextrins might form different inclusion complexes with GA and EA and this strategy has been used with some success for the analysis of guaiacol and its derivatives in whiskey<sup>21</sup>. In particular, GA forms an inclusion complex with 2-hydroxylpropyl  $\beta$ -CD to improve the solubility of this acid for the treatment of *Candida albicans* films<sup>22</sup>. In general, a broad peak with a noticeable shoulder was observed with all tested CDs. Peak deconvolution was performed to assign the presence of GA and EA (**Figure 4.9**). Evidently, an upstream separation scheme is required to quantify the unknown levels of these two acids.

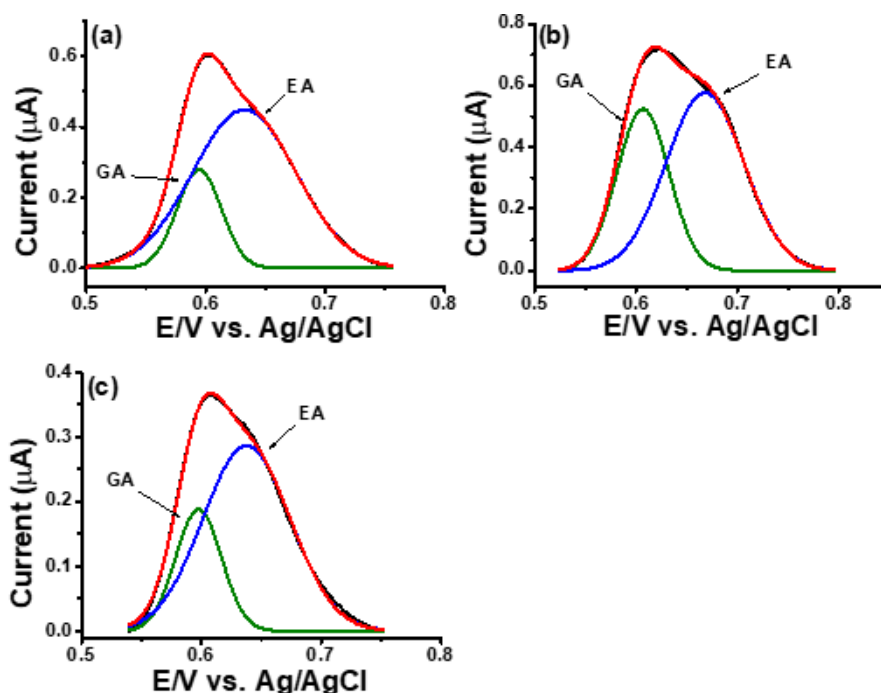


**Figure 4.9.** Resolved SWV of a standard mixture (10  $\mu\text{M}$  GA and 3  $\mu\text{M}$  EA) upon application of peak deconvolution using Origin Pro 8.5.1. The supporting electrolyte was 100 mM phosphate buffer, pH 2 with 5 % EtOH containing (a) 1 %  $\alpha$ -CD, (b) 1 % S- $\beta$ -CD and (c) 1 % HP $\beta$ -CD. Detection was achieved on the BDD electrode vs. Ag/AgCl.

#### 4.3.5 HPLC coupled with the BDD electrode for separation and analysis of GA and EA

Isocratic elution was first investigated for the separation of GA and EA. However, due to the large difference in polarity between the analytes, it proved difficult to sufficiently retain GA without high retention and significant peak broadening of EA occurring. Therefore, gradient elution was applied to shorten the run time and provide sufficient retention of the analytes. The separation was achieved in a linear gradient elution profile with a binary mobile phase mixture of 10 mM formate buffer, pH 3 (A) and ACN (B). The gradient profile involved an initial 2 % B which was followed by a linear increase to 30 % B until 3 min. The next linear increase was until 40 % B to 5 min followed by re-equilibration from 5 to 8 min with 2 % B. A buffer of pH 3 was chosen as it ensures GA (lowest  $\text{pK}_a \sim 4.4$ ) is in its unionised form, enabling its increased retention. The flow rate was set at 1.5 mL/min, the maximum allowed flow rate compatible with the ECD system (**Figure 4.10**).



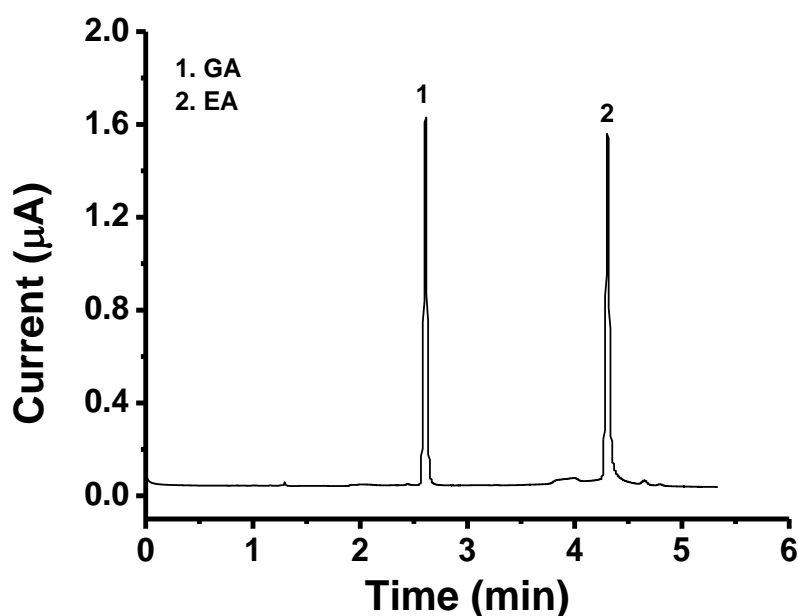


**Figure 4.10.** A 50  $\mu\text{M}$  standard mixture of GA and EA. Column: Agilent XDB  $C_{18}$  (4.6 x 150 mm, 5  $\mu\text{m}$ ), mobile phase flow rate: 1.5 mL/min, injection volume: 5  $\mu\text{L}$ , oxidation potential: + 1.4 V on the BDD electrode vs. Pd/H<sub>2</sub>.

Experiments were then conducted to determine the optimum detection potential by establishing the relationship between the applied working electrode potential and the detector response for the analytes. At + 1.6 V and + 1.8 V, a noticeable increase in background current and baseline drift occurred. The baseline noise also increased due to the electro-oxidation of possible impurities present in the mobile phase. The oxidation potential of + 1.4 V provided sufficient sensitivity with low background noise, therefore, it was chosen as the optimum detection potential (**Figures 4.11 and 4.12**).

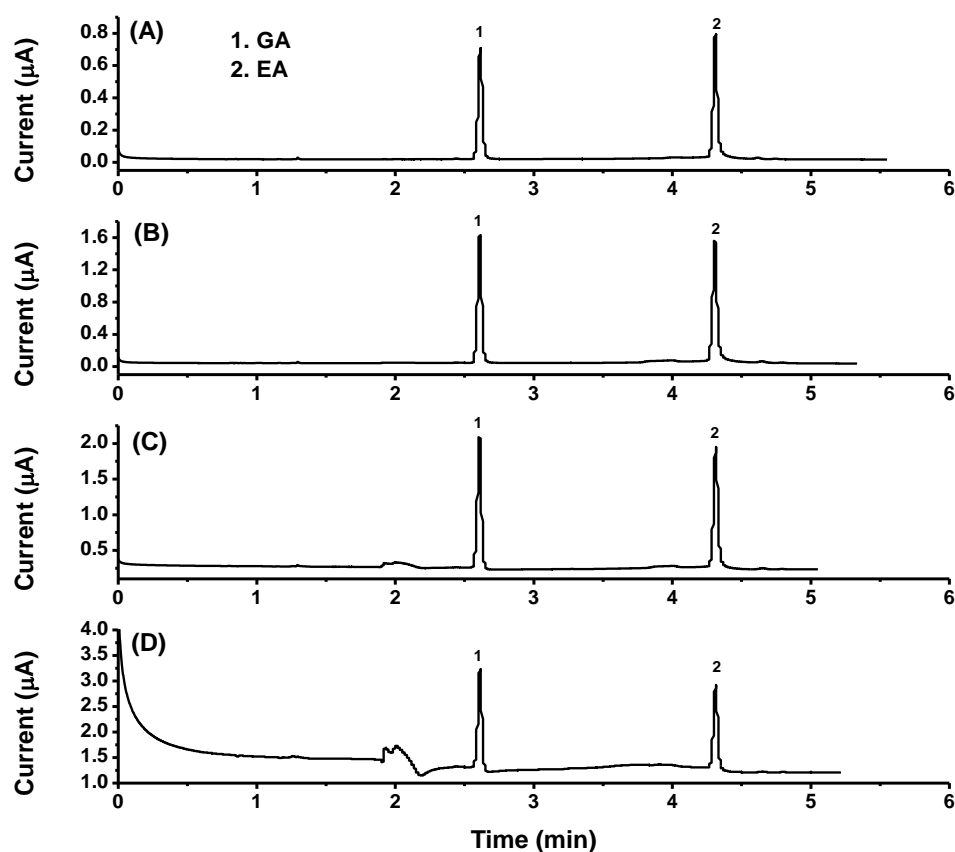


**Figure 4.11.** The effect of oxidation potential on the detection of 100  $\mu\text{M}$  each of GA and EA. Oxidation potential: (A) + 1.2 V, (B) + 1.4 V, (C) + 1.6 V and (D) + 1.8 V on the BDD electrode vs.  $\text{Pd}/\text{H}_2$ . Column: Agilent XDB  $\text{C}_{18}$  (4.6 x 150 mm, 5  $\mu\text{m}$ ), mobile phase flow rate: 1.5 mL/min, injection volume: 5  $\mu\text{L}$ .

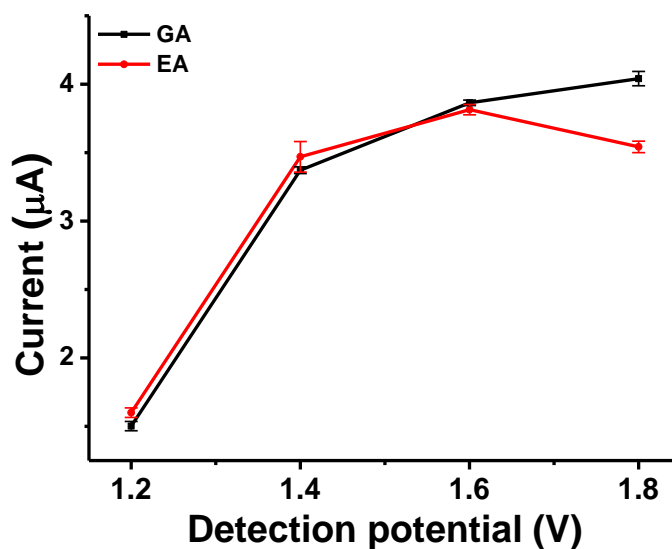


**Figure 4.12.** The plot of detection potential (V) versus current ( $\mu\text{A}$ ) on the BDD electrode vs.  $\text{Pd}/\text{H}_2$ . Column: Agilent XDB  $\text{C}_{18}$  (4.6 x 150 mm, 5  $\mu\text{m}$ ), mobile phase flow rate: 1.5 mL/min, injection volume: 5  $\mu\text{L}$ .

#### 4.3.6 Analytical performance for the analysis of GA and EA in whiskey

Analytical parameters such as linearity of calibration curves, LODs and precision data were determined for ellagic and gallic acids (**Table 4.1**). The LODs of GA and EA were 60 and 200 nM, respectively, considerably lower than the LODs determined with UV detection under the same separation conditions (**Table 4.2**), and also lower than previously reported LC-UV methods<sup>23–25</sup>. Calibration curves were evaluated based on the relationship between the concentrations and the corresponding peak areas of the acids. All measurements were performed in triplicate with linearity from 1–30 µM. Calibration curves and plots are presented in **Figure 4.13**. Intra-day and inter-day precision were in the range of 0.23–0.47 % and 0.64–1.02 % RSD, respectively.

**Table 4.1.** Linear regression parameters of calibration curves and precision data for EA and GA detected with HPLC-ECD at + 1.4 V.

Analyte	Linear range (µM)	Linear regression equation	Correlation coefficient ( $R^2$ )	Intra-day (%) <sup>a</sup>	Inter-day (%) <sup>b</sup>
GA	1–30	$I = 6.32 \times 10^{-8} C + 2.89 \times 10^{-10}$	0.999	0.47	1.02
EA	1–30	$I = 4.25 \times 10^{-8} C - 6.77 \times 10^{-9}$	0.995	0.23	0.64

<sup>a</sup> Intra-day (%) calculated from five measurements within one experiment for the retention time at 100 µM of each standard.

<sup>b</sup> Inter-day (%) calculated from five measurements within four different experiments for the retention time at 100 µM of each standard.

**Table 4.2.** LODs obtained with ECD and UV detection.

Analyte	LOD <sup>a</sup> HPLC-ECD	LOD <sup>b</sup> HPLC-UV
GA	60 nM	1 µM
EA	200 nM	1.5 µM

<sup>a</sup> LOD (S/N=3) at + 1.4 V.

<sup>b</sup> LOD (S/N=3) at 272 nm.

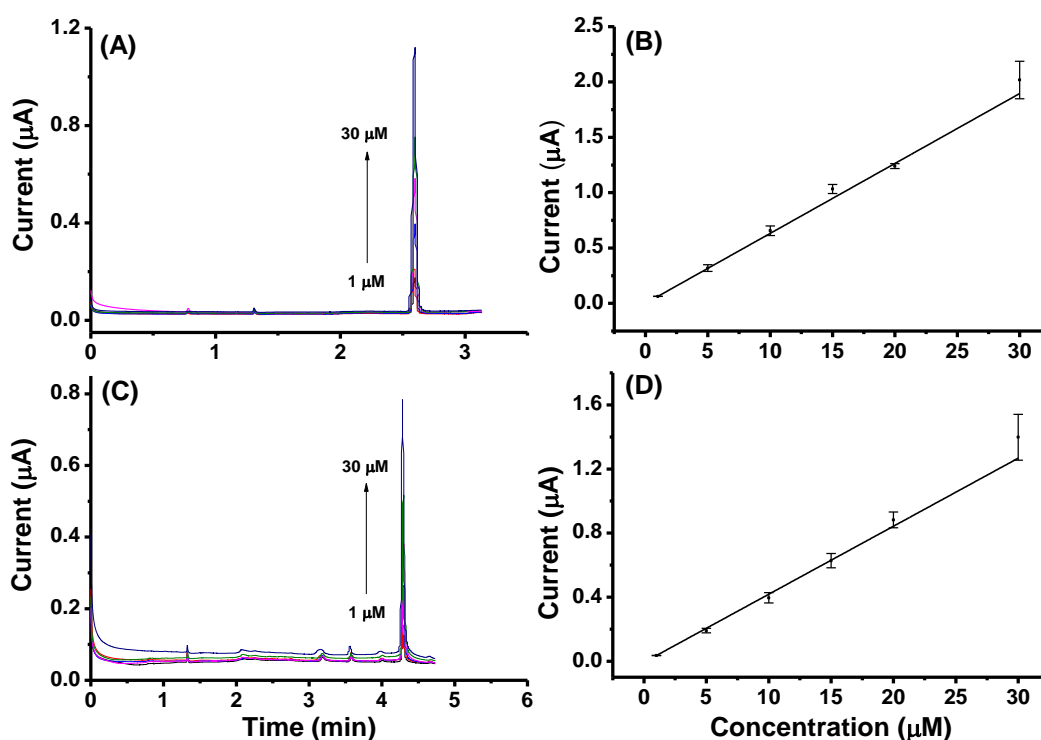


**Figure 4.13.** (A) Calibration curve and (B) plot of GA and (C) calibration curve and (D) plot of EA. Column: Agilent XDB  $C_{18}$  column (4.6 x 150 mm, 5  $\mu$ m), mobile phase flow rate: 1.5 mL/min, injection volume: 5  $\mu$ L, oxidation potential: + 1.4 V on the BDD electrode vs. Pd/H<sub>2</sub>.

#### 4.3.7 Detection of gallic and ellagic acids in whiskey samples

The optimal HPLC-ECD method was then applied to determine the concentrations of GA and its derivative, EA in three whiskey samples (**Figure 4.14**). Highland (14-year-old) whiskey was found to contain higher concentrations than both Islay (10-year-old) and Scotch (exact age unknown) whiskeys (**Table 4.3**). This is expected, as the concentrations of gallic and ellagic acids in whiskey are proven to increase with an increase in maturation age<sup>26</sup>. RSD % values of 1.4-3.19 % and 1.31-2.85 % for the peak areas of GA and EA, respectively, in the whiskeys (n=3), indicate high reliability in the concentrations of the acids determined. Concentrations of 1-35  $\mu$ M and 8-99  $\mu$ M of GA and EA, respectively, are reported in unidentified Scotch whiskeys<sup>27</sup>. EA was also identified as the predominant phenolic constituent in both single-malt Scotch (~33  $\mu$ M) and blended Scotch (~17  $\mu$ M) whiskey<sup>28</sup>. The presence of other peaks in the whiskey samples, encompassing several phenolic compounds, have previously been identified and reported by HPLC coupled with a BDD electrode<sup>29</sup>.

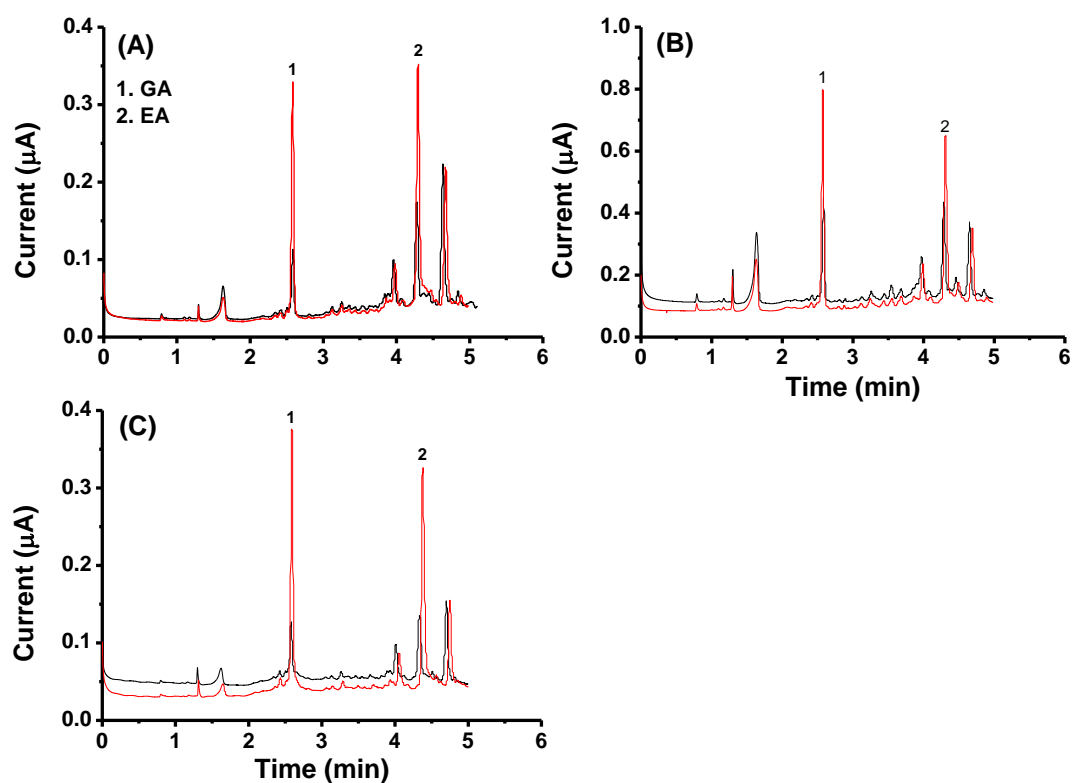


**Figure 4.14.** Representative HPLC-ECD chromatograms of (A) Islay whiskey, (B) Highland whiskey and (C) Scotch whiskey. Whiskey (black line) and spiked with 10  $\mu\text{M}$  each of GA and EA (red line). Column: Agilent XDB  $\text{C}_{18}$  (4.6  $\times$  150 mm, 5  $\mu\text{m}$ ), mobile phase flow rate: 1.5 mL/min, injection volume: 5  $\mu\text{L}$ , oxidation potential: + 1.4 V on the BDD electrode vs.  $\text{Pd}/\text{H}_2$ .

**Table 4.3.** The concentrations of gallic and ellagic acids in three whiskey samples ( $n = 3$ ).

Analyte	$\mu\text{M}$		
	Islay	Highland	Scotch
GA	$7.98 \pm 0.17$	$33.77 \pm 1.6$	$5.86 \pm 0.41$
EA	$25.10 \pm 1.15$	$55.41 \pm 0.7$	$15.85 \pm 1.24$

## 4.4 Conclusions

Electro-oxidation of EA and GA at low pH produces two anodic peaks, with two smaller cathodic peaks for EA and three smaller cathodic peaks for GA, indicating quasi-reversible processes at the electrode surface. At high pH, there was a noticeable reduction in peak intensities as a result of chemical deprotonation of these two acids. HPLC-ECD was successfully applied for the detection of GA and EA in Islay,

Highland and Scotch whiskeys. GA and EA are identified as possible discriminants for single malt whiskey<sup>14</sup>. Higher concentrations of both acids were found in Highland whiskey due to a longer period of maturation of this whiskey compared to its counterparts. As GA and EA are naturally occurring polyphenols, the nanomolar detection achieved with HPLC-ECD at a BDD electrode may prove attractive towards their detection in the food and medical fields. GA has also been used extensively in the manufacturing of paper, ink dye and tanning<sup>30</sup>, whereas its dimer is used in food preservation<sup>31</sup>.

## 4.5 References

1. Shahidi, F. & Yeo, J. D. Bioactivities of phenolics by focusing on suppression of chronic diseases: A review. *Int. J. Mol. Sci.* **19**, 1–16 (2018).
2. Dai, J. & Mumper, R. J. Plant phenolics: Extraction, analysis and their antioxidant and anticancer properties. *Molecules* **15**, 7313–7352 (2010).
3. Cabrera, C., Artacho, R. & Giménez, R. Beneficial effects of green tea—A review. *J. Am. Coll. Nutr.* **25**, 79–99 (2006).
4. Muir, R. M. *et al.* Mechanism of gallic acid biosynthesis in bacteria (*Escherichia coli*) and walnut (*Juglans regia*). *Plant Mol. Biol.* **75**, 555–565 (2011).
5. Sharma, M. *et al.* Effects of fruit ellagitannin extracts, ellagic acid, and their colonic metabolite, urolithin A, on Wnt signaling. *J. Agric. Food Chem.* **58**, 3965–3969 (2010).
6. Vivas, N. *et al.* Impact of ethanol content on the scavenging activities of oak wood C-glycosidic ellagitannins. Application to the evaluation of the nutritional status of spirits. *J. Inst. Brew.* **119**, 116–125 (2013).
7. Cabrera, C., Mejia-Lopez, H., Navarro-Alarcon, M., Olalla, M. Determination of gallic acid in commercial brandies using high performance liquid chromatography. *Cienc. Tecnol. Aliment* **3**, 13–20 (2000).
8. Sangeetha, N. S. & Narayanan, S. S. A novel bimediator amperometric sensor for electrocatalytic oxidation of gallic acid and reduction of hydrogen peroxide. *Anal. Chim. Acta* **828**, 34–45 (2014).
9. Ghaani, M. *et al.* Development of an electrochemical nanosensor for the determination of gallic acid in food. *Anal. Methods* **8**, 1103–1110 (2016).
10. Tashkhourian, J., Ana, S. F. N., Hashemnia, S. & Hormozi-Nezhad, M. R. Construction of a modified carbon paste electrode based on TiO<sub>2</sub> nanoparticles for the determination of gallic acid. *J. Solid State Electrochem.* **17**, 157–165

(2013).

11. Mitranță, V. A., Cheregi, M. C. & David, I. G. Alternative methods for antioxidants determination. *Proceedings* **29**, 35 (2019).
12. Sakthinathan, S. *et al.* A highly selective and sensitive detection of ellagic acid by using ethylenediamine ligand based cobalt (II) complex modified glassy carbon electrode. *Int. J. Electrochem. Sci.* **12**, 6829–6841 (2017).
13. Guiberteau-Cabanillas, A. *et al.* Electroanalytical behavior of gallic and ellagic acid using graphene modified screen-printed electrodes. Method for the determination of total low oxidation potential phenolic compounds content in cork boiling waters. *Electroanalysis* **27**, 177–184 (2015).
14. Stupak, M., Goodall, I., Tomaniova, M., Pulkrabova, J. & Hajslova, J. A novel approach to assess the quality and authenticity of Scotch whisky based on gas chromatography coupled to high resolution mass spectrometry. *Anal. Chim. Acta* **1042**, 60–70 (2018).
15. Abdel-Hamid, R. & Newair, E. F. Electrochemical behavior of antioxidants: I. Mechanistic study on electrochemical oxidation of gallic acid in aqueous solutions at glassy-carbon electrode. *J. Electroanal. Chem.* **657**, 107–112 (2011).
16. Tóth, I. Y. *et al.* Mechanism of in situ surface polymerization of gallic acid in an environmental-inspired preparation of carboxylated core-shell magnetite nanoparticles. *Langmuir* **30**, 15451–15461 (2014).
17. Romero-Montero, A. *et al.* Growth of epithelial cells on films of enzymatically synthesized poly(gallic acid) crosslinked to carboxymethylcellulose. *RSC Adv.* **7**, 17660–17669 (2017).
18. Eslami, A. C., Pasanphan, W., Wagner, B. A. & Buettner, G. R. Free radicals produced by the oxidation of gallic acid: An electron paramagnetic resonance study. *Chem. Cent. J.* **4**, 1–4 (2010).
19. Simić, A. Z. *et al.* Study of ellagic acid electro-oxidation mechanism.



*Monatshefte für Chemie* **144**, 121–128 (2013).

20. Thakur, K. & Pitre, K. S. Polarographic (DCP & DPP) determination of ellagic acid in strawberries & pharmaceutical formulations. *J. Chinese Chem. Soc.* **55**, 143–146 (2008).
21. Hayes, P. E., Glennon, J. D., Buzid, A. & Luong, J. H. T. Simultaneous electroanalysis of guaiacol and its analogs based on their differential complexation with  $\alpha$ -cyclodextrin on Nafion modified boron-doped diamond electrode. *Electroanalysis* **32**, 119–127 (2020).
22. Teodoro, G. R. *et al.* Gallic acid/hydroxypropyl- $\beta$ -cyclodextrin complex: Improving solubility for application on in vitro/in vivo *Candida albicans* biofilms. *PLoS One* **12**, 1–15 (2017).
23. Fernandes, F. H. A., de Batista, R. S. A., de Medeiros, F. D., Santos, F. S. & Medeiros, A. C. D. Development of a rapid and simple HPLC-UV method for determination of gallic acid in *Schinopsis brasiliensis*. *Brazilian J. Pharmacogn.* **25**, 208–211 (2015).
24. Shalavadi, M. H., Chandrashekhar, V. M., Muchchandi, I. S. High-performance liquid chromatography analysis of gallic acid and kaempferol in chloroform and ethanol extract of *Cassia hirsuta* seeds. *Int. J. Green Pharm.* **13**, 236–241 (2019).
25. Assunção, P. I. D., Conceição, E. C. Da, Borges, L. L. & Paula, J. A. M. De. Development and validation of a HPLC-UV method for the evaluation of ellagic acid in liquid extracts of *Eugenia uniflora* L. (Myrtaceae) leaves and its ultrasound-assisted extraction optimization. *Evidence-based Complement. Altern. Med.* **2017**, 1–9 (2017).
26. Koga, K., Taguchi, A., Koshimizu, S., Suwa, Y., Yamada, Y., Shirasaka, N., Yoshizumi, H. Reactive oxygen scavenging activity of matured whiskey and its active polyphenols. *J. Food Sci.* **72**, 212–217 (2007).
27. Bukovsky-Reyes, S. E. R., Lowe, L. E., Brandon, W. M. & Owens, J. E.

Measurement of antioxidants in distilled spirits by a silver nanoparticle assay. *J. Inst. Brew.* **124**, 291–299 (2018).

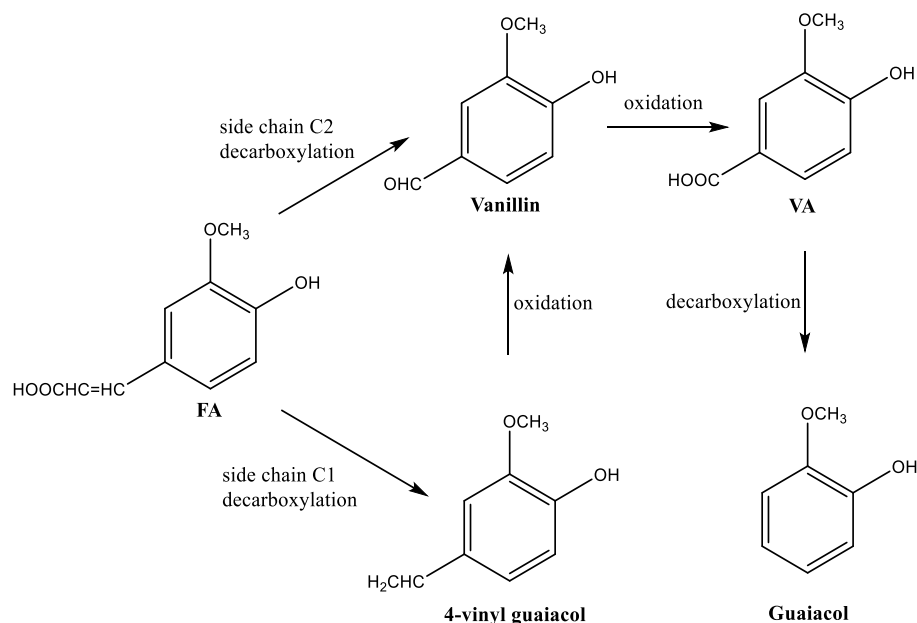
28. Goldberg, D. M., Hoffman, B., Yang, J. & Soleas, G. J. Phenolic constituents, furans, and total antioxidant status of distilled spirits. *J. Agric. Food Chem.* **47**, 3978–3985 (1999).
29. Hayes, P. E., Luong, J. H. T., Gilchrist, E. S., Buzid, A. & Glennon, J. D. Profiling of phenolic flavorings using core-shell reversed-phase liquid chromatography with electrochemical detection at a boron-doped diamond electrode. *J. Chromatogr. A* **1612**, 460649 (2020).
30. Covington, A. D. Modern tanning chemistry. *Chem. Soc. Rev.* 111–126 (1997).
31. Kumar, A. S., Ji, Y. M., Sornambikai, S., Chen, P. Y., Shih, P. Flow injection analysis of ellagic acid in cosmetic skin-whitening creams using a dendritic nanostructured copper-gold alloy plated screen-printed carbon electrode. *Int. J. Electrochem. Sci.* **6**, 5344–5356 (2011).

## **Chapter 5**

**Rapid nanomolar detection of guaiacol from its precursors  
using a core-shell reversed-phase column coupled with a  
boron-doped diamond electrode**

## 5.1 Introduction

Pasteurisation followed by storage of fruit juice and beverages at low pHs was considered effective to prevent bacterial spoilage until an incident occurred in Germany that involved pasteurised apple juice<sup>1</sup>. *Alicyclobacillus acidoterrestris* (*A. acidoterrestris*), a species from the genus *Alicyclobacillus*, was identified as the microorganism that was responsible for the spoilage while some later incidents were caused by other *Alicyclobacillus* species (spp.)<sup>2</sup>. *Alicyclobacillus* spp. are Gram-positive, non-pathogenic, thermophilic and acidophilic spore-forming bacteria. The major lipid components of the bacterial membrane are  $\omega$ -alicyclic fatty acids, which might forbear heat and acid tolerance. Thus, these bacteria can survive during the pasteurisation process and subsequently can germinate in fruit juices and beverages. *Alicyclobacillus* spp. are capable of growing in a wide temperature range of 20-70 °C and in pHs from 2.5 to 6<sup>3</sup>. It is difficult to detect spoilage by *Alicyclobacillus* spp. as there are no obvious indications of contamination. No gas is released and there are no significant changes in the fruit juice pH or turbidity. However, the contaminated juice exhibits a medicinal or antiseptic-like off-flavour, and guaiacol (2-methoxyphenol) has been identified as the metabolite responsible. Sensory recognition thresholds for guaiacol in apple juice are reported to be between 4 nM and 16 nM<sup>4-6</sup>. It is known from the metabolic pathway of *Alicyclobacillus* spp., that guaiacol is metabolised from ferulic acid (FA) through two intermediates: vanillin and vanillic acid (VA)<sup>3</sup> (**Scheme 5.1**). The two precursors of guaiacol are VA and vanillin<sup>7,8</sup>. However, the conversion of VA to guaiacol is faster than that of vanillin to guaiacol<sup>7</sup>. Guaiacol cannot be produced in the absence of *Alicyclobacillus* spp., nor can *Alicyclobacillus* spp. produce guaiacol in the absence of its precursors<sup>7</sup>. Guaiacol production is affected by storage temperature, heat shock, incubation temperature<sup>3</sup>, and *Alicyclobacillus* spp. cell density. A strong odour is detectable after four days when the bacterial population reaches 10<sup>5</sup> colony-forming units (CFU)/mL<sup>9</sup>.



**Scheme 5.1.** Guaiacol formation scheme from lignin as the starting product<sup>3</sup>.

Considering the serious economic implications of spoilage for manufacturers, rapid and sensitive methods are required for its detection. Traditional microbiological culturing methods, although sensitive, are prolonged (they can require 2-10 days to produce a result) and, therefore, not practical for the routine monitoring of contamination. Cells/spores detection is carried out through use of enzyme-linked immunosorbent assays (ELISA)<sup>10</sup>, magnetic fluorescent nanocomposites<sup>11</sup>, and Fourier-transform-infrared spectroscopy (FTIR)<sup>12</sup>, with an analysis time ranging from 1.5 h to 3 days. Nucleic acid-based methods are carried out using polymerase chain reaction (PCR)<sup>13,14</sup>. The detection of *A. acidoterrestris* in apple juice by measuring the impedance change through the formation of CO<sub>2</sub> is reported<sup>15</sup>. An artificial sensing system, i.e., electronic nose<sup>16</sup>, has been reported to offer limits of detection (LODs) that range from 2 µM to 4 µM for guaiacol in apple juice.

Gas chromatography (GC) and high-performance liquid chromatography (HPLC) are the most frequently applied analytical techniques for guaiacol detection in fruit juices. A LOD of 4 nM was obtained using solid-phase microextraction (SPME) and GC-mass spectrometry (GC-MS) with selective ion monitoring<sup>17</sup>. Bianchi *et al.* determined the volatile profile of orange juice that was contaminated with *A. acidoterrestris*, whilst they also confirming that guaiacol was not produced when the cell density was below 10<sup>5</sup> CFU/mL<sup>18</sup>. HPLC with ultra-violet (UV) detection can be

applied to investigate the formation of guaiacol from its precursors<sup>7,8,19</sup>. HPLC-UV offers similar detection sensitivity to that offered by spectrophotometric methods<sup>20</sup>. The determination of levels of phenolic acids, such as vanillin and VA, through use of capillary electrophoresis (CE) with field-amplified sample stacking (FASS), has recently been reported<sup>21</sup>.

A boron-doped diamond (BDD) electrode offers several appealing features that include anti-fouling properties together with low and stable background currents<sup>22,23</sup>. Direct electrochemical sensing of guaiacol through the use of a BDD electrode that has been modified with Nafion is reported to achieve a LOD of 200 nM<sup>24</sup>. A LOD of 160 nM for vanillin is achieved using a BDD electrode without surface modification<sup>25</sup>. HPLC together with electrochemical detection (ECD) provides enhanced selectivity and sensitivity in comparison with UV detection, hence it suitable for the determination of extremely low levels of electrochemically active compounds. HPLC-ECD that is based on a diamond electrode offers an LOD of 3.9 and 5.7 nM for guaiacol and vanillin, respectively, in vanilla extract with a total analysis duration of ~ 19 min<sup>26</sup>. VA, FA, and vanillin have also been detected in wort and beer<sup>27</sup>, and in honey<sup>28</sup>, through the application of HPLC coupled to a glassy carbon electrode (GCE). HPLC-ECD with a BDD electrode also offers sensitive detection of antioxidants<sup>29</sup>, benzodiazepines<sup>30</sup>, parabens<sup>31</sup>, and beverage flavourings<sup>32</sup>.

This study reports the optimisation and validation of an HPLC-ECD method that employs a BDD electrode for the simultaneous nanomolar detection of guaiacol and its three precursors in fruit juices and beverages. Of importance is the system's capability to separate and detect guaiacol and its precursors within 60 s with LODs ranging from 10-30 nM.

## **5.2 Experimental**

### **5.2.1 Reagents, standard solutions, and samples**

Ammonium formate, ammonium acetate, formic acid, acetic acid, phosphoric acid, sodium phosphate monobasic, acetonitrile (ACN), VA, vanillin, FA, and guaiacol of the highest analytical grade were purchased from Sigma-Aldrich (Dublin, Ireland). Stock solutions (5 mM) of the four standards were prepared in ACN daily before use.

Working solutions were prepared by addition of the stock solutions to the mobile phase. Aqueous solutions were prepared in deionised water (Millipore, Ireland). A beverage sample was purchased from a local supermarket in Co. Cork, Ireland. Before injection, 500  $\mu\text{L}$  of the beverage sample was filtered through an Econofltr Nylon membrane (13 mm, 0.2  $\mu\text{m}$ ) and diluted with 1000  $\mu\text{L}$  of the mobile phase.

### 5.2.2 Cyclic voltammetry

Cyclic voltammetry (CV) was applied to investigate the electrochemical behaviour of VA, vanillin, FA, and guaiacol. The electrochemical cell consists of three electrodes; a BDD working electrode (B/C ratio in the gaseous phase of 1000 ppm, 3 mm diameter, Windsor Scientific, Slough Berkshire, UK), an Ag/AgCl/3 M KCl reference electrode (BASi Analytical Instruments, West Layette, IN), and a Pt wire counter electrode (Sigma-Aldrich, Dublin, Ireland). A supporting electrolyte consisting of 100 mM phosphate buffer, pH 2 was used in all measurements. Electroanalysis was performed by a CHI1040A electrochemical workstation (CH Instrument, Austin, TX).

### 5.2.3 Apparatus

The chromatographic analyses were carried out using an Agilent HPLC system (Agilent 1200 LC series) containing a binary pump (model G1312B), degasser (model G1379B), autosampler (model G1367D), and a UV diode array detector (model G1315C). The Agilent Chemstation software was utilised for instrument control and UV data analysis. HPLC separation was based on a HALO C<sub>18</sub> core-shell column (3.0 x 50 mm) consisting of 2.7  $\mu\text{m}$  particles, (Apex Scientific, Co. Kildare, Ireland). The thin layer flow cell (volume = 0.7  $\mu\text{L}$ , Apex Scientific, Kildare, Ireland) encompassed a working BDD electrode (8 mm diameter), a HyREF (Pd/H<sub>2</sub>) reference electrode, and a carbon loaded polytetrafluoroethylene (PTFE) counter electrode. CHI660E electrochemical workstation was applied for data analysis (CH Instrument, Austin, Texas). Prior to analysis, the electrode was wiped with acetone followed by H<sub>2</sub>O. When not in use, the electrode was stored in the flow cell.

### 5.2.4 Chromatographic conditions

The four analytes were separated isocratically using a mobile phase of 10 mM formate, pH 3: ACN (83:17, v/v, %). A mobile phase of pH 4.5 and 6 was prepared using acetate buffer at a concentration 10 mM. The mobile phase was filtered daily through a 0.45  $\mu\text{m}$  Nylon Whatman filter (Sigma-Aldrich) and then sonicated. The column was equilibrated for 20 min before analysis. The total analysis time was below 60 s with a corresponding flow rate of 1.3 mL/min. The analyses were conducted at a column temperature of 25  $^{\circ}\text{C}$  with an injection volume of 5  $\mu\text{L}$ . HPLC-ECD was set at + 1.6 V and HPLC-UV detection was performed at 210 nm.

### 5.2.5 Method validation

The proposed method was validated in terms of linearity and linear range, LODs, and intra-day and inter-day precision. The linearity and linear range were established through the analytical curve determined at six concentration levels. All analyses were performed in triplicate and the data presented as mean  $\pm$  standard deviation (SD). A signal-to-noise (S/N) ratio of 3 and 10 were used for LODs and LOQs, respectively. The method precision, i.e., the relative standard deviation (RSD) was determined by five repetitive measurements of a mixture (50  $\mu\text{M}$  of each standard) within one day (intra-day) and five measurements of the same concentrations over five days (inter-day).

## 5.3 Results and discussion

### 5.3.1 Electrochemical behaviour of VA, vanillin, FA, and guaiacol

Representative CVs of the four analytes in a potential range of - 0.5 to + 1.5 V are shown in **Figure 5.1**. VA exhibits a sharp oxidation peak at + 1.04 V with two reduction peaks at + 0.31 V and + 0.87 V in the reverse scan (**Figure 5.1A**). VA molecules undergo a first oxidation step involving the liberation of one proton ( $\text{H}^+$ ) and two electrons ( $\text{e}^-$ ), leading to the formation of three phenoxonium carbocations in mesomeric forms (A), (B) and (C). Based on the electronic effects of methoxy and carboxy groups, the carbocation (A) was the most stable and rapidly subject to hydrolysis to form 3,4-dioxobenzoic acid (A') and methanol (**Scheme 5.2**). This



reaction pathway of VA oxidation by the electro-Fenton process has also been suggested by Rekik *et al.*<sup>33</sup> and only one pronounced oxidation step was observed in the CV. In the reverse scan, the reduction of (A') led to the formation of protocatechuic acid (PCA) as represented by a noticeable reduction peak (**Figure 5.1A**).

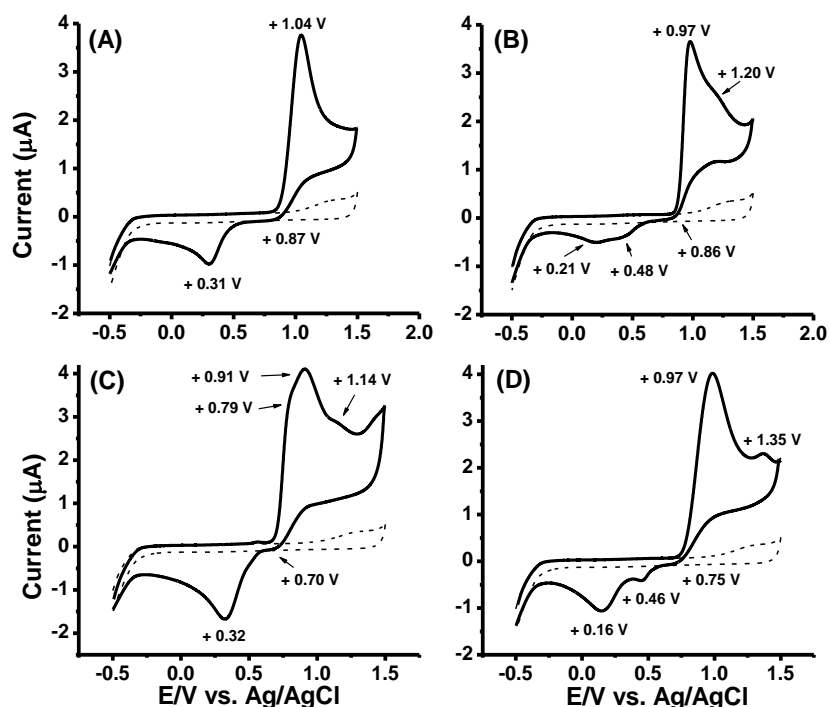
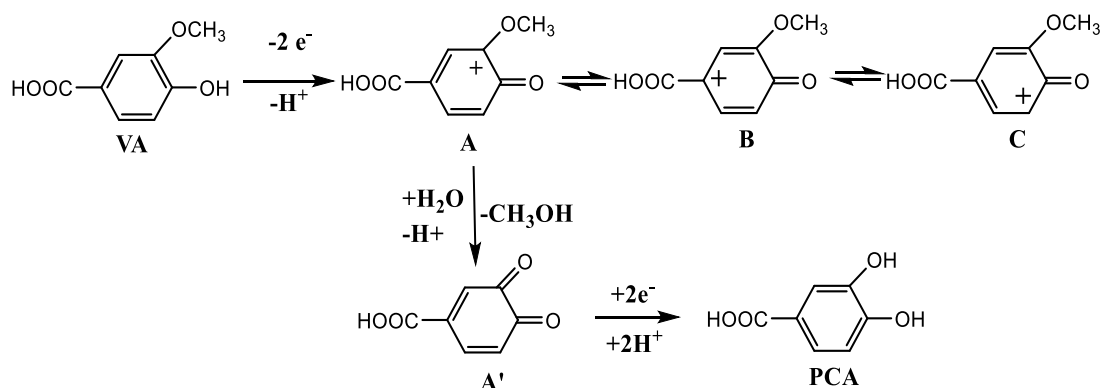


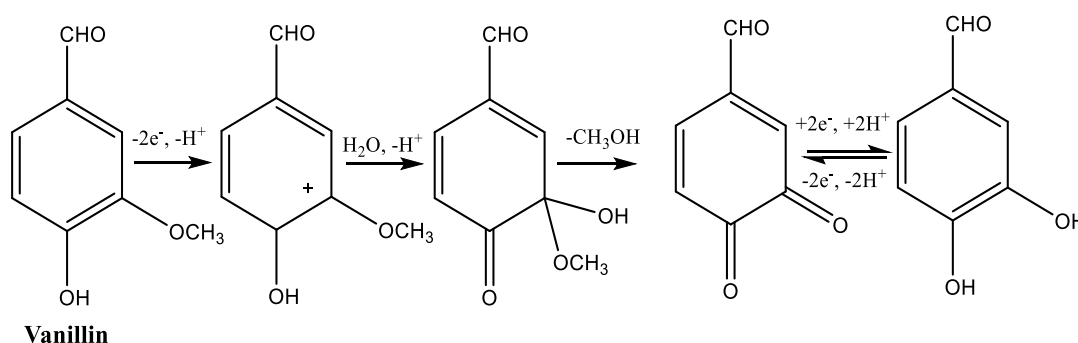
**Figure 5.1.** CV response in the absence (dashed lines) and presence (solid lines) of 100  $\mu\text{M}$  each for (A) VA, (B) vanillin, (C) FA and (D) guaiacol on the bare BDD electrode vs. Ag/AgCl in 100 mM phosphate buffer, pH 2, with a scan rate of 100  $\text{mV s}^{-1}$ .



**Scheme 5.2.** Electrochemical oxidation pathway of VA.

The CV of vanillin shows an oxidation peak at + 0.97 V with a slight shoulder peak evident at + 1.2 V, while in the reverse scan three small reduction peaks are visible at + 0.21, + 0.48 and + 0.86 V (**Figure 5.1B**). A similar oxidation pathway should be

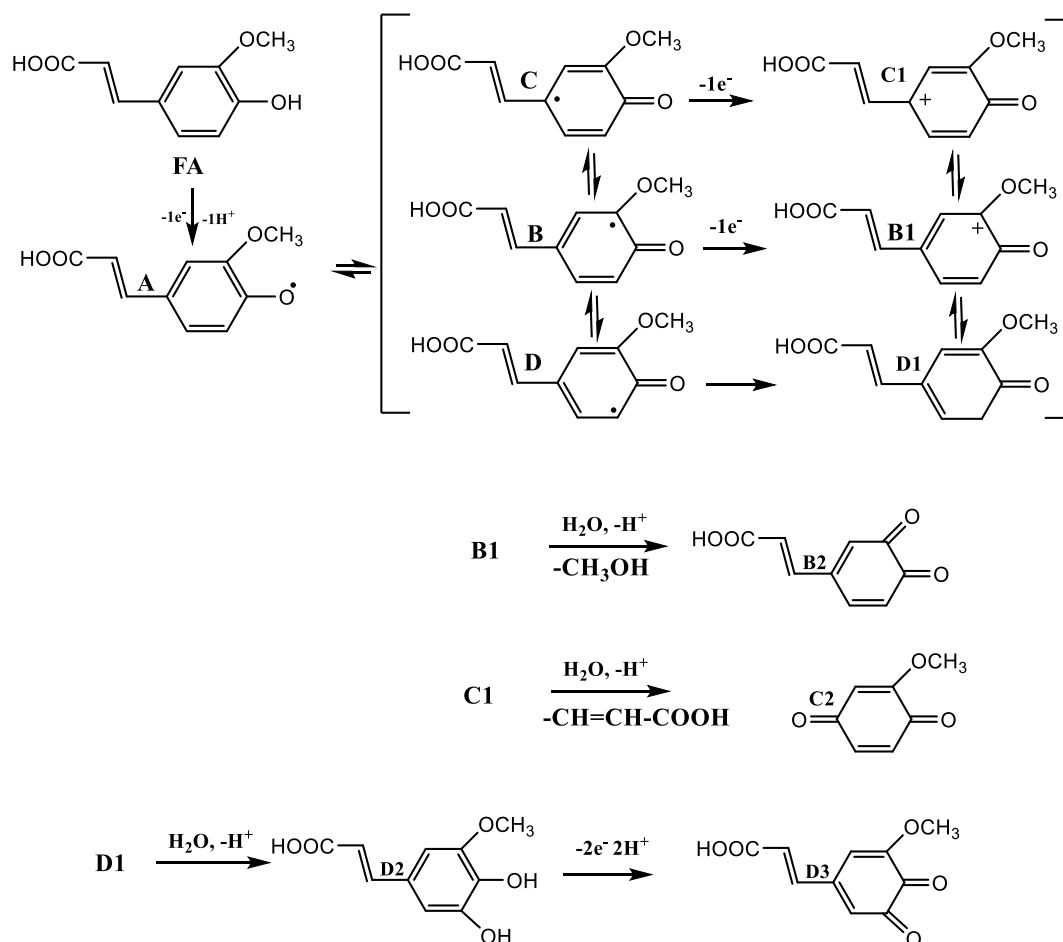
expected from the oxidation of vanillin considering the presence of -CHO in this compound versus the -COOH group in VA. Vanillin first undergoes a  $-2e^-/-H^+$  oxidation followed a hydrolysis reaction to form 1,2-benzoquinone (or ortho-benzoquinone) with the loss of its methoxy substituent (**Scheme 5.3**). Thus, one oxidation peak was expected from the oxidation of vanillin to form 1,2-benzoquinone that was subsequently reduced by the BDD electrode via  $+2e^-/+2H^+$ . This pathway of vanillin oxidation has also been suggested in the electrochemical study of vanillin by a platinum (Pt) electrode in ACN with tetrabutylammonium hexafluorophosphate (TBAHFP) as the supporting electrolyte<sup>34</sup>.



**Scheme 5.3.** The electrochemical oxidation of vanillin to form a 1,2-benzoquinone derivative.

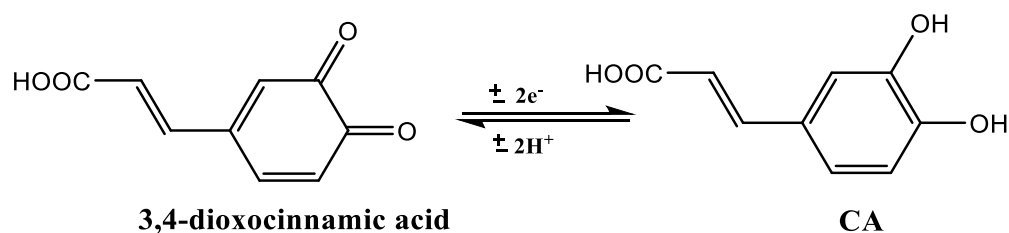
FA displays a broad oxidation peak at + 0.91 V with shoulder peaks evident at + 0.79 V and + 1.14 V. One small reduction peak occurs + 0.70 V with a larger reduction peak at + 0.32 V (**Figure 5.1C**). The oxidation pathway of FA deserves a brief discussion because it involves several products. FA molecules undergo a first electron transfer (loss of one proton and one electron) leading to the formation of phenoxy radicals as represented by four mesomeric forms A, B, C, and D (**Scheme 5.4**). Considering the electronic effects of methoxy, carboxyvinyl, and oxo groups, radical B is the most stable. It then undergoes a second electron transfer to form the carbocation B1. Finally, B1 is subject to hydrolysis to yield 3,4-dioxocinnamic acid (B2) and methanol. Therefore, only one large broad peak was observed from the oxidation wave. C and D are insignificant and subject to a second electron transfer to form the carbocation C1 and D1, respectively. The oxidation of radical C1 leads to the formation of methoxyparabenzoquinone (C2). The carbocation D1 is hydroxylated to 3,4-dihydroxy-5-methoxycinnamic acid (D2), followed by oxidation to yield 3,4-

dioxo-5-methoxycinnamic acid (D3). A detailed discussion of the oxidation of FA can be found elsewhere<sup>35</sup>.



**Scheme 5.4.** The electrochemical oxidation pathway of FA.

The reverse scan of FA exhibited one pronounced peak and a very small second peak, which implied the formation of 3,4-dioxocinnamic acid. During the reverse scan, this acid was reduced to caffeic acid (CA) (**Scheme 5.5**).



**Scheme 5.5.** The reduction of 3,4-dioxocinnamic acid to CA.

It should be noted that the second and smaller reduction peak in the reverse scan could be attributed to the reduction of C2 and D3 to their corresponding reduced forms.

The CV of guaiacol (**Figure 5.1D**) exhibits a broad oxidation peak at + 0.97 V and a small shoulder peak at + 1.35 V. Three reduction peaks are visible at + 0.16, + 0.46 and + 0.75 V. The electrochemical oxidation of guaiacol has previously been discussed.

### 5.3.2 Optimisation of HPLC separation conditions

Guaiacol and its precursors were separated isocratically using a HALO C<sub>18</sub> core-shell column. Initially, the mobile phase was investigated using different ratios of 10 mM formate (pH 3): ACN (v/v) at a flow rate of 1 mL/min, with optimisation based on achieving the fastest analysis time with a satisfactory resolution. With 20 % ACN, vanillin, and FA co-eluted while broader peaks were observed with 15 % ACN. A mobile phase containing 17 % ACN provided a desirable resolution with a rapid analysis time, therefore, it was chosen as the optimum ACN content of the mobile phase (**Figure 5.2**).

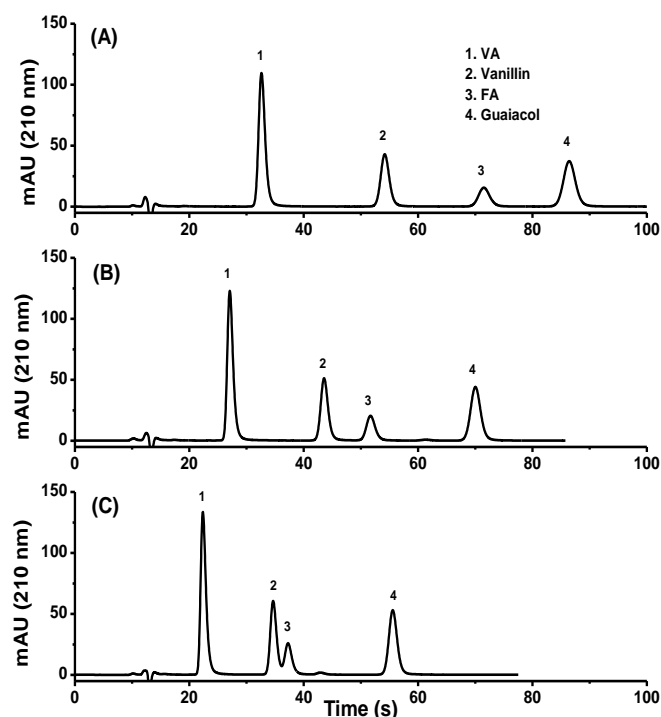


**Figure 5.2.** The effect of mobile phase % ACN on the retention time of 50  $\mu$ M each of VA, vanillin, FA and guaiacol. Mobile phase: ACN:10 mM formate pH 3 (v/v), (A) 15:85, (B) 17:83, (C) 20:80. Column: HALO C<sub>18</sub> core-shell (3.0 x 50 mm, 2.7  $\mu$ m), flow rate: 1 mL/min, injection volume: 5  $\mu$ L, UV detection: 210 nm.

The effect of % ACN on the capacity factor ( $k$ ) of the analytes is shown in **Figure 5.3**.

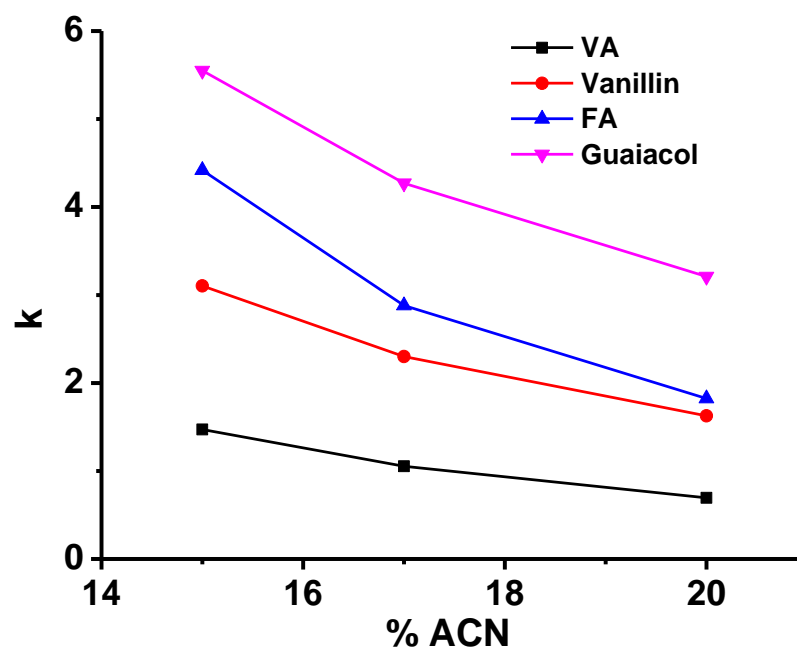


**Figure 5.3.** A plot of % ACN versus  $k$ . Mobile phase: ACN:10 mM formate pH 3 (v/v), at 15, 17 and 20 % ACN. Column: HALO  $C_{18}$  core-shell (3.0 x 50 mm, 2.7  $\mu$ m), flow rate: 1 mL/min, injection volume: 5  $\mu$ L, UV detection: 210 nm.

The effect of mobile phase pH on the selectivity of the analytes was investigated in the range of pH 3-6. The retention of VA and FA decreased as the pH increased, while vanillin and guaiacol remained constant. At pH 4.5, VA (pKa ~ 4.1) and FA (pKa ~ 4.4) are in their ionised state, resulting in their reduced hydrophobicity and eluting as unretained compounds at pH 6. Vanillin (pKa ~ 7.4) and guaiacol (pKa ~ 9.9) were unaffected by this change in pH (**Figure 5.4**). The influence of pH on the  $k$  of the analytes is illustrated in **Figure 5.5**.

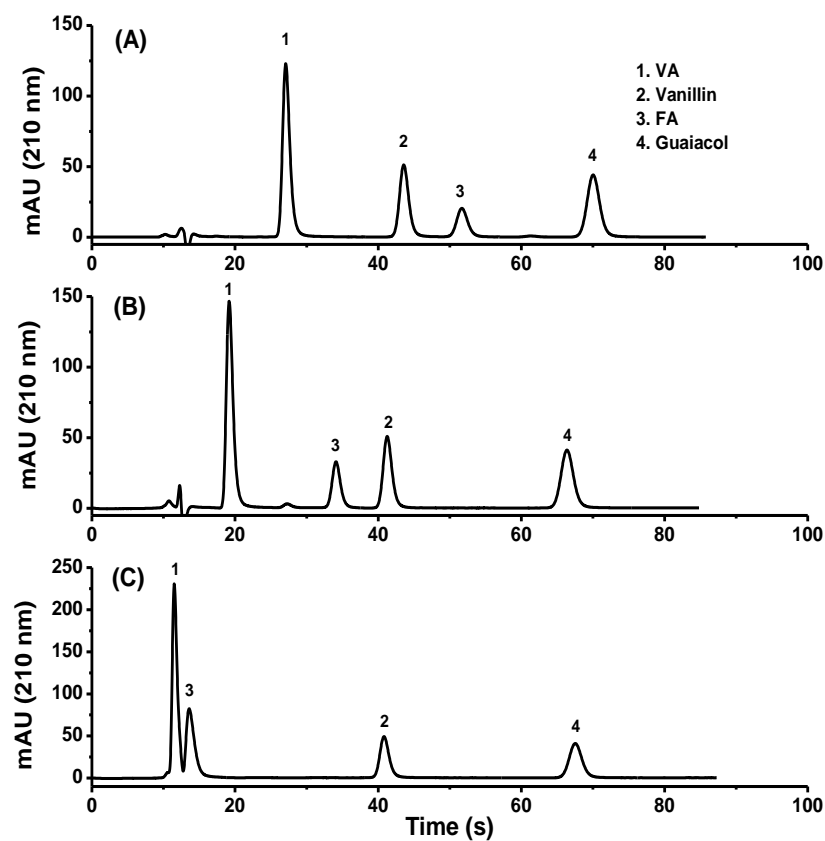


**Figure 5.4.** The effect of the mobile phase pH on the retention time of 50  $\mu\text{M}$  each of VA, vanillin, FA and guaiacol. Mobile phase: 17:83, (A) ACN:10 mM formate pH 3, (B) ACN:10 mM acetate pH 4.5, and (C) ACN:10 mM acetate pH 6. Column: HALO  $\text{C}_{18}$  core-shell (3 x 50 mm, 2.7  $\mu\text{m}$ ), flow rate: 1 mL/min, injection volume: 5  $\mu\text{L}$ , UV detection: 210 nm.

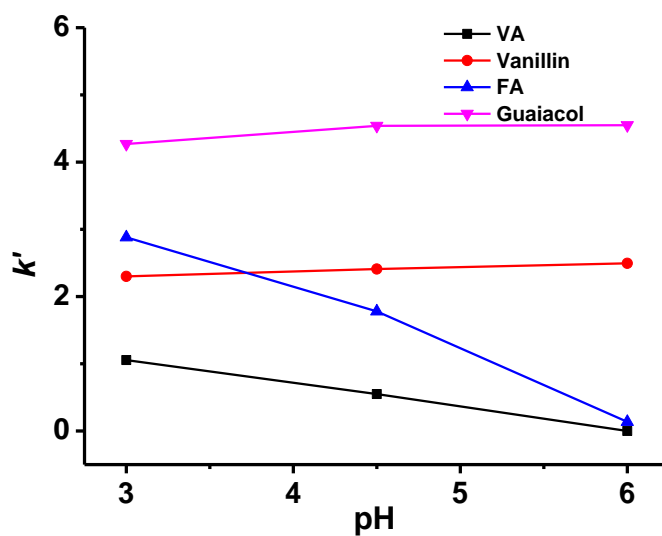


**Figure 5.5.** The plot of pH versus  $k'$ . Mobile phase: ACN:10 mM formate pH 3, 17:83 (v/v) at pH 3, 4.5, and 6. Column: HALO  $\text{C}_{18}$  core-shell (3.0 x 50 mm, 2.7  $\mu\text{m}$ ), flow rate: (A) 0.7 mL/min, (B) 1 mL/min, (C) 1.3 mL/min, injection volume: 5  $\mu\text{L}$ , UV detection: 210 nm.

The mobile phase flow rate was evaluated in the range of 0.7-1.3 mL/min. with a flow rate of 1.3 mL/min giving better peak shape and an analysis time of less than 60 s (**Figure 5.6**). Slower flow rates gave longer run times with broader peaks, while flow rates over 1.3 mL/min were not possible due to higher back pressures generated.

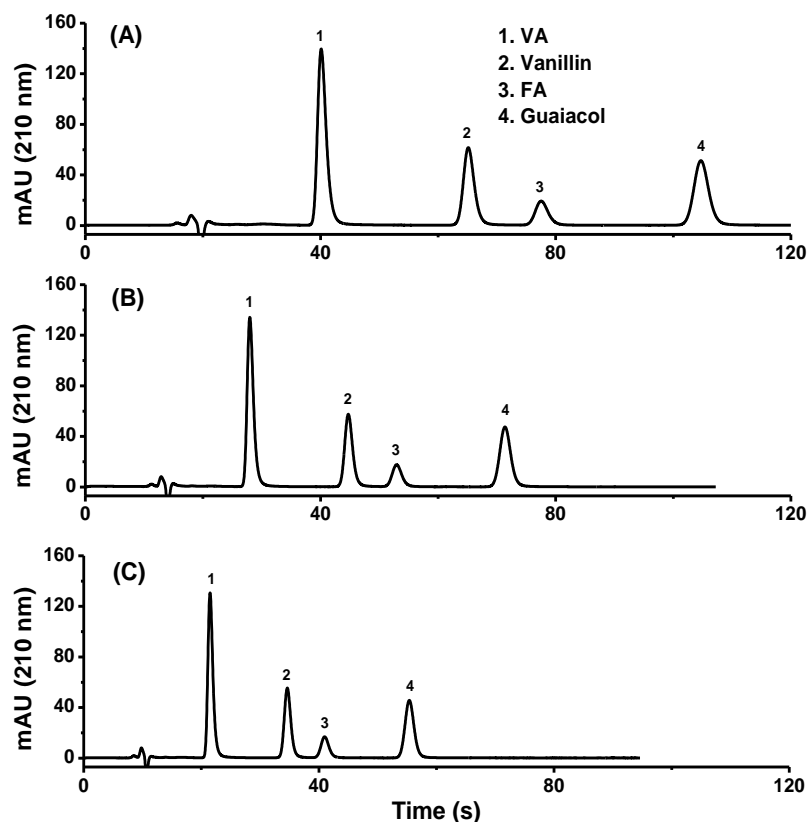


**Figure 5.6.** The effect of the mobile phase flow rate on the retention time of 50  $\mu$ M each of VA, vanillin, FA and guaiacol. Mobile phase: ACN:10 mM formate pH 3, 17:83 (v/v). Column: HALO C<sub>18</sub> core-shell (3.0 x 50 mm, 2.7  $\mu$ m), flow rate: (A) 0.7 mL/min, (B) 1 mL/min, (C) 1.3 mL/min, injection volume: 5  $\mu$ L, UV detection: 210 nm.

### 5.3.3 Selection of detection potential

The required oxidation potential of the four analytes was determined using hydrodynamic voltammetry. The hydrodynamic voltammograms of the analytes investigated in the range of + 1.4 to + 2.0 V under the optimum separation conditions are shown in **Figure 5.7**. Vanillin and VA had a greater oxidation at + 1.8 V, while guaiacols maximum oxidation occurred at + 1.6 V and FA at + 1.4 V. Electro-oxidation of possible impurities present in the mobile phase produces a higher background current and baseline drift at + 1.8 V, therefore, + 1.6 V was chosen as the

optimum oxidation potential for detection. The effect of detection potential (V) on the peak areas of the analytes is shown in **Figure 5.8**.

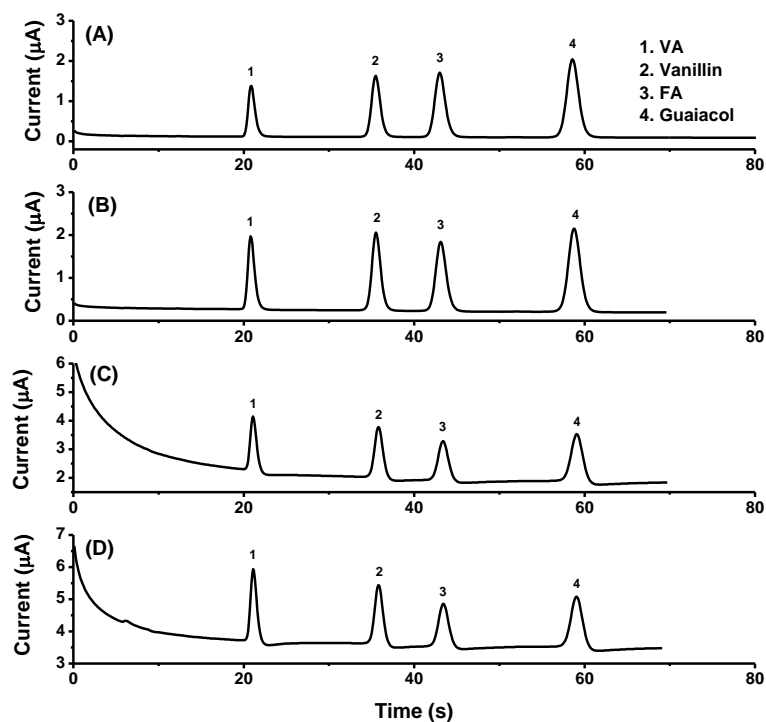


**Figure 5.7.** The effect of oxidation potential on the detection of 50  $\mu\text{M}$  each of VA, vanillin, FA and guaiacol. Oxidation potential: (A) + 1.4 V, (B) + 1.6 V, (C) + 1.8 V and (D) + 2.0 V on the BDD electrode vs. Pd/H<sub>2</sub>. Mobile phase: ACN:10 mM formate pH 3, 17:83 (v/v). Column: HALO C<sub>18</sub> core-shell (3.0 x 50 mm, 2.7  $\mu\text{m}$ ), flow rate: 1.3 mL/min, injection volume: 5  $\mu\text{L}$ .

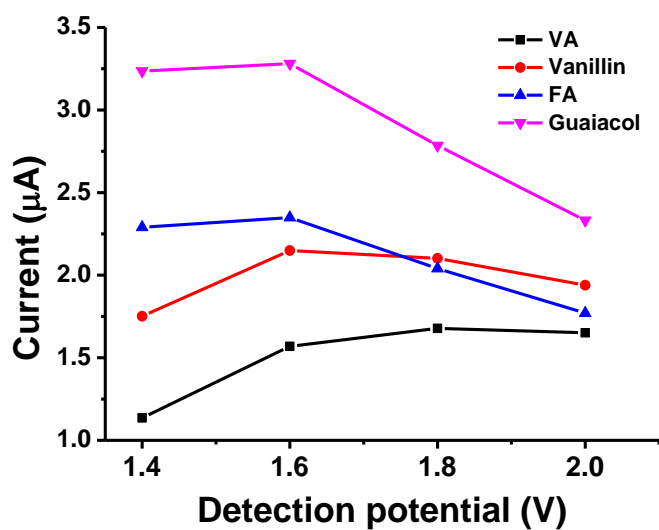


**Figure 5.8.** The plot of detection potential (V) versus current ( $\mu\text{A}$ ) on the BDD electrode vs. Pd/H<sub>2</sub>. Mobile phase: ACN:10 mM formate pH 3 17:83, (v/v). Column: HALO C<sub>18</sub> core-shell (3 x 50 mm, 2.7  $\mu\text{m}$ ), flow rate: 1.3 mL/min, injection volume: 5  $\mu\text{L}$ .



A representative chromatogram of a mixed standard solution containing the four analytes determined under optimum conditions is shown in **Figure 5.9**. Retention factors (*k*) of 2.3, 4.6, 5.9 and 8.3, for VA, vanillin, FA and guaiacol, respectively, indicate satisfactory retention of the analytes under the optimised separation conditions.

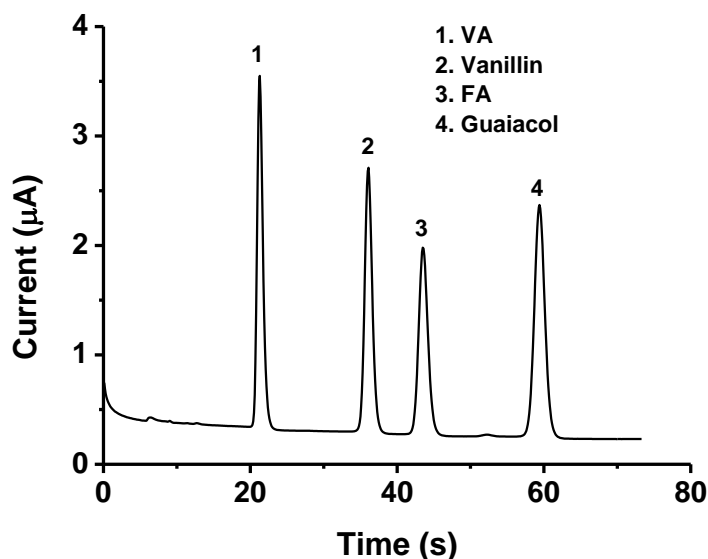


**Figure 5.9.** A representative HPLC-ECD chromatogram of a mixed standard solution (50  $\mu$ M each of VA, vanillin, FA, and guaiacol). Mobile phase: ACN:10 mM formate pH 3, 17:83 (v/v). Column: HALO  $C_{18}$  core-shell (3.0 x 50 mm, 2.7  $\mu$ m), flow rate: 1.3 mL/min, injection volume: 5  $\mu$ L, oxidation potential: + 1.6 V on the BDD electrode vs. Pd/H<sub>2</sub>.

#### 5.3.4 Analytical performance

Under the optimum experimental conditions, the LODs for ECD were determined as 10-30 nM, significantly lower than those achieved with UV detection (**Table 5.1**). The LODs obtained with ECD compare favourably with those determined for guaiacol and vanillin using HPLC-BDD in a previous report<sup>26</sup>, and are also lower than the LODs determined for guaiacol<sup>24</sup> and vanillin<sup>25</sup> using direct electrochemical sensing with a BDD electrode (**Table 5.2**). LOQs were estimated as 50 nM for guaiacol and FA, 70 nM for vanillin, and 90 nM for VA.

**Table 5.1.** The LODs obtained with ECD and UV detection.

Analyte	HPLC-ECD <sup>a</sup>	HPLC-UV <sup>b</sup>
<b>VA</b>	30 nM	0.1 µM
<b>vanillin</b>	20 nM	0.5 µM
<b>FA</b>	10 nM	1 µM
<b>guaiacol</b>	10 nM	0.3 µM

<sup>a</sup> LOD ( $S/N = 3$ ) at + 1.6 V.

<sup>b</sup> LOD ( $S/N = 3$ ) at 210 nm.

**Table 5.2.** A comparison of literature LODs.

Analyte	Electrode material	LOD (nM)
<b>VA</b>	Capillary electrophoresis (CE) – carbon disk electrode	1500 <sup>36</sup>
	HPLC – pulse amperometry	25 <sup>37</sup>
<b>vanillin</b>	HPLC diamond working electrode	5.7 <sup>26</sup>
	BDD electrode	160 <sup>25</sup>
	Carbon nanotube screen-printed electrode (CNT-SPE)	1030 <sup>38</sup>
<b>FA</b>	Graphene modified GCE	200 <sup>39</sup>
	Carbon nanotubes (CNTs) modified GCE	100 <sup>40</sup>
	HPLC-pulse amperometry	50 <sup>37</sup>
<b>guaiacol</b>	HPLC diamond working electrode	3.9 <sup>26</sup>
	Nafion modified BDD electrode	200 <sup>24</sup>
	HPLC-ECD at a BDD electrode	20 <sup>32</sup>
	Laccase SPE	50 <sup>41</sup>

The calibration curves of the four analytes were constructed by plotting the peak areas against the corresponding concentrations of the standard solutions. Six concentration levels (ranging from 1-40 µM) were determined and each sample analysed in triplicate. The regression coefficient ( $R^2$ ) for all analytes was greater than 0.999. Intra-day precision was in the range of 1.85 - 3.23 % and inter-day precision in the range of

1.91 - 2.75 % (**Table 5.3**), demonstrating the suitability of this method for the analysis of guaiacol and its precursors. The calibration curves and plots are shown in **Figures 5.10 and 5.11**.

**Table 5.3.** Linear regression parameters of calibration curves and precision data for the phenolic compounds detected with HPLC-ECD at + 1.6 V.

Analyte	Linear range (μM)	Linear regression equation	Correlation coefficient ( $R^2$ )	Intra-day (%) <sup>a</sup>	Inter-day (%) <sup>b</sup>
<b>VA</b>	1-40	$I = 3.86 \times 10^{-8} C - 4.27 \times 10^{-9}$	0.999	2.62	2.42
<b>vanillin</b>	1-40	$I = 5.79 \times 10^{-8} C - 1.12 \times 10^{-8}$	0.999	2.28	2.11
<b>FA</b>	1-40	$I = 5.34 \times 10^{-8} C - 9.96 \times 10^{-8}$	0.999	3.23	2.75
<b>guaiacol</b>	1-40	$I = 8.43 \times 10^{-8} C - 2.28 \times 10^{-8}$	0.999	1.85	1.91

<sup>a</sup> Intra-day (%) calculated from five measurements within one experiment for the retention time at 50 μM of each standard.

<sup>b</sup> Inter-day (%) calculated from five measurements within five different experiments for the retention time at 50 μM of each standard.

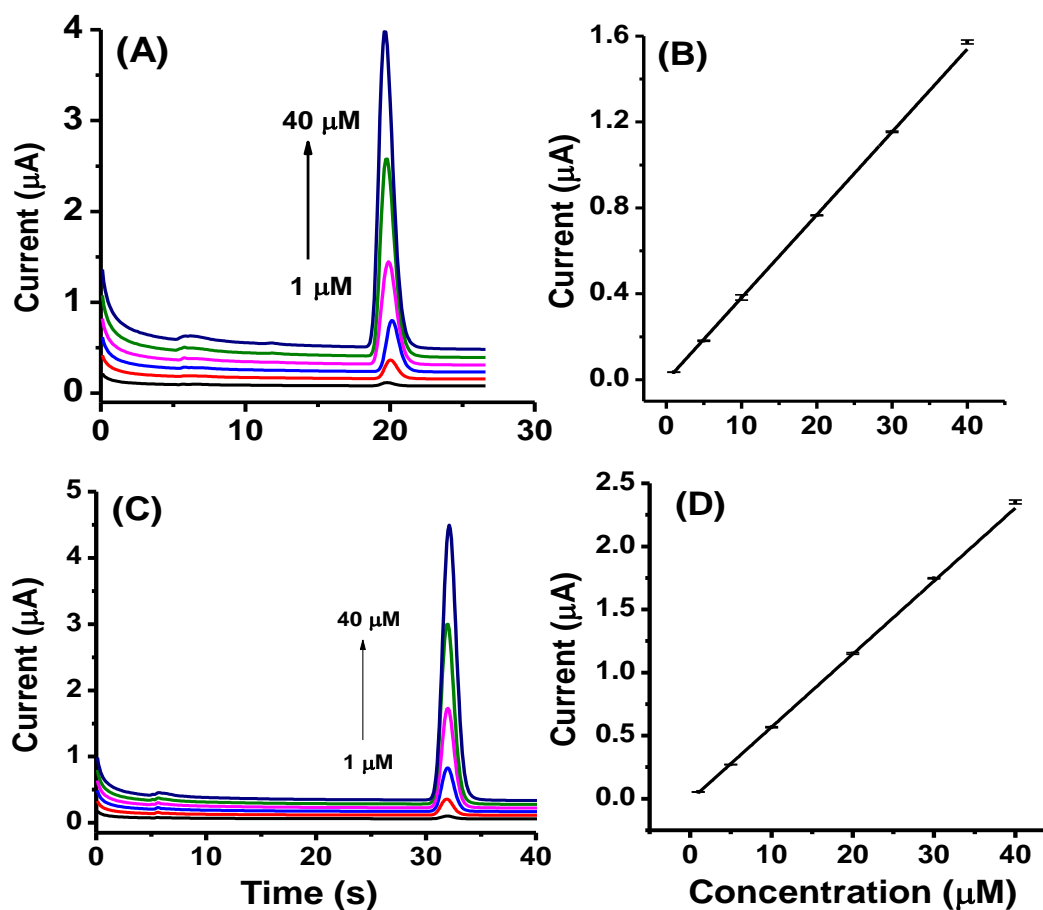


**Figure 5.10.** (A) The calibration curve and (B) plot of VA; (C) calibration curve and (D) plot of vanillin. Mobile phase: ACN:10 mM formate pH 3, 17:83 (v/v). Column: HALO C<sub>18</sub> core-shell (3 x 50 mm, 2.7 μm), flow rate: 1.3 mL/min, injection volume: 5 μL, oxidation potential: + 1.6 V on the BDD electrode vs. Pd/H<sub>2</sub>.

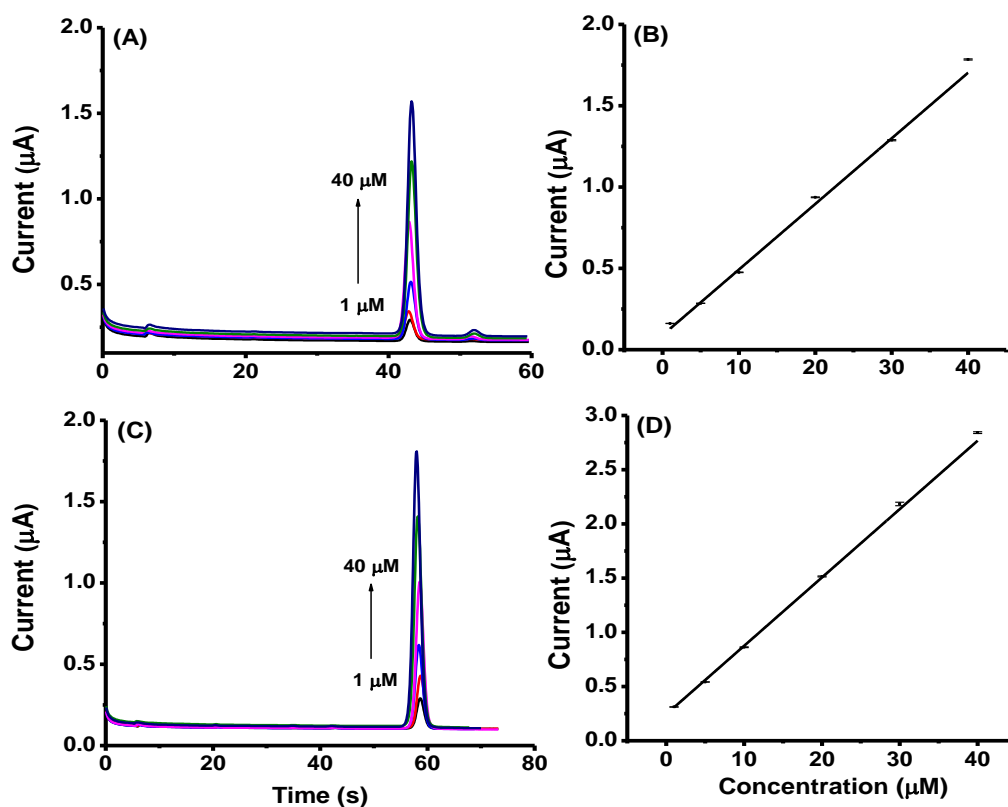


**Figure 5.11.** (A) Calibration curve and (B) plot of FA; (C) calibration curve and (D) plot of guaiacol. Mobile phase: ACN:10 mM formate pH 3, 17:83 (v/v). Column: HALO C<sub>18</sub> core-shell (3 x 50 mm, 2.7 μm), flow rate: 1.3 mL/min, injection volume: 5 μL, oxidation potential: + 1.6 V on the BDD electrode vs. Pd/H<sub>2</sub>.

### 5.3.5 Beverage sample analysis

The applicability of the proposed HPLC-ECD method was evaluated by analysing an energy drink purchased from a local supermarket (n=3). This is a well-known energy drink widely used by athletes. It consists of preservatives, flavourings, emulsifiers, sweeteners, glucose syrup, maltodextrin, citric acid, ascorbic acid, vitamins, and colouring. Before injection, the samples were filtered through an Econofltr Nylon membrane, removing any particles which may cause column degradation. Spiking experiments, with known concentrations of the four standards, were applied to identify the precursors present (**Figure 5.12**). Based on the calibration curves, concentrations of  $2.39 \pm 0.25$  μM and  $7.24 \pm 0.08$  μM of VA and vanillin, respectively, were determined. The absence of guaiacol indicates that *Alicyclobacillus* spp. were not present in this particular beverage sample. This method applies to all beverage

samples, however, depending on the composition of the sample, more detailed sample preparation may be required.

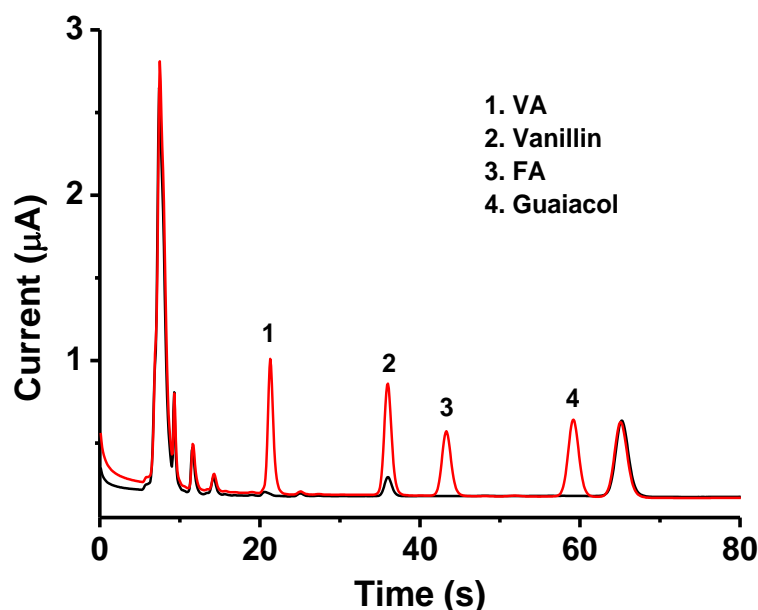


**Figure 5.12.** A representative HPLC-ECD chromatogram of an energy drink (black line) and spiked energy drink (red line) with 10  $\mu\text{M}$  of each standard. Mobile phase: ACN:10 mM formate pH 3, 17:83 (v/v). Column: HALO  $C_{18}$  core-shell (3.0 x 50 mm, 2.7  $\mu\text{m}$ ), flow rate: 1.3 mL/min, injection volume: 5  $\mu\text{L}$ , oxidation potential: + 1.6 V on the BDD electrode vs. Pd/H<sub>2</sub>.

## 5.4 Conclusions

A rapid and sensitive HPLC-ECD method was optimised for the simultaneous determination of the taint producing metabolite, guaiacol, together with its phenolic precursors; VA, vanillin, and FA. As spoilage may occur at any point during the production process, the rapid nanomolar detection achieved with this method provides manufacturers with early confirmation of beverage spoilage, thereby avoiding considerable financial losses associated with production. HPLC-ECD provides an alternative to the classical microbiological methods, significantly reducing both the preparation and analysis times. This system may also be miniaturised and applied for on-line quality control analysis. Future work will include the application of this method to beverage samples suspected of *Alicyclobacillus* spp. contamination.

## 5.5 References

1. Cerny, G., Hennlich, W., Poralla, K. Spoilage of fruit juice by bacilli: Isolation and Characterisation of the Spoilage organism. *Zeitschrift fuer Leb. Untersuchung und Forschung* **179**, 224 (1984).
2. Smit, Y., Cameron, M., Venter, P. & Witthuhn, R. C. *Alicyclobacillus* spoilage and isolation - A review. *Food Microbiol.* **28**, 331–349 (2011).
3. Chang, S. S. & Kang, D. H. *Alicyclobacillus* spp. in the fruit juice industry: history, characteristics, and current isolation/detection procedures. *Crit. Rev. Microbiol.* **30**, 55–74 (2004).
4. Orr, R. V., Shewfelt, R. L., Huang, C. J., Tefera, S., Beuchet, L. R. Detection of guaiacol produced by *Alicyclobacillus acidoterrestris* in apple juice by sensory and chromatographic analyses, and comparison with spore and vegetative cell populations. *J. Food Prot.* **63**, 1517–1522 (2000).
5. Eisele, T. A. & Semon, M. J. Best estimated aroma and taste detection threshold for guaiacol in water and apple juice. *J. Food Sc* **70**, 2003–2005 (2005).
6. Siegmund, B. & Pöllinger-Zierler, B. Odor thresholds of microbially induced off-flavor compounds in apple juice. *J. Agric. Food Chem.* **54**, 5984–5989 (2006).
7. Witthuhn, R. C., van der Merwe, E., Venter, P. & Cameron, M. Guaiacol production from ferulic acid, vanillin and vanillic acid by *Alicyclobacillus acidoterrestris*. *Int. J. Food Microbiol.* **157**, 113–117 (2012).
8. Cai, R. *et al.* Precursors and metabolic pathway for guaiacol production by *Alicyclobacillus acidoterrestris*. *Int. J. Food Microbiol.* **214**, 48–53 (2015).
9. Pettipher, G. L., Osmundson, M. E. & Murphy, J. M. Methods for the detection and enumeration of *Alicyclobacillus acidoterrestris* and investigation of growth and production of taint in fruit juice and fruit juice-containing drinks. *Lett. Appl. Microbiol.* **24**, 185–189 (1997).
10. Li, J., Huang, R., Xia, K. & Liu, L. Double antibodies sandwich enzyme-linked immunosorbent assay for the detection of *Alicyclobacillus acidoterrestris* in

- apple juice concentrate. *Food Control* **40**, 172–176 (2014).
11. Wang, Z. *et al.* Synthesis of multifunctional fluorescent magnetic nanoparticles for the detection of *Alicyclobacillus* spp. in apple juice. *Food Res. Int.* **114**, 104–113 (2018).
  12. Wang, J. *et al.* Discrimination of *Alicyclobacillus* strains using nitrocellulose membrane filter and attenuated total reflectance Fourier transform infrared spectroscopy. *J. Food Sci.* **76**, 137–142 (2011).
  13. Connor, C. J., Luo, H., McSpadden Gardener, B. B. & Wang, H. H. Development of a real-time PCR-based system targeting the 16S rRNA gene sequence for rapid detection of *Alicyclobacillus* spp. in juice products. *Int. J. Food Microbiol.* **99**, 229–235 (2005).
  14. Osopale, B. A., Witthuhn, C. R., Albertyn, J. & Oguntinyinbo, F. A. Culture dependent and independent genomic identification of *Alicyclobacillus* species in contaminated commercial fruit juices. *Food Microbiol.* **56**, 21–28 (2016).
  15. Fernández, P., Gabaldón, J. A. & Periago, M. J. Detection and quantification of *Alicyclobacillus acidoterrestris* by electrical impedance in apple juice. *Food Microbiol.* **68**, 34–40 (2017).
  16. Huang, X. C., Guo, C. F., Yuan, Y. H., Luo, X. X. & Yue, T. L. Detection of medicinal off-flavor in apple juice with artificial sensing system and comparison with test panel evaluation and GC-MS. *Food Control* **51**, 270–277 (2015).
  17. Pérez-Cacho, P. R., Danyluk, M. D. & Rouseff, R. GC-MS quantification and sensory thresholds of guaiacol in orange juice and its correlation with *Alicyclobacillus* spp. *Food Chem.* **129**, 45–50 (2011).
  18. Bianchi, F. *et al.* Characterisation of the volatile profile of orange juice contaminated with *Alicyclobacillus acidoterrestris*. *Food Chem.* **123**, 653–658 (2010).
  19. Bahçeci, K. S., Gökmen, V. & Acar, J. Formation of guaiacol from vanillin by *Alicyclobacillus acidoterrestris* in apple juice: A model study. *Eur. Food Res.*



*Technol.* **220**, 196–199 (2005).

20. Bahçeci, K. S. & Acar, J. Determination of guaiacol produced by *Alicyclobacillus acidoterrestris* in apple juice by using HPLC and spectrophotometric methods, and mathematical modeling of guaiacol production. *Eur. Food Res. Technol.* **225**, 873–878 (2007).
21. White, B., Smyth, M. R. & Lunte, C. E. Determination of phenolic acids in a range of Irish whiskies, including single pot stills and aged single malts, using capillary electrophoresis with field amplified sample stacking. *Anal. Methods* **9**, 1248–1252 (2017).
22. Luong, J. H. T., Male, K. B. & Glennon, J. D. Boron-doped diamond electrode: synthesis, characterization, functionalization and analytical applications. *Analyst* **134**, 1965–79 (2009).
23. Zhang, W. *et al.* Recent development of carbon electrode materials and their bioanalytical and environmental applications. *Chem. Soc. Rev.* **45**, 715–752 (2016).
24. Hayes, P. E., Glennon, J. D., Buzid, A. & Luong, J. H. T. Simultaneous electroanalysis of guaiacol and its analogs based on their differential complexation with  $\alpha$ -cyclodextrin on Nafion modified boron-doped diamond electrode. *Electroanalysis* **32**, 119–127 (2020).
25. Yardim, Y., Gulcan, M. & Şenturk, Z. Determination of vanillin in commercial food product by adsorptive stripping voltammetry using a boron-doped diamond electrode. *Food Chem.* **141**, 1821–1827 (2013).
26. Takahashi, M., Sakamaki, S. & Fujita, A. Simultaneous analysis of guaiacol and vanillin in a vanilla extract by using high-performance liquid chromatography with electrochemical detection. *Biosci. Biotechnol. Biochem.* **77**, 595–600 (2013).
27. Vanbeneden, N., Delvaux, F. & Delvaux, F. R. Determination of hydroxycinnamic acids and volatile phenols in wort and beer by isocratic high-performance liquid chromatography using electrochemical detection. *J. Chromatogr. A* **1136**, 237–242 (2006).

28. Zhu, Z. *et al.* Sugaring-out assisted liquid-liquid extraction coupled with high performance liquid chromatography-electrochemical detection for the determination of 17 phenolic compounds in honey. *J. Chromatogr. A* **1601**, 104–114 (2019).
29. Siangproh, W., Rattanarat, P. & Chailapakul, O. Reverse-phase liquid chromatographic determination of  $\alpha$ -lipoic acid in dietary supplements using a boron-doped diamond electrode. *J. Chromatogr. A* **1217**, 7699–7705 (2010).
30. Martins, I., de Souza Canaes, L., Doretto, K. M. & Rath, S. Boron-doped diamond electrode coupled to liquid chromatography: Application to simultaneous determination of benzodiazepines. *Electroanalysis* **22**, 455–462 (2010).
31. Martins, I. *et al.* Determination of parabens in shampoo using high performance liquid chromatography with amperometric detection on a boron-doped diamond electrode. *Talanta* **85**, 1–7 (2011).
32. Hayes, P. E., Luong, J. H. T., Gilchrist, E. S., Buzid, A. & Glennon, J. D. Profiling of phenolic flavourings using core-shell reversed-phase liquid chromatography with electrochemical detection at a boron-doped diamond electrode. *J. Chromatogr. A* **1612**, 460649 (2020).
33. Rekik, R., Hamza, M., Jaziri, M. & Abdelhedi, R. Electrochemical oxidation of vanillic acid by electro-Fenton process: Toward a novel route of protocatechuic acid electrosynthesis. *Arab. J. Chem.* **13**, 357–365 (2020).
34. Lee, J. H. Q., Lauw, S. J. L. & Webster, R. D. The electrochemical study of vanillin in acetonitrile. *Electrochim. Acta* **211**, 533–544 (2016).
35. Trabelsi, S. K., Tahar, N. B., Trabelsi, B. & Abdelhedi, R. Electrochemical oxidation of ferulic acid in aqueous solutions at gold oxide and lead dioxide electrodes. *J. Appl. Electrochem.* **35**, 967–973 (2005).
36. Cao, Y., Lou, C., Fang, Y. & Ye, J. Determination of active ingredients of *Rhododendron dauricum* L. by capillary electrophoresis with electrochemical detection. *J. Chromatogr. A* **943**, 153–157 (2002).

37. Freitas, P. V., da Silva, D. R., Beluomini, M. A., da Silva, J. L. & Stradiotto, N. R. Determination of phenolic acids in sugarcane vinasse by HPLC with pulse amperometry. *J. Anal. Methods Chem.* **2018**, (2018).
38. Chen, L., Chaisiwamongkhol, K., Chen, Y. & Compton, R. G. Rapid electrochemical detection of vanillin in natural vanilla. *Electroanalysis* **31**, 1067–1074 (2019).
39. Zhang, Y. *et al.* Rapid electrochemical detection of ferulic acid based on a graphene modified glass carbon electrode. *Anal. Methods* **5**, 3834–3839 (2013).
40. Yu, Y. Y., Wu, Q. S., Wang, X. G. & Ding, Y. P. Electrochemical determination of ferulic acid in Chinese traditional medicine Xiao Yao Pills at electrode modified with carbon nanotube. *Russ. J. Electrochem.* **45**, 170–174 (2009).
41. Freire, R. S., Duran, N., Wang, J. & Kubota, L. T. Laccase-based screen printed electrode for amperometric detection of phenolic compounds. *Anal. Lett.* **35**, 29–38 (2002).

## **Chapter 6**

### **Summary and Future work**

## 6.1 Summary

**Chapter 1** provided a background to plant secondary metabolites; their production, classification and physiological properties. The main focus of the introduction was the description of the boron-doped diamond (BDD) electrode, and amperometric and coulometric detectors used in high-performance liquid chromatography (HPLC) – electrochemical detection (ECD). Specific examples of HPLC coupled to ECD for the detection of phenolic compounds in foods, beverages and plants, were also presented.

In **Chapter 2**, the detection of guaiacol and its analogues, distinct flavours in whiskey, foods, and beverages was reported. These analytes display different inclusion complexes with  $\alpha$ -cyclodextrin ( $\alpha$ -CD) and can be separated on a Nafion modified BDD electrode. The stable Nafion layer preconcentrates the analyte- $\alpha$ -CD complexes prior to electroanalysis by square wave voltammetry (SWV) to enhance detection sensitivities. This sensing mode together with peak deconvolution successfully identified guaiacol, 4-ethylguaiacol (4-EG), three cresol isomers, and phenols in a popular whiskey brand. The results obtained were corroborated by HPLC. Anodic oxidation at + 2 V in phosphate, pH 7 proved an effective method to renew the electrode surface after its exposure to the guaiacols. This robust approach circumvents several drawbacks associated with the use of enzymes and nanomaterials for the analysis of such analytes as reported in the literature.

**Chapter 3** reports the application of a HPLC method coupled with a BDD electrode for the simultaneous determination of phenol, 4-ethylphenol (4-EP), guaiacol, 4-EG, 4-vinylguaiacol (4-VG), eugenol, and *o*, *m*- and *p*-cresol. The separation was performed on a reversed-phase HALO C<sub>18</sub> core-shell column (3.0 x 50 mm, 2.7  $\mu$ m) with a mobile phase comprising 10 mM formate, pH 3, and 15 % acetonitrile (v/v), at a flow rate of 1.5 mL/min, corresponding to a total run time of 9 min. The ECD was set at + 1.5 V vs. Pd/H<sub>2</sub> in oxidative mode. Under optimised operating conditions, good linearity was obtained for the nine phenolics with corresponding coefficients of determination ( $R^2$ ) above 0.998. The limits of detection (LODs, S/N = 3) were in the range of 10 nM - 1  $\mu$ M, with an 80-fold increase in sensitivity for guaiacol achieved with ECD over ultraviolet (UV) detection. This sensitive and selective HPLC-ECD method was successfully applied for the identification and quantification of the nine

phenolics in Islay, Irish, Scotch, and Highland whiskey samples, with significantly higher concentrations of the flavourings determined in Islay whiskey.

In **Chapter 4**, the electrochemistry of gallic acid (GA) and ellagic acid (EA), two markers of authentic whiskey, were investigated by cyclic voltammetry (CV) and SWV using a bare BDD electrode. CVs indicated that the electro-oxidation of both GA and EA were quasi-reversible processes, with their electro-oxidation significantly affected by pH. SWV, together with CDs in the electrolyte proved unsuccessful in separating the GA and EA oxidation peaks. HPLC coupled with a BDD electrode was applied for the sensitive detection of both acids. The separation was achieved with a reversed phase C<sub>18</sub> column (4.6 x 150 mm, 5 µm) using a gradient elution of 10 mM formate, pH 3 (A) and acetonitrile (ACN) (B), with a flow rate of 1.5 mL/min. The BDD electrode poised at + 1.4 V offered the LOD (S/N = 3) of 60 and 200 nM for GA and EA, respectively, considerably lower than those achieved with UV detection. The optimised method was then applied to the detection of GA and EA in Islay, Highland and Scotch whiskeys, with the highest concentrations of both acids found in a 14-year-old Highland whiskey.

**Chapter 5** described a rapid reversed-phase chromatographic separation coupled with a BDD electrode for the analysis of guaiacol (2-methoxyphenol), a food and beverage spoilage metabolite, and its precursors; vanillic acid (VA), vanillin, and ferulic acid (FA). The electro-oxidation mechanisms of such electroactive analytes were investigated by CV to form the basis for their baseline separation and detection. The optimal separation was based on a HALO C<sub>18</sub> core-shell column (3.0 x 50 mm, 2.7 µm) with a mobile phase of 10 mM formate, pH 3: acetonitrile (ACN) (83:17 v/v), at a flow rate of 1.3 mL/min. Guaiacol was separated from its three precursors in 60 s with the BDD electrode set at + 1.6 V vs. Pd/H<sub>2</sub>. The detection limits of these analytes ranged from 10 – 30 nM; about 30-fold more sensitive for guaiacol than the results obtained by UV detection. The method was applicable for the analysis of guaiacol and its precursors from a popular commercial drink.

## 6.2 Future work

Future work involves the application of computer-based modelling for HPLC method development and optimisation. Varying individual parameters one-at-a-time while the other parameters are fixed, may not lead to the optimum separation conditions<sup>1</sup>. Computer-based modelling such as the DryLab software package can efficiently predict chromatograms as multiple method parameters are varied once a small number of experiments have been carried out<sup>2,3</sup>. This has the benefit of enabling shorter method development time and minimising analysis costs, while it is particularly useful for complex samples such as whiskey.

Counterfeits of single malt whiskey are a growing problem for the industry. Recently 40 % of 55 single malt Scotch and Japanese whiskeys were found to be either counterfeits or whiskeys not distilled in the year stated, while 100 % of malt whiskeys claiming to be from 1900 or earlier were fake<sup>4</sup>. It is estimated that £41 million worth of rare whiskey currently circulating and present in collections is adulterated<sup>5</sup>. GA and EA have been identified as possible discriminants for single malt whiskey, indicative of the longer periods of malt whiskey maturation. Future work will involve the application of the developed methods to identify counterfeit whiskeys.

Food fraud (FF), a practice whereby sellers try to increase revenues through counterfeiting and adulteration processes, is estimated to affect 10 % of all foods sold, with a continuous increase expected<sup>6</sup>. Foods that are most often targeted for FF include edible oils, dairy products, beverages and meat products. HPLC coupled with mass spectrometric (MS) detection is widely used in food adulteration analysis. However, as phenolic compounds are the most common biomarkers used to identify food adulteration, chromatographic separation followed by electrochemical detection offers the advantage of high sensitivity at less cost. In particular, it provides high selectivity for phenolic compounds which may be useful for complex food samples.

These methods are also applicable for the discovery and detection of antioxidants in food and beverages. Intake of antioxidants from the diet is associated with improved health and less incidence of oxidative damage diseases such as heart disease and cancer.

This research has relied on the use of commercial silica which is the most widely used stationary phase material in liquid chromatography (LC). Its properties, including high mechanical stability, large surface area, high porosity, ease of functionality and resistance to swelling in organic solvents, make it favourable over other chromatographic supports such as alumina and titania. The bare silica surface consists of hydroxyl groups and can itself be used as a stationary phase for hydrophilic interaction liquid chromatography (HILIC). Bare silica is most often functionalised with long chain hydrocarbons to form stationary phases that are widely used in reversed-phase liquid chromatography (RPLC).

The use of natural fibres over silica as stationary phase material has a number of advantages. Natural fibres are cheap and easily accessible. Their natural characteristics mean they can be used without modification, thereby eliminating the time required for synthesis, and the use of environmentally harmful organic solvents. One key advantage as a chromatographic phase is their ability to operate at relatively low back pressures, favouring rapid separations. Additionally, they have good analyte mass transfer characteristics<sup>7</sup>. The disadvantage of natural fibres as stationary phases is their poorer column packing homogeneity.

Cellulose (cotton) and wool are the most widely studied natural fibres. They are known to contain a higher specific surface area than synthetic polymers. The degree of functionality of cellulose and wool will vary depending on the origin of the natural material. It is this natural variability, that to date, prevents their use in commercial columns for routine analysis. Cellulose consists of a surface that can function as either a hydrophilic or hydrophobic phase, and through deprotonation of the hydroxyl groups can function as a weak cation-exchanger. Wool is a proteinaceous fibre primarily harvested from sheep. It contains up to 20 amino acids and has the ability to function as a weak anion and cation exchanger, and as HILIC and RPLC phases<sup>8</sup>. Their investigation as cheap, accessible and alternative stationary phases is of future endeavours.



### 6.3 References

1. Chester, T. L. & Stalcup, A. M. Interactions between minimum run time, modifier concentration, and efficiency parameters in a high performance liquid chromatography separation. *J. Chromatogr. A* **1218**, 218–228 (2011).
2. Molnar, I. Computerized design of separation strategies by reversed-phase liquid chromatography: Development of DryLab software. *J. Chromatogr. A* **965**, 175–194 (2002).
3. Popovic, I., Ivanovic, D., Medenica, M., Malenovic, A. & Jancic-Stojanovic, B. LC determination of lercanidipine and its impurities using Drylab software and experimental design procedures. *Chromatographia* **67**, 449–454 (2008).
4. Scottish Universities Environmental Research Centre. (2020). Available at: [https://www.gla.ac.uk/research/az/suerc/news/headline\\_768202\\_en.html](https://www.gla.ac.uk/research/az/suerc/news/headline_768202_en.html). (Accessed: 3rd June 2021)
5. BBC News. (2018). Available at: <https://www.bbc.com/news/uk-scotland-scotland-business-46566703>. (Accessed: 3rd June 2021)
6. Pereira, A. G. *et al.* State-of-the-art of analytical techniques to determine food fraud in olive oils. *Foods* **10**, 1–24 (2021).
7. Marcus, R. K. Use of polymer fiber stationary phases for liquid chromatography separations: Part II - Applications. *J. Sep. Sci.* **32**, 695–705 (2009).
8. Marcus, R. K. Use of polymer fiber stationary phases for liquid chromatography separations: Part I - Physical and chemical rationale. *J. Sep. Sci.* **31**, 1923–1935 (2008).